2017-06-01

Active Control of Cylindrical Shells Using the Weighted Sum of Spatial Gradients (WSSG) Control Metric

Pegah Aslani
Brigham Young University

Active Control of Cylindrical Shells Using the Weighted Sum of Spatial Gradients (WSSG) Control Metric

Pegah Aslani

A dissertation submitted to the faculty of
Brigham Young University
in partial fulfillment of the requirements for the degree of

Doctor of Philosophy

Scott D. Sommerfeldt, Chair
Jonathan D. Blotter
Timothy W. Leishman
Kent L. Gee
John S. Colton

Department of Physics and Astronomy

Brigham Young University

ABSTRACT

Active Control of Cylindrical Shells Using the
Weighted Sum of Spatial Gradients
(WSSG) Control Metric

Pegah Aslani
Department of Physics and Astronomy, BYU
Doctor of Philosophy

Cylindrical shells are common structures that are often used in industry, such as pipes, ducts, aircraft fuselages, rockets, submarine pressure hulls, electric motors and generators. In many applications it is desired to attenuate the sound radiated from the vibrating structure. There are both active and passive methods to achieve this purpose. However, at low frequencies passive methods are less effective and often an excessive amount of material is needed to achieve acceptable results. There have been a number of works regarding active control methods for this type of structure. In most cases a considerable number of error sensors and secondary sources are needed. However, in practice it is much preferred to have the fewest number of error sensors and control forces possible. Most methods presented have shown considerable dependence on the error sensor location. The goal of this dissertation is to develop an active noise control method that is able to attenuate the radiated sound effectively at low frequencies using only a small number of error sensors and secondary sources, and with minimal dependence on error sensor location. The Weighted Sum of Spatial Gradients control metric has been developed both theoretically and experimentally for simply supported cylindrical shells. The method has proven to be robust with respect to error sensor location. In order to quantify the performance of the control method, the radiated sound power has been chosen. In order to calculate the radiated sound power theoretically, the radiation modes have been developed for cylindrical shells. Experimentally, the radiated sound power without and with control has been measured using the ISO 3741 standard. The results show comparable, or in some cases better, performance in comparison with other known methods. Some agreement has been observed between model and experimental results. However, there are some discrepancies due to the fact that the actual cylinder does not appear to behave as an ideal simply supported cylindrical shell.

Keywords: cylindrical shells, active structural acoustic control, active noise control, radiation modes

ACKNOWLEDGMENTS

I would like to express my deep gratitude to my adviser, Dr. Scott D. Sommerfeldt, for all his kind help and patience, and insightful discussions throughout my dissertation. He has been my rock, my mentor and my friend throughout my PhD and I could not have done this without him. During my time as Dr. Sommerfeldt's student, not only have I had one of my best professional learning experiences, but I have also learned about kindness, honesty and all the righteous values that dignify being a human, as well as a true scholar, from the example he has set for me. I am truly indebted and thankful to Dr. Jonathan Blotter, Dr. Timothy Leishman, Dr. Kent Gee, Dr. Traci Neilsen, Dr. John Colton and Dr. Yin Cao for their kind and countless help and guidance. I am obliged to thank Brigham Young University and everyone in this organization who supported me during my studies in Provo. Enormous thanks to my dear parents, Davood and Farzaneh, for their support and encouragement and teaching me about the value of learning and education. In spite of this long distance, their love and support has always been with me. Most sincere thanks to my dearest sister Fatemeh, who always has been an inspiration to me to seek diligence and excellence in everything I do, including this dissertation. She is the reason I can see beyond the horizon during challenging times. In the end I will never forget to thank deeply my dear friends, the Olson, Hendricks and Sommerfeldt families, for their help and support all along my studies in Provo.

Contents

List of Figures

List of Tables

Nomenclature

(z^*, θ^*) Coordinates of the primary force

(z^{**}, θ^{**}) Coordinates of the control force

α The weight applied to the first spatial gradient term

α_c Convergence factor

$\bar{P}$ Time averaged sound power

β The weight applied to the second spatial gradient term

β_c Penalty factor

δ The weight applied to the third spatial gradient term

η Viscous damping factor

γ The weight applied to the fourth spatial gradient term

γ_c Leakage factor

$\hat{e}_z$ The unit vector along the axial direction

$\hat{e}_\theta$ The unit vector along the circumferential direction

$\hat{e}_r$	The unit vector along the radial direction
Λ	Matrix of eigenvalues
λ_i	Eigenvalue
$\hat{\mathbf{H}}$	Estimate of the secondary path transfer function
$\mathbf{d}$	Vector of the spatial gradients at the sensor location due to the primary force
$\mathbf{e}$	Vector of error terms
$\mathbf{G}$	Vector of the spatial gradients at the sensor location due to the control force
$\mathbf{H}$	Secondary path transfer function
$\mathbf{Q}$	Matrix of eigenvectors
$\mathbf{r}$	Filtered reference signal
$\mathbf{u}_c$	Vector of control forces
$\mathbf{W}$	Control filter
$\mathbf{x}$	Reference signal
μ	Step size
μ_p	Poisson's ratio
ω	Angular frequency
ϕ	Coincidence angle
ρ	Density of air

ρ_s	Structural density
θ	Circumferential coordinate in the cylindrical coordinate system
ε_{ii}	Membrane strains
$\vec{r}$	Spatial vector
ζ_k	Modal damping coefficient
a	Radius
a_i	Accelerometer reading
c	Speed of sound
D	Bending stiffness
E	Young's modulus
f	Frequency in Hz
g	Secondary path transfer function
h	Thickness
H_m^2	mth order Hankel function of the second kind
h_i	Secondary path transfer function coefficients
J	Cost function
K	Membrane stiffness
k	Wavenumber

K_m mth order modified Hankel function

k_{ij} Bending strains

L Length

m Circumferential mode number

M_{zz} Function of bending moment along axis

N Number of elements representing the discretized structure

n Axial mode number

$N_{\theta\theta}$ Function of membrane forces along circumference

$N_{z\theta}$ Function of membrane forces along axis and circumference

N_{zz} Function of membrane forces along axis

p Pressure

P_3 Point load

$Q_{\theta r}$ Function of bending moments along the circumference and the normal

Q_{zr} Function of bending moments along the axis and the normal

R Radiation resistance matrix

r Radial coordinate in the cylindrical coordinate system

S The surface area of the structure

t Time in seconds

T_{60} Reverberation time to decay by 60 dB

u Structural velocity

u_z The displacement along the axial direction

u_θ The displacement along the circumferential direction

v Acoustic velocity

w The displacement along the radial (normal) direction

w_i Control filter coefficients

x First cartesian coordinate

y Second cartesian coordinate

y_i Radiation mode amplitude

y_{ci} Control output signal

Z Radiation impedance

z Third cartesian coordinate. Axial coordinate in the cylindrical coordinate system

Chapter 1

Introduction

1.1 Background

In recent decades, with the further advancement of industry and the growth of population, noise has become a more common part of everyday life. However, in many cases this can degrade the quality of life, and therefore, for safety and health reasons, the reduction of noise is often desired. Noise control methods can be divided into two main classes of passive and active methods. Passive methods, which go back longer in time, are known to reduce radiated sound by utilizing techniques that absorb or insulate the sound field [1]. Examples of passive techniques are sound barriers, damping materials, insulation, stiffened structures, etc. Passive methods are generally effective at high frequencies, while they often fail to be an effective control solution at low frequencies. This can be further explained by considering the longer wavelength at low frequencies in comparison with the shorter wavelength at higher frequencies. Furthermore, applying passive methods usually requires provisions for both additional mass and the space required [2]. At lower frequencies, in the case of transmission problems, the transmission loss obeys the mass law. In order to achieve the needed attenuation, often a considerable amount of mass is needed. In the case of problems

where attenuation through the use of absorbent materials is desired, due to the longer wavelength at low frequencies, bulkier materials are generally required in order to achieve the same amount of attenuation that can be obtained at higher frequencies. On the other hand, the performance of active control methods rely on the phase error between the ideal control signal and the control signal actually applied. At low frequencies, this phase error (which corresponds to a small timing error) is much smaller than at high frequencies, where this timing error corresponds to a much larger phase error.

As an alternative method to address these shortcomings, about eighty years ago a new control method was introduced as "Active Noise Control" (ANC) which referred to the generation of "anti noise" or "cancelling noise" [3]. This idea relied on the basic concept of destructive interference; that is, one could insert acoustical waves through a secondary source into the system, in such a way that the amplitude and phase of the secondary source results in destructive interference with the primary disturbance. This method has proven to be an effective control method at low frequencies [4]. However, unwanted noise is often created due to vibrating structures. Active noise control methods that are based on modifying the sound field are not always effective for this type of problem. About two decades ago, a form of active noise control known as "Active Structural Acoustic Control" (ASAC) was developed, with the aim of reducing radiated sound from vibrating structures more effectively. This method is based on directly controlling the vibration field of the structure rather than the sound field [5]. In this method, the control input is directly applied to the vibrating structure.

Cylindrical shells are often used in industry, such as pipes, ducts, aircraft fuselages, rockets, submarine pressure hulls, electric motors and generators [6, 7]. There are many applications in which it is desired to reduce the sound radiated from the vibrating structure. In recent years, there has been considerable research related to active control of radiated sound from cylindrical shells. Some of the early efforts for active noise control of cylindrical shells were initiated

in the 1980s by NASA, since the traditional methods dictated a mass law for low-frequency control, while for aerospace vehicles maximum noise reduction is desired with minimum additional weight [8–10]. Further work was done modeling and taking experimental data for active control of aircraft fuselages by Bullmore and others [11–17]. In the following years, some advancements were achieved in better understanding the relation between the vibration of the structure and the radiated sound. This created a breakthrough for ASAC, since understanding the interaction between the vibrating structure and the radiated pressure in the surrounding medium provides deeper understanding and direction for the development of active control metrics. This was done by decomposing the sound field into a set of orthogonal basis functions by discretizing the vibrating structure as a set of elementary radiators, and incorporating this discretization into the radiation resistance matrix, also known as the radiation resistance operator [18–20]. The solution to the eigenvalue problem of the radiation operator yields the so-called radiation modes, which present velocity patterns that radiate acoustically into the surrounding medium. The efficiency of each mode is determined by its corresponding eigenvalue [21, 22]. In other words, the radiation mode shapes are the visualization of the orthogonal basis functions used to decompose the sound field. This progress proved to be an important tool in active structural acoustic control, since it can provide a means of identifying the most efficient modes and targeting them in the ASAC approach, or of forcing the structure to couple with the weak (less efficient) modes [23–26].

In 1993, Thomas and Nelson, implemented active control of sound transmission in cylindrical shells by minimizing the vibrational energy and the acoustic potential energy. However, these methods did not prove to be very robust and effective [27,28]. In 1993, Naghshineh and Koopmann showed that the radiated power can be represented as a truncated series of the orthogonal eigenvectors of the radiation resistance matrix. They utilized this concept in order to numerically apply active control to a clamped-clamped beam, by direct minimization of the radiated power [24]. Later in 1998, they applied the same concept to find the acoustic basis functions or radiation modes

for active control of cylindrical shells, by assuming interior source points as well as source points on the surface of the structure [29]. By expressing the total radiated sound power as a quadratic function in terms of primary and secondary forces, they minimized the radiated sound power to obtain the optimal control force. The results showed reasonable amounts of attenuation, although a considerable number of error sensors was required to reproduce the results in the model.

In 1997, Pan and Hansen presented a theoretical analysis of active control of harmonic power transmission in a semi-infinite cylindrical shell using a circumferential array of error sensors and control forces. They were able to obtain good control results using several control forces [30]. In 1998, in a work by Wang and Vaicaitis, active control of sound transmission through cylindrical shells was done using velocity and sound pressure rate feedback control [31]. They observed good results with respect to the amount of attenuation achieved. However, the practicality of the method remained in question.

There are a number of studies where active vibration control has been investigated as an approach for active noise control of the cylinders [32–37, 39–41]. For instance, in 2000, with further progress in the design of actuators and sensors, Goddu and McDowell used active fiber composite actuators and the adaptive least-mean-square (LMS) algorithm to minimize the error signal from an accelerometer mounted on the cylindrical structure [42]. Even though these methods are often easy to implement, the resulting performance can be limited, since error sensors could mistakenly be located along nodal lines and limit the control performance. In another work by Song in 2002, external piezoelectric panels were used on the outer surface of thick-walled cylindrical shells in order to decrease the dependence of the control performance on the dynamic characteristics of the shell. However, some of the panel dynamics, including both the low-frequency feedthrough due to electromechanical coupling and the high-frequency resonance due to sensor dynamics, limited the performance [43].

In 2011, Jin and Liu implemented active control on a cylindrical shell through minimization of

the structural kinetic energy, as well as the radiated sound power, which resulted in global control at resonance frequencies as well as controlling spillover at off-resonance frequencies [44]. Even though this method could be modeled efficiently, the practicality of the method is almost out of the question, since a considerable number of sensors are needed to estimate the global kinetic energy, as well as the radiated sound power. In 2012, Cao and Sun used piezoelectric stack force actuators to control the sound radiated from a cylindrical shell [45]. The control forces were obtained by minimizing the axial displacement and the radiated pressure as different cost functions.

In 2013, Kim and Sohn applied active vibration control to a finite cylindrical shell in water, by designing an optimal control algorithm using micro-fiber composites as actuators and sensors [46]. In other work by Shen and Wen, active control of a cylindrical shell was implemented by applying different control methods, such as inverted displacement, velocity and acceleration-feedback control strategies [47]. At the same time, another active control approach was presented by Cao and Shi, using actuator patches and negative feedback control for a piezoelectric laminated cylindrical shell [48]. In 2014, Ma and Jin applied active structural control to a cylindrical shell, combined with a passive vibration isolation system [49]. They were able to obtain the control forces by minimization of different cost functions such as vibratory power transmitted, structural kinetic energy and acoustic radiated power.

1.2 Motivation

Different active control approaches have been developed for reducing the radiated sound power from cylindrical shells. However, there are different issues that need to be considered in comparing them. Often, the control is implemented by minimizing a choice of a quadratic objective function. In many cases, the radiated sound power or the kinetic energy of the structure (or in other words the squared velocity field of the structure) has been chosen as a cost function to be minimized and

to provide the optimal control force for the system. However, measuring and therefore minimizing the sound power or velocity field is not practical in general, since an accurate estimate of the radiated power or the velocity field requires a large number of sensors. In many cases, when it comes to an industrial scale, utilizing a large number of sensors and control forces is not practical. In some other methods in which a smaller number of sensors is required, such as some active vibration control approaches, the sensitivity to the error sensor location remains as a potential problem, since locating the error sensors on the nodal lines could degrade the control performance significantly. In addition, it is possible that simply suppressing the vibration will not effectively attenuate the radiated sound.

Therefore, it is desired to develop an active control metric that is very effective, while also requiring only a small number of error sensors and control forces. Importantly, it should have minimal sensitivity to the error sensor location. If the chosen control metric is correlated with the radiated sound power, the control results will be closer to the best possible performance for attenuating the radiated sound for any current configuration.

In a 1994 paper by Sommerfeldt and Nashif, the authors used an "Energy Density (ED)" objective function for active noise control purposes that showed better performance in comparison with other methods available [50]. It is interesting to note the properties of this function, which make it a suitable objective function. First, its spatial variance is low, meaning there was little error sensor location dependence. Second, global results are possible using localized measurements. Third, the energy density field is correlated with the global sound field. Last but not least, this is a quadratic function that allowed for the identification of a unique optimal state.

So the question arises as to whether it is possible to find an objective function with similar features for ASAC purposes. As a starting point, the velocity field and velocity gradients were observed for a simply supported plate, which included the transverse velocity field as well as the rocking motion due to the gradients in the x and y directions, along with a twisting term. Figure

1.1 presents each of the velocity fields mentioned above for a (1,1) mode of a simply supported plate. It was observed that there are some similarities between each of these velocity fields and the first four most efficient radiation modes of a simply supported plate, presented in Fig. 1.2.

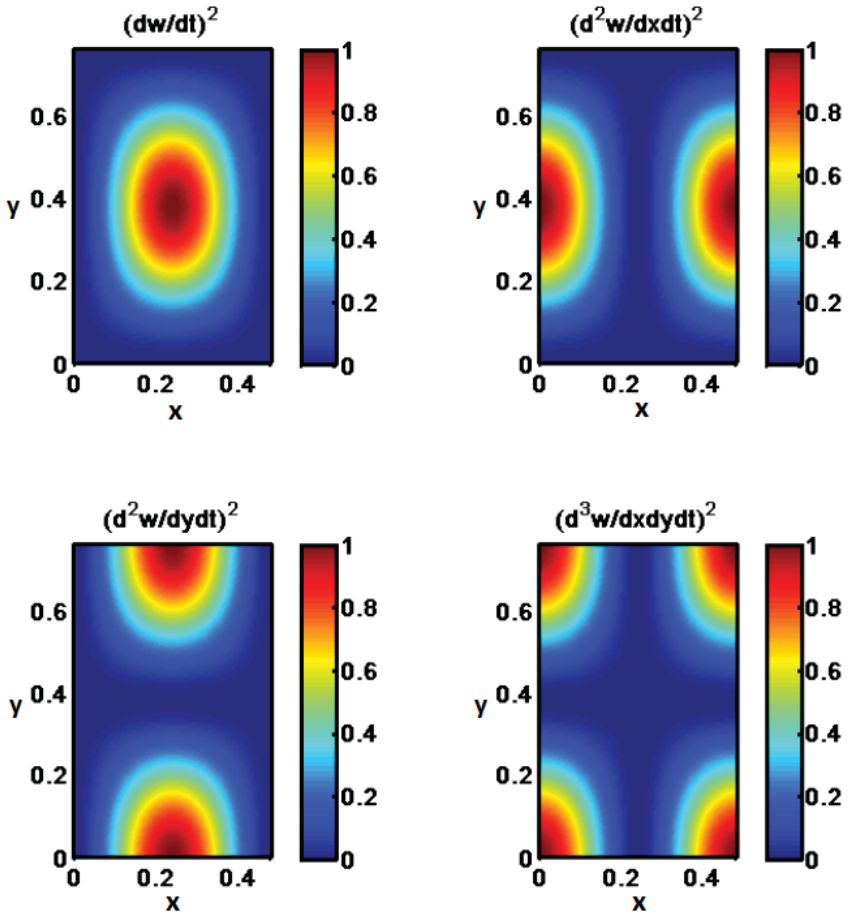

Figure 1.1 The velocity gradients for the (1,1) mode of a simply supported plate.

These similarities suggested that minimizing the velocity gradients might minimize the radiated sound power. In order to incorporate the desired features mentioned before, it was decided to add the squared velocity gradients while multiplying each term by proper weights so that it returns a function that is more uniform and less spatially variant. This has been demonstrated in Fig. 1.3 for a single mode. This uniformity should result in little sensitivity to error sensor locations.

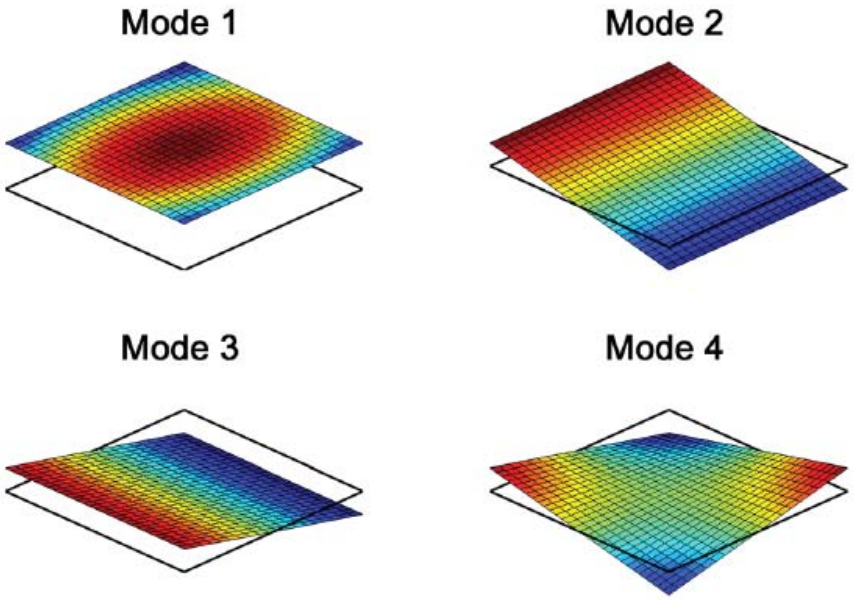

Figure 1.2 The four most efficient radiation modes for a simply supported plate.

Furthermore, since the individual terms were related to radiation modes, it was hoped it would result in effective global control. The resulting control metric was referred to as *Vcomp* and is given by [51]

$$Vcomp = \alpha(\frac{\partial w}{\partial t})^2 + \beta(\frac{\partial^2 w}{\partial x \partial t})^2 + \delta(\frac{\partial^2 w}{\partial y \partial t})^2 + \gamma(\frac{\partial^3 w}{\partial x \partial y \partial t})^2. \tag{1.1}$$

The implementation of this method requires only four closely-spaced sensors to detect the gradient terms through the finite-difference method. Since a harmonic excitation is considered, the velocity gradients are actually spatial gradients that are scaled and therefore Eq. (1.1) could also be written as

$$WSSG = \alpha(w)^2 + \beta(\frac{\partial w}{\partial x})^2 + \delta(\frac{\partial w}{\partial y})^2 + \gamma(\frac{\partial^2 w}{\partial x \partial y})^2, \tag{1.2}$$

which was then referred to as the weighted sum of spatial gradients (WSSG) [52]. This control

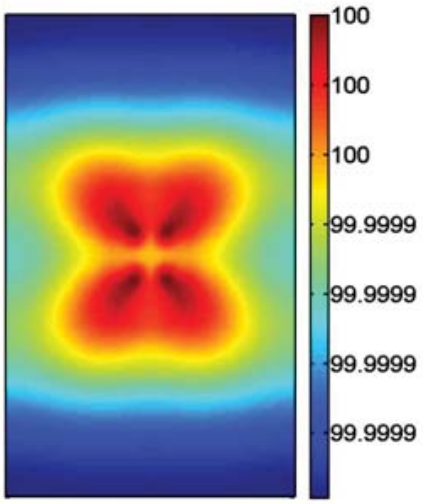

Figure 1.3 Uniformity of the Vcomp function when utilizing proper weights for a (1,1) mode of a simply supported plate. Note the very small range on the color axis.

metric was then developed for the case of flat panels or plates [53–55].

1.3 Objective of this dissertation

The focus of this dissertation is to develop and investigate an ASAC approach for thin-walled cylindrical shells, both theoretically and experimentally, which contains the desired features mentioned previously and is able to effectively attenuate the radiated sound power. A weighted sum of spatial gradients (WSSG) control metric will be developed for this type of geometry. This ASAC method is designed to achieve control approximating the minimization of the radiated power. Its main objective is to obtain global control of the radiated sound power, using a minimal number of sensors and control forces, while having minimal sensitivity to error sensor location. It is also desired to improve on some of the issues discussed above, such as convenience and accuracy, as well as to avoid control spill-over effects.

In order to quantify the performance of the control method, a suitable assessment metric is

needed. The radiated sound power has been chosen as this quantifying metric. In order to calculate the radiated sound power numerically, it is useful to develop the radiation modes for this type of geometry, something that has not been fully developed in the literature. Experimentally, the radiated sound power is measured using the methods of the ISO 3741 standard [56].

1.4 Outline of the dissertation

In the following chapter of this dissertation, the methodology and the procedures necessary to develop and investigate the WSSG control metric is reviewed. In Chapter 3, the concept of radiation modes is introduced. In addition, the development of radiation modes, as well as the results for the radiation mode shapes for cylindrical shells, are presented. Subsequently, the numerical model of the cylindrical shell, as well as the control metric used and the control results obtained, are presented in Chapter 4. Chapter 5 contains the details of the experimental setup, as well as the experimental results. Finally, Chapter 6 presents the conclusions of this dissertation and some recommendations for future work.

Chapter 2

Methodology and procedures

2.1 Theoretical background

2.1.1 Structural behavior

In order to control the sound radiated from a vibrating structure, it is important to first understand its governing dynamics and structural response. This also provides useful information for analyzing the interaction between the structure and the surrounding medium. There have been extensive studies related to shell theory; for a comprehensive review, the reader is referred to the work of Leissa [57], or more recently, Amabili and Paidoussis [58]. However, this work focuses on simply supported cylindrical shells and only a brief history of the related work is mentioned here.

In 1888, Love used the Kirchhoff assumptions for plates and established a theory called the classic theory of thin shells, which is in fact, an extension to Euler-Bernoulli beam theory [59]. Love considered a middle surface plane with a thin elastic layer of material on either side of the plane. This theory is now known as Love's first approximation theory and has been used as a foundation for many other theories, which were developed later. In the 1930s, Donnell and Mushtari developed a theory in which both membrane and bending actions and their interactions

were considered. This is one of the simplest forms of shell theory, and includes simplifications such as neglecting the tangential displacements and their derivatives in the bending component of the strain. This theory provides a good approximation for shallow shells. However, it does not provide sufficient accuracy for circular cylindrical or deep shells [60]. The term deep shells refers to shells that are thin with respect to their radii of curvature and whose deflections are reasonably small. In 1959, Timoshenko presented a theory based on Love's theory presented in 1944, which then became known as Love-Timoshenko shell theory. One of the simplifications made in this theory was to neglect the ratio of the radial coordinate to the radius of the curvature in the strain equations [61].

In 1962, Flugge developed Love's theory further using higher orders. Using his theory, one could obtain the strain-displacement relations and changes of curvature of the middle surface of a cylindrical shell [62]. For the interested reader, there are additional works regarding the vibration of a simply supported cylindrical shell [63–75]. In 1981, Soedel was able to apply normal solutions to Love's theory and obtained three closed-form solutions for the natural frequencies and mode shape coefficients for a simply supported circular cylindrical shell [76]. In a work by Farshidianfar and Oliazadeh, different shell theories such as Donnell-Mushtari, Love-Timoshenko and Soedel were compared. They reported that some theories such as Love-Timoshenko, Arnold-Warburton, Flugge Byrne-Lur'ye, Reissner-Naghdi-Berry, Sanders, Vlasov, and Soedel produce the same results with respect to predicting the natural frequencies and mode shapes of the shell. Based on experimental data, they also stated that Soedel's model was one of the theories that provided more accurate results than some of the other theories and suggested that the Donnell-Mushtari theory is not as precise as other theories [77].

For the purpose of this dissertation, Soedel's model of a simply supported shell has been chosen. The reason for this choice has been the simplicity of the closed-form solutions which facilitates the numerical modeling of the shell, as well as having sufficient accuracy. In the

following section, Soedel's model of a simply supported shell will be briefly discussed.

2.1.2 Soedel's model of a simply supported circular cylindrical shell

2.1.2.1 Love's equations of motion for a cylindrical shell

The coordinate system used in Soedel's shell theory consists of the curvilinear coordinates defined on the neutral surface. As defined by Euler-Bernoulli beam theory, the neutral surface is within the thickness of the cylinder and is the surface between the areas of compression and tension where no stress or strain exists. The curvilinear coordinates describe the longitudinal displacement of the shell in the tangential direction along the axis, $\hat{e}_z$, the tangential displacement along the circumference, $\hat{e}_\theta$, as well as the transverse displacement along the normal direction of the shell, $\hat{e}_r$ [78]. In order to assign notations to the displacement along each of these directions, the displacement along the axis will be referred to as u_z, the displacement along the circumference as u_θ, and the normal displacement will be referred to as w.

Having defined a suitable coordinate system, Soedel developed the strain-displacement as well as the strain-stress relations [79]. In developing these relations, some simplifications and approximations were considered, such as neglecting the shear deflections and assuming that the displacement along the tangential directions varied linearly through the shell thickness [80].

Membrane forces and the bending moments are obtained by integrating all stresses acting on the shell along the normal direction. Assuming a thin-walled shell, an additional Love simplification can be applied by neglecting the term containing the ratio of radial curvilinear coordinate to the radius of curvature [81].

In order to better understand the effect of moments and forces, Soedel divided the strains into groups of membrane strains (ε_{ii}, where $i = 1, 2, 3$) that were independent of normal curvilinear coordinates, as well as the bending strains i.e., change-in-curvature (k_{ij}, where $i, j = 1, 2, 3$), which are proportional to the normal curvilinear coordinate. Using Hamilton's principle and

applying all these simplifications while taking into account all the membrane forces and bending moments, Soedel derives Love's equation of motion for a thin-walled cylindrical shell due to any pressure load [82].

2.1.2.2 Soedel's model for a simply supported cylindrical shell

Figure 2.1 shows a schematic of a simply supported shell with length L and radius a.

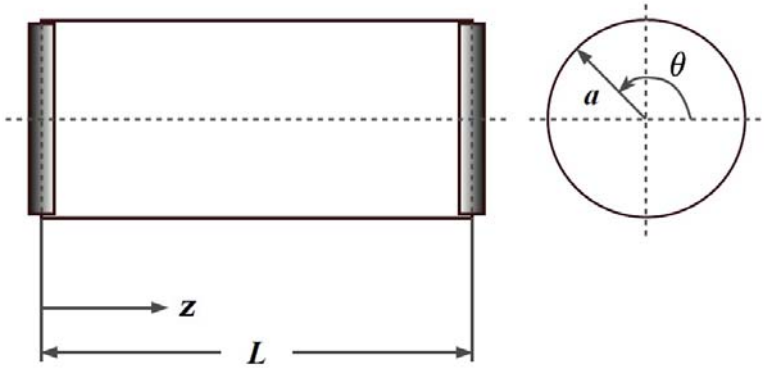

Figure 2.1 A simply supported circular cylindrical shell.

The simply supported boundary condition requires that

$$\begin{aligned} w\,(z = 0,\, \theta,\, t) &= 0 \\ u_\theta\,(z = 0,\, \theta,\, t) &= 0 \\ M_{zz}(z = 0,\, \theta,\, t) &= 0 \\ N_{zz}(z = 0,\, \theta,\, t) &= 0 \end{aligned} \tag{2.1}$$

as well as

$$\begin{aligned} w\,(z\,=\,L,\,\theta,\,t) &= 0 \\ u_\theta\,(z\,=\,L,\,\theta,\,t) &= 0 \\ M_{zz}(z\,=\,L,\,\theta,\,t) &= 0 \\ N_{zz}(z\,=\,L,\,\theta,\,t) &= 0, \end{aligned} \tag{2.2}$$

where N_{zz} is the membrane force due to the stress along the axis and M_{zz} is the bending moment in the axial direction. Applying the simply supported boundary condition, the equations of motion for the cylindrical shell can be written as

$$\begin{aligned} \tfrac{\partial N_{zz}}{\partial z} + \tfrac{1}{a}\tfrac{\partial N_{z\theta}}{\partial \theta} - \rho h \tfrac{\partial^2 u_z}{\partial t^2} &= 0 \\ \tfrac{\partial N_{z\theta}}{\partial z} + \tfrac{1}{a}\tfrac{\partial N_{\theta\theta}}{\partial \theta} + \tfrac{Q_{\theta r}}{a} - \rho h \tfrac{\partial^2 u_\theta}{\partial t^2} &= 0 \\ \tfrac{\partial Q_{zr}}{\partial z} + \tfrac{1}{a}\tfrac{Q_{\theta r}}{\partial \theta} - \tfrac{N_{\theta\theta}}{a} - \rho h \tfrac{\partial^2 w}{\partial t^2} &= 0, \end{aligned} \tag{2.3}$$

where $N_{\theta\theta}$ is a function of the membrane force along the circumferential direction and $N_{z\theta}$ is a function of the membrane forces along the axis and circumference. In addition, $Q_{\theta r}$ is a function of bending moments along the normal and the circumferential directions, and Q_{zr} is a function of bending moments along the normal and the axial directions. Finally, ρ is the density of the shell and h is the shell thickness.

Soedel assumed the following time harmonic solution

$$\begin{aligned} u_z(z,\,\theta,\,t) &= U_z(z,\,\theta)e^{j\omega t} \\ u_\theta(z,\,\theta,\,t) &= U_\theta(z,\,\theta)e^{j\omega t} \\ w(z,\,\theta,\,t) &= W_0(z,\,\theta)e^{j\omega t}, \end{aligned} \tag{2.4}$$

where

$$\begin{aligned} U_z(z,\,\theta) &= A\,\cos\left(\tfrac{n\pi z}{L}\right)\cos(m(\theta-\phi)) \\ U_\theta(z,\,\theta) &= B\,\sin\left(\tfrac{n\pi z}{L}\right)\sin(m(\theta-\phi)) \\ W_0(z,\,\theta) &= C\,\sin\left(\tfrac{n\pi z}{L}\right)\cos(m(\theta-\phi)). \end{aligned} \tag{2.5}$$

Here, n is the axial mode number, m is the circumferential mode number and ϕ is an arbitrary phase. Substituting this solution into Eq. (2.3) yields

$$\begin{bmatrix} \rho h\omega^2 - k_{11} & k_{12} & k_{13} \\ k_{21} & \rho h\omega^2 - k_{22} & k_{23} \\ k_{31} & k_{32} & \rho h\omega^2 - k_{33} \end{bmatrix} \begin{Bmatrix} A \\ B \\ C \end{Bmatrix} = 0, \tag{2.6}$$

where the bending strains are defined as

$$\begin{aligned} k_{11} &= K\left[\left(\tfrac{n\pi}{L}\right)^2 + \tfrac{1-\mu_p}{2}\left(\tfrac{m}{a}\right)^2\right] \\ k_{12} &= k_{21} = K\tfrac{1+\mu_p}{2}\,\tfrac{n\pi}{L}\,\tfrac{m}{a} \\ k_{13} &= k_{31} = \tfrac{\mu_p K}{a}\tfrac{n\pi}{L} \\ k_{22} &= \left(K + \tfrac{D}{a^2}\right)\left[\tfrac{1-\mu_p}{2}\left(\tfrac{n\pi}{L}\right)^2 + \left(\tfrac{m}{a}\right)^2\right] \\ k_{23} &= k_{32} = -\tfrac{K}{a}\tfrac{m}{a} - \tfrac{D}{a}\tfrac{m}{a}\left[\left(\tfrac{n\pi}{L}\right)^2 + \left(\tfrac{m}{a}\right)^2\right] \\ k_{33} &= D\left[\left(\tfrac{n\pi}{L}\right)^2 + \left(\tfrac{m}{a}\right)^2\right]^2 + \tfrac{K}{a^2}, \end{aligned} \tag{2.7}$$

where K is the membrane stiffness and is defined as $K = Eh/(1-\mu_p^2)$ and D is the bending stiffness defined as $D = Eh^3/12(1-\mu_p^2)$. Here, E is Young's modulus and μ_p is Poisson's ratio.

In order to solve for the natural frequencies, one can reach the following eigen-equation by setting the determinant of Eq. (2.6) equal to zero, i.e.,

$$\omega^6 + q_1\omega^4 + q_2\omega^2 + q_3 = 0, \tag{2.8}$$

where

$$\begin{aligned} q_1 &= -\tfrac{1}{\rho h}\,(k_{11} + k_{22} + k_{33}) \\ q_2 &= \tfrac{1}{(\rho h)^2}\,(k_{11}k_{33} + k_{22}k_{33} + k_{11}k_{22} - k_{23}^2 - k_{12}^2 - k_{13}^2) \\ q_3 &= \tfrac{1}{(\rho h)^3}\,(k_{11}k_{23}^2 + k_{22}k_{13}^2 + k_{33}k_{12}^2 + 2k_{12}k_{23}k_{13} - k_{11}k_{22}k_{33}). \end{aligned} \tag{2.9}$$

Solving the eigen-equation, the solution for the natural frequencies will be

$$\begin{aligned} \omega_{1nm}^2 &= -\tfrac{2}{3}\sqrt{q_1^2 - 3q_2}\,\cos\tfrac{\alpha_s}{3} - \tfrac{q_1}{3} \\ \omega_{2nm}^2 &= -\tfrac{2}{3}\sqrt{q_1^2 - 3q_2}\,\cos\tfrac{\alpha_s + 2\pi}{3} - \tfrac{q_1}{3} \\ \omega_{3nm}^2 &= -\tfrac{2}{3}\sqrt{q_1^2 - 3q_2}\,\cos\tfrac{\alpha_s + 4\pi}{3} - \tfrac{q_1}{3}, \end{aligned} \tag{2.10}$$

where

$$\alpha_s = \cos^{-1}\frac{27q_3 + 2q_1^3 - 9q_1q_2}{2\sqrt{(q_1^2 - 3q_2)^3}}. \tag{2.11}$$

Therefore, for every set of mode numbers n,m there are three natural frequencies, where the lowest is associated with the transverse displacement component, whereas the other two are usually an order of magnitude higher and correspond to the displacements in the tangential directions. For

every set of mode numbers n,m, there are different amplitude coefficients, given by A,B and C determined by the subscript $(i = 1,2,3)$ corresponding to each of the natural frequencies. One can solve for these coefficients in terms of C, i.e,

$$\begin{aligned} \frac{A_i}{C_i} &= -\frac{\begin{vmatrix} k_{13} & k_{12} \\ k_{23} & \rho h\omega_{inm}^2 - k_{22} \end{vmatrix}}{\kappa}, \\ \frac{B_i}{C_i} &= -\frac{\begin{vmatrix} \rho h\omega_{inm}^2 - k_{11} & k_{13} \\ k_{21} & k_{23} \end{vmatrix}}{\kappa}, \end{aligned} \tag{2.12}$$

where

$$\kappa = \begin{vmatrix} \rho h\omega_{inm}^2 - k_{11} & k_{12} \\ k_{21} & \rho h\omega_{inm}^2 - k_{22} \end{vmatrix}. \tag{2.13}$$

Therefore, the three natural modes associated with the three solutions of the natural frequencies obtained from the eigen-equation are

$$\begin{Bmatrix} U_z \\ U_\theta \\ W_0 \end{Bmatrix}_i = C_i \begin{Bmatrix} \frac{A_i}{C_i} \cos\left(\frac{n\pi z}{L}\right) \cos(m(\theta-\phi)) \\ \frac{B_i}{C_i} \sin\left(\frac{n\pi z}{L}\right) \sin(m(\theta-\phi)) \\ \sin\left(\frac{n\pi z}{L}\right) \cos(m(\theta-\phi)) \end{Bmatrix}. \tag{2.14}$$

2.1.3 Forced vibration of circular cylindrical shell by modal expansion

Finding the natural frequencies, and subsequently the natural modes, sets the framework for a complete orthogonal set of basis functions that can span a vector space. Hence, one of the main purposes for finding the natural frequencies and their corresponding mode shapes is to be able to

describe any general behavior of the structure, for instance in the presence of a force load. This can be done through modal expansion, with the forces presumably independent of the motion of the shell. When a force excitation is applied to the structure, all the modes are excited but with different modal amplitudes. A cylindrical shell is a continuous system with infinite degrees of freedom. Therefore, one can describe the general solution for the structural response as a superposition of all the natural modes. Using the technique of superposition of orthogonal modes, Soedel gives the general steady-state, transverse displacement of a simply supported shell as

$$w(z,\ \theta,\ t)\ =\ \frac{2P_3}{\rho haL\pi}\ \sum_{m=1}^{\infty}\sum_{n=1}^{\infty}\frac{\sin(n\pi z^*/L)\sin(n\pi z/L)\ \cos m(\theta-\theta^*)}{\varepsilon_m\omega_{nm}^2\sqrt{[1\ -\ (\omega/\omega_{nm})^2]^2\ +\ 4\zeta_{nm}^2(\omega/\omega_{nm})^2}}\ \sin(\omega t\ -\ \phi_{nm}), \tag{2.15}$$

where P_3 is the normal point load, (z^*, θ^*) are the coordinates where the point load is applied and ω is the driving frequency of the force load [83]. The Neumann factor ε_m is defined as

$$\varepsilon_m\ =\ \begin{cases} 1, & m \neq 0 \\ 2, & m = 0 \end{cases} \tag{2.16}$$

and ζ_{nm} is called the modal damping coefficient defined as

$$\zeta_{nm}\ =\ \frac{\eta}{2\rho h\omega_{nm}}, \tag{2.17}$$

where η is the viscous damping ratio. Treating the shell as a simple harmonic oscillator, the solutions can result in a subcritical, critical and supercritical damping case, depending on whether $\zeta_{nm} < 1$, $\zeta_{nm} = 1$ or $\zeta_{nm} > 1$, respectively.

In Eq. (2.15), the phase lag ϕ_{nm} is defined as

$$\phi_{nm}\ =\ \tan^{-1}\frac{2\zeta_{nm}(\omega/\omega_{nm})}{1\ -\ (\omega/\omega_{nm})^2}. \tag{2.18}$$

Equation (2.15) is the expression that will be used in this dissertation to represent the vibrational response of the cylindrical shell.

2.1.4 The weighted sum of spatial gradients

Within the last few decades, there has been great interest in attenuating the radiating sound from structures and being able to control the structural vibration in such a way that it will decrease the sound radiation. This has led to the development of Active Structural Acoustic Control (ASAC). In many applications regarding the reduction of sound from vibrating structures, it is often more efficient to control the structure directly, in order to modify the vibration field that radiates sound, rather than directly attenuating the sound field itself. ASAC was first introduced in 1987 by Fuller, and additional research has been done since then [84–115] . The central aspect of an active control process is optimization with respect to a cost function (objective function), and hence, the cost function plays a principle role in an active control system.

For active control of sound fields, the radiated pressure is generally the primary metric for sensing and optimization. Specific applications may require either a single microphone or an array of microphones. In many applications, where the radiated or the transmitted sound is due to a vibrating structure, such as an engine in a confined space, there are limitations on the compactness of the sensing and the control system. In many cases, it is much easier to use structural sensors than acoustical sensors, in terms of designing a compact control system. In addition, it is often more efficient to control the vibrating structure to reduce the sound radiated than trying to attenuate the sound field after the sound radiation. These factors have motivated the desire to develop cost functions that utilize structural error signals that will result in efficient attenuation of the sound radiation.

There have been numerous studies focused on controlling the vibration of structures, using an array of structural sensors and controlling the vibration at discrete points [89, 116–118]. However,

it is important to note that controlling the vibration alone does not guarantee optimal, or even significant, sound power attenuation. Therefore, it is important to understand the mechanism by which the vibrating structure couples with the surrounding medium to create acoustic radiation. Hence, for an effective ASAC approach, the cost function should not only utilize structural metrics, but also result in efficient attenuation of the acoustic radiation.

One of the early methods developed to achieve this was the volume velocity control metric, in which the square of the integrated volume velocity is minimized [117, 119]. The radiated sound power is dependent on the structural volume velocity, so this method has demonstrated some effectiveness. However, sensing and obtaining a reasonable estimate of the volume velocity requires a global measurement, which is not practical. An array of sensors is typically used to approximate this, but the number of sensors required can grow very quickly. Similar approaches have been taken in controlling the global kinetic energy, the global potential energy and the radiated sound power of the vibrating structure [27, 28, 120]. However, they all share a common shortcoming in the sense that they all need global sensing techniques. Because of this, a valuable cost function would be one that results in global attenuation using only local measurements. But, even when using local measurements, there can be limitations on sensor locations, due to the presence of nodal lines and sensing issues, just as is the case for sound field control.

As noted by Sommerfeldt and Nashif, the optimal placement of sensors is a function of the cost function [50]. They developed an active control metric that proved to perform better than other commonly used methods. In fact, it is very instructive to take a closer look at their work which was designed for controlling an enclosed sound field. While a cost function with a simple acoustic metric, such as the squared pressure, can create control in the vicinity of the microphones, one may typically encounter sound power enhancement at other locations, resulting in localized control. In addition, the sensors must be located away from nodal regions for effective control. To address these challenges, Sommerfeldt and Nashif developed a cost function consisting of the

acoustic energy density [121, 122]. This was a very effective choice, since the dependence of the cost function on more than one acoustic variable made it robust with respect to sensing capabilities. The energy density of the enclosed field is a more uniform field that greatly reduces the location dependence of the error sensors and provided global results by performing local measurements. The cost function also had a quadratic form which is a desirable characteristic of the control system, since it ensures the presence of a global minimum. While this proved to be very effective for the sound field control, it is not directly applicable for ASAC, since it does not utilize structural control and sensing. That being the case, it is desirable to acquire a cost function that is not only robust and effective in giving the best possible attenuation of the radiated sound power, but would also rely on a compact and local sensing technique, with minimal dependence on the sensor location. Furthermore, it would encompass a quadratic form to ensure a global optimal solution and most importantly, the cost function would be correlated with the radiated sound power.

A key aspect in making a cost function robust with respect to sensor location is multi-parameterizations. In 2010, Fisher developed a preliminary cost function for active structural acoustic control of plates that would incorporate all the key factors mentioned above. In spite of its rather easy implementation, it has shown promising correlations with the radiated sound power [26]. The development of this metric involved studying the squared velocity gradients for the first mode of a simply supported plate. These velocity gradients contained the "breathing motion," two "rocking" motions in the perpendicular directions of the plate, and a twisting term which incorporates the mixed gradients in both directions. Figure 2.2 demonstrates each of the velocity gradient fields for the (1,1) mode of a simply supported plate.

Intuitively, the next step was to find any links between the structure's vibration field and how it is able to couple with the acoustic medium to radiate sound. This leads to the concept of radiation modes, which are a set of orthogonal basis functions that can be used to decompose the radiated sound field. Using the space spanned by the radiation modes, one can expand the radiated power

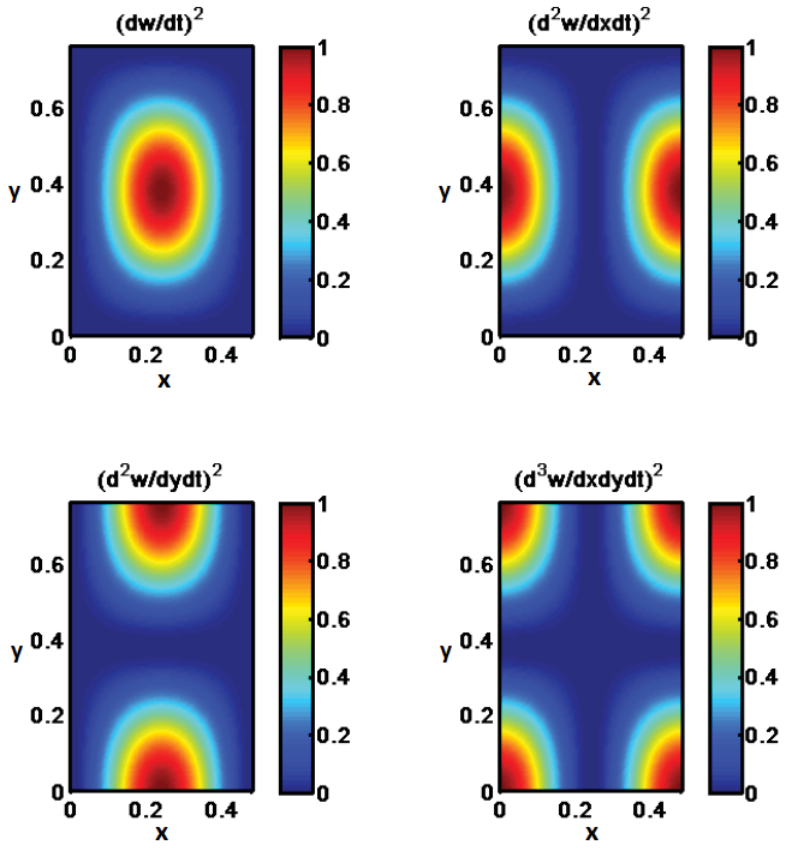

Figure 2.2 The squared velocity gradient fields for the (1,1) mode of a simply supported plate.

in terms of radiation modes, and therefore use modal expansion in order to calculate the radiated sound power, where the modal coefficients are determined by the structural vibration. These are referred to as independent velocity distributions that are attributed to the eigenvectors of the radiation resistance matrix. Each of these modes is able to radiate sound in accordance with its corresponding efficiency that is determined by its corresponding eigenvalue. This concept will be discussed in further detail in Chapter 3. Searching for connecting links between the vibration field and the sound radiation led to a comparison of the four velocity gradient fields to the first four most efficient radiation modes for a plate. Figure 2.3 presents the first four most efficient radiation modes for a plate.

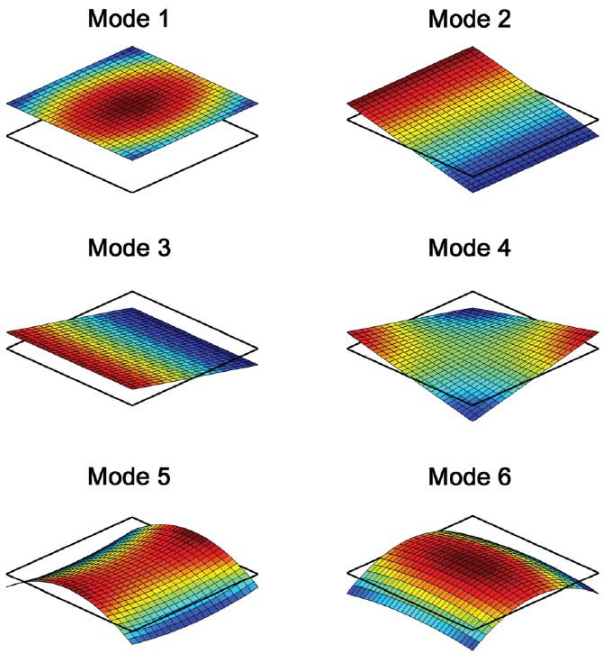

Figure 2.3 The four most efficient radiation modes of a plate.

A quick comparison between Figs. 2.3 and 2.2 reveals a noticeable similarity between the radiation modes and the velocity gradients. This suggested that controlling and minimizing the gradient terms could lead to attenuating the radiated sound power. Fisher incorporated these velocity gradients into a cost function with proper weighting so that when added together, it would create a uniform field, thereby reducing spatial variance. One can see this by looking at Fig. 2.2 and observing that by utilizing proper weights, the anti-nodal regions of one term can fill in the nodal regions of another term when the terms are added together. It was shown that the proper weights are proportional to the inverse of the structural wavenumber squared, for the case of a single mode. The addition of the velocity gradients in a squared form gives the cost function the desired quadratic form. The cost function obtained by this addition was named V_{comp}, standing for the composite velocity field [51]. This cost function is shown in Fig. 2.4. One can note its uniformity by looking at the range of the colorbar shown in the figure.

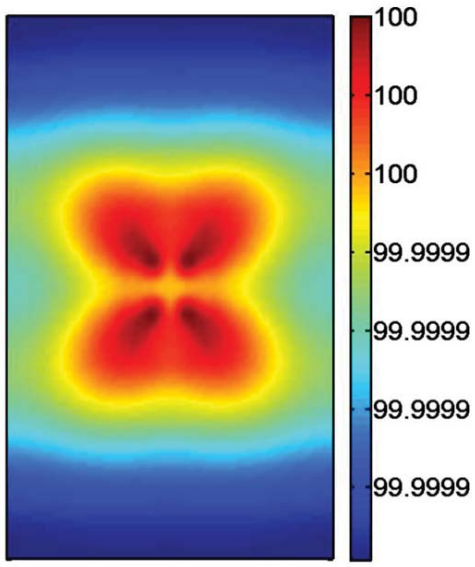

Figure 2.4 The cost function, V_{comp}.

The spatial uniformity of the V_{comp} cost function contributes to this metric being robust with respect to the error sensor location. In 2014, this method was experimentally validated for a simply supported plate by Hendricks [52]. It was also renamed as the "Weighted Sum of Spatial Gradients" (WSSG) in order to more accurately describe the quantity, since the velocity gradients were in fact based on the spatial derivatives of the vibration field. This method has also been investigated for the case of a clamped plate, as well as for a ribbed plate [55]. The experimental results suggest reasonable agreement between the modeled control and the experimental results. In 2015, Cao showed that the weights used for the WSSG control metric can be optimized in order to enhance the control performance. The results showed that there is a wide range for nearly optimized weights and also that they can be parameterized in terms of flexural rigidity and the mass per unit area. They presented both theoretical and experimental results, implementing the optimized weights for control of simply supported and clamped plates, which showed more effective control performance overall [53, 54].

It was the objective of this dissertation to develop and model the weighted sum of spatial gradients (WSSG) control metric for a simply supported cylindrical shell and to validate it experimentally. Viewing an unwrapped cylinder as a plate, one can envision modeling the WSSG control metric for a simply supported cylindrical shell by taking the spatial gradients along the primary axes of the cylinder, i.e., z and θ, where Eq. (2.15) will be utilized in describing the overall vibration field of the shell using a point-force excitation.

The spatial gradient terms will contain a breathing term, which consists of only the normal displacement w, two "rocking" terms with derivatives along the z and θ directions, i.e., $\partial w/\partial z$ and $\partial w/\partial \theta$, and a twisting term consisting of derivatives in both directions, $\partial^2 w/\partial z \partial \theta$. These terms are described analytically in the following equations:

$$w(z,\theta,t) = \frac{2P_3}{\rho haL\pi} \sum_{m=1}^{\infty}\sum_{n=1}^{\infty} \frac{\sin(n\pi z^*/L)\sin(n\pi z/L)\cos m(\theta-\theta^*)}{\varepsilon_m \omega_{nm}^2 \sqrt{[1-(\omega/\omega_{nm})^2]^2 + 4\zeta_{nm}^2(\omega/\omega_{nm})^2}} \sin(\omega t - \phi_{nm}) \quad (2.19)$$

$$\frac{\partial w(z,\theta,t)}{\partial z} = \frac{2P_3}{\rho haL\pi} \sum_{m=1}^{\infty}\sum_{n=1}^{\infty} \frac{n\pi}{L} \frac{\sin(n\pi z^*/L)\cos(n\pi z/L)\cos m(\theta-\theta^*)}{\varepsilon_m \omega_{nm}^2 \sqrt{[1-(\omega/\omega_{nm})^2]^2 + 4\zeta_{nm}^2(\omega/\omega_{nm})^2}} \sin(\omega t - \phi_{nm}) \quad (2.20)$$

$$\frac{\partial w(z,\theta,t)}{\partial \theta} = \frac{2P_3}{\rho haL\pi} \sum_{m=1}^{\infty}\sum_{n=1}^{\infty} -m \frac{\sin(n\pi z^*/L)\sin(n\pi z/L)\sin m(\theta-\theta^*)}{\varepsilon_m \omega_{nm}^2 \sqrt{[1-(\omega/\omega_{nm})^2]^2 + 4\zeta_{nm}^2(\omega/\omega_{nm})^2}} \sin(\omega t - \phi_{nm}) \quad (2.21)$$

$$\frac{\partial^2 w(z,\theta,t)}{\partial z \partial \theta} = \frac{2P_3}{\rho haL\pi} \sum_{m=1}^{\infty}\sum_{n=1}^{\infty} \frac{-nm\pi}{L} \frac{\sin(n\pi z^*/L)\cos(n\pi z/L)\sin m(\theta-\theta^*)}{\varepsilon_m \omega_{nm}^2 \sqrt{[1-(\omega/\omega_{nm})^2]^2 + 4\zeta_{nm}^2(\omega/\omega_{nm})^2}} \sin(\omega t - \phi_{nm}), \quad (2.22)$$

where (z,θ) are the coordinates of the sensor location. One can see that the spatial derivative terms are weighted through the summation by the flexural wave numbers along each direction where the

derivative has been taken. In general, the weights are proportional to the inverse of the flexural wavenumber squared. At a given resonance frequency, the weight will be dominantly determined by the flexural wavenumber of the corresponding mode shape as the denominator in Eqs. (2.19) - (2.22) approaches zero for that resonance mode. In order to analytically construct the WSSG cost function and to preserve the quadratic form desired, one can square the spatial gradient terms and add them with the proper choice of weights to construct WSSG:

$$WSSG = \alpha w^2 \; + \; \beta(\frac{\partial w}{\partial z})^2 \; + \; \delta\frac{1}{a^2}(\frac{\partial w}{\partial \theta})^2 \; + \; \gamma\frac{1}{a^2}(\frac{\partial^2 w}{\partial z \partial \theta})^2, \tag{2.23}$$

where the first weight, α, can be chosen to be 1, and the other weights are chosen in such a way that they would normalize each term with respect to the first term to make the cost function as spatially uniform as possible. This ensures the insensitivity and robustness of the method with respect to sensor location and makes point measurements possible in order to achieve global control results.

2.1.4.1 Modeling the WSSG control metric

2.1.4.1.1 Optimization. In order to numerically model active control using the WSSG control metric, an early requirement is to acquire the transfer function of the secondary path, g, i.e., the cancellation path between the secondary (control) source and the error sensors. Analytically, this is achieved using Eq. (2.15) and applying the coordinates of the secondary source in (z^{**}, θ^{**}) so that the transfer function of the secondary path and its spatial gradients can be written as

$$g(z,\theta,t) = \frac{2}{\rho haL\pi}\sum_{m=1}^{\infty}\sum_{n=1}^{\infty}\frac{\sin(n\pi z^{**}/L)\sin(n\pi z/L)\cos m(\theta-\theta^{**})}{\varepsilon_m\omega_{nm}^2\sqrt{[1-(\omega/\omega_{nm})^2]^2} \; + \; 4\zeta_{nm}^2(\omega/\omega_{nm})^2}\sin(\omega t-\phi_{nm}) \tag{2.24}$$

$$\frac{\partial g(z,\theta,t)}{\partial z} = \frac{2}{\rho haL\pi}\sum_{m=1}^{\infty}\sum_{n=1}^{\infty}\frac{n\pi}{L}\frac{\sin(n\pi z^{**}/L)\cos(n\pi z/L)\cos m(\theta-\theta^{**})}{\varepsilon_m\omega_{nm}^2\sqrt{[1-(\omega/\omega_{nm})^2]^2} \; + \; 4\zeta_{nm}^2(\omega/\omega_{nm})^2}\sin(\omega t-\phi_{nm}) \tag{2.25}$$

$$\frac{\partial g(z,\theta,t)}{\partial \theta} = \frac{2}{\rho haL\pi} \sum_{m=1}^{\infty} \sum_{n=1}^{\infty} -m \frac{\sin(n\pi z^{**}/L)\sin(n\pi z/L)\sin m(\theta-\theta^{**})}{\varepsilon_m \omega_{nm}^2 \sqrt{[1-(\omega/\omega_{nm})^2]^2 + 4\zeta_{nm}^2(\omega/\omega_{nm})^2}} \sin(\omega t - \phi_{nm}) \tag{2.26}$$

$$\frac{\partial^2 g(z,\theta,t)}{\partial z \partial \theta} = \frac{2}{\rho haL\pi} \sum_{m=1}^{\infty} \sum_{n=1}^{\infty} \frac{-nm\pi}{L} \frac{\sin(n\pi z^{**}/L)\cos(n\pi z/L)\sin m(\theta-\theta^{**})}{\varepsilon_m \omega_{nm}^2 \sqrt{[1-(\omega/\omega_{nm})^2]^2 + 4\zeta_{nm}^2(\omega/\omega_{nm})^2}} \sin(\omega t - \phi_{nm}), \tag{2.27}$$

where (z,θ) are the coordinates of the sensor location as mentioned for Eqs. (2.19) - (2.22).

Suppose **d** is a vector that contains the spatial gradient terms due to the primary force in Eqs. (2.19) - (2.22), with weighting applied. Similarly, the notation **G** will be used for the vector that includes the spatial derivatives of the transfer function between the secondary source and the error sensors, as indicated in Eqs. (2.24) - (2.27) with weighting applied. Thus,

$$\mathbf{d^T} = [\sqrt{\alpha}w,\ \sqrt{\beta}\frac{\partial w}{\partial z},\ \sqrt{\delta}\frac{1}{a}\frac{\partial w}{\partial \theta},\ \sqrt{\gamma}\frac{1}{a}\frac{\partial^2 w}{\partial z \partial \theta}] \tag{2.28}$$

$$\mathbf{G^T} = [\sqrt{\alpha}g,\ \sqrt{\beta}\frac{\partial g}{\partial z},\ \sqrt{\delta}\frac{1}{a}\frac{\partial g}{\partial \theta},\ \sqrt{\gamma}\frac{1}{a}\frac{\partial^2 g}{\partial z \partial \theta}], \tag{2.29}$$

where the superscript **T** denotes the matrix transpose.

One can view each of the weighted gradient terms as one of the error components in an error vector. In general, one can establish the error signal vector as

$$\mathbf{e} = \mathbf{d} + \mathbf{G}\mathbf{u_c} \tag{2.30}$$

where $\mathbf{u}_c$ is the vector of complex control forces with dimensions of $N \times 1$, where N is the number of control forces applied and contains both amplitude and phase information of the control forces. If there are M error signals, $\mathbf{d}$ will have dimensions of $M \times 1$, and $\mathbf{G}$ will have dimensions of $M \times N$. In this case, since four spatial gradients are utilized, $M = 4$.

In order to create the quadratic form, the cost function will be formed as the inner product of $\mathbf{e}$, given by

$$J = \mathbf{e}^H\mathbf{e} = \mathbf{d}^H\mathbf{d} + \mathbf{d}^H\mathbf{G}\mathbf{u}_c + \mathbf{u}_c^H\mathbf{G}^H\mathbf{d} + \mathbf{u}_c^H\mathbf{G}^H\mathbf{G}\mathbf{u}_c. \tag{2.31}$$

This can be minimized with respect to both the real and imaginary parts of the vector of control forces, $\mathbf{u}_c$, to yield [123]

$$\frac{\partial J}{\partial \mathbf{u}_{cR}} + j\frac{\partial J}{\partial \mathbf{u}_{cI}} = 2\mathbf{G}^H\mathbf{G}\mathbf{u}_c + 2\mathbf{G}^H\mathbf{d}. \tag{2.32}$$

In order to find the optimal value for the vector of control forces, $\mathbf{u}_{\mathbf{c}-\mathbf{opt}}$, this equation is set equal to zero, which results in

$$\mathbf{u}_{c-opt} = -[\mathbf{G}^H\mathbf{G}]^{-1}\mathbf{G}^H\mathbf{d}. \tag{2.33}$$

As long as $\mathbf{G}^H\mathbf{G}$ is not singular, Eq. (2.33) provides the optimal value for $\mathbf{u}_c$ that will provide the optimal attenuation of J, i.e, the WSSG control metric. Simplifying the notation as

$$\begin{aligned} \mathbf{A} &= \mathbf{G}^H\mathbf{G} \\ \mathbf{b} &= \mathbf{G}^H\mathbf{d} \\ c &= \mathbf{d}^H\mathbf{d}, \end{aligned} \tag{2.34}$$

the optimum value obtained in Eq. (2.33) can be expressed as

$$\mathbf{u}_{c-opt} = -\mathbf{A}^{-1}\mathbf{b} \tag{2.35}$$

and the minimized cost function will have the form of

$$\mathbf{J}_{min} = c - \mathbf{b}^{H}\mathbf{A}^{-1}\mathbf{b}. \tag{2.36}$$

Since a quadratic form of the error vector has been minimized, by substituting Eq. (2.33) in Eq. (2.30), one can find the residual error signal as

$$\mathbf{e}_{resid} = (1-\mathbf{G}\mathbf{G}^{\dagger})\mathbf{d}, \tag{2.37}$$

where $\mathbf{G}^{\dagger}$ is the pseudo-inverse of $\mathbf{G}$.

2.1.5 The radiated sound power

While measuring and monitoring the WSSG control metric provides a means of evaluating the performance of the control metric within the vibration field, it does not provide any sense of the acoustical performance. In order to evaluate the acoustical performance of this metric, it is important to find a suitable acoustical metric. In this case, the radiated sound power has been chosen. In order to model and compute the radiated sound power numerically, the coupling between the structural vibration and the surrounding medium, and consequently the resultant acoustic radiation, is used to develop an effective means of calculating the sound power. Due to

the lengthy details, the method developed to compute the radiated sound power will be discussed in Chapter 3.

2.2 Experimental background

2.2.1 Active noise control

Active noise control is a technique designed to reduce unwanted noise by introducing an additional sound field. An active control system is an integration of electronics, transducers and acoustics that is designed to reduce the unwanted noise by introducing acoustic waves into the system that makes an additional sound field. In principle, this additional sound field is of equal amplitude and opposite phase at the point(s) of interest. One can say that Lord Rayleigh may be the first to do experiments on acoustic wave superposition in 1878 [124], in which he observed "Points of Silence" by moving around and observing minima and maxima of loudness. However, more developed ideas of noise cancellation began with H. Coanda in 1930, followed by German physicist P. Lueg in 1933, who patented the idea of noise cancellation in ducts [125]. However, due to the limitations of data processing, and analog hardware, the implementation was difficult and the results achieved were limited. Although there was some additional work by Olsen to develop feedback control for rooms and ducts in the 1950s, there was not much significant development in active noise control until the 1980s [126]. With advancements in hardware and data processing, researchers began extending past ideas into many different control techniques and applications [127].

While simple wave superposition is the basic idea for active control, it often is only capable of producing local control results. Generally, for any class of active noise control involving acoustical or structural systems, there are a few mechanisms that can lead to global sound attenuation. One can classify these as 1) achieving control by unloading the radiation impedance of the primary source, due to the secondary source being located in close proximity to the primary source, with

respect to the acoustic wavelength, 2) enforcing control by utilizing modal rearrangement between the modes of an enclosed space or a structure, in such a way that the amplitudes and phases of the modes are altered to achieve attenuation of the sound power, or 3) in the case of active control of a structure, increasing the impedance of the structural modes and consequently decreasing their amplitudes [89]. In general, a control approach can be a combination of these mechanisms.

2.2.2 Signal processing for active noise control

2.2.2.1 Filtered-x LMS algorithm

In order to implement the active control, digital filters are used to process the signals in real time. Here in this work, finite impulse response (FIR) filters are used due to their stability. The optimal solution for the filter coefficients is obtained from a mean-square or a cost function and is usually obtained by minimizing the cost function, which will provide a system of linear equations. In order to ensure that the solution of this system of equations is the optimal solution, the cost function is required to have a quadratic form. The hyperparabolic surface characteristic of a quadratic function ensures the presence of a global minimum rather than having many local minima.

Having no delays between the reference and the error signal corresponds to a minimum phase system (meaning that all the poles of the system transfer function in the Z domain lie within the unit circle, which ensures that the system is causal and stable). This system can correspond to a simple case of electronic noise cancellation. However, for an actual physical system, a delay will always exist between the reference signal and the error signal as the reference signal is propagated through the plant transfer function. The transfer function of a system such as a vibrating structure is often not minimum phase, due to the delays that appear in the system response. If this delay is not taken into account, it can create instabilities in the algorithm, since the inverse of the transfer function can be unstable due to causality issues and phase differences. Therefore, the adaptive algorithm needs to be able to account for delays in the plant response, as well as in the secondary

path response.

The secondary path includes everything between the control output and the error sensors, which can include the physical system being controlled, data converters, analog anti-aliasing filters and reconstruction filters. For a moderately to highly damped system, the model of the secondary path can be described using an FIR filter. Therefore, most adaptive feedforward algorithms require some means of identifying the secondary path transfer function, which is often done by introducing an identification noise to the secondary (control) source, and then adaptively minimizing the difference between the actual sensor response and the output of the estimate of the secondary path transfer function. This procedure is usually called system identification [132].

Figure 2.5 demonstrates the block diagram for the control implementation. In Fig. 2.5, H and $\hat{H}$ represent the response of the secondary path and the estimate of the response of the secondary path, which can be represented in terms of filter coefficients.

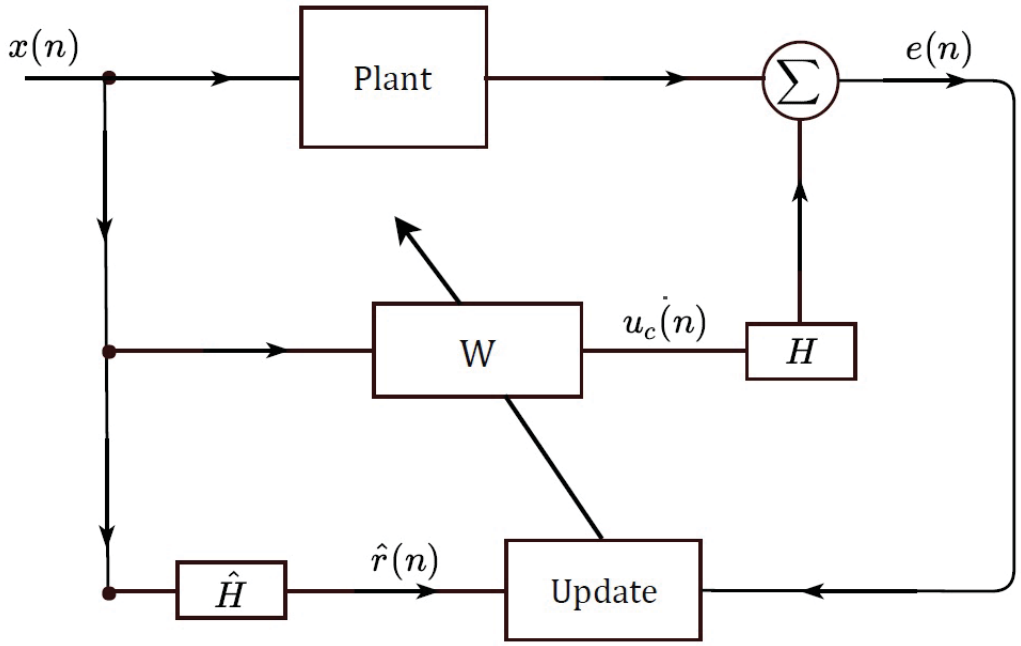

Figure 2.5 Block diagram of the filtered-x LMS algorithm.

As demonstrated in Fig. 2.5, $x(n)$ is the reference signal and for a single channel filter, the error signal, $e(n)$, at a specific error sensor location can be written in terms of the secondary path response $h(n)$ [$H(f)$ in the frequency domain], the disturbance signal $d(n)$ (which is the reference signal filtered by the plant response) and the control output $u_c(n)$:

$$e(n) = d(n) + \sum_{j=0}^{J-1} h_j(n) u_c(n-j), \tag{2.38}$$

where the second term describes the convolution of the secondary path response and the control output in the time domain, and J is the number of samples considered for this convolution [50]. The control output can be written as

$$u_c(n) = \sum_{i=0}^{I-1} w_i x(n-i), \tag{2.39}$$

where w_i are the coefficients of the control filter. Substituting this into Eq. (2.38) yields

$$e(n) = d(n) + \sum_{j=0}^{J-1} \sum_{i=0}^{I-1} h_j(n) w_i(n) x(n-j-i). \tag{2.40}$$

One can change the order of convolutions in Eq. (2.40) such that

$$e(n) = d(n) + \sum_{i=0}^{I-1} w_i \Big[\sum_{j=0}^{J-1} h_j(n) x(n-i-j) \Big]. \tag{2.41}$$

This can be written as

$$e(n) = d(n) + \sum_{i=0}^{I-1} w_i(n) r(n-i), \tag{2.42}$$

where $r(n)$ is the reference signal filtered by the secondary path response. One can perform the convolution by representing the filtered reference signal and the filter coefficients in a vector form, such that

$$e(n) = d(n) + \mathbf{w}^T \mathbf{r}, \tag{2.43}$$

where

$$\mathbf{w} \;=\; [w_0 \; w_1 \;\; \ldots \;\; w_{I-1}]^T \tag{2.44}$$

$$\mathbf{r} \;=\; [r(n) \; r(n-1) \;\; \ldots \;\; r(n-I+1)]^T. \tag{2.45}$$

In order to find the optimum value for the filter coefficients, one needs to construct the quadratic form of the error signal as the cost function, which is really the mean-square error or the power of the error signal, i.e., $J = E[e^2(n)]$, where E is the expectation value operator. It can be shown that the optimal solution for minimizing this cost function with respect to the control filter coefficients can be written as

$$\mathbf{w_{opt}} = \mathbf{A}^{-1}\mathbf{b}, \tag{2.46}$$

where $\mathbf{A}$ is a symmetric matrix, which is equal to the auto-correlation of the filtered reference signal, and $\mathbf{b}$ is the cross correlation between the filtered reference signal and the disturbance signal. This means that a time history of the signals is required, which produces delays as well as a computational load proportional to I^2. To avoid these problems, one can make the filter adaptive, such that the filter coefficients are updated in an iterative manner in time, rather than waiting to calculate one single set of optimal coefficients. In order to adaptively update the control filter coefficients in real time, one can adapt a least-mean-square algorithm, which relies on the steepest (gradient) descent technique. The steepest descent technique is an optimization approach in which the filter coefficients are updated using the negative gradient of the mean-square error surface. Hence, one can write the equation for updating the filter coefficients in terms of the gradient of the cost function with respect to the filter coefficients, i.e.,

$$\mathbf{w}(new) = \mathbf{w}(old) - \mu \frac{\partial J}{\partial \mathbf{w}}(old), \tag{2.47}$$

where μ is the step size that governs the speed of convergence. It can be shown that $\frac{\partial J}{\partial \mathbf{w}}$ can be written as

$$\frac{\partial J}{\partial \mathbf{w}} = -2E[e(n)\mathbf{r}(n)]. \tag{2.48}$$

In order for the filter coefficients to be updated frequently, it is preferred to use an instantaneous estimate of the gradient (stochastic gradient) that is calculated at each sample time, rather than an averaged value over time or in other words trying to calculate the expectation value $E[\mathbf{r}(n)e(n)]$. Therefore, the adaptation algorithm can be written as

$$\mathbf{w}(n+1) = \mathbf{w}(n) - \alpha_c e(n)\mathbf{r}(n), \tag{2.49}$$

where $\alpha_c = 2\mu$ is the convergence coefficient.

This algorithm is known as the filtered-reference-LMS or filtered-x LMS algorithm. Since in practice, an estimate of the secondary path transfer function, $\hat{H}(z)$, is obtained through system identification rather than the true transfer function $H(z)$, a more accurate expression for the adaptive update is

$$\mathbf{w}(n+1) = \mathbf{w}(n) - \alpha_c e(n)\hat{\mathbf{r}}(n) \tag{2.50}$$

Filtering the reference signal properly time aligns the cross-correlation between the control signal and the desired signal, which plays an important role in the stability and convergence of the algorithm. Adding another filter to model the secondary path transfer function adds to the signal processing load. Therefore, it is desirable to represent the secondary path transfer function

efficiently with the least number of coefficients. However, if too few coefficients are incorporated into the system, that can also potentially degrade the performance and the stability. It has generally been reported that reducing the coefficients to as few as 20 nonzero coefficients will still be able to provide robust performance [133]. This also depends on whether the secondary path transfer function is being estimated for a tonal disturbance or a broadband disturbance. For instance, for a tonal reference signal, in principle an FIR filter with two coefficients can be adequate, although for other reasons, more than two coefficients are typically used [134].

In terms of convergence, the same analysis for the LMS algorithm applies here, with the difference that the Hessian matrix is no longer the autocorrelation of the reference signal, but is the autocorrelation of the filtered reference signal, i.e., $\mathbf{A} = E[\,\hat{\mathbf{r}}(n)\hat{\mathbf{r}}^T(n)]$. This matrix can be represented in terms of its eigenvectors and eigenvalues, as well. Going through a similar analysis, the condition for stability and convergence comes down to $\mid 1 - \alpha_c\Lambda \mid < 1$. Here Λ is the matrix of eigenvalues for the matrix $\mathbf{A}$.

In terms of convergence, it has been shown that the convergence factor should satisfy the following condition,

$$0 < \alpha_c < \frac{2Re(\lambda_i)}{\mid \lambda_i \mid^2}, \tag{2.51}$$

where λ_i indicates the eigenvalues of the autocorrelation between the actual filtered reference signal and its estimate, i.e. $\mathbf{A} = E[\mathbf{r}(n)\hat{\mathbf{r}}(n)]$ [135]. In general, since the secondary path transfer function $\hat{\mathbf{H}}$, is only an estimate, the autocorrelation matrix is not necessarily positive definite, meaning that due to phase differences the eigenvalues can be complex. Therefore, the stability of the method depends on whether the real part of each eigenvalue is positive or negative. If all the signs are positive then the algorithm will converge rather than diverge in an oscillatory fashion. However, if one of the signs is negative, the system will not be stable.

A solution to this problem can be to use a leakage factor, which is also known as the leaky

LMS algorithm. For this algorithm, the cost function will take the form

$$J_2 \;=\; E[e^2(n)] \;+\; \beta_c\, \mathbf{w}^T\mathbf{w} \tag{2.52}$$

where β_c regularizes the algorithm and prevents divergence. The adaptation equation then becomes

$$\mathbf{w}(n+1) \;=\; (1 \;-\; \alpha_c\beta_c)\mathbf{w}(n) \;-\; \alpha_c\hat{\mathbf{r}}(n)e(n). \tag{2.53}$$

For convenience, we can set $(1-\alpha_c\beta_c) = \gamma_c$, where γ_c is called the leakage factor. With its addition, the algorithm will now converge given that the real part of the eigenvalues of $E[\hat{\mathbf{r}}(n)\mathbf{r}^T \;+\; \gamma_c\mathbf{I}]$ are positive. With this new convention, if $\gamma_c = 1$, i.e., $(\beta_c = 0)$, this will collapse to the conventional filtered-x LMS algorithm. However, if $\gamma_c < 1$ $(\beta_c > 0)$, this can improve the robustness of the algorithm by ensuring that any eigenvalues with small negative real parts will now have positive real parts. The trade-off is that the attenuation that can be achieved will not be as large as when the model of the secondary path is perfect.

The precision and accuracy of the estimate of the secondary path play an important role in the convergence of the system. If the phase difference between the exact and the estimated transfer functions is less than 90^o, the system will converge and be stable. However, if this phase difference is larger than 90^o, the system will not be stable. Within this stability region, as the phase difference grows larger, the convergence must occur more slowly in order to maintain stability. Thus, the best performance occurs when the phase error is kept small.

2.2.3 Implementing the weighted sum of spatial gradients

While one can model the WSSG control metric using an analytical solution and its derivatives, as well as a point location for the sensor, in order to implement WSSG in practice, it is necessary to sense the spatial gradients on the structure using common structural sensors. Accelerometers have been chosen as the structural sensors. Since a harmonic disturbance force is assumed, the

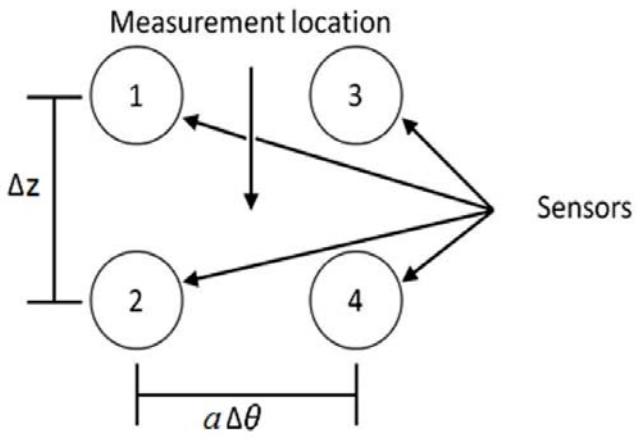

Figure 2.6 The configuration of 4 closely spaced sensors.

accelerations are proportional to the displacements such that they can be used directly to sense the WSSG terms. This is done using a compact integrated set of accelerometers that essentially acts as being at a single sensor location, due to the close spacing. Four accelerometers are used and configured as shown in Fig. 2.6.

Using this configuration, one can utilize the finite-difference method in order to extract the spatial gradients from the accelerometer readings as follows:

$$\begin{aligned} w &= \frac{a_1+a_2+a_3+a_4}{4} \\ \frac{dw}{dz} &= \frac{a_1-a_2+a_3-a_4}{2\Delta z} \\ \frac{1}{a}\frac{dw}{d\theta} &= \frac{-a_1-a_2+a_3+a_4}{2a\Delta\theta} \\ \frac{1}{a}\frac{d^2w}{dzd\theta} &= \frac{-a_1+a_2+a_3-a_4}{a\Delta z\Delta\theta}, \end{aligned} \tag{2.54}$$

where a_1, a_2, a_3 and a_4 are the readings of the four accelerometers, and Δz is the distance between a_1 and a_2, as well as between a_3 and a_4 along the axis of the cylinder. In addition, $a\Delta\theta$ is the

distance between a_1 and a_3, as well as a_2 and a_4 along the circumference. Since Eq. (2.54) is only the first term of the Taylor-series expansion, it contains a truncation error on the order of (Δz^2), meaning that the larger the spacing between the sensors, the larger the truncation error will be. On the other hand, there are also errors due to random noise present in the signals from the sensors. Since some of the spatial gradient terms are obtained using subtraction of the accelerometer readings, if the accelerometers are spaced too closely and the noise floor is similar in magnitude to the magnitude of the difference between the two sensor signals, the finite difference term will not be reliable. Thus, it is best to put the sensors farther apart to decrease this error. One can see that there is a trade off between spacing the accelerometers closer or farther apart. Hendricks has shown through an optimization process that the optimal distance for reducing these errors is about 1 inch (0.0254 m) [52]. With this configuration, the accelerometer signals are input to the DSP in real time, where finite difference processing is used to obtain the four terms comprising WSSG. The main core of the algorithm is based on the filtered-x LMS algorithm. However, the adaptive update equation is modified to incorporate the WSSG gradient terms obtained from the accelerometer array.

2.2.3.1 Modified filtered-x LMS algorithm

In order to apply the filtered-x LMS algorithm to the WSSG control metric, one needs to adjust the algorithm to incorporate the gradient of the WSSG control metric. Hence, the algorithm described in the following will be referred to as the modified Filtered-x algorithm. A schematic of the block diagram of this algorithm is demonstrated in Fig. 2.7.

In this application, the excitation signal from the generator is input to the control system as a reference signal. Considering the WSSG control metric, one can see that four transducers, such as accelerometers, are needed in order to obtain the spatial gradients. These accelerometers correspond to subscripts 1, 2, 3 and 4 in Fig. 2.7. During the control operation, the response of

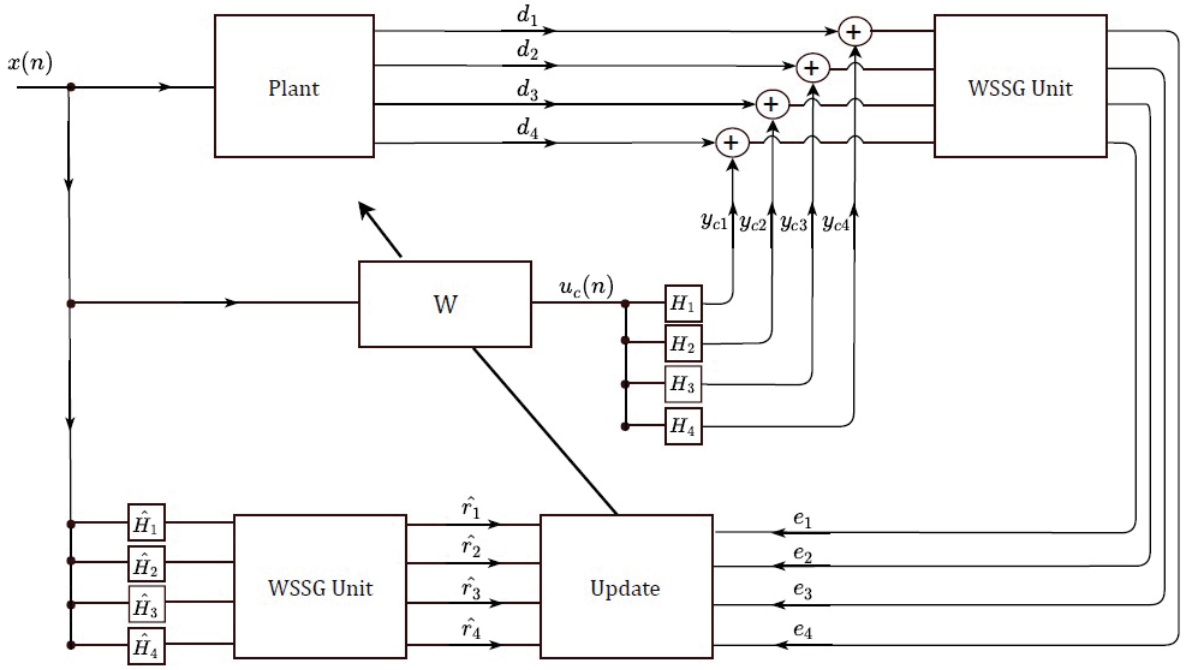

Figure 2.7 Block diagram of the modified filtered-x LMS algorithm.

each accelerometer is composed of the plant response through the primary path, resulting in the disturbance signals d_1, d_2, d_3 and d_4 respectively, and the secondary path response, resulting in the control signals, y_{c1}, y_{c2}, y_{c3} and y_{c4}. These signals physically add together, so that the response of each accelerometer corresponds to $d_i + y_{ci}$, where $i = \{1,\ 2,\ 3,\ 4\}$. These four accelerometer signals are then processed according to Eq. (2.54) to yield the spatial gradients. This additional processing is denoted by "WSSG Unit" in the block diagram.

Figure 2.8 illustrates the operations of the WSSG unit. In this figure, I_1, I_2, I_3 and I_4 are the four accelerometer inputs and O_1, O_2, O_3 and O_4 are the four outputs of the WSSG unit function. Inputting the components $d_i + y_{ci}$ to the WSSG unit function, the error signals e_1, e_2, e_3 and e_4 corresponding to $2\alpha w$, $2\beta\,\partial w/\partial z$, $2\delta/a\ \partial w/\partial\theta$ and $2\gamma/a\ \partial^2 w/\partial z\partial\theta$ respectively, are generated and used to update the control filter coefficients.

Previous to beginning control, the estimate of the secondary path between the secondary

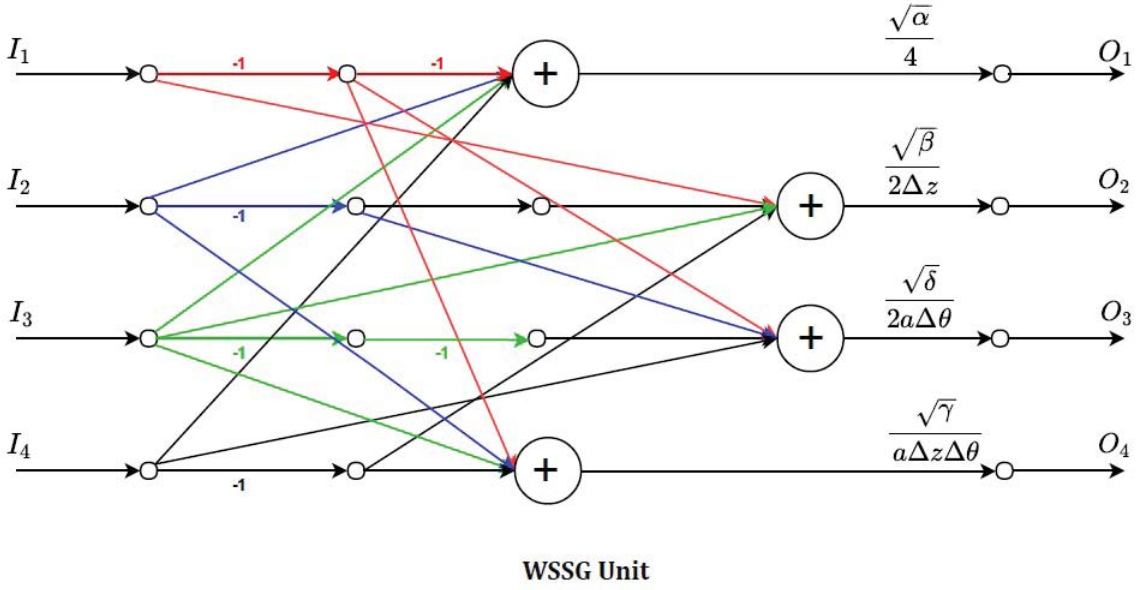

Figure 2.8 Block diagram of the WSSG unit.

(control) source to each of the accelerometers is obtained through off-line system identification and is denoted as $\hat{\mathbf{H}}_1$, $\hat{\mathbf{H}}_2$, $\hat{\mathbf{H}}_3$ and $\hat{\mathbf{H}}_4$, respectively, with respect to accelerometers 1, 2, 3 and 4. During the control operation, the reference signal is filtered by the estimates of each of the secondary paths, producing four signals that are then processed by the WSSG unit in order to produce the modified filtered reference signals, $\hat{\mathbf{r}}_1$, $\hat{\mathbf{r}}_2$, $\hat{\mathbf{r}}_3$ and $\hat{\mathbf{r}}_4$, which are used for updating the control filter coefficients along with the vector of error signals, according to Eq. (2.50). The updated control filter coefficients are then implemented in the control filter.

Equation (2.50) provides the general form for updating the control filter coefficients. In order to clarify exactly how these terms apply the WSSG control metric, the following equations expand each of the modified error signals in terms of their constitutive elements:

$$
\begin{aligned}
e_1 &= \sqrt{\alpha}[\tfrac{d_1+d_2+d_3+d_4}{4} + \mathbf{u_c}^T\left[\tfrac{\hat{\mathbf{H}}_1+\hat{\mathbf{H}}_2+\hat{\mathbf{H}}_3+\hat{\mathbf{H}}_4}{4}\right]] \\
e_2 &= \sqrt{\beta}[\tfrac{d_1-d_2+d_3-d_4}{2\Delta z} + \mathbf{u_c}^T\left[\tfrac{\hat{\mathbf{H}}_1-\hat{\mathbf{H}}_2+\hat{\mathbf{H}}_3-\hat{\mathbf{H}}_4}{2\Delta z}\right]] \\
e_3 &= \sqrt{\delta}[\tfrac{-d_1-d_2+d_3+d_4}{2a\Delta\theta} + \mathbf{u_c}^T\left[\tfrac{-\hat{\mathbf{H}}_1-\hat{\mathbf{H}}_2+\hat{\mathbf{H}}_3+\hat{\mathbf{H}}_4}{2a\Delta\theta}\right]] \\
e_4 &= \sqrt{\gamma}[\tfrac{-d_1+d_2+d_3-d_4}{a\Delta\theta\Delta z} + \mathbf{u_c}^T\left[\tfrac{-\hat{\mathbf{H}}_1+\hat{\mathbf{H}}_2+\hat{\mathbf{H}}_3-\hat{\mathbf{H}}_4}{a\Delta\theta\Delta z}\right]],
\end{aligned}
\tag{2.55}
$$

where $\mathbf{u}_c(t) = \mathbf{W}^T\mathbf{X}$. One can use these terms to form the cost function involving the error signals as

$$
J = \sum_{i=1}^{4} e_i^* e_i. \tag{2.56}
$$

In order to find the gradients required to be incorporated in Eq. (2.53), one takes the gradient of the cost function, with respect to the control filter coefficients, as

$$
\frac{\partial J}{\partial \mathbf{w}} = \sum_{i=1}^{4} 2e_i \frac{\partial e_i}{\partial \mathbf{w}}, \tag{2.57}
$$

where

$$
\begin{aligned}
2e_1\tfrac{\partial e_1}{\partial \mathbf{w}} &= 2e_1[\tfrac{\hat{\mathbf{H}}_1+\hat{\mathbf{H}}_2+\hat{\mathbf{H}}_3+\hat{\mathbf{H}}_4}{4}]^T\mathbf{X} \\
2e_2\tfrac{\partial e_2}{\partial \mathbf{w}} &= 2e_2\left[\tfrac{\hat{\mathbf{H}}_1-\hat{\mathbf{H}}_2+\hat{\mathbf{H}}_3-\hat{\mathbf{H}}_4}{2\Delta z}\right]^T\mathbf{X} \\
2e_3\tfrac{\partial e_3}{\partial \mathbf{w}} &= 2e_3\left[\tfrac{-\hat{\mathbf{H}}_1-\hat{\mathbf{H}}_2+\hat{\mathbf{H}}_3+\hat{\mathbf{H}}_4}{2a\Delta\theta}\right]^T\mathbf{X} \\
2e_4\tfrac{\partial e_4}{\partial \mathbf{w}} &= 2e_4\left[\tfrac{-\hat{\mathbf{H}}_1+\hat{\mathbf{H}}_2+\hat{\mathbf{H}}_3-\hat{\mathbf{H}}_4}{a\Delta z\Delta\theta}\right]^T\mathbf{X}.
\end{aligned}
\tag{2.58}
$$

On that account, the error signal vector in Eq. (2.50) is formed as

$$\mathbf{e}^T = [e_1\ e_2\ e_3\ e_4], \tag{2.59}$$

where the filtered reference signal vector at each time instant is described in the following fashion:

$$\hat{\mathbf{R}} = \begin{bmatrix} \left[\frac{\hat{\mathbf{H}}_1 + \hat{\mathbf{H}}_2 + \hat{\mathbf{H}}_3 + \hat{\mathbf{H}}_4}{4}\right]^T \mathbf{X} \\ \left[\frac{\hat{\mathbf{H}}_1 - \hat{\mathbf{H}}_2 + \hat{\mathbf{H}}_3 - \hat{\mathbf{H}}_4}{2\Delta z}\right]^T \mathbf{X} \\ \left[\frac{-\hat{\mathbf{H}}_1 - \hat{\mathbf{H}}_2 + \hat{\mathbf{H}}_3 + \hat{\mathbf{H}}_4}{2a\Delta\theta}\right]^T \mathbf{X} \\ \left[\frac{-\hat{\mathbf{H}}_1 + \hat{\mathbf{H}}_2 + \hat{\mathbf{H}}_3 - \hat{\mathbf{H}}_4}{a\Delta z\Delta\theta}\right]^T \mathbf{X} \end{bmatrix}. \tag{2.60}$$

Hence, one can write the vector of error signals as well as the filtered reference signal as

$$\mathbf{e}(n) = \begin{bmatrix} e_1(n) \\ e_2(n) \\ e_3(n) \\ e_4(n) \end{bmatrix}, \tag{2.61}$$

$$\hat{\mathbf{r}}(n) = \begin{bmatrix} \hat{\mathbf{R}}^T(n) \\ \hat{\mathbf{R}}^T(n-1) \\ \vdots \\ \hat{\mathbf{R}}^T(n-I+1) \end{bmatrix}. \tag{2.62}$$

Therefore the update equation can be written as

$$\mathbf{w}(n+1) \ = \ \mathbf{w}(n) \ - \ \alpha_c \hat{\mathbf{r}}(n)\mathbf{e}(n). \tag{2.63}$$

Hence, one can use this setting in order to program the DSP to process and update the control filter coefficients. As the algorithm keeps updating, the control filter will eventually reach the optimal value in Eq. (2.33).

Chapter 3

Analysis of the external radiation from circular cylindrical shells

3.1 Introduction

It is often desirable to know the level of sound radiated from a structure and to understand the structural response that causes the radiation. A suitable metric for quantifying the sound field is the radiated sound power. There are generally two analytical methods for calculating the radiated sound power. The first method utilizes the amplitudes of the structural modes through use of the power transfer matrix, and is computationally expensive to implement [136, 137].

The second method utilizes the decomposition of the sound field into orthogonal acoustic basis functions, called acoustic radiation modes, by discretizing the vibrating structure as a set of elementary radiators, and incorporating this discretization into the radiation resistance matrix [19, 20]. In comparison with the first method, this method of using the radiation resistance matrix is typically less intensive to implement.

In 1990, Borgiotti suggested using a modal expansion for representing the radiated sound

field. He introduced the concept of the radiation operator, which operates on the structural velocity and yields the far-field radiated pressure [19]. The eigenvectors of this operator create a set of basis functions associated with the radiated sound power that are known as the radiation modes. Each eigenvector describes the independent velocity distribution for that radiation mode. The eigenvalues of the radiation operator describe the radiation efficiency of each eigenvector, and describe how efficiently each velocity distribution is able to couple with the surrounding medium and contribute to the radiated sound power. This approach was a significant departure from traditional structural approaches in that the radiation is described in terms of an orthogonal decomposition of the acoustic field (radiation modes) rather than utilizing the orthogonal decomposition of the structural field that results in structural modes. One result of this approach is that the acoustic field can generally be characterized by a significantly smaller number of radiation modes, whereas a structural mode approach generally results in the need for retaining a very large number of structural modes.

Borgiotti introduced the concept of spatial and radiation filtering to decompose the velocity of the structure into radiating and non-radiating components [25]. As an example, Borgiotti solved the radiation problem numerically using the radiation operator for external radiation from a finite cylinder with flat endcaps, using a Fourier series. He then presented the eigenvectors of this operator as singular velocity patterns and radiation patterns for the circumferentially symmetric zero-order modes [19, 25].

About the same time, in 1990, Photiadis introduced singular value decomposition (SVD) as a tool to perform the eigenvalue analysis for acoustic radiation problems [21]. He solved the radiation problem for external radiation from a finite cylindrical shell with hemispherical end caps. He was able to present the eigenfunctions in the wavenumber domain, but again only for the zero-order modes. Bringing the concept of efficiencies (eigenvalues) into the wavenumber domain, Photiadis addressed the effect of wavenumber filtering in terms of coincidence, as well as being

able to identify supersonic and subsonic components.

In the same year, Sarkissian developed a new operator, called the radiation resistance operator, which provided a more efficient means of calculating radiation modes [20]. Using spherical harmonics as the set of basis functions for the radiation problem, she developed the general case of the radiation resistance operator, using a numerical boundary element method. She presented some of the zero-order radiation modes (source modes) at a single frequency for radiation from a finite cylinder with flat endcaps, as well as some of the eigenvalues as a function of the spherical harmonics index.

In 1995, Chen and Ginsberg used the reciprocity properties between pressure and velocity to analyze the radiation resistance of structures and presented some numerical results for radiation modes of a spheroidal body [138]. In 1998, Naghshineh and Koopmann used a wave superposition technique to estimate the interior sound field inside a cylindrical shell with endcaps. Using the wave superposition method, they used a limited number of point sources inside the shell to generate the interior acoustic field rather than the large number of monopoles utilized by the boundary element method. They were able to present analytical expressions for the elements of the radiation resistance matrix for the interior radiation of the shell [18, 29].

In 1998, Cazzalato and Hansen obtained the radiation modes for the interior sound field in a cylindrical shell by solving the eigenvalue problem for the acoustic potential energy rather than the radiated sound power, using numerical methods. They tried to apply active noise control to the radiated sound inside the shell by sensing the radiation modes obtained from the acoustic potential energy [139].

Radiation modes also provide a means to better understand the sound radiated from a vibrating structure, which can be very beneficial. For instance, radiation modes can be utilized for active structural acoustic control (ASAC) purposes. Knowing the radiation modes for a certain structure allows one to target the most efficient radiation modes as a means of attenuating the radiated sound

power [26, 137, 139]. They can also be used as spatial and radiation filters in active control [25]. Another approach that utilizes radiation modes for ASAC would be to force the structure to couple most efficiently with weak radiators, in order to reduce the radiated sound [23, 24].

In this paper, the case of external radiation from a cylindrical shell in an infinite baffle has been investigated and an analytical solution has been developed for the radiation resistance operator for external radiation. Due to the geometry of the shell, Fourier basis functions have been used rather than spherical harmonics. Although the shapes of the radiation modes bear a resemblance to the structural modes, they are fundamentally different in that 1) they do not satisfy the structural boundary conditions, and 2) they result from an orthogonal decomposition of the acoustic field, rather than the structural response. Radiation modes for external radiation from the cylindrical shell are presented for higher non-symmetric modes that represent both axial and circumferential dependence. The results illustrate two important features of the external radiation modes that have not been reported in the literature: 1) the frequency dependence of the radiation modes, including the appearance of the “leapfrog effect", and 2) the grouping of eigenvalues, both of which will be discussed in the following sections.

In the remainder of this paper, a brief review of radiated sound power is provided to motivate the concept of the radiation resistance operator. With this background, an analytical solution is developed to yield the radiation resistance operator that describes the external radiation from a cylindrical shell in an infinite baffle, and which leads to the radiation modes. The radiation modes are presented and some of their important characteristics are discussed.

3.2 Acoustic radiated sound power

For a vibrating structure, the time-averaged radiated sound power can be expressed as

$$\bar{P}(f) \;=\; \frac{1}{2}\int \mathrm{Re}\{\; \hat{u}(\vec{r},f)^{*}\cdot\; \hat{p}(\vec{r},f)\}dS, \tag{3.1}$$

where $\hat{u}(\vec{r},f)^{*}$ is the complex conjugate of the normal velocity of the vibrating structure in the frequency domain, which is equal to the acoustic particle velocity at the surface, and $\hat{p}(\vec{r},f)$ denotes the radiated pressure as a function of space and frequency [140]. The hat symbol ($\hat{}$) over any variable indicates a complex quantity. The integration is defined over the surface of the vibrating structure.

For practical implementation, the radiated sound power can be expressed in vector form, by discretizing the structure which converts the integration into a summation of elementary radiators, given by

$$\bar{P}(f) \;=\; \sum_{i=1}^{N} \frac{1}{2}\, A_i\, \mathrm{Re}\{\hat{u}_i^{*}\cdot\; \hat{p}_i\}, \tag{3.2}$$

where i is the index of each element and A_i is the corresponding surface area of that element [141–144].

Expressing the velocity and pressure of all the elements in terms of vectors allows the total radiated power to be expressed as

$$\bar{P}(f) \;=\; \frac{S}{2N}\, \mathrm{Re}\{\hat{\mathbf{u}}^{H}\cdot\; \hat{\mathbf{p}}\}, \tag{3.3}$$

where S is the total surface area of the vibrating structure and N is the total number of equal-area elements that represent the vibrating structure. Bold typeface is used to indicate vector or matrix quantities. However, the radiated pressure can also be expressed in terms of the radiation impedance and the structural velocity as

$$\hat{\mathbf{p}} \;=\; \hat{\mathbf{Z}}\hat{\mathbf{u}}, \tag{3.4}$$

where $\hat{\mathbf{Z}}$ is a symmetric matrix which contains the mutual and self-impedances associated with each element, and we have explicitly made use of the fact that the fluid and structural velocities are equal at the surface of the structure. Substituting Eq. (3.4) into Eq. (3.3) results in

$$\bar{P}(f) \;=\; \frac{S}{2N}\,\mathrm{Re}\Big\{\hat{\mathbf{u}}^H\hat{\mathbf{Z}}\hat{\mathbf{u}}\Big\} \;=\; \hat{\mathbf{u}}^H\mathbf{R}\hat{\mathbf{u}}, \tag{3.5}$$

where $\mathbf{R}$ is the radiation resistance matrix and is obtained as $\mathbf{R} = \frac{S}{2N}\,\mathrm{Re}\{\hat{\mathbf{Z}}\}$. Since $\mathbf{R}$ is a positive definite symmetric matrix, it can be expressed as $\mathbf{R} = \mathbf{Q}^T\Lambda\mathbf{Q}$, where $\mathbf{Q}$ is the matrix containing the eigenvectors corresponding to the radiation modes and Λ is a diagonal matrix of the eigenvalues [145]. As a result, the radiated acoustic power can be expressed as

$$\bar{P} \;=\; \sum_{i=1}^{N} \lambda_i \,|\, y_i \,|^2, \tag{3.6}$$

where $\hat{\mathbf{y}} = \mathbf{Q}\hat{\mathbf{u}}$ is the vector of radiation mode amplitudes, y_i is the amplitude of the ith mode, and λ_i is related to the efficiency of the ith mode. The radiation modes have been discussed in the literature using various names, but each approach has its basis in the concept of decomposing the acoustic field into orthogonal basis functions that describe the acoustic radiation [19–21, 25, 137].

3.3 Radiation resistance matrix — Planar structures

To better understand the development of the radiation resistance matrix for cylindrical structures, the development for planar structures is briefly reviewed. In the early 1990s, a number of researchers investigated the radiation resistance matrix for planar structures, such as beams and plates [24, 137, 146, 147]. In 1993, Elliott and Johnson developed an analytical expression for the radiation resistance operator for planar structures using monopoles as elementary radiators [137]. To determine the elements of the radiation matrix, the acoustic response at the jth element on the

structure due to the excitation at the ith element on the structure is used. For a baffled planar structure, Elliott and Johnson used the well-known expression

$$R_{ij} = \frac{S}{2N} \mathrm{Re}\{\hat{z}_{ij}\} = \frac{\rho_0 \omega^2 S_i^2}{4\pi c} \mathrm{sinc}(k \mid \vec{r}_{ij} \mid), \tag{3.7}$$

where ρ_0 is the density of the surrounding medium, c is the phase speed in the fluid, ω is the angular frequency of excitation, k is the corresponding acoustic wave number, and $\vec{r}_{ij}$ is the vector between elements i and j [137].

This expression is in terms of the direct distance between element i and element j. However, when looking to develop radiation modes for external radiation from a baffled cylinder, where the interior radiation does not contribute to the exterior radiation, this expression can be somewhat misleading, since the dominant path of interaction is the curved path between the elements on the surface of the cylinder rather than the Cartesian vector. Therefore, a different approach must be taken in order to obtain the external radiation from a baffled cylinder.

3.4 Radiation resistance matrix — Cylindrical shells

A number of models that describe the radiated pressure and the radiation impedance for cylindrical shells have been developed. One of the first models, based on an infinitely-long cylinder, was developed by Junger in the 1950s [148–150]. In 1954, Robey derived a numerical expression for the radiation impedance of an array of finite cylinders [151]. In 1958, Sherman developed an expression for the mutual- and self-radiation impedances of two vibrating rectangular pistons on an infinitely-long cylinder with non-periodic boundary conditions [152]. In 1967, Junger developed an expression for the pressure field due to multiple pistons on a cylindrical baffle [153]. In addition, he solved the problem for a vibrating infinite strip of finite width, as well as for pistons on a cylinder. This problem was also studied by Morse and Ingard [154]. Soedel provides an expression

for the radiated acoustic pressure from a finite cylindrical shell [155].

In the remainder of this section, the radiation-resistance matrix for external radiation from a cylinder, baffled on both ends, is developed. Like some other methods, the development of the radiation resistance matrix is based on discretizing the surface of the cylinder into small elements, determining the contributions of each element vibrating independently, and then incorporating those responses into the radiation resistance matrix. The radiation matrix can then be diagonalized, resulting in the acoustic radiation modes that can be used to efficiently determine the radiated sound power. These radiation modes are fundamentally different than the structural vibration modes, which are also often used to study coupled structure/fluid problems, in that the radiation modes are orthogonal on the acoustic space, while the vibration modes are orthogonal on the structural space. The fundamental contributions of this work are: 1) previous methods have only examined the axisymmetric radiation modes, where this development investigates both axial and circumferential modes, and 2) the development is based on cylindrical basis functions which match the geometry more closely than spherical harmonics, which have been used in previous methods.

In the following sections, the expression for the free-field radiated pressure in cylindrical coordinates is reviewed. This expression is then used to develop the radiation impedance for a baffled cylinder with simply-supported periodic boundary conditions, from which the radiation modes are obtained.

3.4.1 Pressure field

An expression for the self- and mutual-radiation impedances for an end-baffled cylindrical shell, as shown in Fig. 3.1, can be readily developed using the radiated pressure from a vibrating element on the surface of the cylinder. Figure 3.1 shows the coordinate systems, several surface elements, and the geometry of the cylinder with length L and radius a.

By solving the homogenous Helmholtz equation using separation of variables in cylindrical

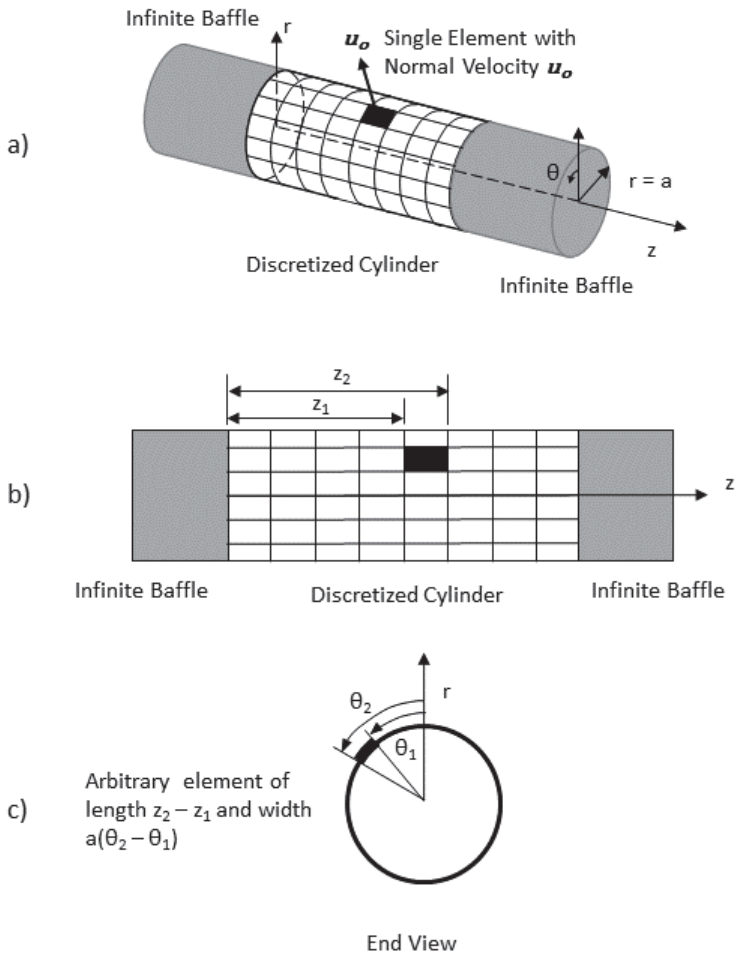

Figure 3.1 a) A vibrating piston element on a discretized baffled cylinder. b) Element size along the axis. c) Element size along the circumference.

coordinates, the solution for an outward propagating pressure wave is expressed as

$$\begin{aligned} \hat{p}(r,\ \theta, z, t) \quad &= \quad \sum_{n=1}^{\infty} \sum_{m=0}^{\infty} (\hat{A}_n \cos(k_z z) + \hat{B}_n \sin(k_z z)) \times \\ &\qquad (\hat{C}_m \cos(m\theta) + \hat{D}_m \sin(m\theta)) H_m^{(2)}(k_r r) e^{\mathrm{j}\omega t}, \end{aligned} \tag{3.8}$$

where n is the axial mode number, m is the circumferential mode number, k_z is the axial wavenumber, $H_m^{(2)}(\ )$ is the cylindrical Hankel function of the second kind, and k_r is the radial wavenumber given by

$$k_r = \sqrt{k^2 - k_z^2}. \tag{3.9}$$

Applying simply supported boundary conditions along z, one finds that $\hat{A}_n = 0$ and $k_z = n\pi/L$. Equations 3.8 and 3.9 can then be expressed as

$$\hat{p}(r, \theta, z, t) = \sum_{n=1}^{\infty} \sum_{m=0}^{\infty} \sin\left(\frac{n\pi z}{L}\right) [\hat{c}_{mn} \cos(m\theta) + \hat{d}_{nm} \sin(m\theta)] H_m^{(2)}(k_r r) e^{j\omega t} \tag{3.10}$$

$$k_r = \sqrt{k^2 - k_z^2} = \sqrt{k^2 - \left(\frac{n\pi}{L}\right)^2}. \tag{3.11}$$

To determine the unknown coefficients, $\hat{c}_{mn}$ and $\hat{d}_{mn}$, a single element of the shell that is small relative to a wavelength is assumed to be vibrating. If the boundaries of the element are defined by $a\theta_1 \leq a\theta \leq a\theta_2$ and $z_1 \leq z \leq z_2$, then the vibration of the shell can be described by

$$\hat{u}(\theta, z) = \begin{cases} u_0 e^{j\omega t} & \theta_1 \leq \theta \leq \theta_2 \, , \, z_1 \leq z \leq z_2 \\ 0 \end{cases} \tag{3.12}$$

Using a Fourier series, the velocity distribution can be expanded in terms of the basis functions used to describe the radiated pressure in cylindrical coordinates, as shown by

$$u(\theta, z) = \sum_{n=1}^{\infty} \sum_{m=0}^{\infty} a_{mn} \cos(m\theta) \sin\left(\frac{n\pi z}{L}\right) + \sum_{n=1}^{\infty} \sum_{m=0}^{\infty} b_{mn} \sin(m\theta) \sin\left(\frac{n\pi z}{L}\right). \tag{3.13}$$

The Fourier series coefficients a_{mn} , b_{mn} are obtained by equating Eqs. 3.12 and 3.13 and using the orthogonality of the trigonometric functions to isolate and solve for a_{mn} and b_{mn}. Using trigonometric identities, along with the assumption that the element size is small compared to a wavelength, allows these coefficients to be simplified to,

$$\begin{cases} a_{mn} &= \frac{-8\ u_0}{\pi^2\ mn}\cos(m\theta_0)\left(\frac{m\Delta\theta}{2}\right)\sin\left(\frac{n\pi z_0}{L}\right)\left(\frac{-n\pi\Delta z}{2L}\right) \\ b_{mn} &= \frac{8\ u_0}{\pi^2\ mn}\sin(m\theta_0)\left(\frac{-m\Delta\theta}{2}\right)\sin\left(\frac{n\pi z_0}{L}\right)\left(\frac{-n\pi\Delta z}{2L}\right) \end{cases} \tag{3.14}$$

where

$$\begin{cases} \Delta\theta &= \theta_2\ -\ \theta_1 \\ \Delta z &= z_2\ -\ z_1 \end{cases} \tag{3.15}$$

and $(\theta_0,\ z_0)$ are the coordinates of the center of the elementary radiator on the surface of the cylinder. As $\Delta\theta$ and Δz go to zero, this will become a delta function velocity distribution.

Using these expressions, the velocity distribution for the shell with the single element vibrating can be expressed as

$$u(\theta,\ z)\ =\ \sum_{n=1}^{\infty}\sum_{m=0}^{\infty}\frac{2u_0\Delta\theta\Delta z}{\pi L}\sin\left(\frac{n\pi z_0}{L}\right)\sin\left(\frac{n\pi z}{L}\right)\cos(m(\theta-\theta_0)). \tag{3.16}$$

Physically, the vibration of this structural element couples to the acoustic fluid through Euler's equation, which is given as

$$\nabla\hat{p}\ =\ -\rho_0\frac{\partial\hat{v}}{\partial t}, \tag{3.17}$$

where ρ_0 is the density of the ambient fluid medium and $\hat{v}$ is the acoustic particle velocity. Assuming time harmonic vibration, Eq. (3.10) can be used to derive an expression for the radial particle velocity as

$$\hat{v}_r(r,\theta,z)\ =\ \frac{-1}{\mathrm{j}\omega\rho_0}\sum_{n=1}^{\infty}\sum_{m=0}^{\infty}k_r\frac{dH_m^{(2)}(k_r r)}{d(k_r r)}\sin\left(\frac{n\pi z}{L}\right)[\hat{c}_{mn}\cos(m\theta)+\hat{d}_{mn}\sin(m\theta)] \tag{3.18}$$

where

$$\frac{\partial(H_m^2(k_r r))}{\partial(k_r r)} = \frac{1}{2}\Big[H_{m-1}^{(2)}(k_r r) - H_{m+1}^{(2)}(k_r r)\Big]. \tag{3.19}$$

By equating Eqs. 3.16 and 3.18 at the surface of the shell, the modal coefficients for the radiated pressure can be determined as

$$v_r(r = a,\, \theta,\, z) = u(\theta,\, z) \tag{3.20}$$

$$\begin{cases} \hat{c}_{mn} &= \frac{2\mathrm{j}\omega\rho_0 u_0 \Delta\theta\Delta z}{\pi L k_r \frac{dH_m^2(k_r a)}{d(k_r a)}} \cos(m\theta_0)\sin(\frac{n\pi z_0}{L}) \\ \hat{d}_{mn} &= \frac{2\mathrm{j}\omega\rho_0 u_0 \Delta\theta\Delta z}{\pi L k_r \frac{dH_m^2(k_r a)}{d(k_r a)}} \sin(m\theta_0)\sin(\frac{n\pi z_0}{L}) \end{cases} \tag{3.21}$$

Using these expressions for $\hat{c}_{mn}$ and $\hat{d}_{mn}$, the pressure created at any location on the cylinder, due to the vibration of any single element, can be determined.

3.4.2 Impedance and radiation resistance matrix

The expressions presented in the previous section enable calculation of the self- and mutual-impedances between any two elements on the shell. The mutual-impedance seen by element i due to element j vibrating can be expressed as

$$\begin{aligned} \hat{Z}_{i,j}(\theta,z) &= \frac{\hat{p}_{i,j}(r = a,\, \theta,\, z)}{\hat{u}_j(\theta,\, z)} \\ &= \frac{2\mathrm{j}\omega\rho_0\Delta\theta\Delta z}{\pi L}\sum_{n,m}^{\infty}\frac{H_m^2(k_r a)}{k_r \frac{dH_m^2(k_r a)}{d(k_r a)}}\sin\left(\frac{n\pi z_i}{L}\right)\sin\left(\frac{n\pi z_j}{L}\right)\cos(m(\theta_i - \theta_j)). \end{aligned} \tag{3.22}$$

This expression holds when k_r is real (i.e. when $\frac{n\pi}{L} < k$). However, when $\frac{n\pi}{L} > k$, k_r becomes imaginary and Eq. (3.22) can be expressed as

$$\hat{Z}_{i,j} = \frac{2\mathrm{j}\omega\rho_0\Delta\theta\Delta z}{\pi L}\sum_{n,m}^{\infty}\frac{K_m(\mid k_r \mid a)}{\mid k_r \mid \frac{dK_m(|k_r|a)}{d(|k_r|a)}}\sin\left(\frac{n\pi z_i}{L}\right)\sin\left(\frac{n\pi z_j}{L}\right)\cos(m(\theta_i - \theta_j)), \tag{3.23}$$

where $K_m(x)$ is the modified Bessel function [156]. Since $K_m(|k_r a|)$ is real, the radiation impedance in Eq. (3.23) is purely reactive, which corresponds to the presence of evanescent wave components. These components only contribute to the near field and they do not need to be considered when computing the far-field radiation or sound power. Thus, for computing radiated sound power, only the region of $\frac{n\pi}{L} < k$ needs to be considered, and Eq. (3.22) applies.

With this expression for the self and mutual radiation impedances, the radiation impedance matrix can be formed. The real part of the radiation impedance matrix gives the radiation resistance matrix as

$$\mathbf{R} = \frac{S}{2N}\mathrm{Re}\left(\begin{bmatrix}\hat{Z}_{11} & \hat{Z}_{12} & \dots & \hat{Z}_{1N}\\ \hat{Z}_{21} & \hat{Z}_{22} & \dots & \hat{Z}_{2N}\\ \vdots & \vdots & \ddots & \vdots\\ \hat{Z}_{N1} & \hat{Z}_{N2} & \dots & \hat{Z}_{NN}\end{bmatrix}\right), \tag{3.24}$$

where S is the surface area of the cylinder and N is the number of elementary radiators necessary to represent the cylinder. Subsequently, as with planar structures, this matrix can be diagonalized to obtain the eigenvectors, or the radiation modes, and their corresponding eigenvalues, which describe how efficiently each radiation mode will be able to contribute to the radiated sound power. The radiation modes can then be projected onto the cylindrical geometry in order to visualize the radiation mode shapes. With the radiation modes determined, one can project any resulting structural velocity field for the shell onto these radiation modes to determine the radiation mode amplitudes. These amplitudes can then be used in conjunction with the resultant radiation mode efficiencies to determine the radiated power, as shown previously in Eq. (3.6). This makes for a

very efficient calculation to determine the radiated sound power, particularly since the number of radiation modes that need to be retained is often rather small.

3.5 Results

The radiation resistance matrix was numerically modeled for a cylindrical shell of length 1 m and radius 0.2 m in an infinite baffle. After the diagonalization, the radiation modes were ordered according to their eigenvalues (i.e. their efficiencies).

Figures 2, 3 and 4 show the nine most efficient radiation mode shapes at frequencies of 300, 400 and 600 Hz, respectively. Zero-order harmonics as well as higher orders which describe both the axial and circumferential dependence of the various modes are presented.

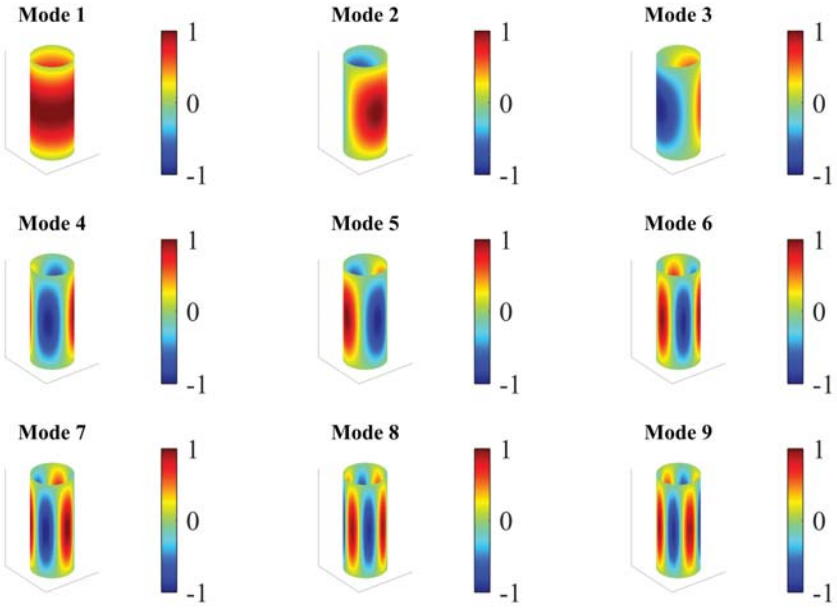

Figure 3.2 Radiation mode shapes at 300 Hz ($ka = 1.11$).

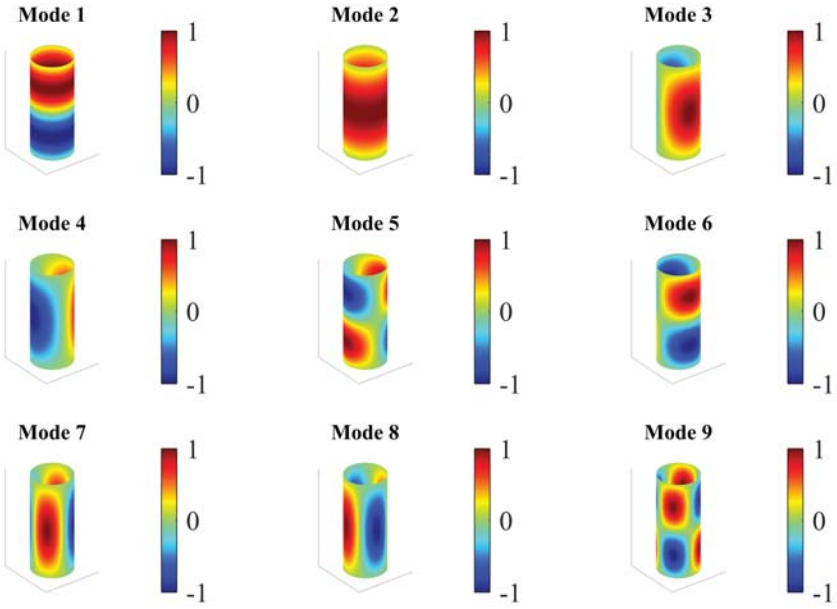

Figure 3.3 Radiation mode shapes at 400 Hz ($ka = 1.48$).

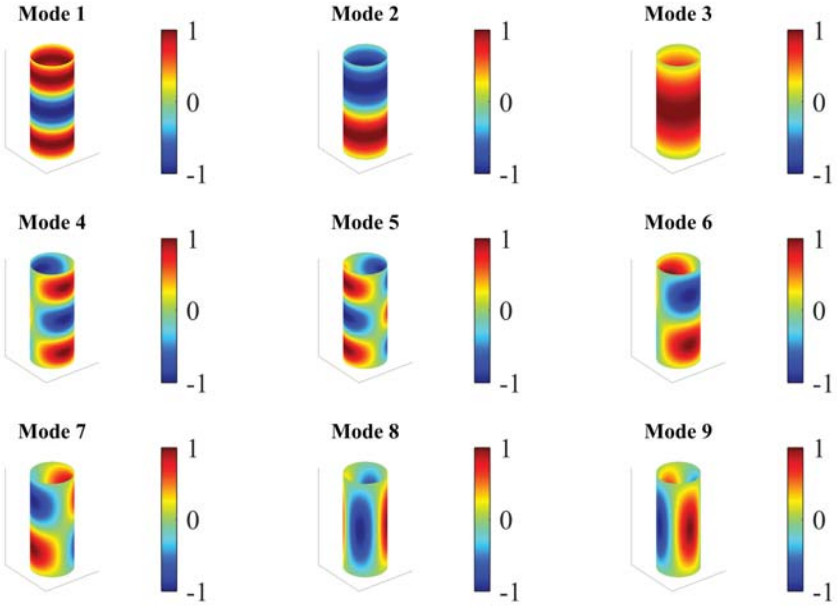

Figure 3.4 Radiation mode shapes at 600 Hz ($ka = 2.22$).

Figures 5, 6 and 7 show the corresponding eigenvalues at each frequency in order of efficiency.

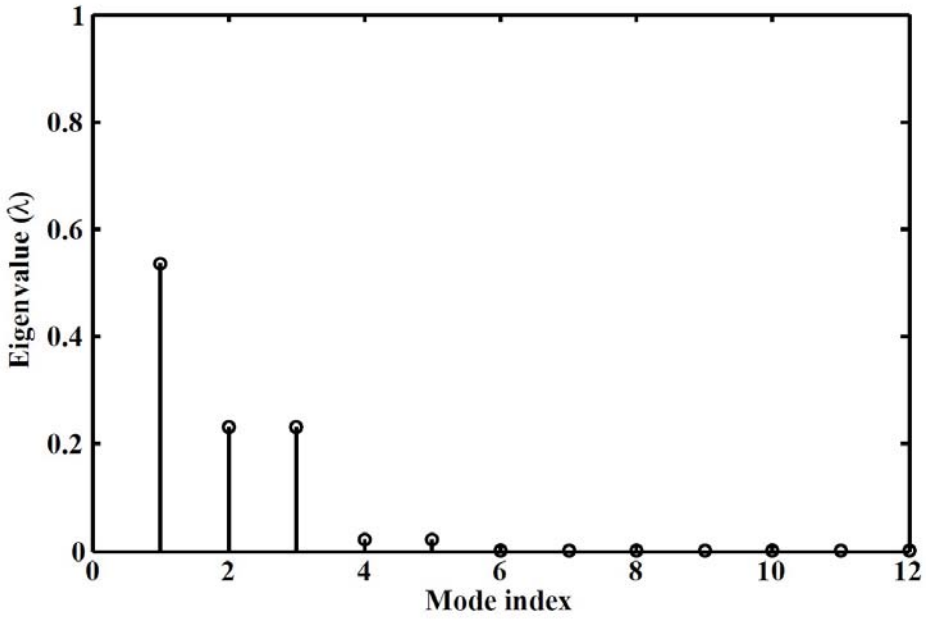

Figure 3.5 Eigenvalues of the 12 most efficient radiation mode shapes at 300 Hz.

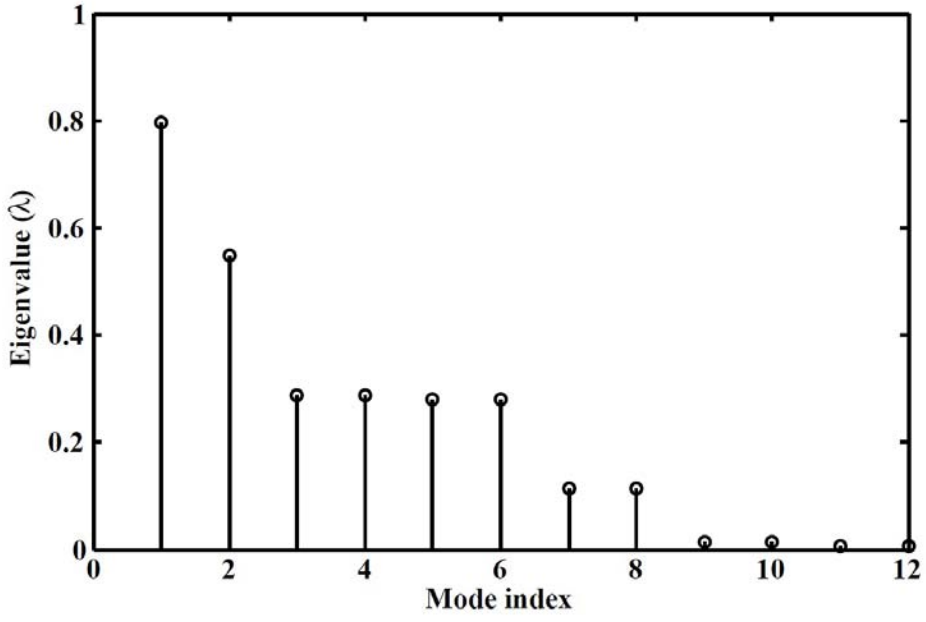

Figure 3.6 Eigenvalues of the 12 most efficient radiation mode shapes at 400 Hz.

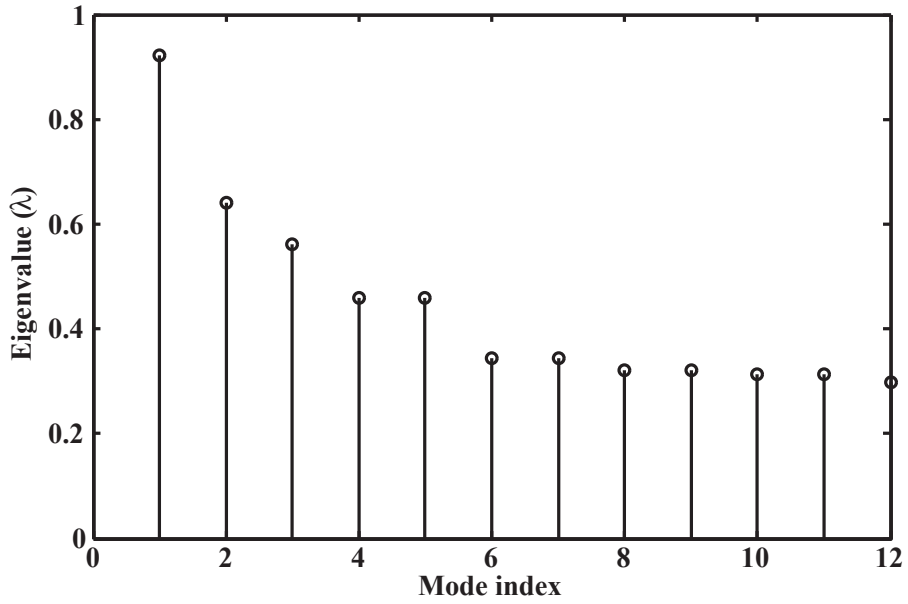

Figure 3.7 Eigenvalues of the 12 most efficient radiation mode shapes at 600 Hz.

These figures demonstrate that as the frequency increases, the eigenvalues become larger and the plateau of efficient eigenvalues becomes longer, indicating that a larger number of modes are required in order to accurately estimate the radiated sound power. These radiation modes demonstrate some important characteristic behaviors that are discussed below.

3.5.1 Frequency dependence

Axial and circumferential modal index numbers are assigned to the modes for clear identification. It is important to note that radiation modes are different than structural modes, and although there are similarities in some of the mode shapes, the use of mode numbers for the radiation modes does not imply any direct connection to the structural modes. Figures 2, 3 and 4 show that as the frequency increases, new efficient radiation modes are introduced and some of the modes that were most efficient at lower frequencies are now reduced in their order of efficiency relative to the new most efficient modes.

Figure 3.8 shows the radiation efficiencies of the (n,m) radiation modes throughout the frequency range. As Fig. 3.8 demonstrates, each group of modes for a particular axial mode number, n, is very inefficient below its particular cut-on or coincidence frequency (shown by the vertical dashed lines). However, above the coincidence frequency, the various modes associated with that axial number increase rapidly in their efficiency. This phenomenon was mentioned for $(n,m=0)$ modes by Junger [148].

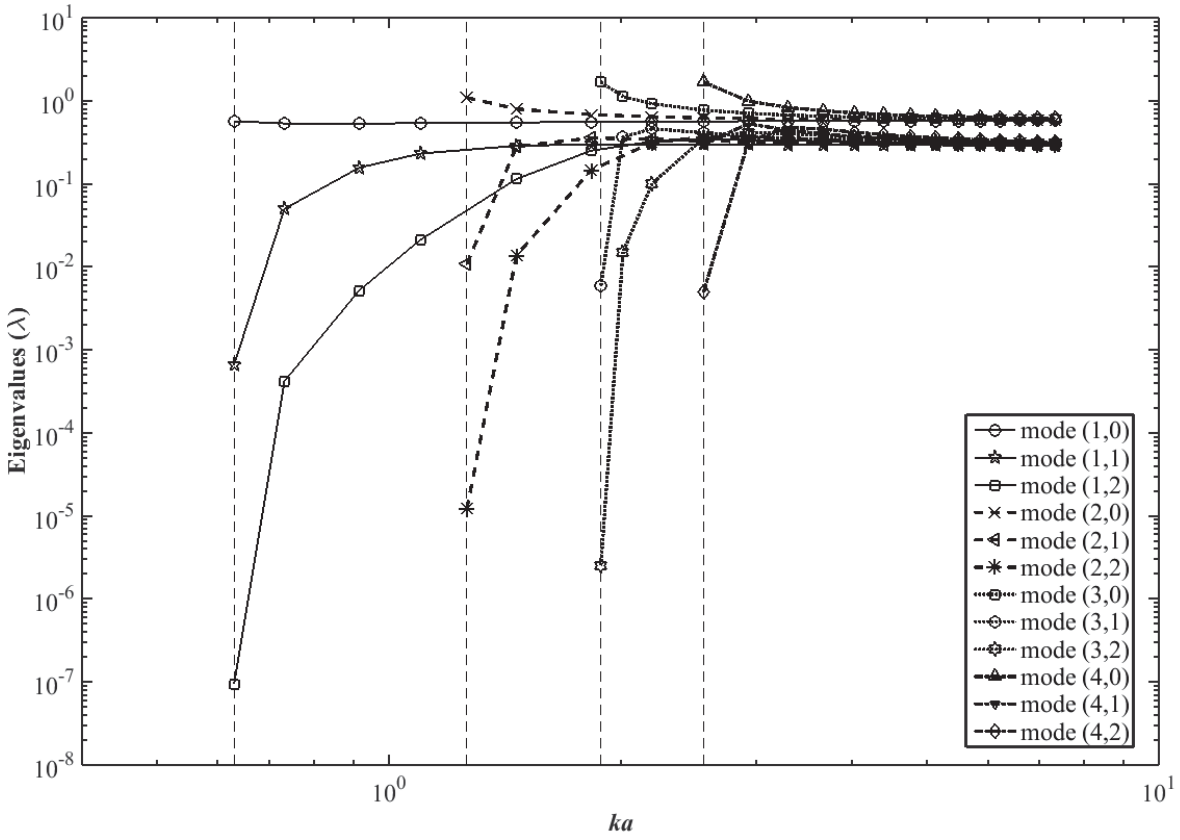

Figure 3.8 Eigenvalues of the (n,m) radiation modes vs. ka, where a is the radius of the cylinder.

This behavior can be further illustrated by comparison to propagation in a waveguide. This concept has been introduced to describe structural behavior, but the same concept can be used

to explain the behavior of the radiation modes. Even though the radiation modes are different than the structural modes and are a function of only geometry and frequency, one can identify a correlation between the geometry of the shell and wavenumber propagation that corresponds to different velocity distributions. With regard to the shell geometry, consider an infinite strip (waves propagating around the circumference of the shell) with a finite width. The finite width introduces quantization of the wavelength that is able to exist along the width of the strip. This in turn introduces cut-on frequencies for the propagation of wavenumbers along the infinite (circumferential) direction [157]. However, due to the infinite path around the circumference, there is no restriction for the circumferential wavenumber, as long as multiple integers of the wavelength can fit along the circumference. Thus, one can consider a finite length cylinder as a finite width strip that has been wrapped around on itself, and therefore, the wave patterns corresponding to different velocity distributions formed along the axial direction can propagate in this infinite path around the cylinder. This is precisely analogous to the behavior of a waveguide corresponding to an infinite strip, as illustrated in Fig. 3.9.

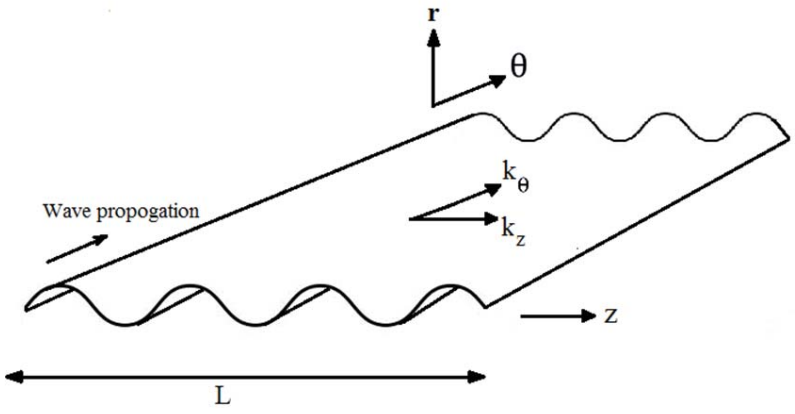

Figure 3.9 Wave propagation along an unwrapped cylinder [157].

Several other properties are also apparent from Fig. 3.8. For instance, one can note the distinct

behavior of the $(n, m = 0)$ modes in comparison with the $(n, m \neq 0)$ modes. The $(n, m = 0)$ modes have eigenvalues that asymptotically approach a higher value than that of the $(n, m \neq 0)$ modes. In addition, the eigenvalues of the $(n, m = 0)$ modes immediately jump to their highest value at their coincidence frequency, and then asymptotically drop down to thier asymptotic value. On the other hand, for the $(n, m \neq 0)$ modes, the eigenvalues start from small values, rise to their highest value and then drop down to a lower asymptotic value for radiation efficiency. According to the general behavior in Fig. 3.8, the modes can be divided into specific groups of $(n, m = 0)$ and $(n, m \neq 0)$ modes.

Another interesting phenomenon that is apparent from Fig. 3.8 is the “leapfrog effect". As can be seen, once a $(n, m = 0)$ mode satisfies the coincidence condition, its radiation efficiency reaches its highest value. As the frequency increases, its radiation efficiency drops off to an asymptotic value. Once the frequency is high enough to satisfy the coincidence condition for the $(n+1, m = 0)$ mode, that new mode jumps above the previous mode in terms of its efficiency.

The property that determines whether a radiation mode is radiating or non-radiating is the relationship of the axial wavenumber to the acoustic wavenumber. At each frequency, radiation modes with different circumferential wavenumbers can potentially be efficient radiators. However, it is the axial wavenumber that determines whether a particular family of mode shapes will be radiating or non-radiating, and it also determines the radiation efficiency of those modes [20, 21]. The physical phenomenon that governs these results is the coincidence effect, which indicates that the structure is able to couple acoustically with the medium and radiate sound efficiently if there is a real angle at which the acoustical wavenumber can be mapped onto the structural wavenumber. This occurs when

$$k_z = k \sin\phi, \tag{3.25}$$

where it will be emphasized that k_z is a wavenumber component associated with the structure, k

is the acoustic wavenumber, and ϕ is the angle defined from the normal. This equation can be used to understand why the various groups of modes increase in their efficiency as they do. For the case of a simply-supported cylindrical shell, k_z is given by $\frac{n\pi}{L}$. Since k_z has integer multiples, the cut-on wavenumbers for the various modes occur at discrete values. Thus, as the frequency increases, there are discrete frequencies where the acoustic wavenumber, k, becomes equal to the next higher allowed value for the modal wavenumber, k_z. Above that coincidence frequency, where $k = \frac{n\pi}{L}$, all radiation modes with axial mode number, n, and any circumferential mode number, m, will begin to radiate and increase in efficiency. In general, as the frequency increases, additional radiation modes are able to satisfy the coincidence condition and therefore enhance the radiated sound power.

This phenomenon can be explained for $(n, m = 0)$ modes by referring to Eqs. 3.9 and 3.25. If $k_z \leq k$, the radiation impedance is resistive for that mode, corresponding to a supersonic condition, and it contributes in radiating sound. However, if $k_z > k$, the radiation impedance is reactive, corresponding to a subsonic condition, which results in that mode being a weak radiator. Hence, for a given structure, it is the relationship between the acoustical and structural wavenumbers that determines the cut-on frequency for the radiation filter. As the frequency increases, higher values of k_z are able to radiate efficiently, and therefore radiation modes with higher axial mode numbers will appear. Photiadis and Sarkissian observed this coincidence effect for the zero order modes in their analysis in the wavenumber domain [20, 21]. However, this is not only limited to the $(n, m = 0)$ modes but holds for $(n, m \neq 0)$ modes as well.

When the coincidence condition first occurs for an $(n, m = 0)$ mode, its radiation impedance becomes resistive and the efficiency of that mode immediately increases as a step function at that cut-on frequency. As the frequency increases, the coincidence effect can be satisfied at different angles, starting at 90^o and ranging down to 0^o, as shown in Fig. 3.10 for the $(5, 0)$ mode. In this figure, each circle corresponds to a different frequency, showing the angle of coincidence and the

radiation efficiency at that frequency. The frequency ranges from 850 Hz for the 90^o coincidence angle, through 2100 Hz for the lowest coincidence angle shown.

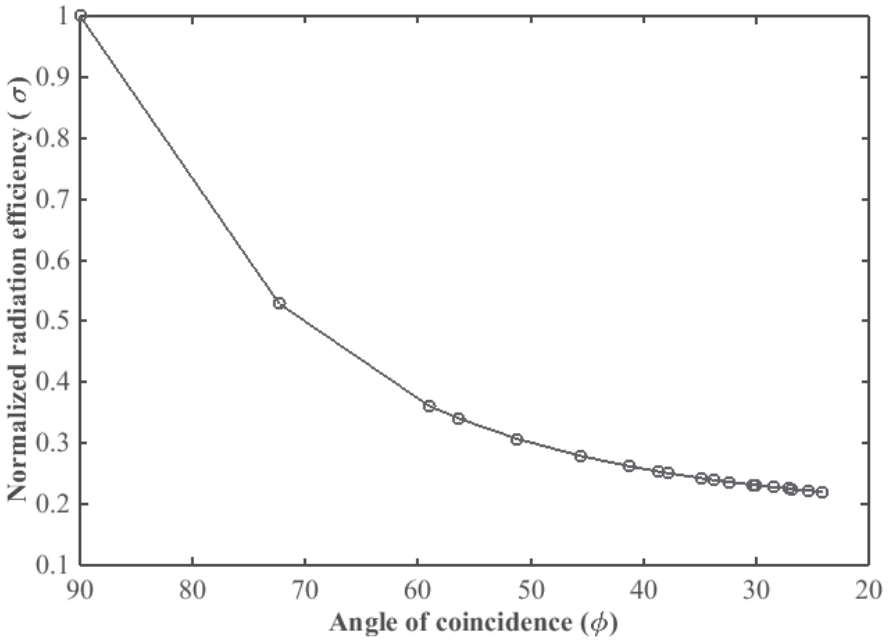

Figure 3.10 Efficiency of the $(5,0)$ mode vs angle of coincidence for frequencies ranging from 850 Hz (90^o) through 2100 Hz (24^o).

In Fig. 3.10, the efficiency is normalized with respect to the maximum efficiency value. However, a radiation mode is the most efficient when it satisfies the coincidence condition at a radiation angle of 90^o, which corresponds to the cut-on frequency. Sarkissian indicates that the mode with the highest efficiency is the one whose axial wavelength is closest to the acoustical wavelength, which is another way of saying that the highest efficiency happens at coincidence angles closest to 90^o [20].

Figure 3.11 shows the radiation efficiency and the angle of coincidence versus frequency for different radiation modes. As the frequency increases, after the cut-on frequency for each mode, the angle of coincidence decreases from 90^o towards 0^o and the efficiency of that mode decreases and approaches an asymptotic value. This explains the reordering of the $(n, m = 0)$ radiation modes

as the frequency increases.

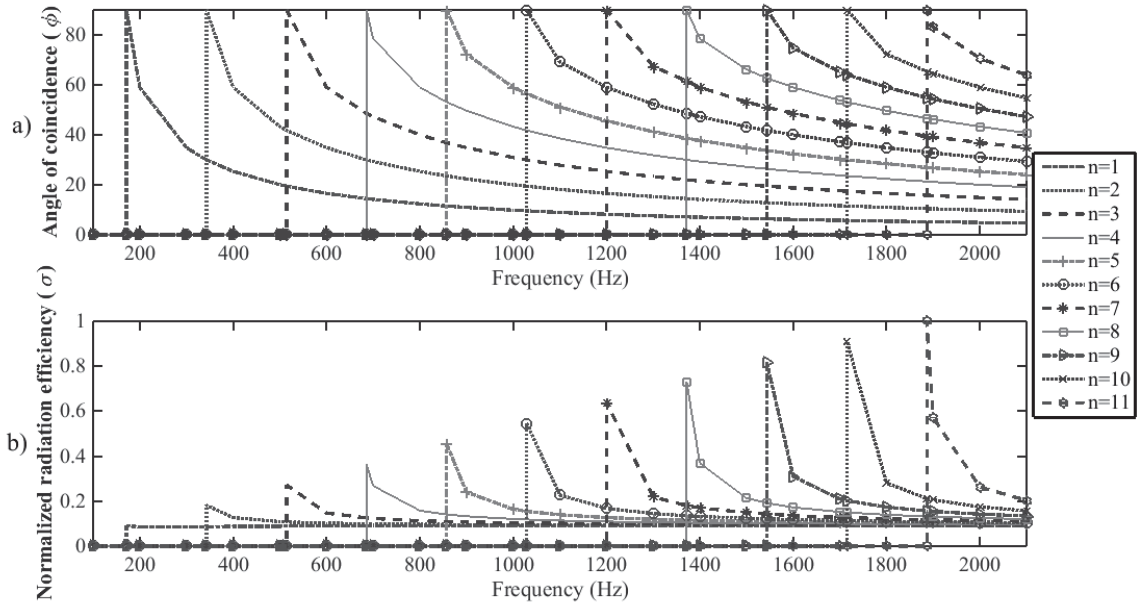

Figure 3.11 a) Angle of coincidence vs. frequency for $(n, m = 0)$ modes. b) Radiation efficiency vs. frequency for $(n, m = 0)$ modes where all the values are normalized with respect to the maximum value for the $(11, 0)$ mode.

Figure 3.11 also suggests that for the $(n, m = 0)$ modes, the higher the axial mode number, n, the more efficient that mode is in the region around its cut-on frequency. This is also consistent with what has been reported in the past [19–21].

Regarding the $(n, m \neq 0)$ modes, a "leapfrog effect" occurs with increasing frequency as the $(n, m+1)$ mode becomes more efficient than the (n, m) mode. Also, unlike the $(n, m = 0)$ modes that exhibit a step function in efficiency at the coincidence condition, the $(n, m \neq 0)$ modes grow in efficiency gradually. There is a frequency span when the mode has not yet satisfied the coincidence condition, but it still radiates as a weak radiator. More insight can be obtained by referring to the bending wave number in the structure, given as

$$k_b^2 = k_z^2 + k_\theta^2, \tag{3.26}$$

where $k_\theta = \frac{m}{a}$. From Eq. (3.9), for the fluid

$$k_r^2 \;=\; k^2 \;-\; k_z^2. \tag{3.27}$$

Considering a family of mode shapes with axial mode number, n, the lowest cut-on frequency which can satisfy the coincidence condition occurs when $k = k_z$ in Eq. (3.27), resulting in $k_r = 0$. For coincidence, $k = k_b$, which means from Eq. (3.26), $k_\theta = 0$. This implies that the $(n, m = 0)$ mode is the first in that group of radiation modes to be turned on and become an efficient radiator. In a similar fashion, a $(n,\ m \neq 0)$ mode can exist as an efficient radiator when

$$k^2 \geq\; k_b^2 \;=\; k_z^2 \;+\; k_\theta^2. \tag{3.28}$$

However, for the region where the $(n, m = 0)$ mode has turned on $(k \geq k_z)$, but $k^2 < k_z^2 + k_\theta^2$ for the $(n, m \neq 0)$ modes, even though the coincidence effect is not yet satisfied for the $(n,\ m \neq 0)$ modes, they can radiate inefficiently as edge mode radiators. As the frequency increases so that k approaches k_b, the efficiency of these edge modes grows until the coincidence condition is satisfied, which explains the gradual growth in the efficiencies of these modes rather than the sudden jump that occurs for the $(n, m = 0)$ modes [158]. The lowest frequency that can satisfy the coincidence condition for a $(n, m \neq 0)$ mode corresponds to $k_c^2 = k_z^2 + k_\theta^2$, where k_c denotes the acoustic wavenumber at coincidence. At this frequency, the radiation mode radiates at an angle of 90^o from the normal. For a specific $(n,\ m)$ mode, as the frequency increases above the coincidence frequency, the coincidence angle decreases so as to satisfy the condition that $(k \sin\phi)^2 = k_c^2 = k_z^2 + k_\theta^2$. The highest efficiency for each specific $(n, m \neq 0)$ mode occurs at the frequency when the coincidence condition is first satisfied at $\phi = 90^o$, similar to the $(n, m = 0)$ modes . Therefore, once the coincidence frequency is reached for a given $(n, m \neq 0)$ mode, that mode's efficiency decreases slightly at higher frequencies, approaching an asymptotic value, as seen in Fig. 3.8. However, as the frequency increases, higher order modes are successively able to

satisfy the coincidence condition at $\phi = 90^o$, and as a result, their efficiencies jump a little higher than the already existing efficient modes. This explains the reordering of the radiation modes in terms of their efficiency as the frequency increases.

3.5.2 Grouping effect

Another interesting characteristic that can be seen in Figs. 3.2-3.4 is the presence of degenerate modes. Symmetry often introduces degeneracy into a system. From Figs. 3.2-3.4 , one can see that for the $(n, m \neq 0)$ modes, there is a degeneracy factor of two for the eigenvalues, due to the circular geometry. For each $(n, m \neq 0)$ mode, the angular response can be described as a function of a sine or cosine function. Therefore, for each $(n, m \neq 0)$ mode, there are two different radiation mode shapes with the same eigenvalue where one is shifted by $\pi/(2m)$ with respect to the other. However, for $(n, m = 0)$ radiation mode shapes there is no such degeneracy and those modes appear as single eigenvalues.

3.6 Conclusions

Radiation modes provide a powerful approach for analyzing acoustic radiation from a structure because of their computational efficiency. Using radiation modes, the acoustic radiation can be characterized though the use of a very small number of modes when compared to the number of structural modes that are typically required to analyze the same acoustic radiation. In this paper, radiation modes to describe the external radiation from a baffled cylindrical shell have been developed analytically, using a Fourier series representation. While symmetric $m = 0$ modes have been studied previously, radiation modes of higher circumferential index, m, have been presented here. By considering the wavenumber domain, it was shown that the coincidence effect plays an important role in the cut-on phenomenon observed for radiation modes with different axial

mode numbers. The coincidence angle at a specific frequency is a determining factor in describing how efficient each group of radiation modes with a given axial mode number is, and this effect is responsible for the “leapfrog effect", where modes with a higher modal number jump above modes with a lower modal number, in terms of their efficiency. In general, the $(n, m = 0)$ radiation modes are the most efficient modes and therefore contribute most significantly to the radiated sound power. Their efficiencies asymptotically approach a value that is higher than the efficiencies associated with the $(n, m \neq 0)$ modes. With increasing frequency, the $(n, m = 0)$ mode with the highest axial index that has met the coincidence condition is the most efficient mode and leads to enhanced radiated sound power. It has also been observed that there is a degeneracy factor of two for the $(n, m \neq 0)$ modes, due to the circular geometry.

Chapter 4

Numerical results

4.1 Natural frequencies

In Chapter 2, Seodel's shell theory was used to describe the dynamic behavior of circular cylindrical shells. In this chapter, a numerical model is presented to describe the dynamic response of a simply supported aluminum cylindrical shell with length 1.206 m, radius 0.0778 m, and thickness 0.0016 m. The modeling has been done using Matlab. The cylinder model is discretized using 2500 elements, with 50 increments along the circumference and 50 elements along the axis of the cylinder. This results in dimensions of each element being 0.024 m along the axis, and 0.01 m along the circumference. The highest frequency considered here is 900 Hz, which corresponds to an acoustic wavelength of 0.38 m. Since the dimensions of the elements considered are significantly less than the smallest acoustic wavelength, the same discretization can be used for all frequencies in the range of interest.

It is also important to consider the sufficient number of terms to include in the summation of Eq. (2.15) to ensure convergence and stability of the simulation. Figure 4.1 shows the convergence trend for differing numbers of terms included for a range of frequencies. The convergence trend

is obtained for the normal displacement at a point location. As can be seen, the convergence is ensured if at least 100 terms are included in the summation. In this work, 200 terms are retained for all simulations as an extra safety factor.

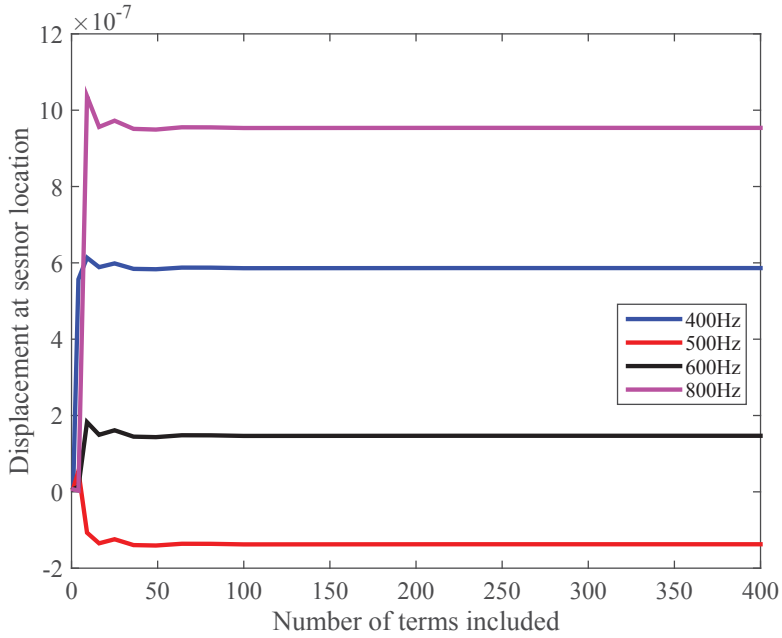

Figure 4.1 Vibration field of the cylindrical shell at 203 Hz representing the (1,2) mode.

To implement the model, parameters corresponding to aluminum are considered. The parameters of the shell used in the simulation are listed in Table 4.1.

Table 4.1 Shell parameters

Parameters	Mathematical symbol	Value	Units
Density	ρ_s	2650	kg/m^3
Poisson's ratio	μ_p	0.334	-
Young's Modulus	E	7.06e+10	Pa
Viscous damping factor	η	0.0085	kg/s

η will not impact the natural frequencies but will modify the resonance amplitudes. This is taken into account when calculating the normal displacement due to a point force in the next section. According to Eq. (2.10), ω_{inm} describes the natural frequencies in the axial, circumferential and normal directions, where $i = 1, 2, 3$ correspond to those directions, respectively.

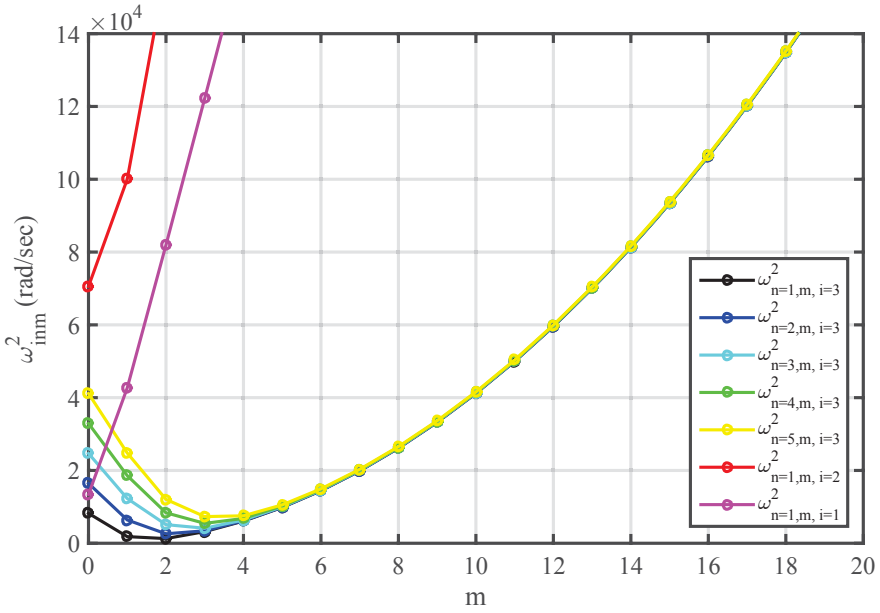

Figure 4.2 ω_{inm} for different axial and circumferential mode numbers.

In Figs.4.2 and 4.3, natural frequencies are shown for some of the vibration modes along the axial, circumferential and normal directions. As can be seen, the frequencies associated with the in-plane axial and circumferential modes are much higher in frequency than the corresponding out-of-plane mode with the same mode number. Since at resonance, the in-plane modes are only able to provide tangential displacement, it is only the modes associated with the normal direction that are able to radiate acoustically at low frequencies and will be considered from this point on.

Figure 4.4 provides a better view of ω_{3nm} at lower modes. Despite the common behavior of beams and plates where lower frequencies are associated with the lowest mode numbers, one can

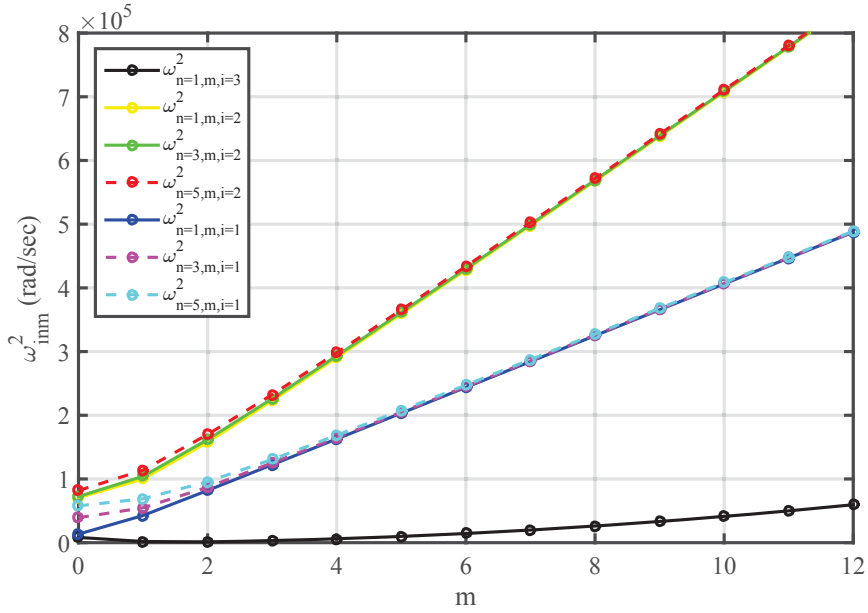

Figure 4.3 ω_{inm} for different axial and circumferential mode numbers.

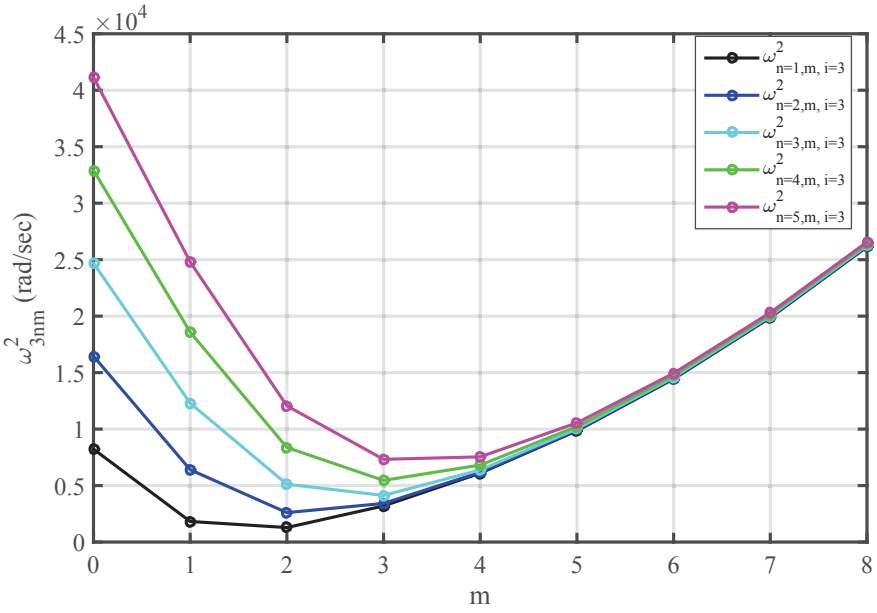

Figure 4.4 ω_{3nm} for different axial and circumferential mode numbers.

see that for the cylindrical shell under study here, the lowest resonance frequency is associated with the $(1,2)$ mode. This behavior results from the curved nature of the shell. By modifying the properties of the shell such as length, radius, thickness, density, Young's modulus, stiffness and so forth, the mode with the lowest frequency can be made to vary.

As mentioned previously, only the normal components of the vibration will be taken into account for looking at acoustic radiation. However, in order to verify the numerical model, the ratios of modal amplitudes in all three different directions were calculated, and the general trend has been verified using Soedel's result for a simply supported shell. Figures 4.5, 4.6 and 4.7 show these ratios, which agree with the trends Soedel has reported [76].

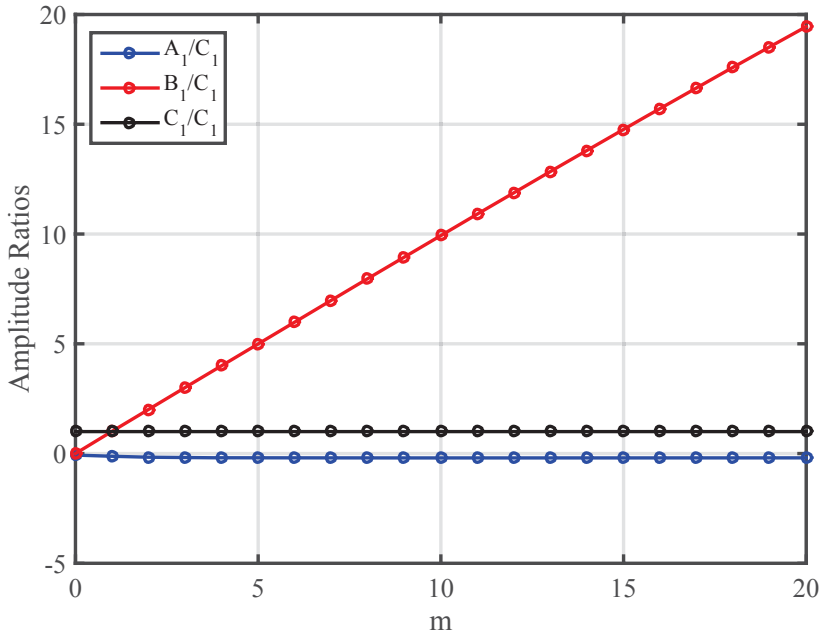

Figure 4.5 Ratios of modal amplitudes for $i = 1, n = 1$.

The natural frequencies associated with the normal displacement are calculated, using the third root shown in Eq. (2.10). Table 4.2 lists all the natural frequencies associated with the normal direction up to 1.5 kHz for this particular shell.

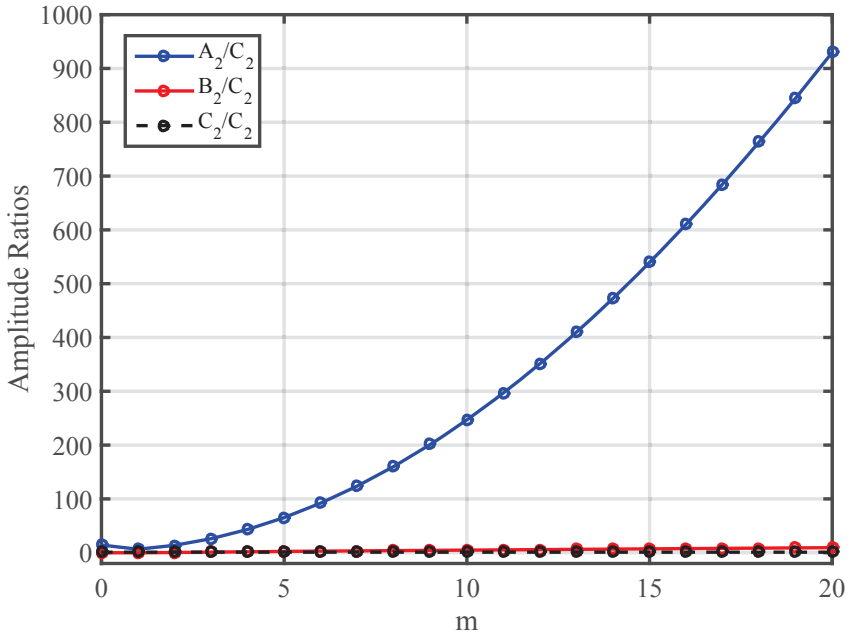

Figure 4.6 Ratios of modal amplitudes for $i = 1, n = 1$.

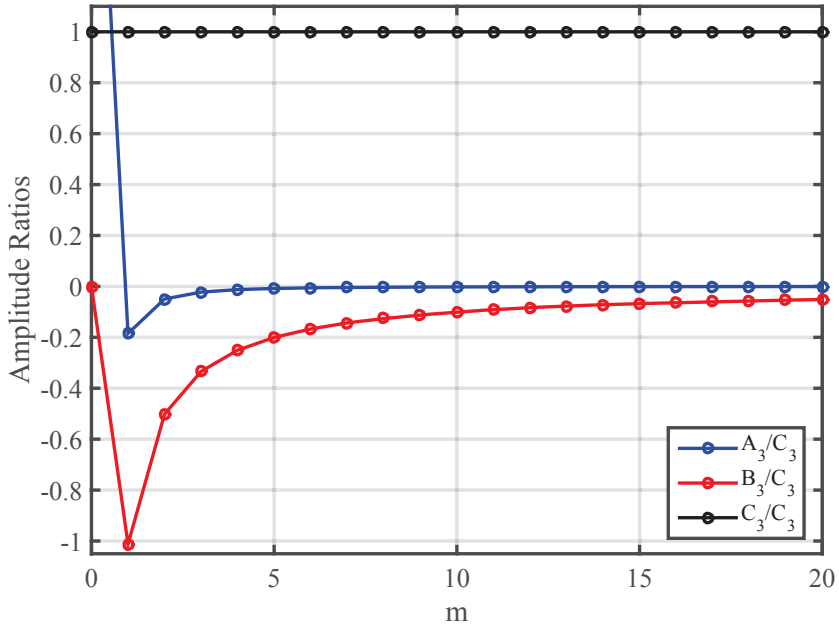

Figure 4.7 Ratios of modal amplitudes for $i = 1, n = 1$.

Table 4.2 Natural frequencies

Frequency (Hz)	n	m
203.06	1	2
290.23	1	1
413.91	2	2
505.27	1	3
540.71	2	3
653.77	3	3
814.28	3	2
866.07	4	3
963.29	1	4
975.87	2	4
1009.45	3	4
1018.83	2	1
1078.33	4	4
1163.40	5	3
1193.87	5	4
1309.59	1	0
1331.94	4	2
1359.94	6	4
1522.00	6	3

As can be seen, the first breathing mode, $(1,0)$, (the mode with the lowest mode numbers) has a natural frequency of 1309.59 Hz which is much higher than other higher order modes, and is a different behavior than what is usually seen for plates and beams.

4.2 Vibration field with a point force

In practice, the cylinder is excited using a point force. Hence, Eq. (2.15) is used to describe the vibration field of the cylinder. The results are simulated using a 20 N point force at the location of (z = 0.1, $\theta = 45^o$). Figures 4.8 - 4.15 show the vibration field of an unwrapped cylinder at the resonance frequencies, using the parameters listed in Table 4.1.

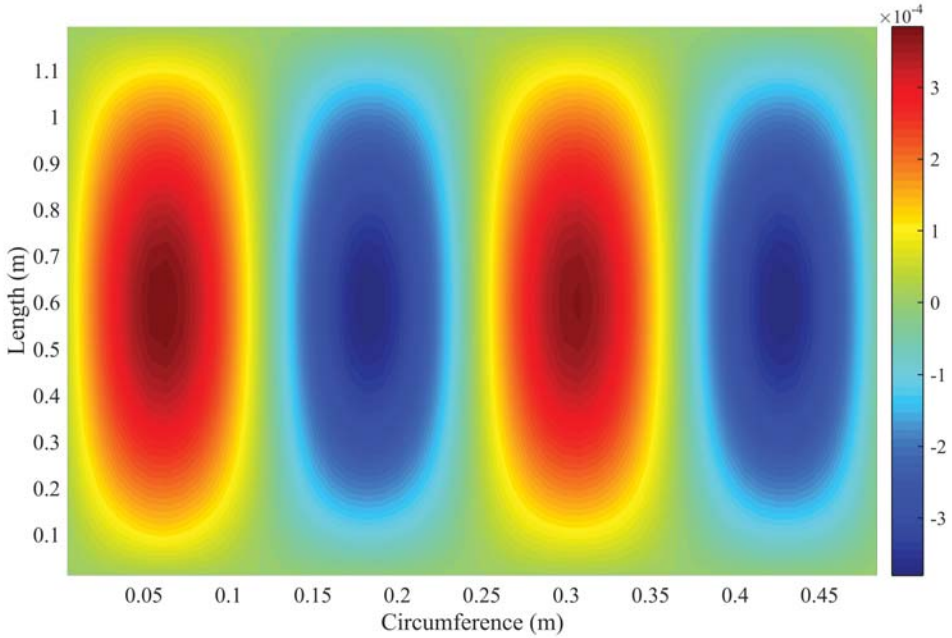

Figure 4.8 Vibration field of the cylindrical shell at 203.06 Hz representing the (1,2) mode.

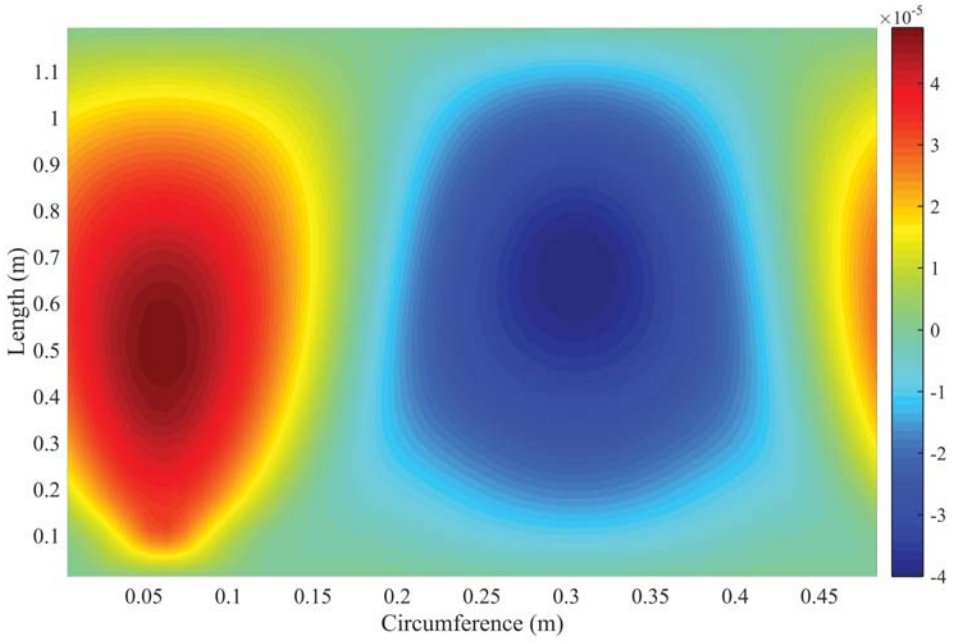

Figure 4.9 Vibration field of the cylindrical shell at 290.23 Hz representing the (1,1) mode.

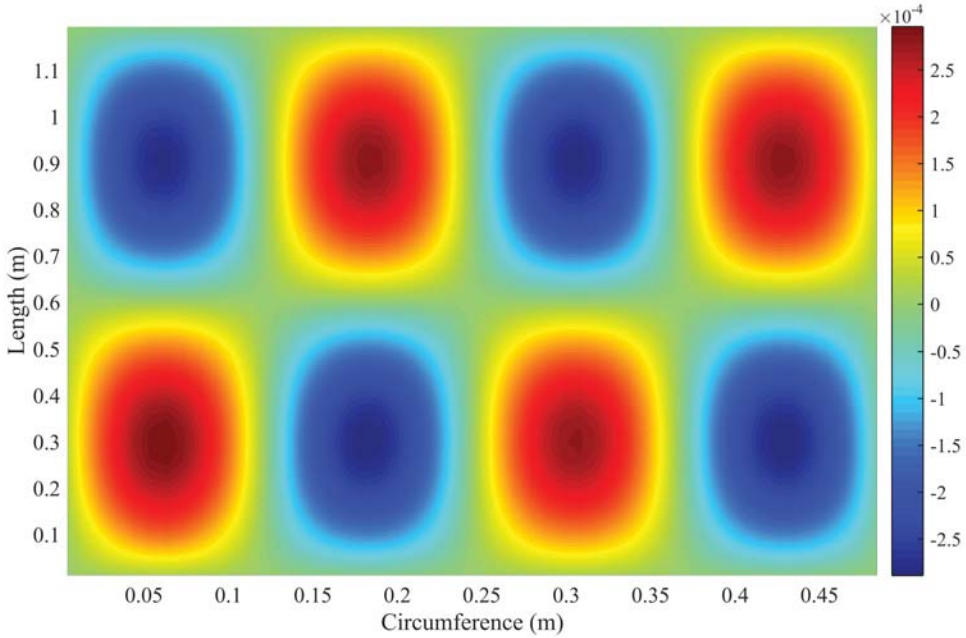

Figure 4.10 Vibration field of the cylindrical shell at 413.91 Hz representing the (2,2) mode.

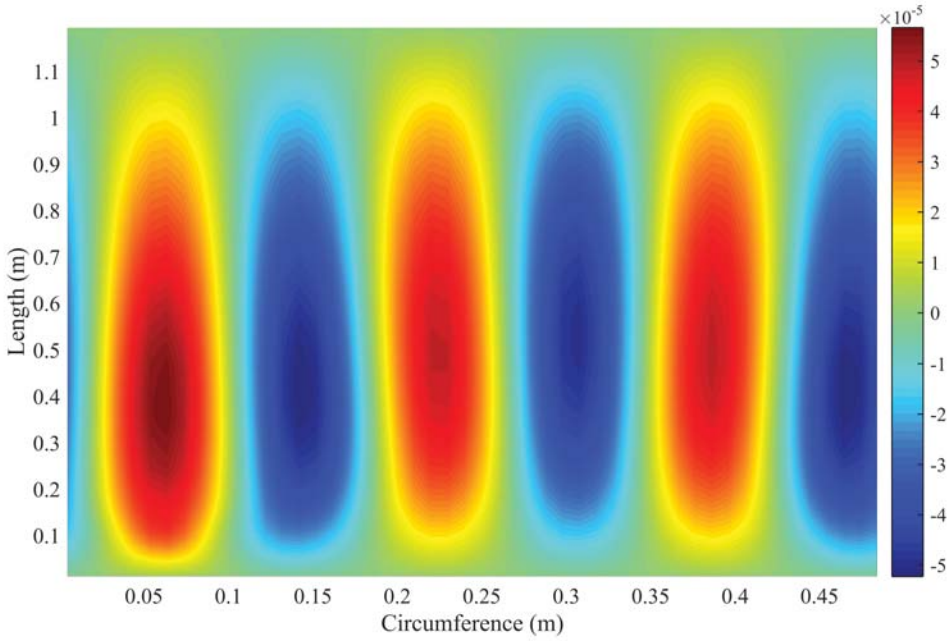

Figure 4.11 Vibration field of the cylindrical shell at 505.27 Hz representing the (1,3) mode.

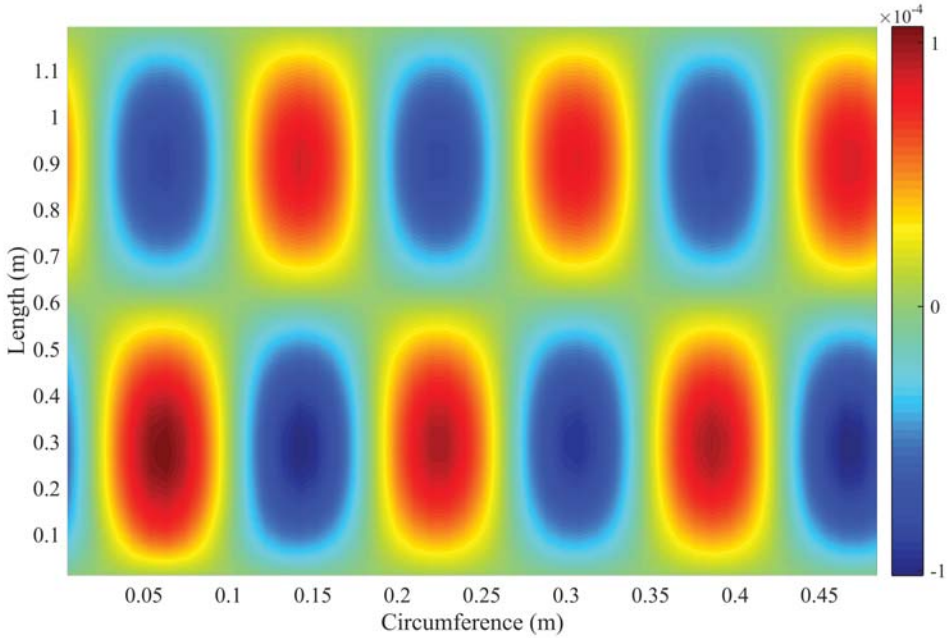

Figure 4.12 Vibration field of the cylindrical shell at 540.71 Hz representing the (2,3) mode.

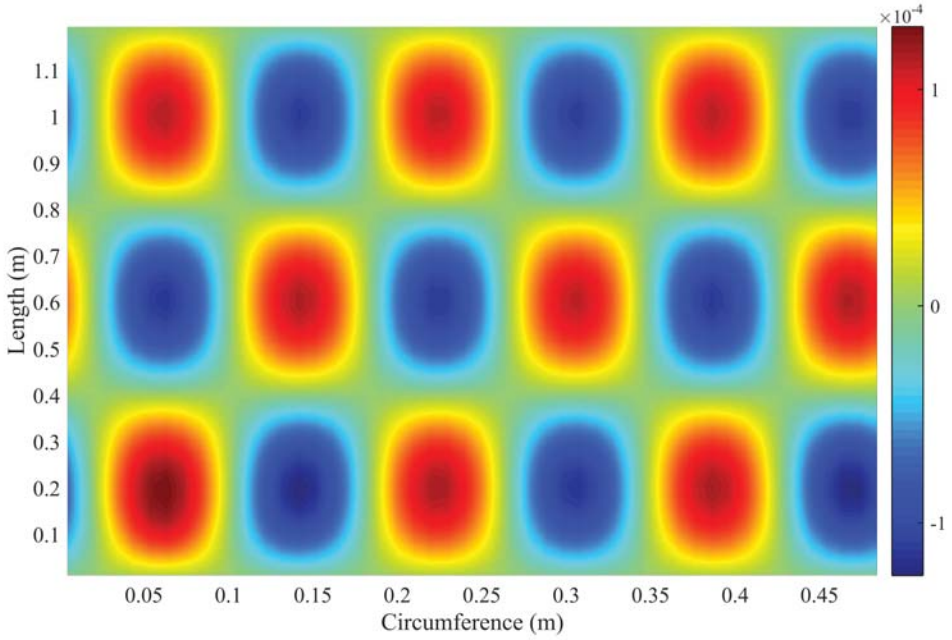

Figure 4.13 Vibration field of the cylindrical shell at 653.77 Hz representing the (3,3) mode.

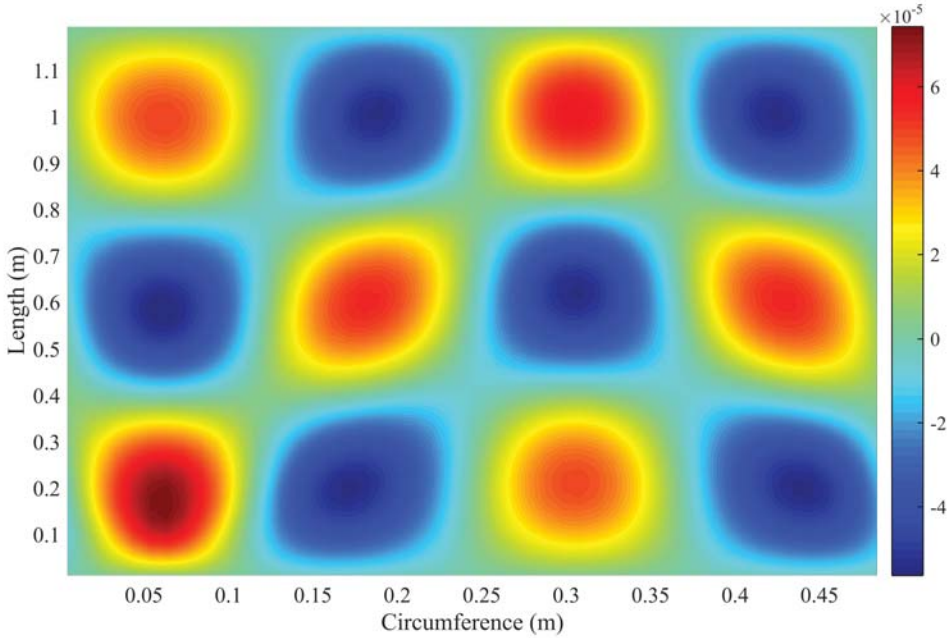

Figure 4.14 Vibration field of the cylindrical shell at 814.28 Hz representing the (3,2) mode.

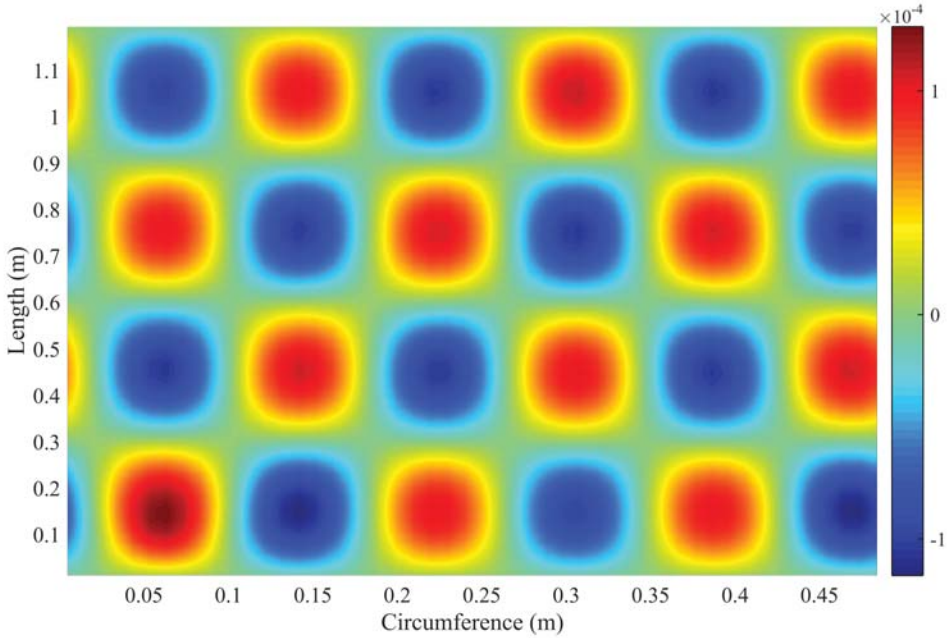

Figure 4.15 Vibration field of the cylindrical shell at 866.07 Hz representing the (4,3) mode.

4.3 WSSG field

Having simulated the normal displacement due to a point force, one can use Eqs. (2.19) - (2.22) to simulate the spatial gradients of the vibration field. This can be calculated at any frequency. However, for the purpose of better illustration, the spatial gradients are demonstrated here for some of the resonance frequencies. Figures 4.16 - 4.23 present the squared spatial gradients for the terms of WSSG at each of the first eight resonance frequencies.

If each of the terms is weighted properly, when added together, the spatial variance of the sum can be greatly reduced, hence creating a fairly uniform field. As mentioned previously, the spatial uniformity of the cost function can significantly diminish the dependence on sensor location.

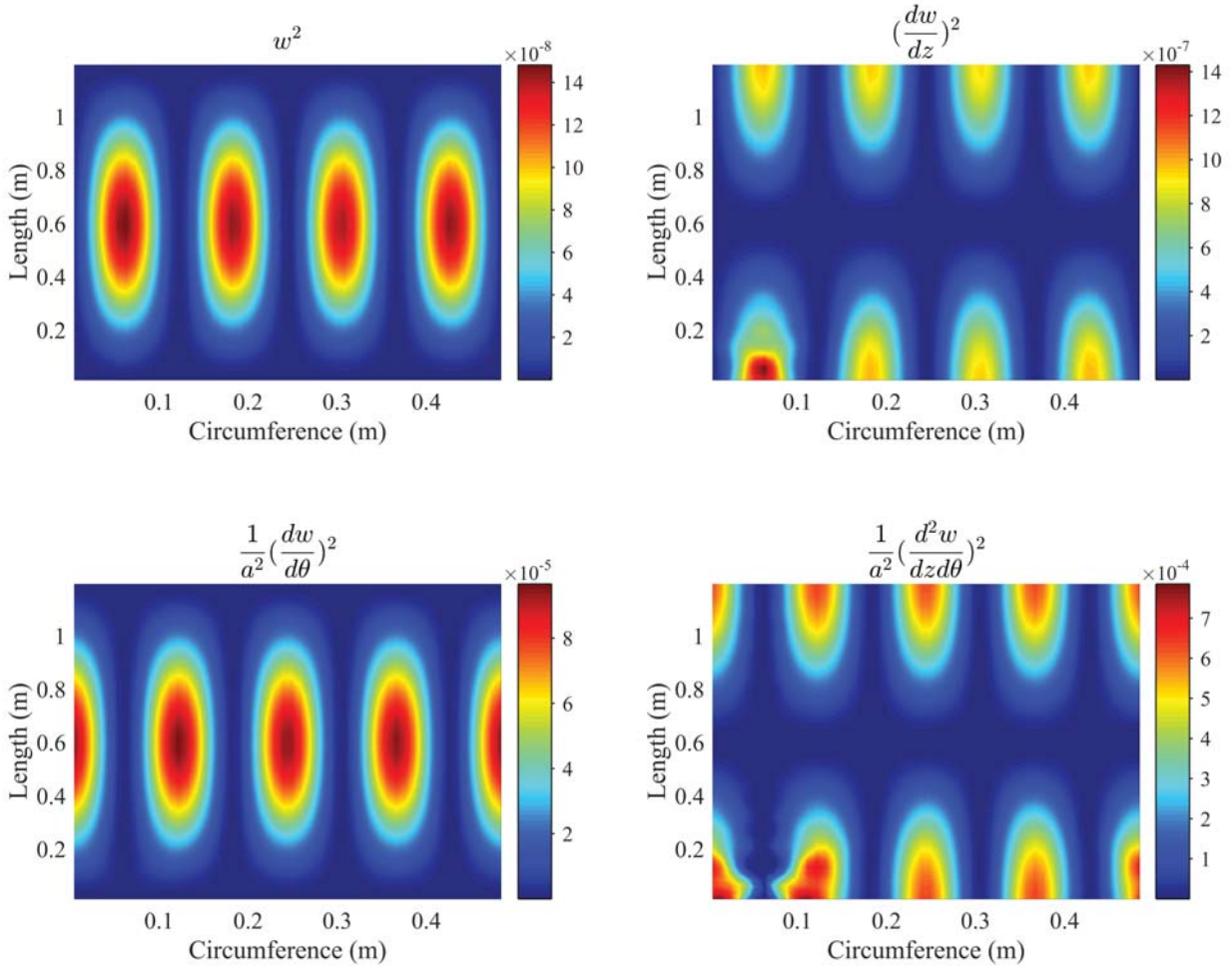

Figure 4.16 Squared spatial gradients for the terms of WSSG at 203.06 Hz for the (1,2) mode.

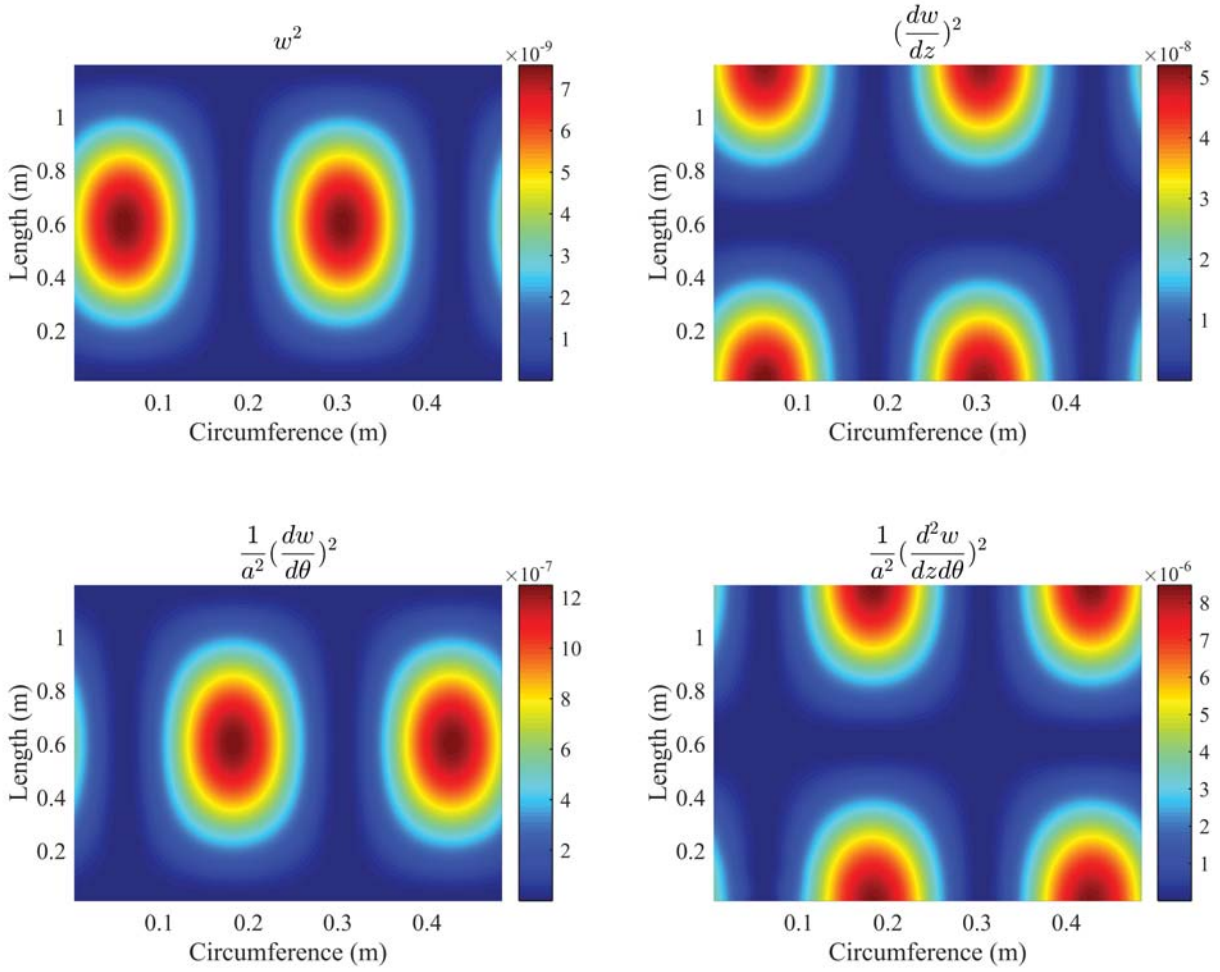

Figure 4.17 Squared spatial gradients for the terms of WSSG at 290.23 Hz for the (1,1) mode.

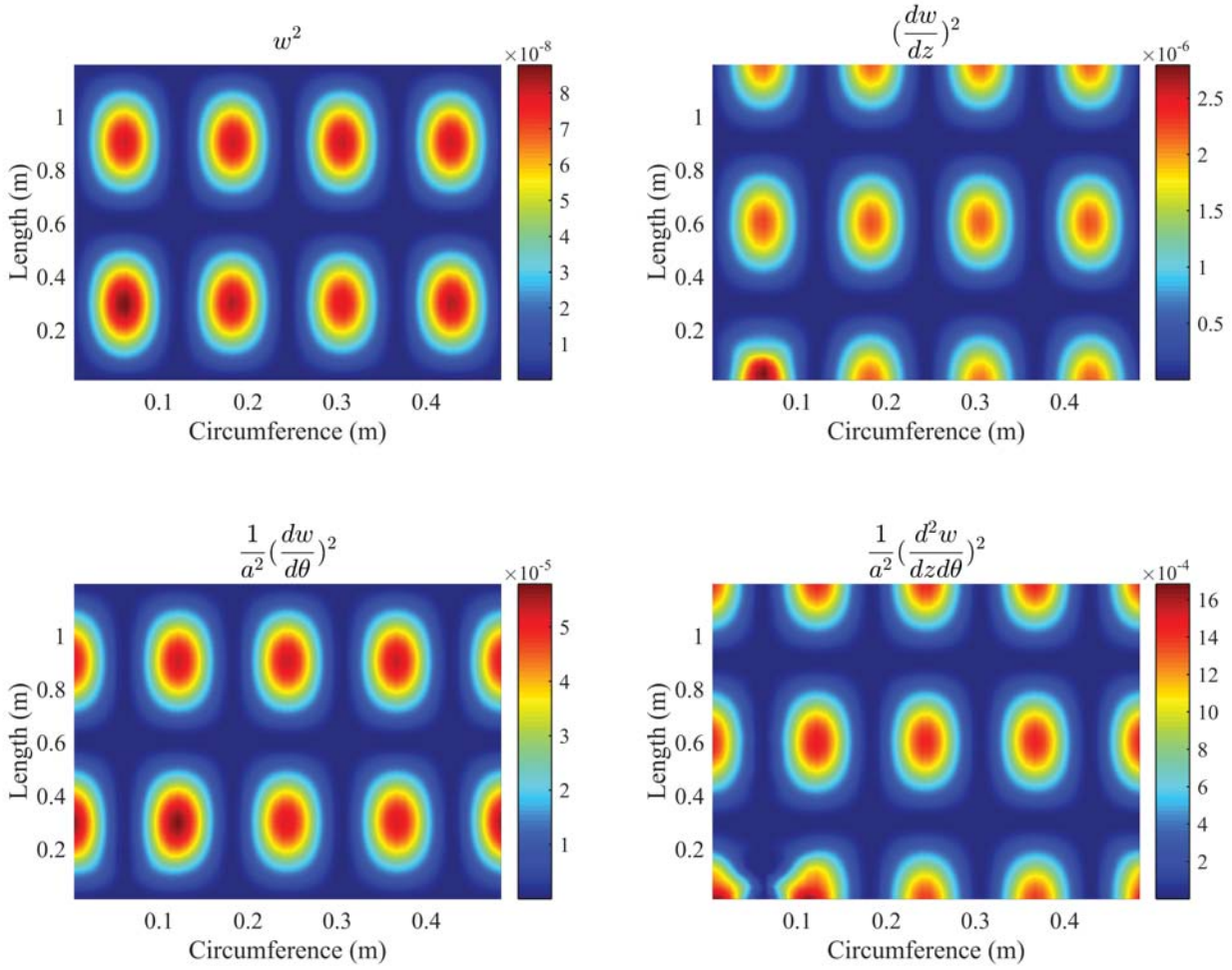

Figure 4.18 Squared spatial gradients for the terms of WSSG at 413.91 Hz for the (2,2) mode.

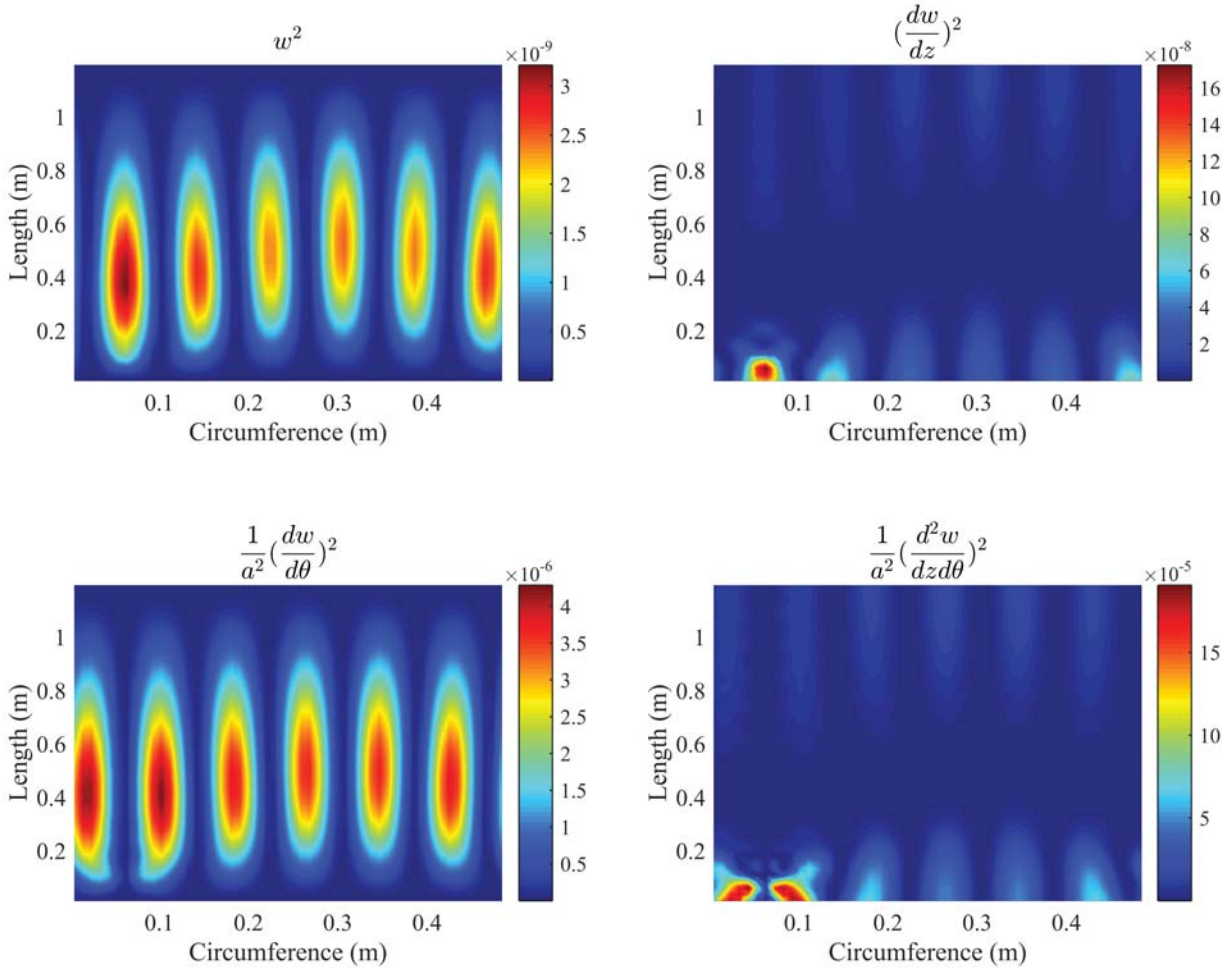

Figure 4.19 Squared spatial gradients for the terms of WSSG at 505.27 Hz for the (1,3) mode.

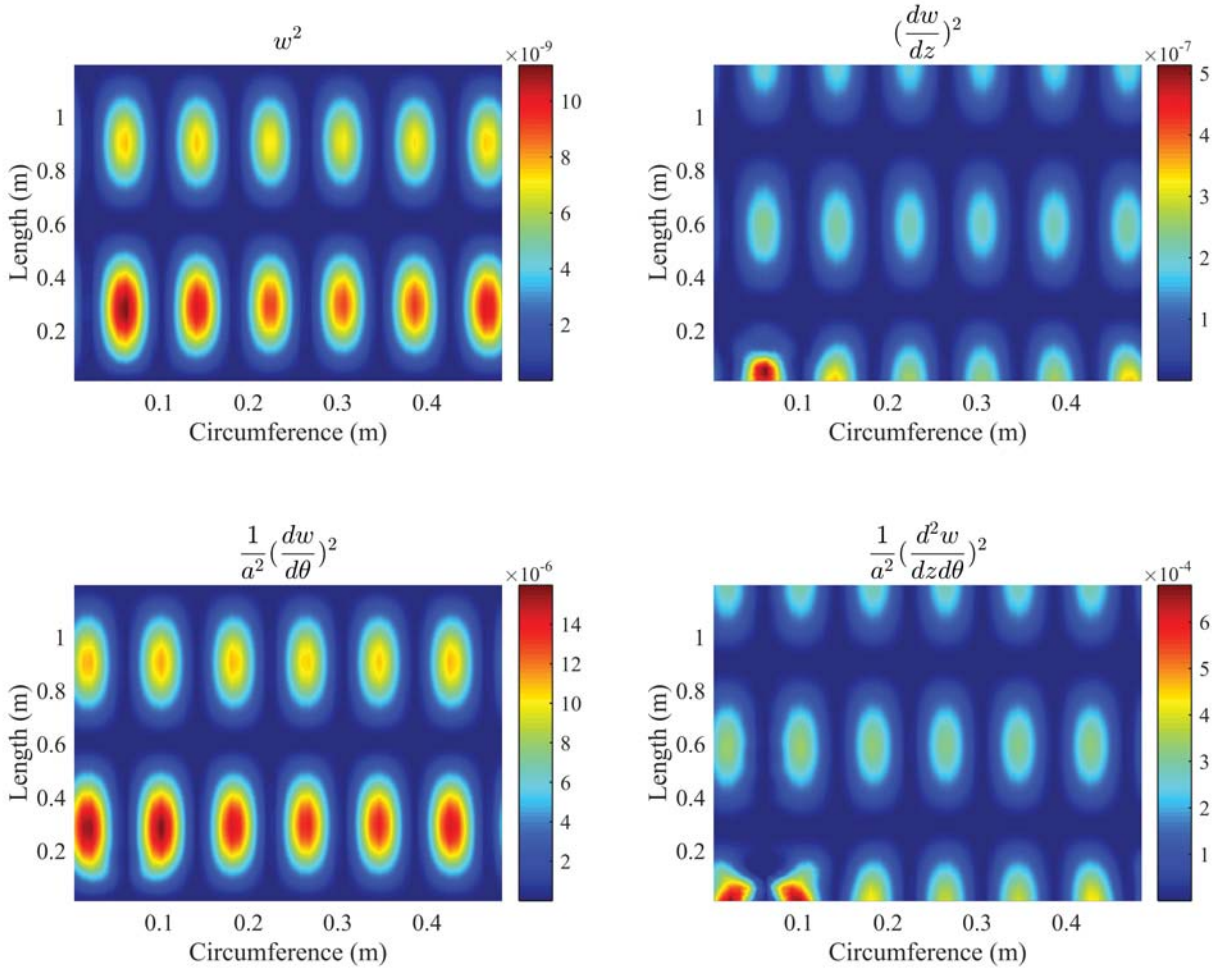

Figure 4.20 Squared spatial gradients for the terms of WSSG at 540.71 Hz for the (2,3) mode.

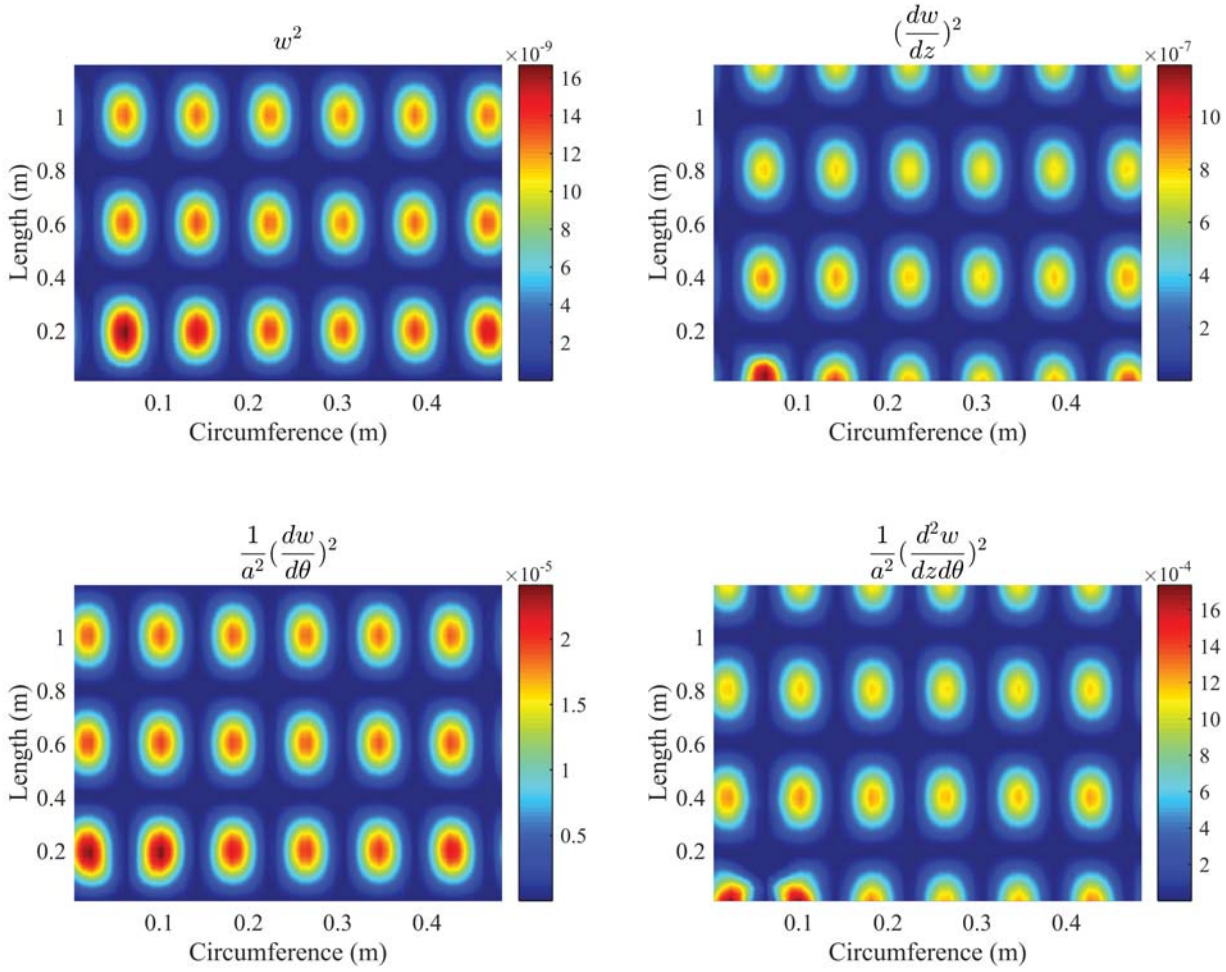

Figure 4.21 Squared spatial gradients for the terms of WSSG at 653.77 Hz for (3,3) mode.

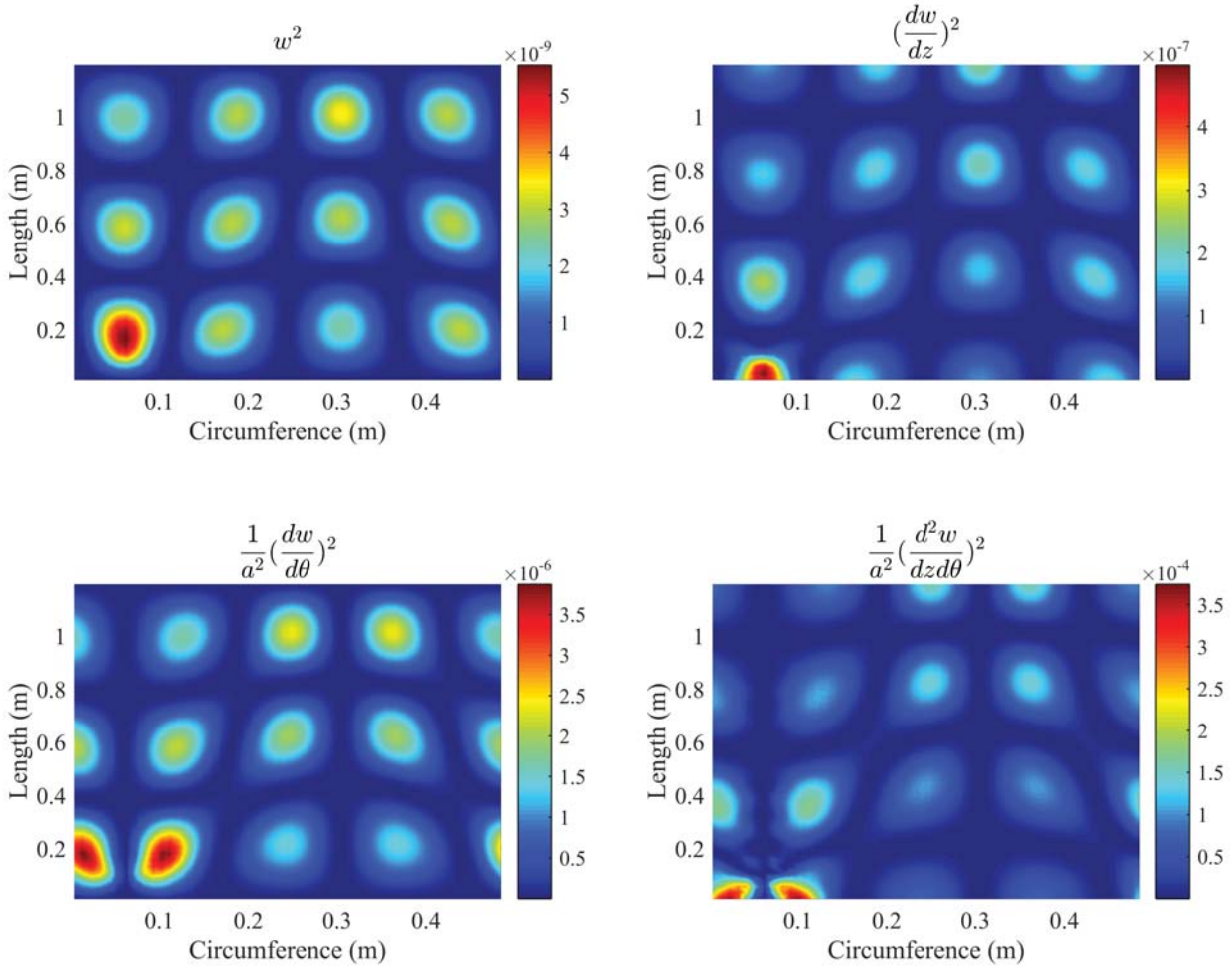

Figure 4.22 Squared spatial gradients for the terms of WSSG at 814.28 Hz for the (3,2) mode.

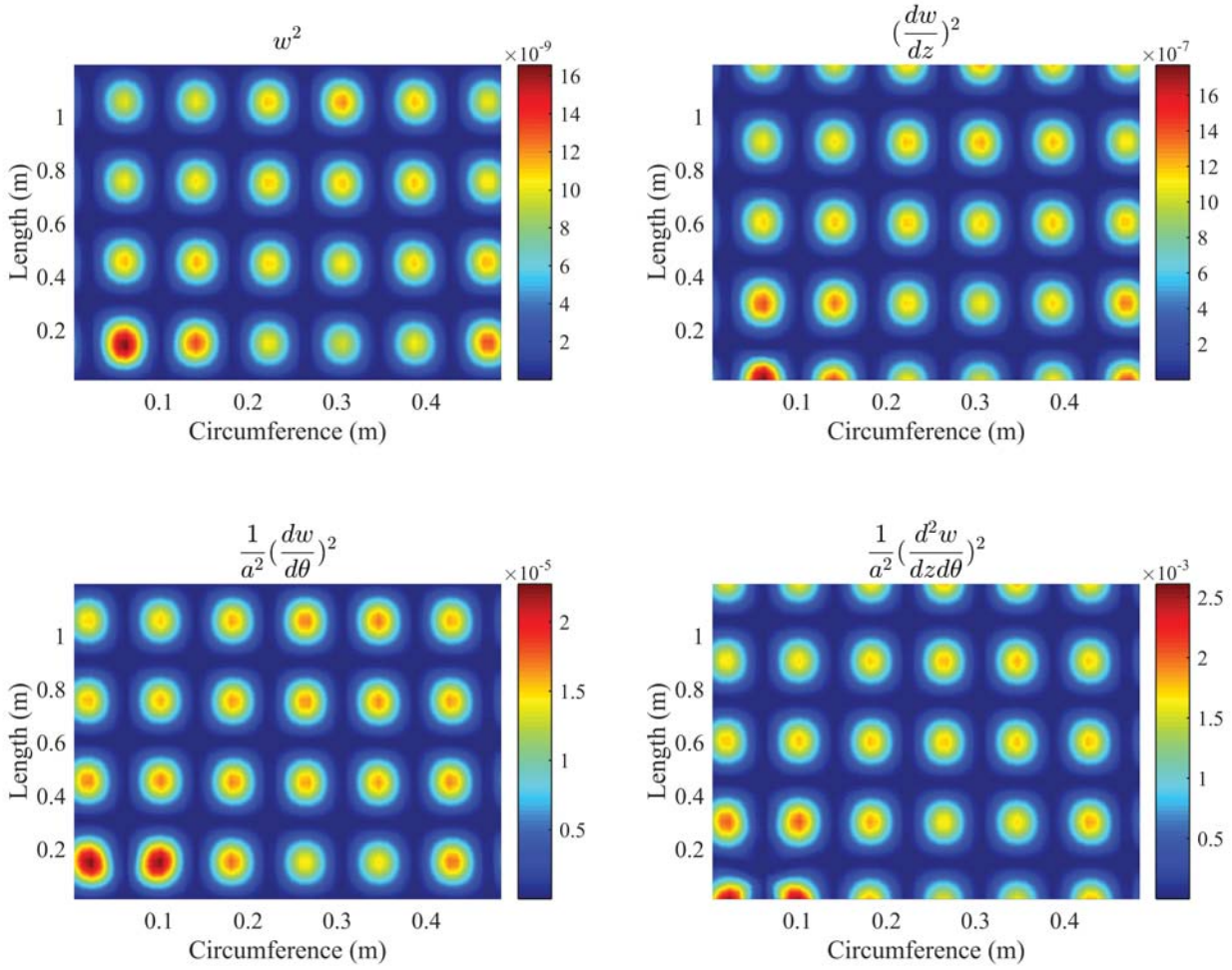

Figure 4.23 Squared spatial gradients for the terms of WSSG at 866.07 Hz for the (4,3) mode.

4.3.1 Weighting the spatial gradients

The next phase of developing WSSG is to find the set of weights that is able to combine these terms in such a way that they result in a uniform field. For each of the resonance frequencies, Eqs. (2.19) - (2.22) indicate that if the coefficient corresponding to the normal displacement is taken to have the value of 1, then the normalized coefficients associated with the other terms would be the inverse of the wavenumber squared along that direction. For a simply supported cylindrical shell, $k_z = \frac{n\pi}{L}$ and $k_\theta = \frac{m}{a}$. If α, β, δ and γ represent the normalizing weights respectively for w, $\frac{dw}{dz}$, $\frac{dw}{d\theta}$ and $\frac{d^2w}{dzd\theta}$, Table 4.3 presents these weights for the first eight resonances.

Simulation results are obtained using Eq. (2.15), which utilizes modal summation in order to express the vibration field. When calculating any of the spatial gradients in Eqs. (2.19) - (2.22), the wavenumber associated with each mode in the modal decomposition is extracted, which is a function of the summation index. Therefore, it is hard to use only one wave number in order to weight the spatial gradients. However, when the frequency of the driving force matches that of any resonance, the wavenumber associated with that mode can be safely used to weight the spatial gradients.

Figures 4.24 - 4.31 plot the WSSG function throughout the unwrapped cylinder for the first eight resonance frequencies, using the weights as described. One can note the degree of uniformity by paying attention to the order of magnitude of the colorbar in Figs.4.24 - 4.31.

The weights given in Table 4.3 are ideal for each resonance mode. However, in terms of a broadband application which can include both resonances and anti-resonances, it is desirable to come up with a single set of weights that is applicable over the frequency range of interest. In this dissertation, the focus of the active noise control approach is on low frequencies and the frequency range of interest is limited to below 900 Hz. In order to obtain the set of weights, one method is to obtain the maximum value of the field for the first spatial gradient term and normalize the second, third and fourth spatial gradient terms with respect to that maximum value and average

Table 4.3 Modal weights

Frequency (Hz)	α	$\beta = \left(\frac{1}{k_z}\right)^2$	$\delta = \left(\frac{1}{k_\theta}\right)^2$	$\gamma = \left(\frac{1}{k_z k_\theta}\right)^2$
203.06	1.0	1.47487e-01	1.51321e-03	2.2318e-04
290.23	1.0	1.47487e-01	6.05284e-03	8.9272e-04
413.91	1.0	3.68718e-02	1.51321e-03	5.5790e-05
505.27	1.0	1.47487e-01	6.72540e-04	9.9190e-05
540.71	1.0	3.68718e-02	6.72540e-04	2.4800e-05
653.77	1.0	1.63874e-02	6.72540e-04	1.1020e-05
814.28	1.0	1.63874e-02	1.51321e-03	2.4797e-05
866.07	1.0	9.21032e-03	6.72540e-04	6.1943e-06

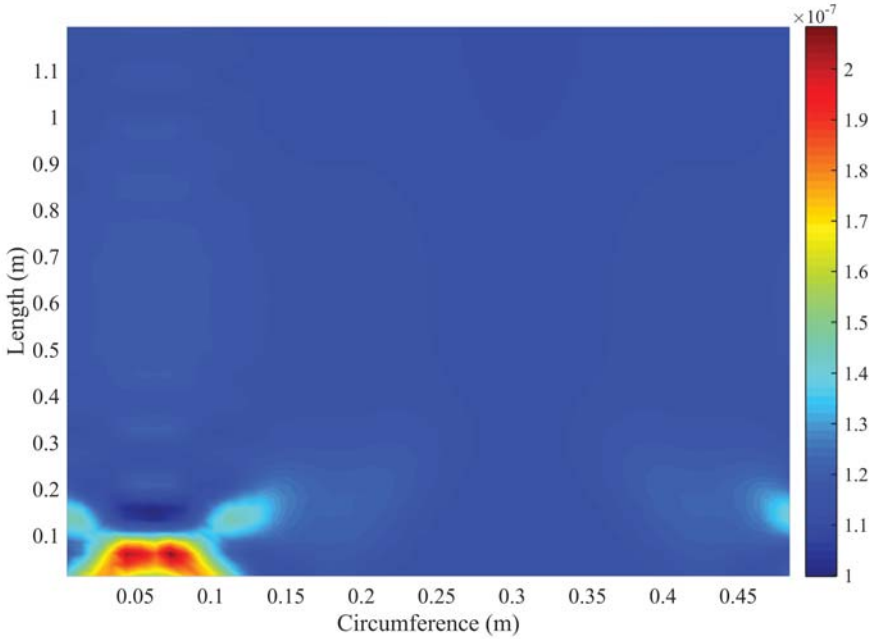

Figure 4.24 WSSG at 203.06 Hz for the (1,2) mode.

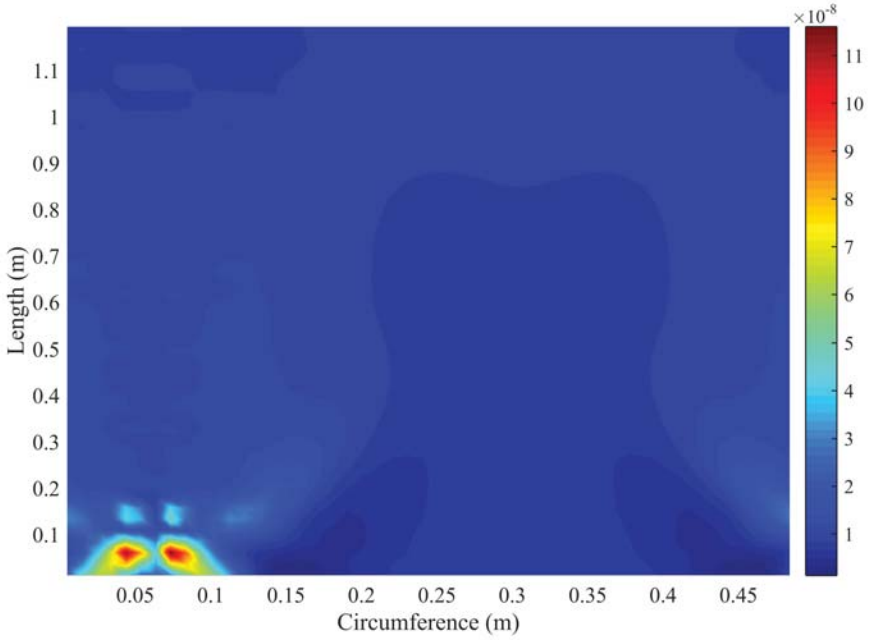

Figure 4.25 WSSG at 290.23 Hz for the (1,1) mode.

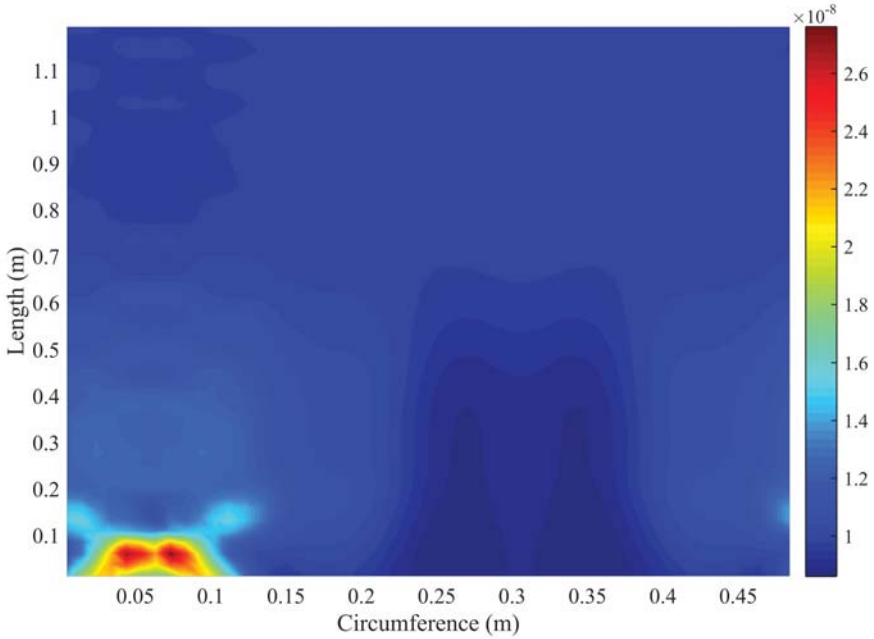

Figure 4.26 WSSG at 413.91 Hz for the (2,2) mode.

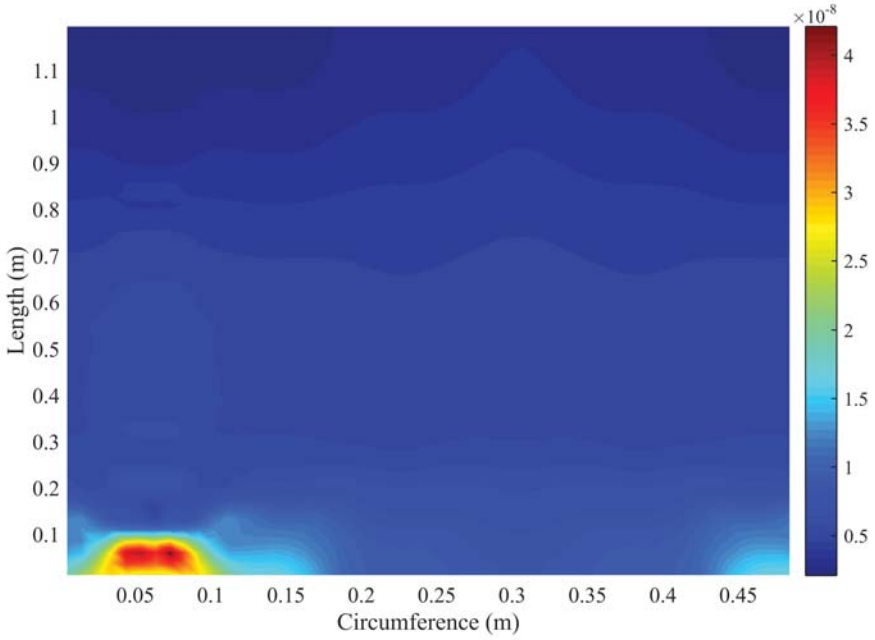

Figure 4.27 WSSG at 505.27 Hz for the (1,3) mode.

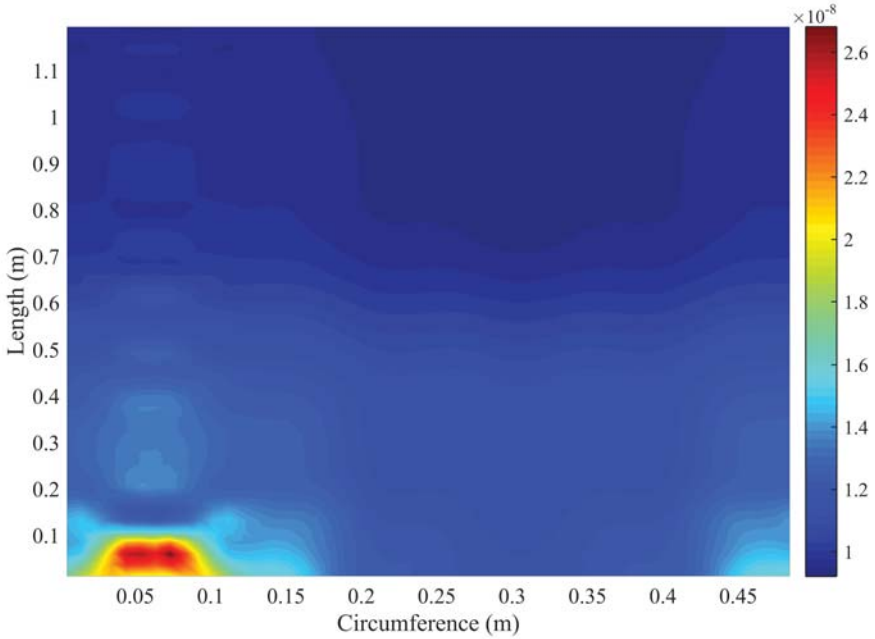

Figure 4.28 WSSG at 540.71 Hz for the (2,3) mode.

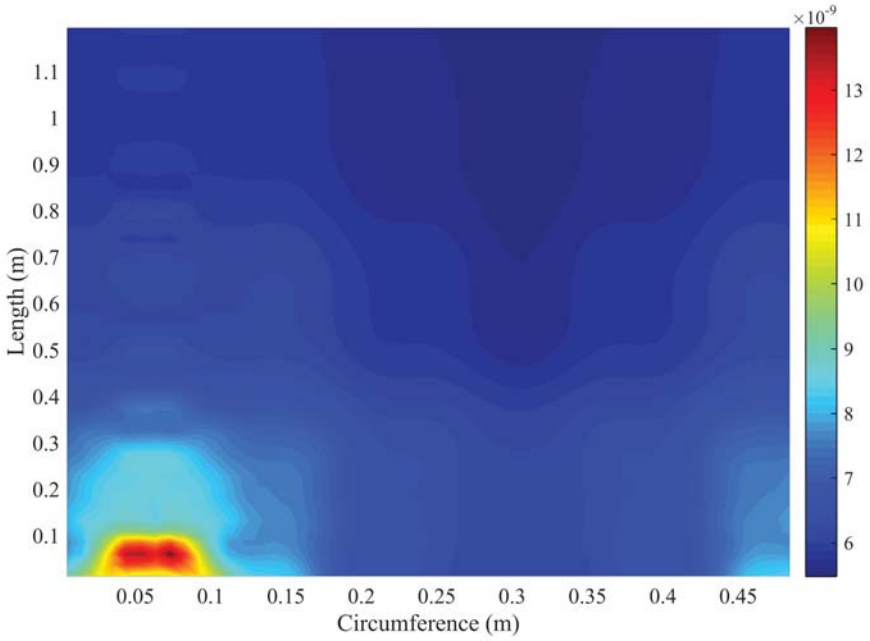

Figure 4.29 WSSG at 653.77 Hz for the (3,3) mode.

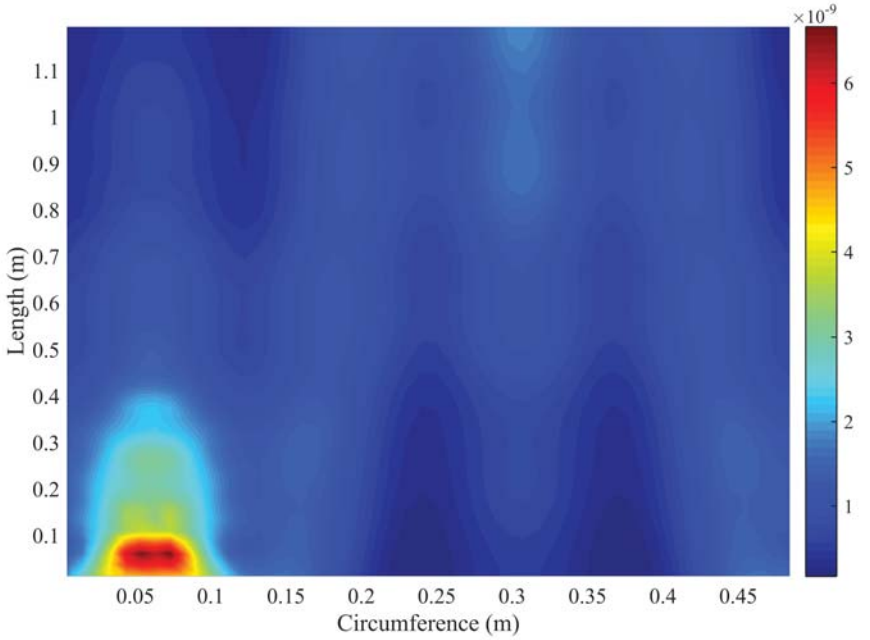

Figure 4.30 WSSG at 814.28 Hz for the (3,2) mode.

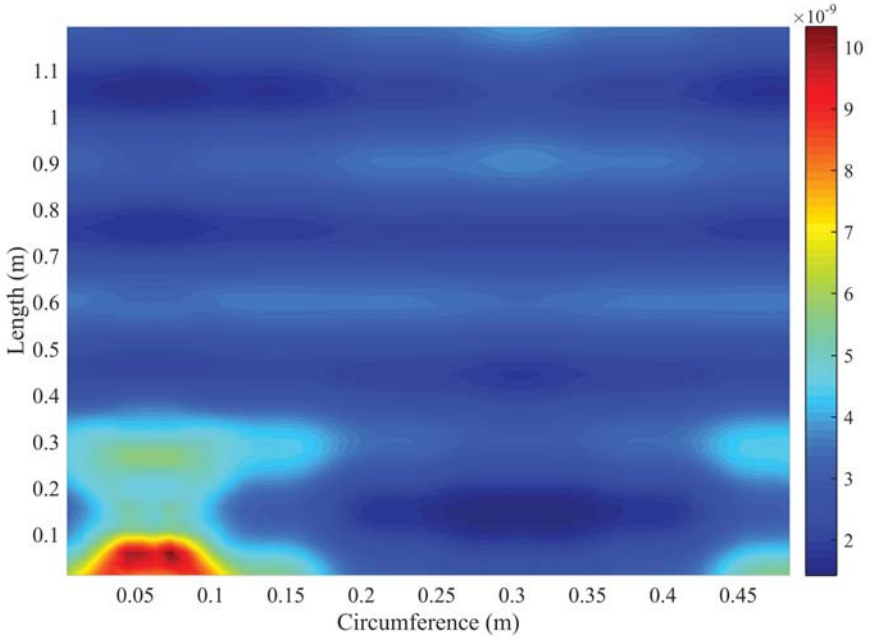

Figure 4.31 WSSG at 866.07 Hz for the (4,3) mode.

this over the frequency range of interest. Another approach would be to calculate the weights for all the resonances present in the frequency range and average them over the number of resonances considered. Through this averaging process, the average weights obtained are given in Table 4.4.

Table 4.4 Average weights

α	β	δ	γ
1.0	0.07	0.0017	1.7e-04

4.4 WSSG control

The method of optimizing WSSG with respect to the secondary force has been explained in Section 2.1.4.1.1. Table 4.5 shows the coordinates for the location of the primary and control sources as

well as the error sensor location. Figure 4.32 shows this configuration and it will be referred to as configuration I.

Table 4.5 Location of sensor and actuators for configuration I.

	Primary Shaker	Control Shaker	Sensor
z (m)	0.1016	1.0478	0.68
θ (degrees)	30	210	305

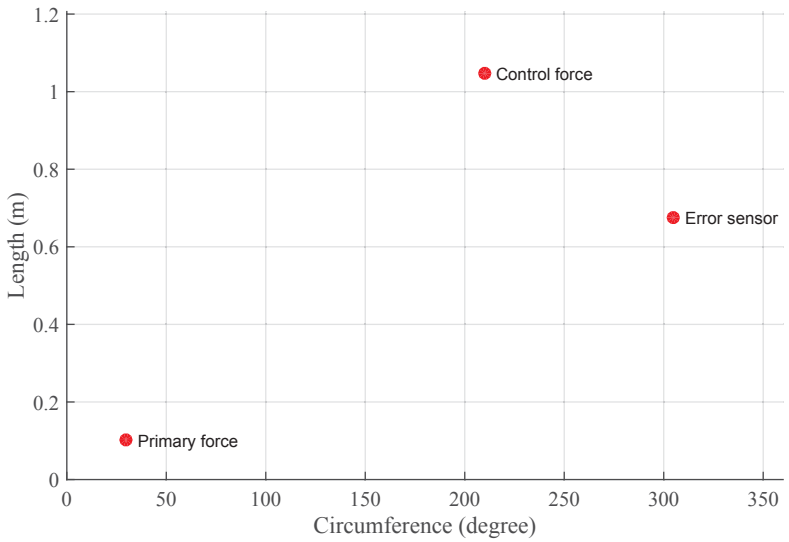

Figure 4.32 Control configuration I.

The forces are chosen to be 180 degrees apart from each other to take the most advantage of the symmetry of the structure. The radiated sound power has been calculated using the radiation resistance matrix described in Chapter 3. As explained previously, the radiated sound power can be obtained according to Eq. (3.6) which utilizes the velocity vector of the structure. The processing involves calculating the velocity for each discretized element, diagonalizing the radiation resistance matrix, obtaining the radiation mode amplitudes as the inner product of the velocity vector and

radiation mode vectors, and summing over the product of the eigenvalues and the squared radiation mode amplitudes. Figure 4.33 shows the calculated radiated sound power before and after control for configuration I.

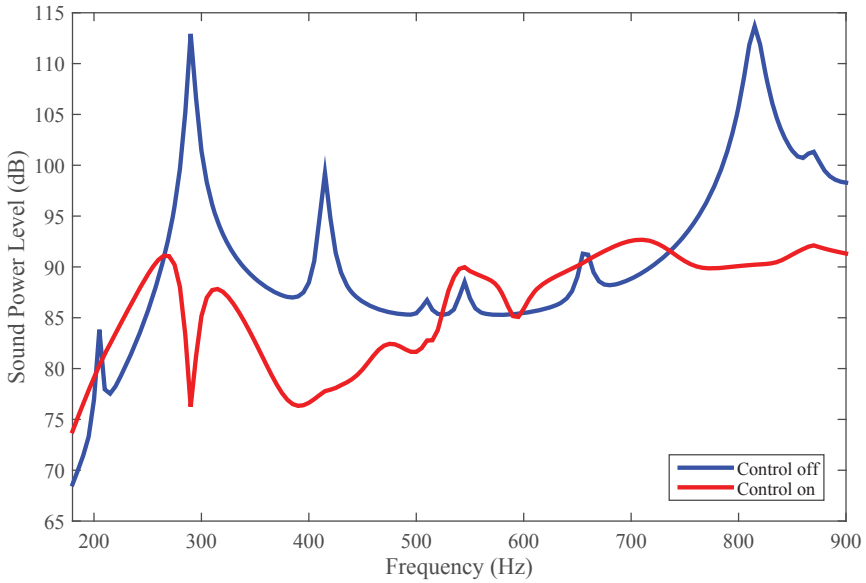

Figure 4.33 Control using the WSSG control metric for configuration I.

As Fig. 4.33 shows, the control metric is effective in attenuating the radiated sound power at nearly all resonance peaks. There are a few frequency regions where the radiated sound power has been enhanced, but overall, the radiated sound power has been attenuated by 11.4 dB over the entire frequency band. Table 4.6 lists the sound power attenuation at each of the resonance peaks. In this table, P_{bc} is the sound power level before control in dB, $P_{ac-WSSG}$ is the sound power level after WSSG control in dB, and ΔP_{WSSG} is the attenuation of the sound power level after applying the WSSG control metric. Tracking WSSG before and after control at the sensor location allows for one way of monitoring and verifying the minimization process, since if the model is accurate at any given frequency, the control system should not make WSSG worse than what it was initially. Figure 4.34 shows the WSSG at the sensor location before and after control.

Table 4.6 Sound power attenuation at each resonance peak

Frequency (Hz)	P_{bc} (dB)	$P_{ac-WSSG}$ (dB)	ΔP_{WSSG} (dB)
203.06	83.83	80.35	3.48
290.23	112.9	76.25	36.65
413.91	99.23	77.78	21.45
505.27	86.73	82.76	3.97
540.71	88.52	89.98	-1.5
653.77	91.30	90.71	0.59
814.28	113.7	90.22	23.5
866.07	101.3	92.12	9.18

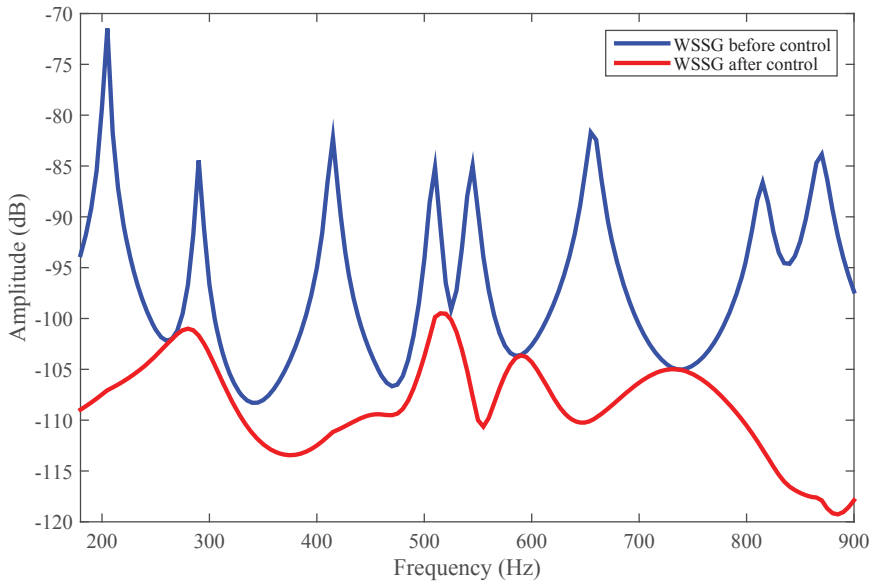

Figure 4.34 WSSG before and after control for configuration I.

As can be seen in Fig. 4.34, WSSG has been attenuated considerably at all the resonance peaks. There are a few anti-resonances where WSSG has not been attenuated, indicating that the best the control system could do was nothing.

Even though WSSG has been minimized at the sensor location, it is interesting to see the impact of this minimization on the WSSG field of the entire structure. Figures 4.35 - 4.42 show the WSSG field of the primary source, the control source and the combined fields together for the first eight resonances. As can be seen, minimization of WSSG at only one sensor location has resulted in attenuation of WSSG for the entire field.

The results shown in Fig. 4.33 have been obtained using Eqs. (2.19) - (2.22). However, in practice, the spatial derivatives are obtained using the finite difference method given in Eq. (2.54). Figure 4.43 shows the control for this configuration using the method described in Eq. (2.54). If the finite differencing is implemented correctly, both methods should lead to approximately the same results.

This implementation results in an overall attenuation of 11.3 dB, which is about 0.1 dB different than the previous method using exact gradients. The overall trend is similar to Fig. 4.33. However, there are slight differences because the four sensor locations associated with the accelerometers are spaced 1 inch from each other resulting in small approximation errors, whereas in the previous method the exact gradients at the sensor location were utilized.

4.5 Performance evaluation

4.5.1 Setting a reference point

Even though Fig. 4.34 demonstrates that WSSG is minimized, it does not provide any information regarding how well the sound field is attenuated. In order to provide a benchmark that can be used to evaluate the effectiveness of the control, one can optimize the attenuation of radiated sound

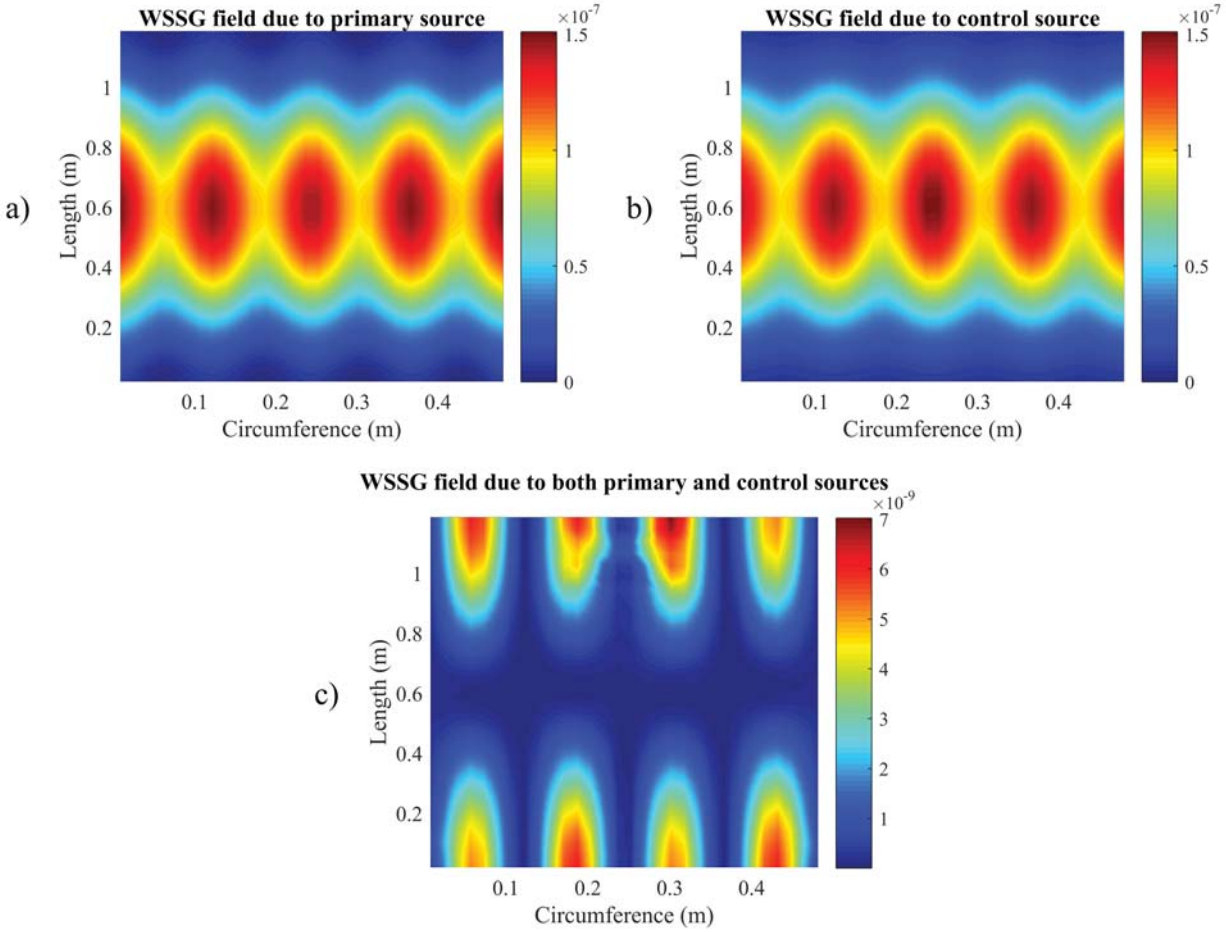

Figure 4.35 WSSG for the shell at a frequency of 203.06 Hz and configuration I for a) the primary force, b) the control force, and c) both the primary and the control forces.

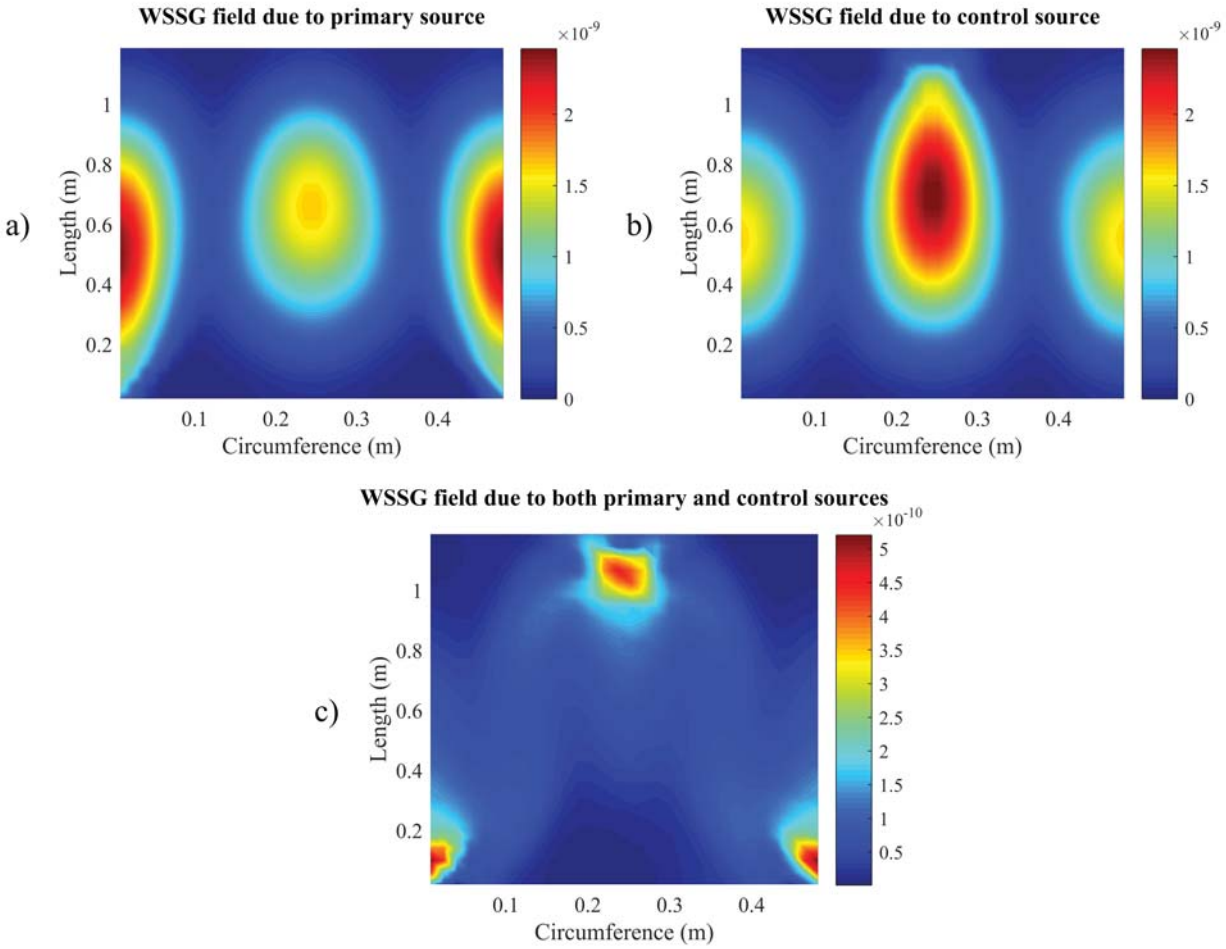

Figure 4.36 WSSG for the shell at a frequency of 290.23 Hz and configuration I for a) the primary force, b) the control force, and c) both the primary and the control forces.

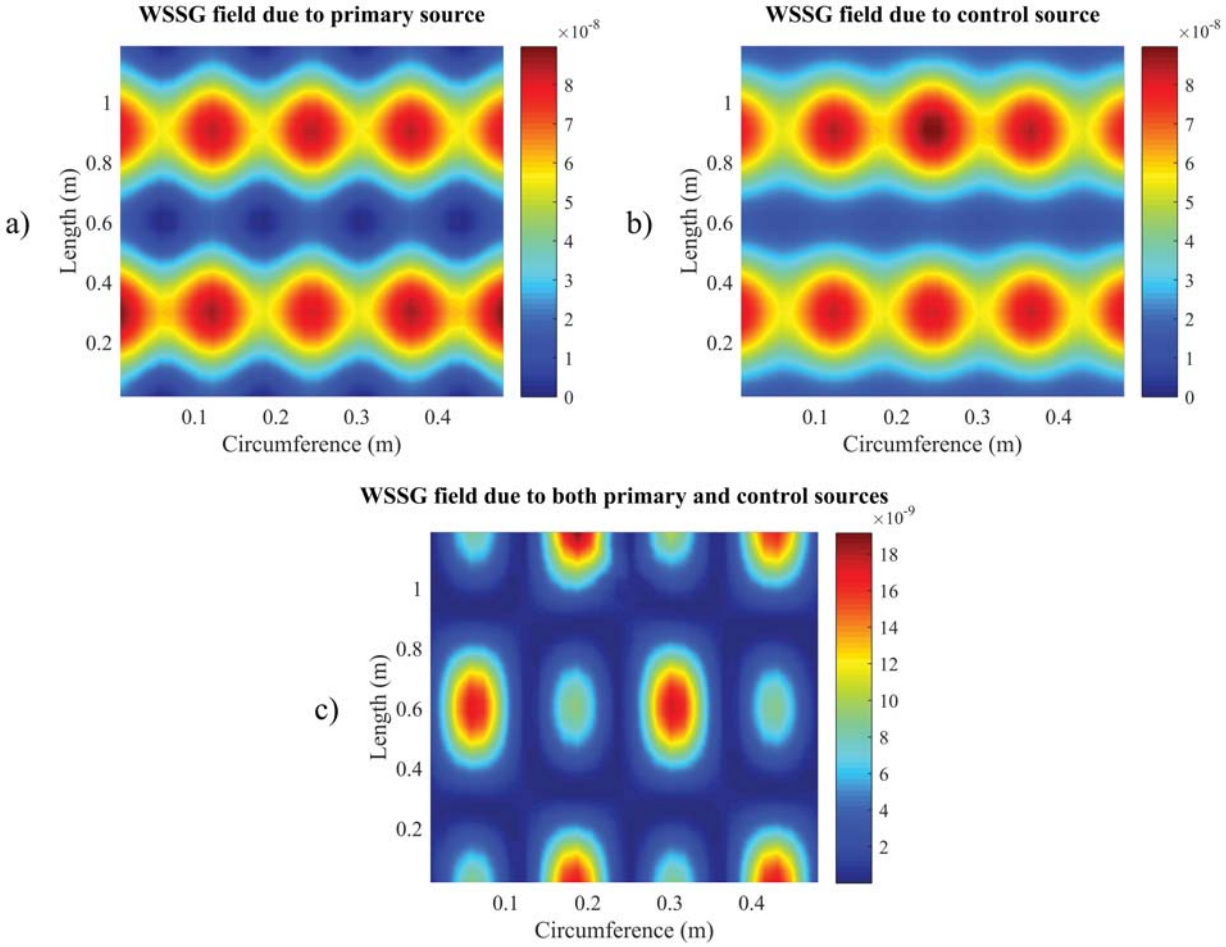

Figure 4.37 WSSG for the shell at a frequency of 413.91 Hz and configuration I for a) the primary force, b) the control force, and c) both the primary and the control forces.

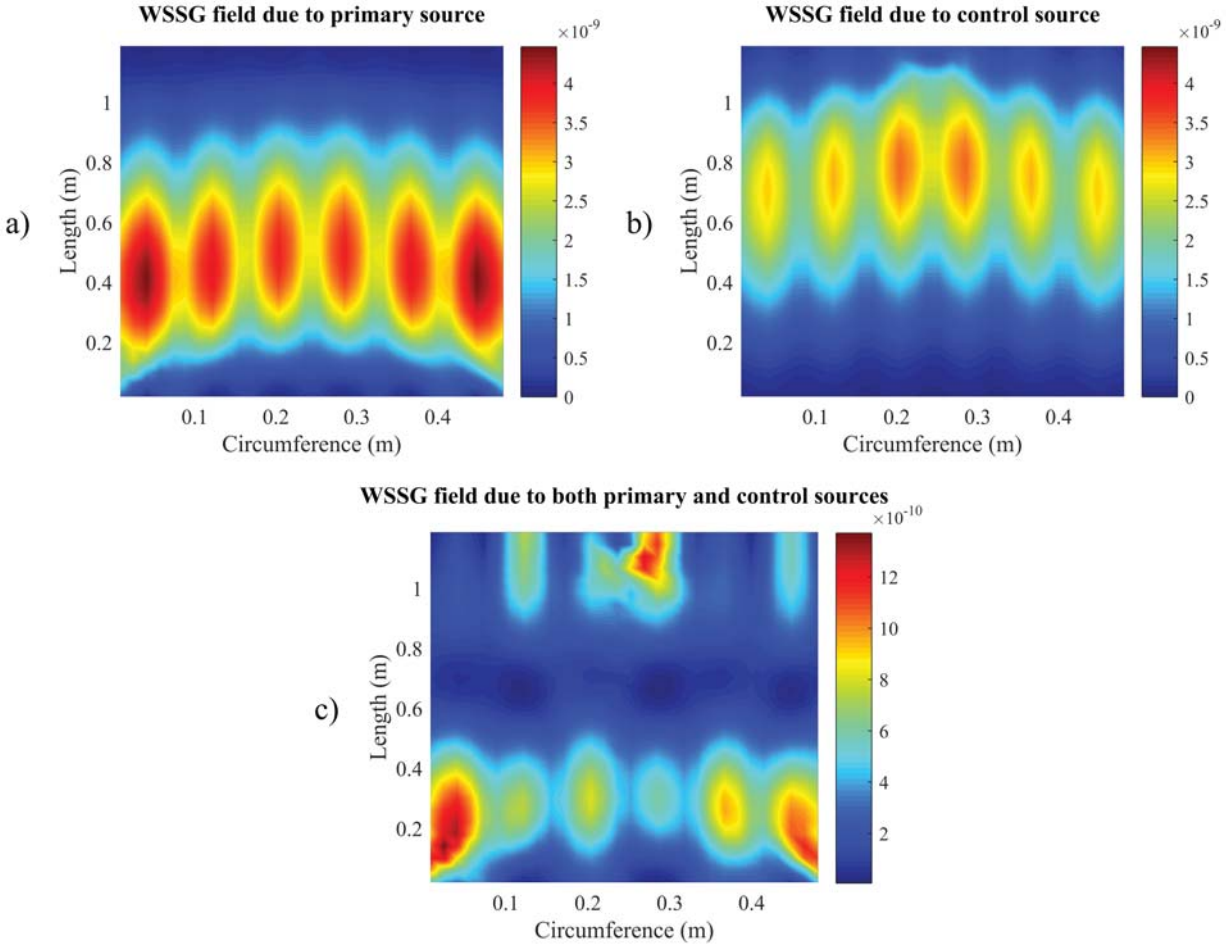

Figure 4.38 WSSG for the shell at a frequency of 505.27 Hz and configuration I for a) the primary force, b) the control force, and c) both the primary and the control forces.

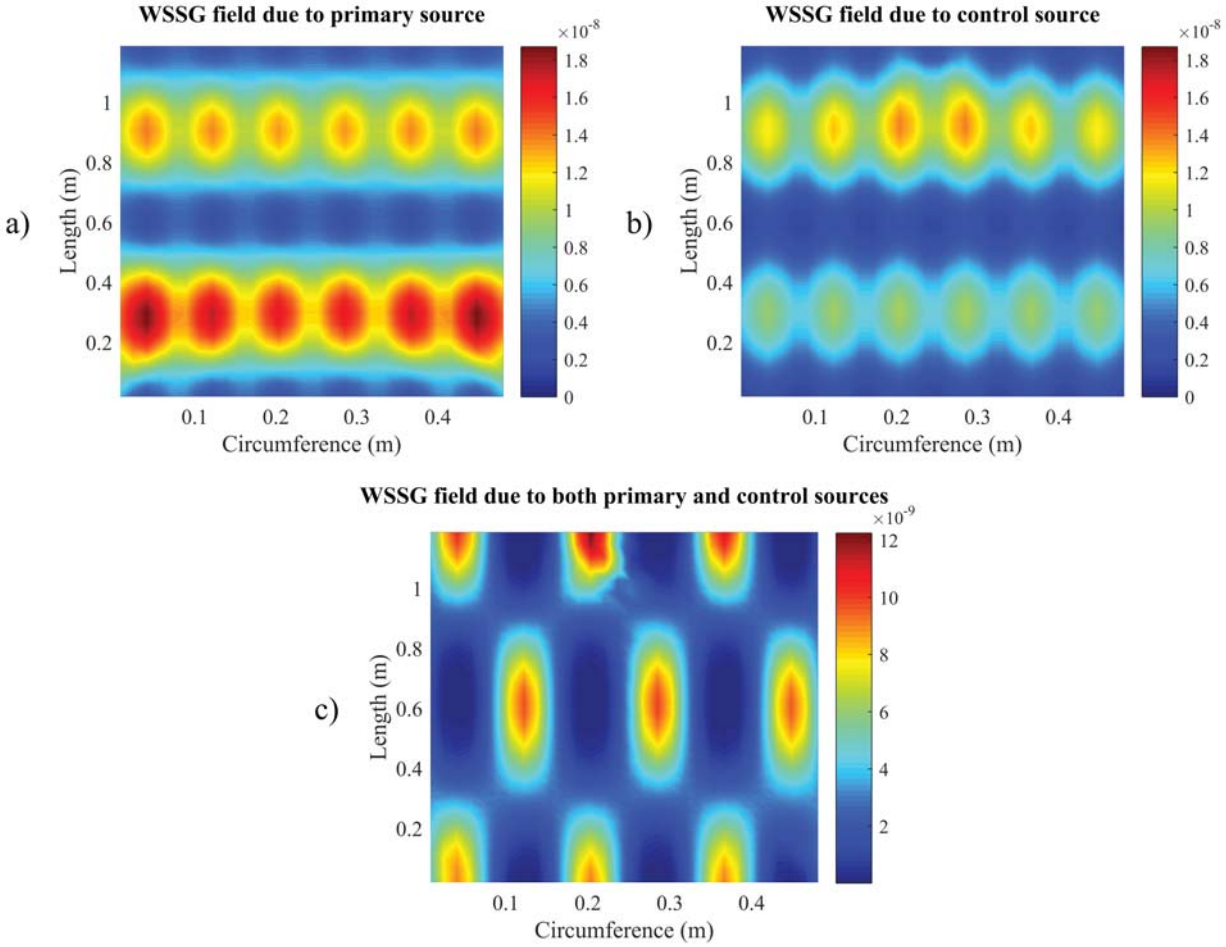

Figure 4.39 WSSG for the shell at a frequency of 540.71 Hz and configuration I for a) the primary force, b) the control force, and c) both the primary and the control forces.

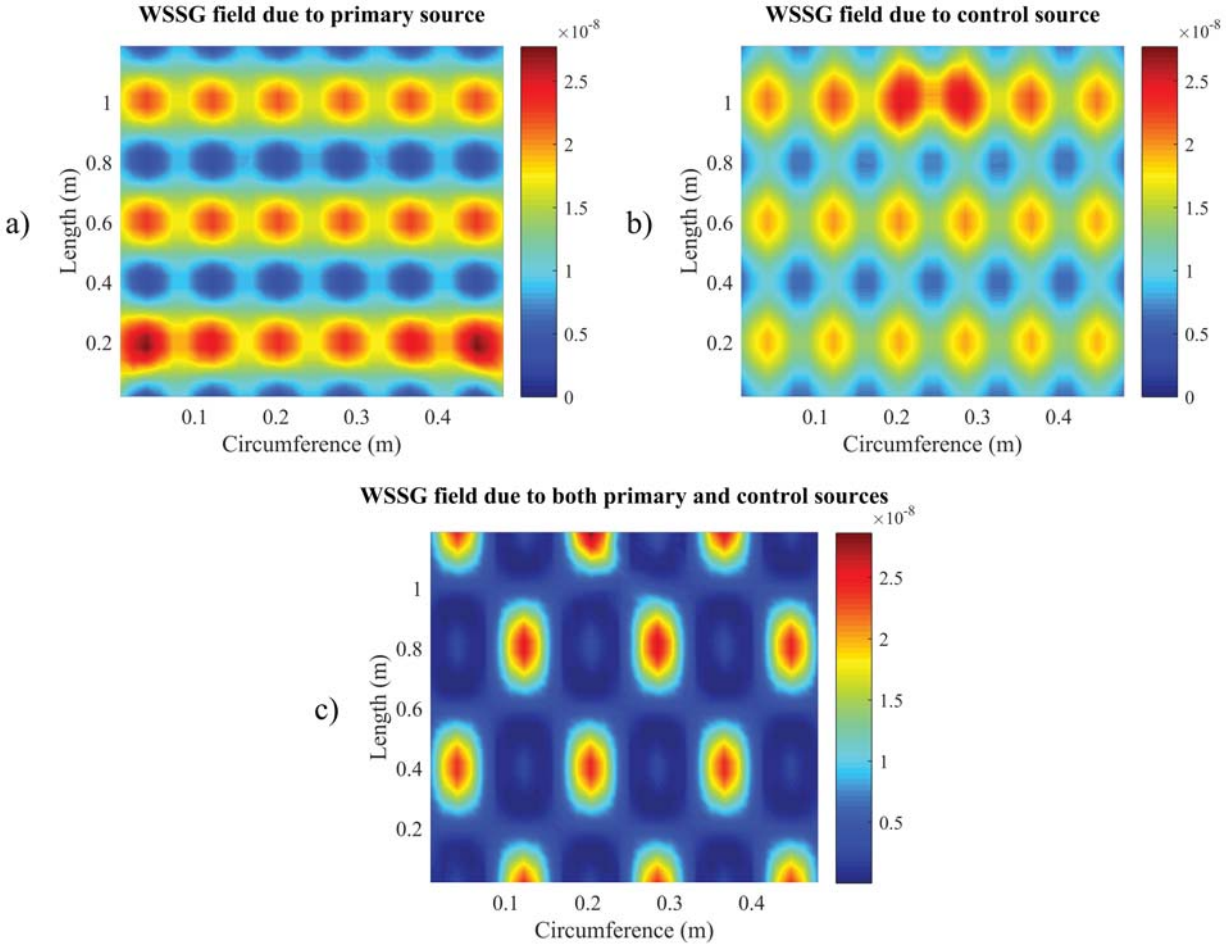

Figure 4.40 WSSG for the shell at a frequency of 653.77 Hz and configuration I for a) the primary force, b) the control force, and c) both the primary and the control forces.

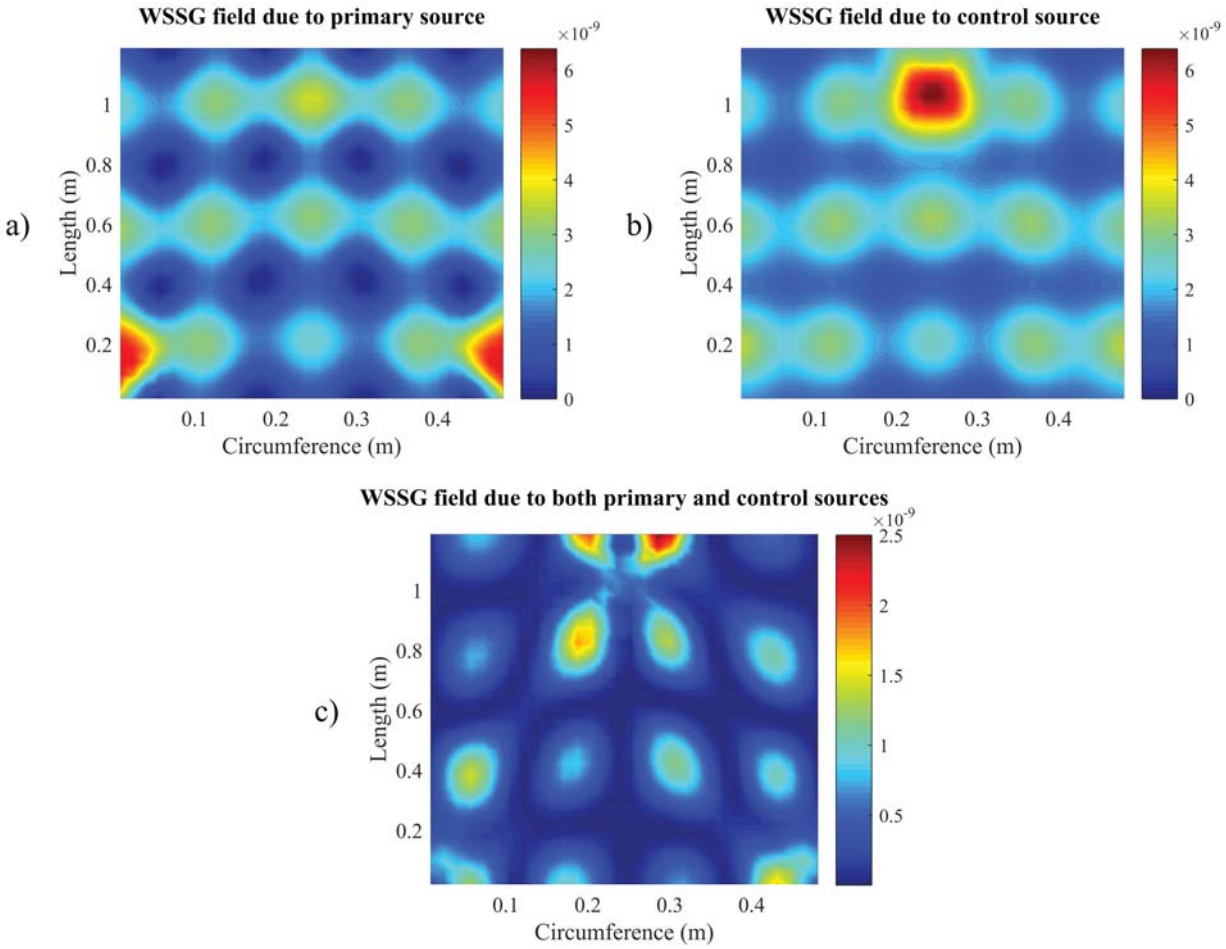

Figure 4.41 WSSG for the shell at a frequency of 814.28 Hz and configuration I for a) the primary force, b) the control force, and c) both the primary and the control forces.

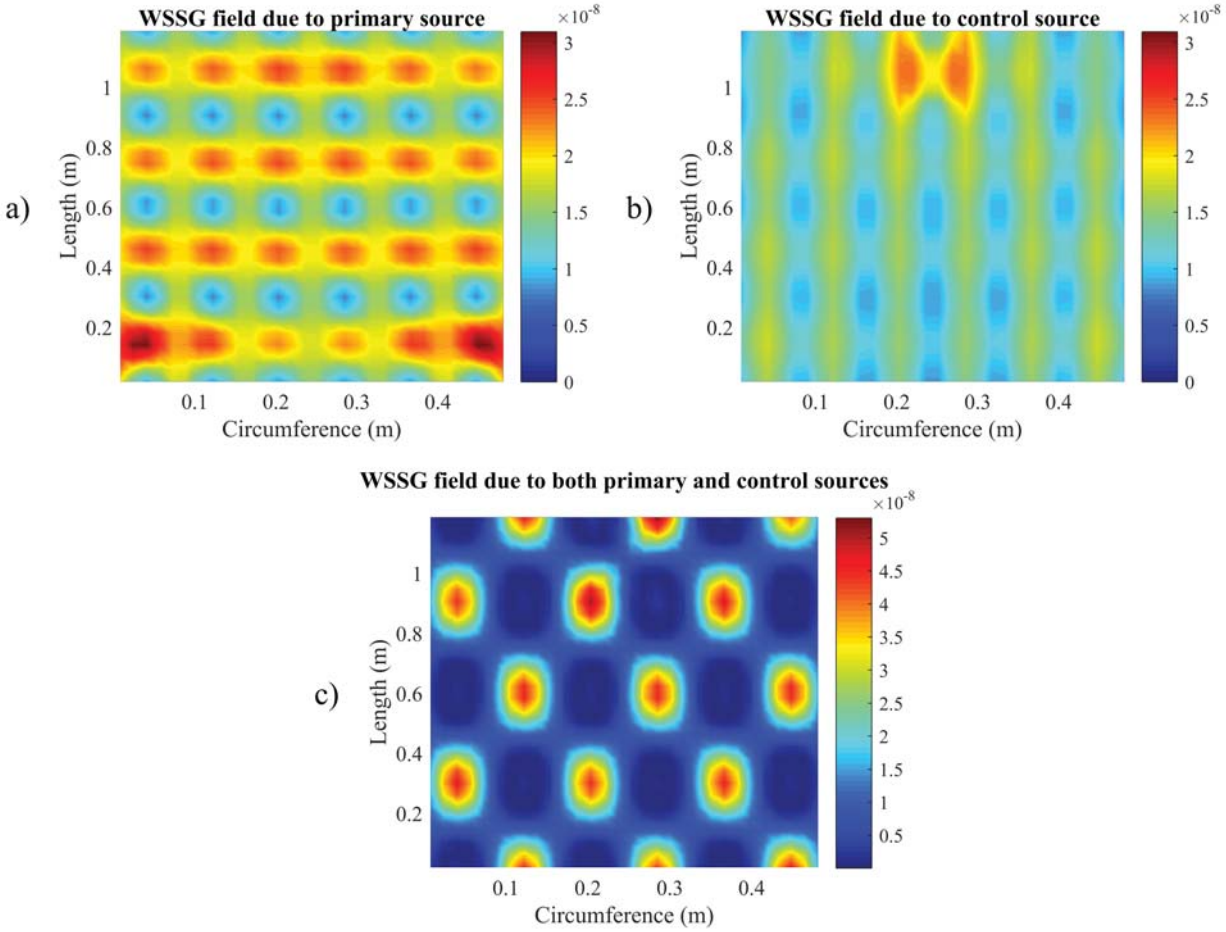

Figure 4.42 WSSG for the shell at a frequency of 866.07 Hz and configuration I for a) the primary force, b) the control force, and c) both the primary and the control forces.

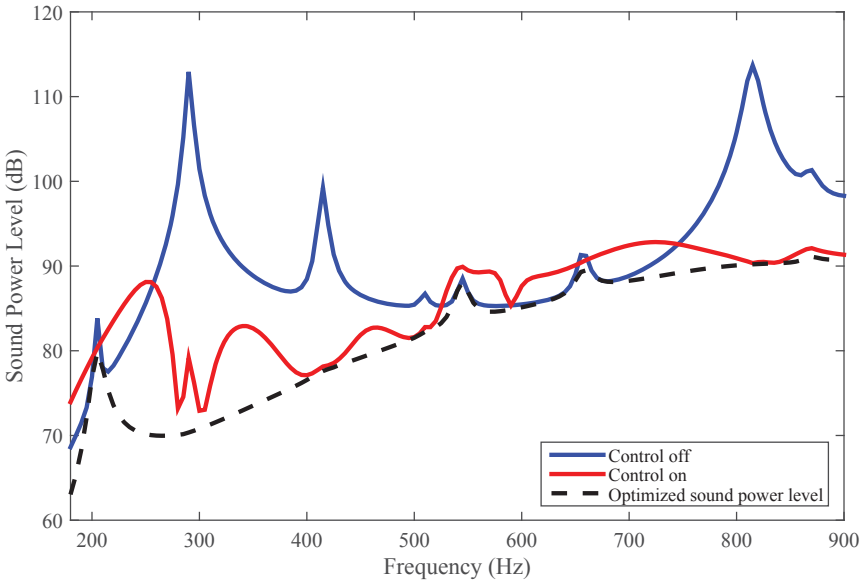

Figure 4.43 Control using the WSSG control metric using the finite difference method.

power with respect to the control force. Although this is not physically practical, it does provide the optimized value of the radiated sound power, which provides the ultimate limit for how much the radiated power can be attenuated.

One can start from the expression for the radiated power in Eq. (3.5), where

$$P = \{\mathbf{u}^H\}[\mathbf{R}]\{\mathbf{u}\} \tag{4.1}$$

In the presence of both the primary and the control source, the velocity field can be decomposed into the velocity field due to the primary force and the field due to the control force. The control field can be expressed as the product of the control force, F_c, and the transfer function, $\mathbf{G}$, between the control force location and each point on the structure, i.e

$$\mathbf{u} = \mathbf{u_p} + F_c\mathbf{G}, \tag{4.2}$$

where $\mathbf{u_p}$ is the primary velocity vector and $\mathbf{G}$ is the transfer function vector between the control

force location and every other element on the structure. Using Eq. (4.2), Eq. (4.1) can be expressed as

$$P = [\mathbf{u_p} + F_c\mathbf{G}]^H \mathbf{R} [\mathbf{u_p} + F_c\mathbf{G}] \tag{4.3}$$

which can be expanded into

$$P = \mathbf{u_p}^H\mathbf{R}\mathbf{u_p} + F_c{}^H\mathbf{G}^H\mathbf{R}\mathbf{u_p} + \mathbf{u_p}^H\mathbf{R}\mathbf{G}F_c + F_c^H\mathbf{G}^H\mathbf{R}\mathbf{G}F_c \tag{4.4}$$

To simplify, we can define

$$C = \mathbf{u_p}^H\mathbf{R}\mathbf{u_p} \tag{4.5}$$

$$B = \mathbf{G}^H\mathbf{R}\mathbf{u_p} \tag{4.6}$$

$$B^H = \mathbf{u_p}^H\mathbf{R}\mathbf{G} \tag{4.7}$$

$$A = \mathbf{u_p}^H\mathbf{R}\mathbf{G}. \tag{4.8}$$

Taking the derivative of Eq. (4.4) with respect to the control force, F_c, the optimal control force will be

$$F_{c-opt} = -A^{-1}B. \tag{4.9}$$

Substituting Eq. (4.9) into Eq. (4.4), the optimized value of the sound power will be

$$P_{min} = C + B^H F_c = C - B^H A^{-1} B. \tag{4.10}$$

This minimized sound power is shown in Fig. 4.44 as the black dashed line. Figure 4.44 compares the control results in Fig. 4.33 with the minimized sound power level from Eq. (4.10). The overall attenuation achieved by minimizing the sound power is 14.0 dB which is comparable to the 11.4

dB achieved by minimizing WSSG. This indicates that minimizing WSSG approximates the ideal solution of minimizing the radiated sound power quite well.

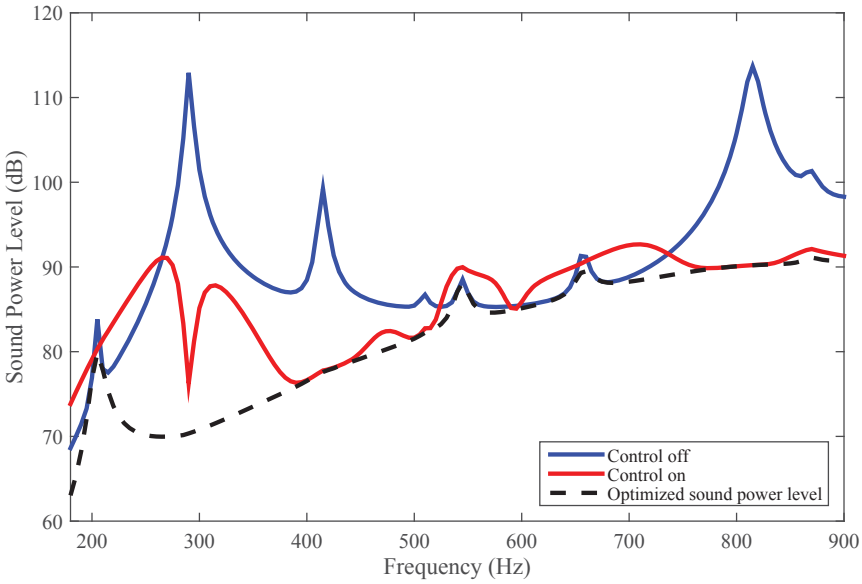

Figure 4.44 Optimized power for configuration I.

The results suggest that even with using a single sensor location, the WSSG control metric is able to perform comparably to minimizing the radiated sound power. The question might arise as to why WSSG would be a better method than minimizing the radiated sound power. The answer lies in Eq. (4.1); one can see that the formulation of Eqs. (4.9) and (4.10) depends on the velocity vector of the structure, meaning that in practice one needs to utilize a large number of sensors distributed over the structure to sense the velocity field globally and hence to minimize the radiated sound power. On the other hand, the WSSG control metric depends only on one or a few sensor locations, at most. WSSG proves to be much easier to implement in practice than minimizing the radiated sound power, and yet it produces comparable results that approximate the ideal solution quite well.

4.5.1.1 Control using modal weights

In order to see the impact of using the averaged weights on the control performance, the WSSG control metric is minimized for each of the resonances using the corresponding weighting coefficients, listed in Table 4.3. The results are then compared to the best possible performance predicted by minimizing the radiated sound power, in order to evaluate the control results. These results are listed in Table 4.7.

Table 4.7 Comparison of WSSG control using modal weights for each resonance and the best possible performance.

Frequency (Hz)	P_{bc} (dB)	$P_{ac-WSSG}$ (dB)	ΔP_{WSSG} (dB)	ΔP_{opt} (dB)
203.06	83.82	80.35	3.47	3.99
290.23	112.9	75.20	37.7	42.5
413.91	99.23	77.69	21.5	21.6
505.27	86.73	82.30	4.43	4.49
540.71	88.52	89.80	-1.28	0.38
653.77	91.30	90.41	0.89	2.00
814.28	113.7	90.21	23.5	23.5
866.07	101.3	92.11	9.21	10.2

In this table, ΔP_{opt} is the attenuation of sound power level due to minimizing the radiated sound power. Comparing the column of ΔP_{WSSG} with the column of ΔP_{opt}, one can see that the WSSG control results are very close to the optimal results. This is significant since it demonstrates that WSSG with one local measurement is able to approximate the optimal results that are obtained using global measurements.

Additionally, comparing the 4th column in Tables 4.7 and 4.6 shows that the performance of the WSSG control metric using the averaged results are very close to the results using the modal

weights. This supports the conclusion that, if it is needed to apply the control to several resonance peaks, using the averaged weights will provide control results almost as good as using the modal weights, which are also very close to the optimal results.

4.5.2 Dependence on error sensor location

In order to show that the WSSG control metric is robust with respect to the sensor location, the control metric is applied to a few more configurations where the location of the primary and control sources are kept the same, but the sensor location is modified.

Figure 4.45 shows the location of the forces and the error sensor for configuration II, which are also listed in Table 4.8. Figure 4.46 presents the control results for configuration II.

Table 4.8 Location of sensor and actuators for configuration II.

	Primary Shaker	Control Shaker	Sensor
z (m)	0.1016	1.0478	0.55
θ (degrees)	30	210	125

Changing the error sensor location to configuration II, the overall attenuation turns out to be 11.2 dB, as compared with 11.4 dB for configuration I.

Figure 4.47 shows one additional case, configuration III, where the coordinates of the actuators and sensor are listed in Table 4.9. The corresponding control results are shown in Fig. 4.48. For this configuration, using the WSSG control metric results in an overall attenuation of 10.6 dB.

One can see that by using different sensor locations, there are only differences of less than 1 dB in the overall amount of attenuation obtained, which demonstrates that the WSSG control metric is robust with respect to error sensor location. As mentioned before, this is a result of the uniformity of the WSSG control metric. The more uniform the objective function (WSSG) is, the less dependence the control method will have on sensor location.

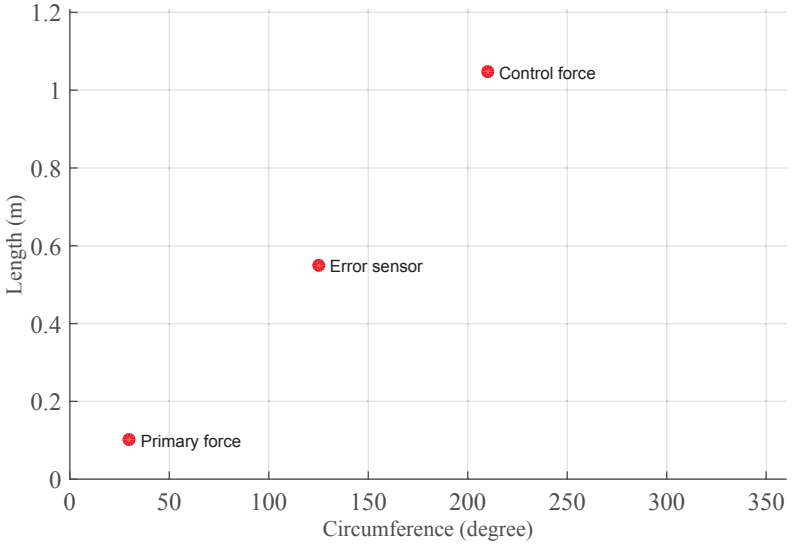

Figure 4.45 Control configuration II.

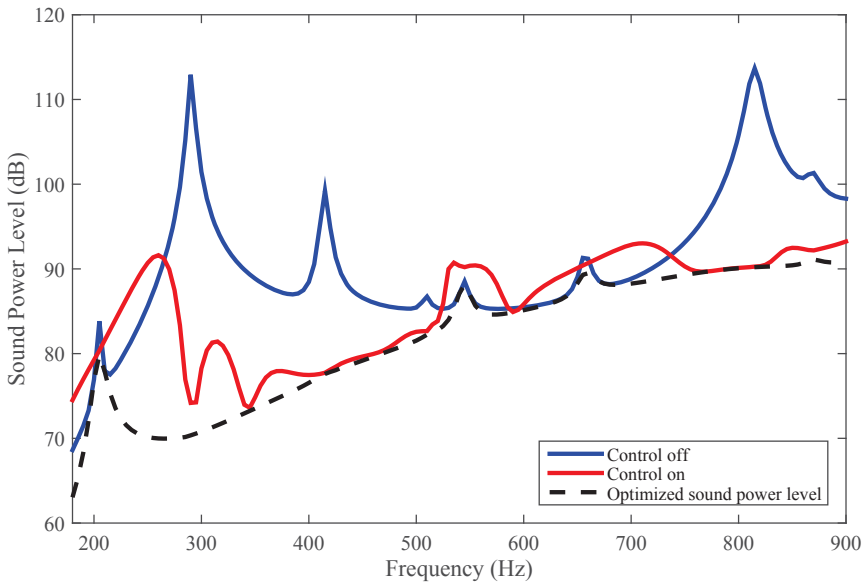

Figure 4.46 Control using WSSG control metric for configuration II.

Table 4.9 Location of sensor and actuators for configuration III.

	Primary Shaker	Control Shaker	Sensor
z (m)	0.1016	1.0478	0.4
θ (degrees)	30	210	280

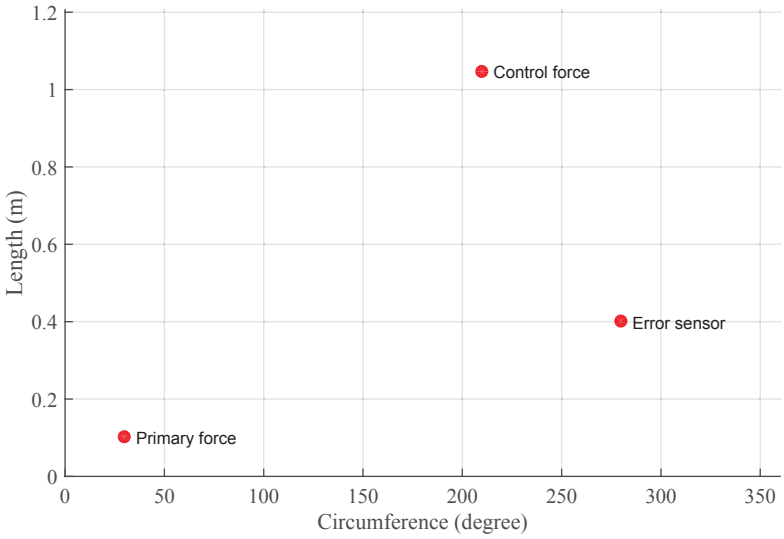

Figure 4.47 Control configuration III.

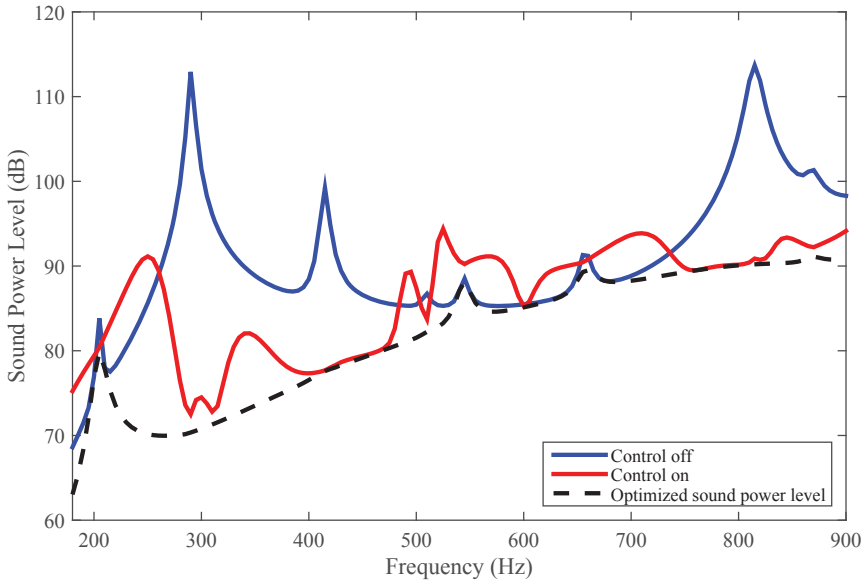

Figure 4.48 Control using WSSG control metric for configuration III.

4.5.3 Dependence on control force location

The control results depend on the location of the control force. In a configuration where the control force location, in terms of geometry, is not a favorable one, then even using the approach of sound power optimization will not yield much improvement. Although source location can be optimized, that is not a focus of this work. Thus, choices for the control force location have been somewhat arbitrary. The focus of this work has been investigating the WSSG control metric. If the WSSG method performs as desired, it should closely match whatever the solution is for minimized sound power, for that given source configuration. A different source configuration is shown in Fig. 4.49 as configuration IV, where its coordinates are listed in Table 4.10. The corresponding control results using WSSG and sound power minimization are shown in Fig. 4.50.

In this configuration, it can be seen that the best performance that can be achieved by minimizing sound power does not show much attenuation, resulting in a total of only 1.1 dB overall attenuation. As can be seen, WSSG performs quite closely to the minimized radiated power,

Table 4.10 Location of sensor and actuators for configuration IV.

	Primary Shaker	Control Shaker	Sensor
z (m)	0.1016	0.6	0.68
θ (degrees)	30	150	305

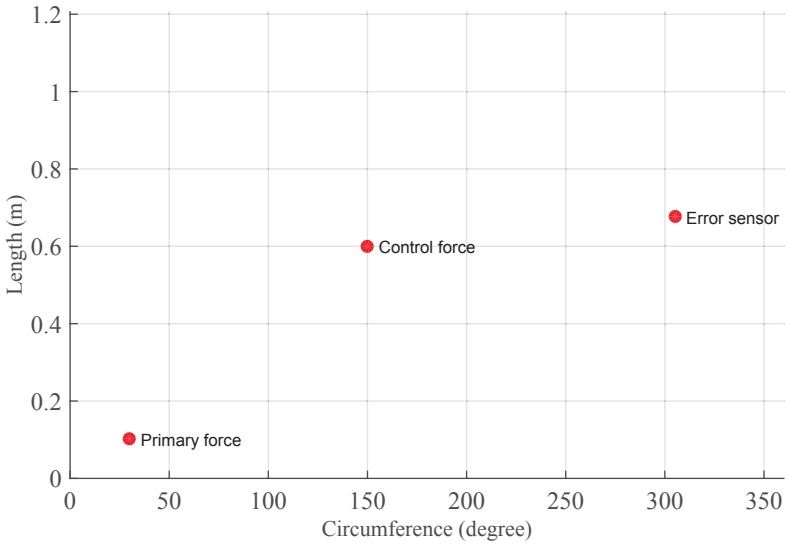

Figure 4.49 Control configuration IV.

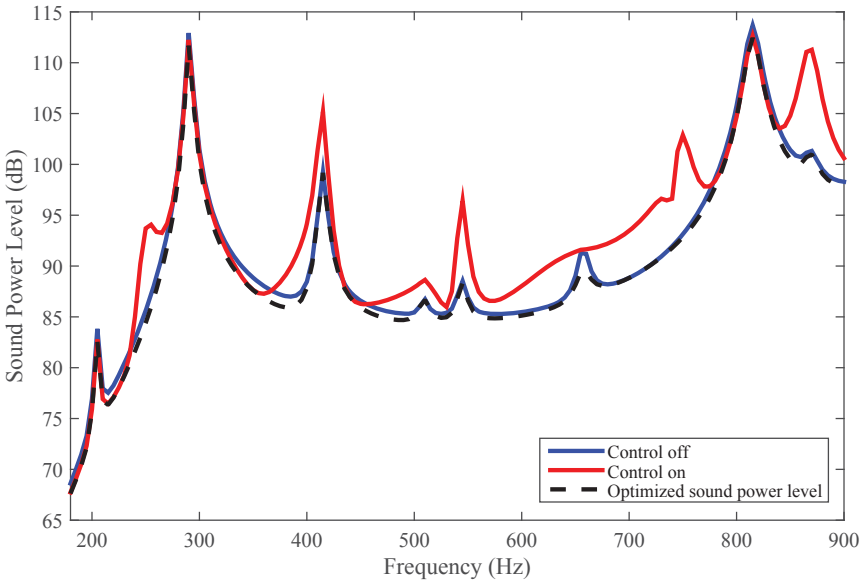

Figure 4.50 Control using WSSG control metric for configuration IV.

with the overall radiated sound power being enhanced by 1.1 dB. There are some frequencies where WSSG control is not doing as well as the minimized sound power control, but overall, it demonstrates performance that is comparable with minimizing sound power.

4.5.4 Summary

In summary, it can be seen that the WSSG control method is very robust with respect to the error sensor location and can approximate the optimal solution of minimizing sound power using only one or a few local measurements. The sound power attenuation that can be achieved is a function of the control force location. This will impact the control results. However, for a poor control force location, the best possible performance will be degraded as well, and the WSSG method is able to perform closely to this.

4.6 Improvements

The uniformity of the WSSG control metric depends on the set of weights that is applied to normalize the spatial gradients. Thus, one can investigate the impact of the normalizing weights on the performance of the control metric. In order to see if the weights chosen are a good choice of weights, one can map the overall attenuation that can be achieved for different values of the weights. Fixing the associated weight with the first term, α, to be equal to 1, one can map out the overall sound power attenuation for different values of the remaining weights, i.e β, δ and γ. Figures 4.51 - 4.53 show the sound power level reduction mapped over the different values of weights, where the colorbar represents the overall sound power level attenuation for each set of weights. As can be seen there are wide regions for different choices of weights that result in high attenuation of the sound power level, which shows that the WSSG method is robust with respect to different choices of weights.

Tables 4.11 - 4.13 present the maximum attenuation of sound power level achieved for Figs.4.51 - 4.53. From these data, the maximum sound power reduction obtained is 12.2 dB which is only 0.8 dB different than the 11.4 dB sound power reduction obtained using the conventional weights (the inverse of the structural wavenumber squared).

The highlighted values show the set of weights that result in maximum sound power level reduction for each setting. As one can see, there is a maximum of 1 dB difference in between the optimal and conventional choice of weights. This means that the WSSG method is robust over a wide range of weights. It also suggests that it may not be necessary to go to great efforts in finding the optimal weights, since there is little difference for many non-optimal sets of weights. Figures 4.54 - 4.56 show the control results for the highlighted weights in Tables 4.11 - 4.13.

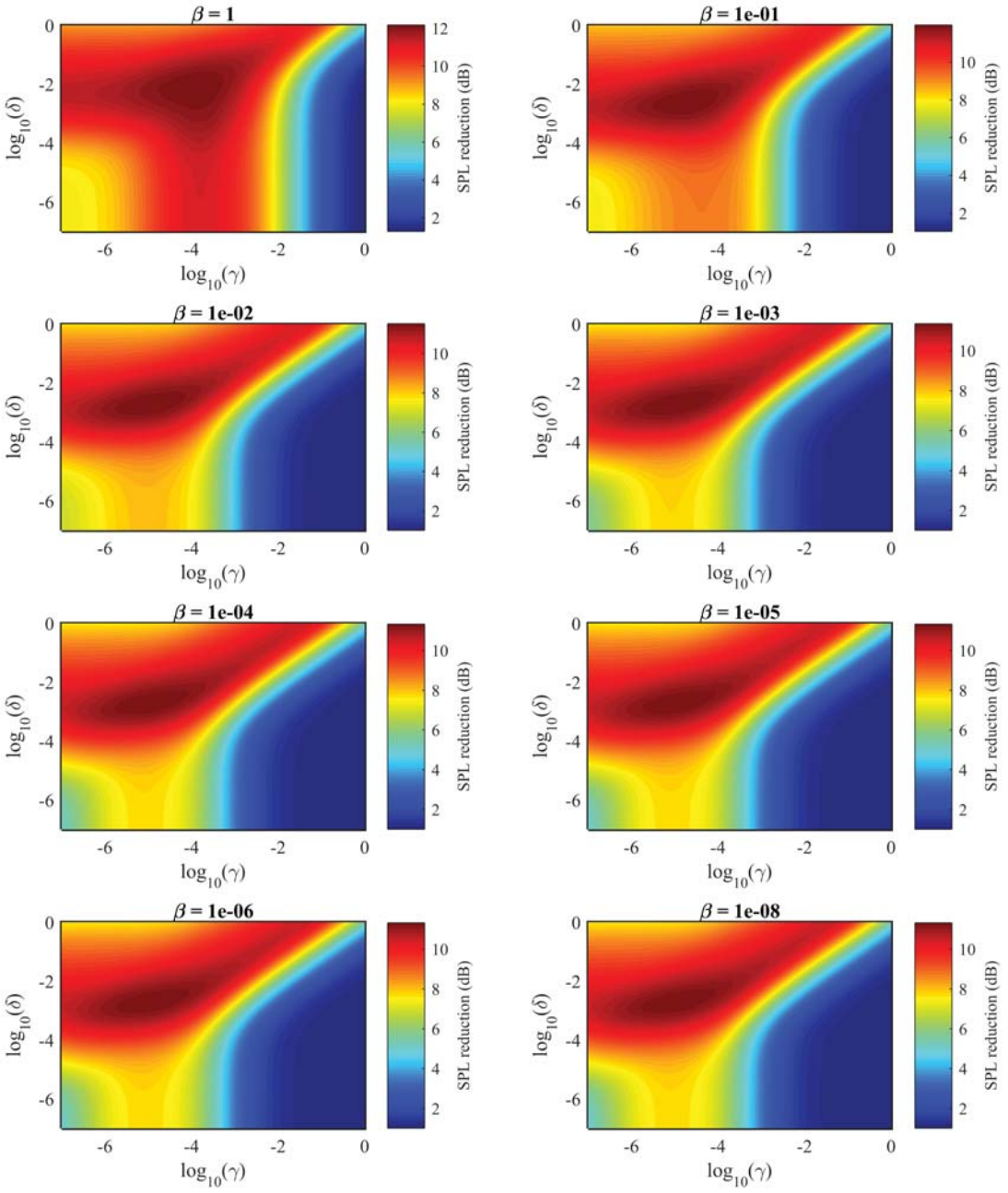

Figure 4.51 Overall sound power level reduction in (dB) as a function of δ and γ for fixed values of β.

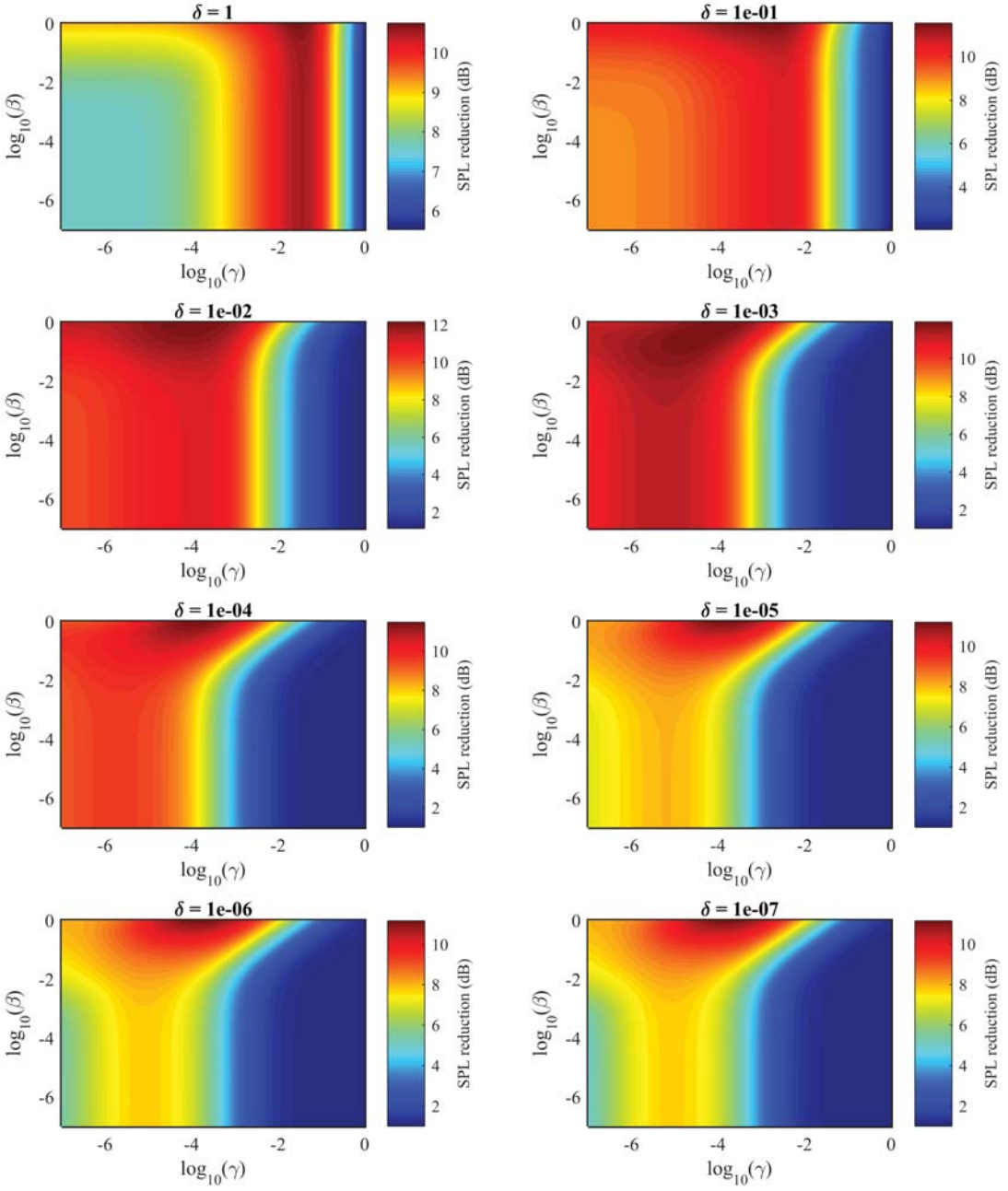

Figure 4.52 Overall sound power level reduction in (dB) as a function of β and γ for fixed values of δ.

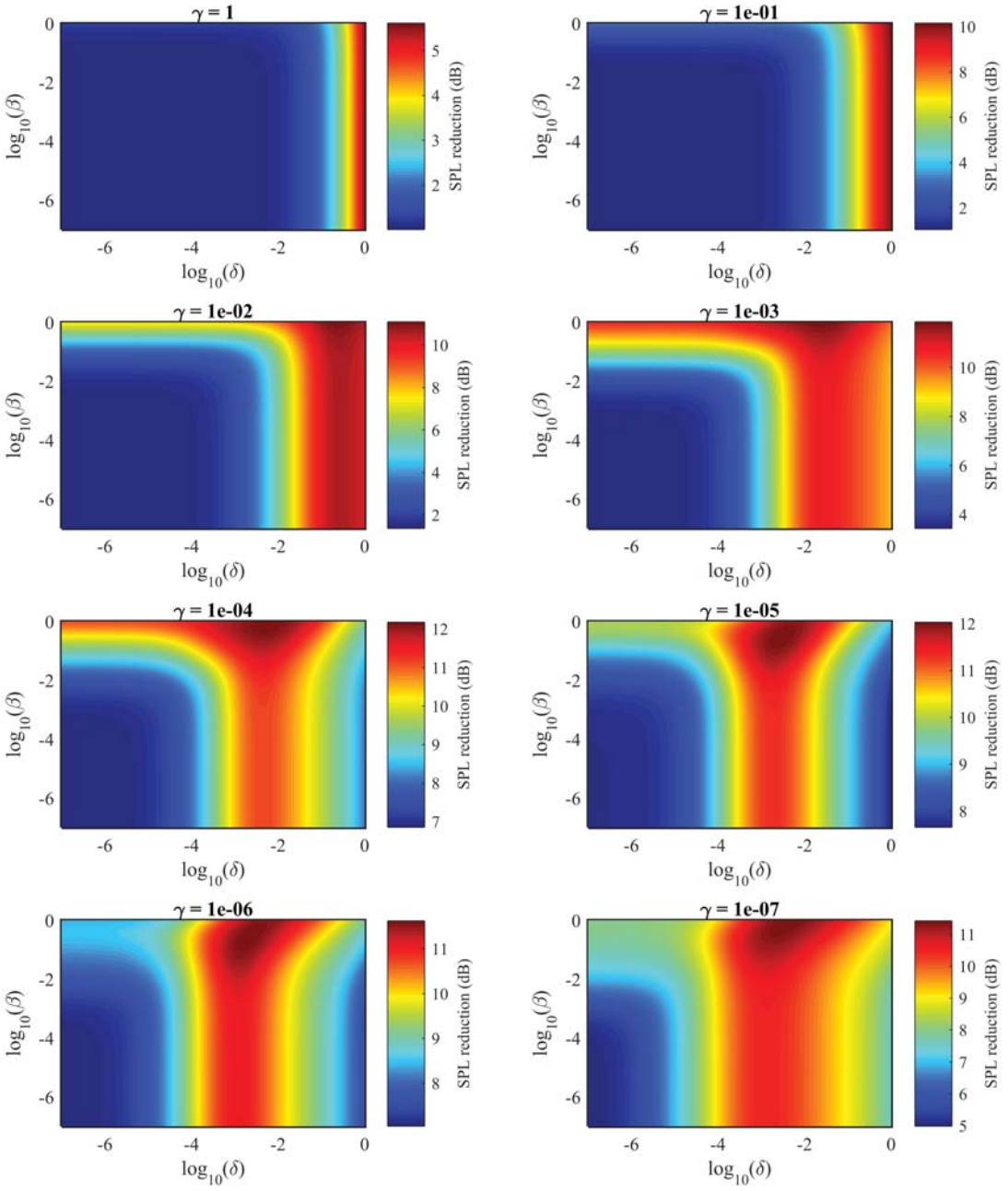

Figure 4.53 Overall sound power level reduction in (dB) as a function of β and δ for fixed values of γ.

Table 4.11 Maximum sound power attenuation and the corresponding values for δ and γ for fixed values of β

β	δ	γ	sound power attenuation (dB)
1.0	*1.39e-04*	*1.39e-04*	*12.2*
1e-01	1.93e-05	1.93e-05	12.0
1e-02	1.39e-05	1.39e-05	11.5
1e-03	1.39e-05	1.39e-05	11.4
1e-04	1.39e-05	1.39e-05	11.3
1e-05	1.39e-05	1.39e-05	11.3
1e-06	1.39e-05	1.39e-05	11.3
1e-07	1.39e-05	1.39e-05	11.3

Table 4.12 Maximum sound power attenuation and the corresponding values for β and γ for fixed values of δ

δ	β	γ	sound power attenuation (dB)
1.0	1	2.68e-02	10.8
1e-01	1	1.39e-03	11.5
1e-02	*1*	*1.39e-04*	*12.2*
1e-03	1	1.39e-04	12.0
1e-04	1	1.39e-04	11.5
1e-05	1	1.39e-04	11.2
1e-06	1	1.39e-04	11.2
1e-07	1	1.39e-04	11.1

Table 4.13 Maximum sound power attenuation and the corresponding values for β and δ for fixed values of γ

γ	β	δ	sound power attenuation (dB)
1.0	1	1	5.60
1e-01	1	1	10.2
1e-02	1	2.68e-01	11.1
1e-03	1	2.68e-02	11.9
1e-04	*1*	*7.19e-03*	*12.2*
1e-05	2.68e-01	2.68e-03	12.0
1e-06	2.68e-01	1.93e-03	11.6
1e-07	1	5.18e-03	11.4

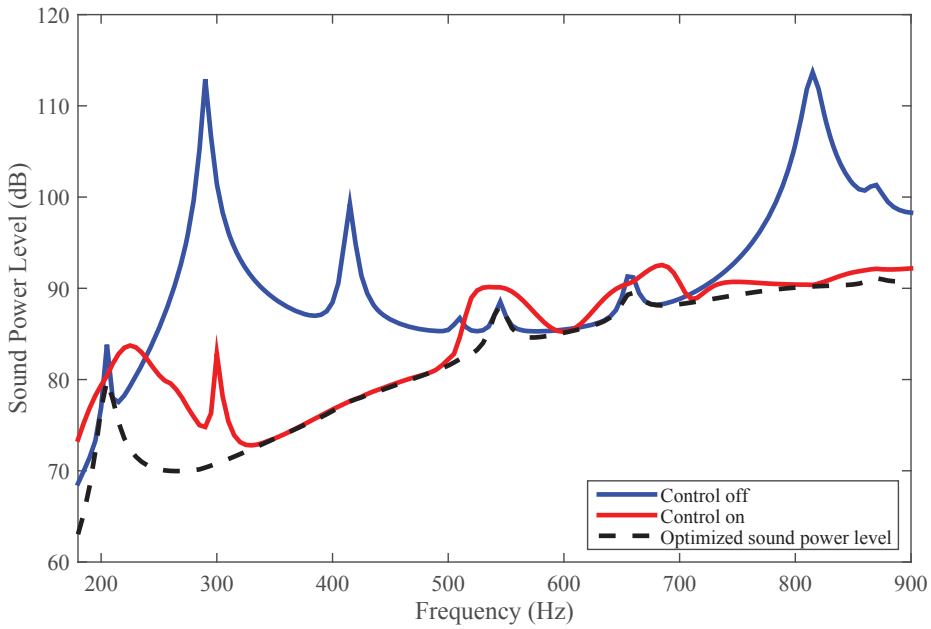

Figure 4.54 WSSG control for configuration I, using the optimized weights in Table 4.11.

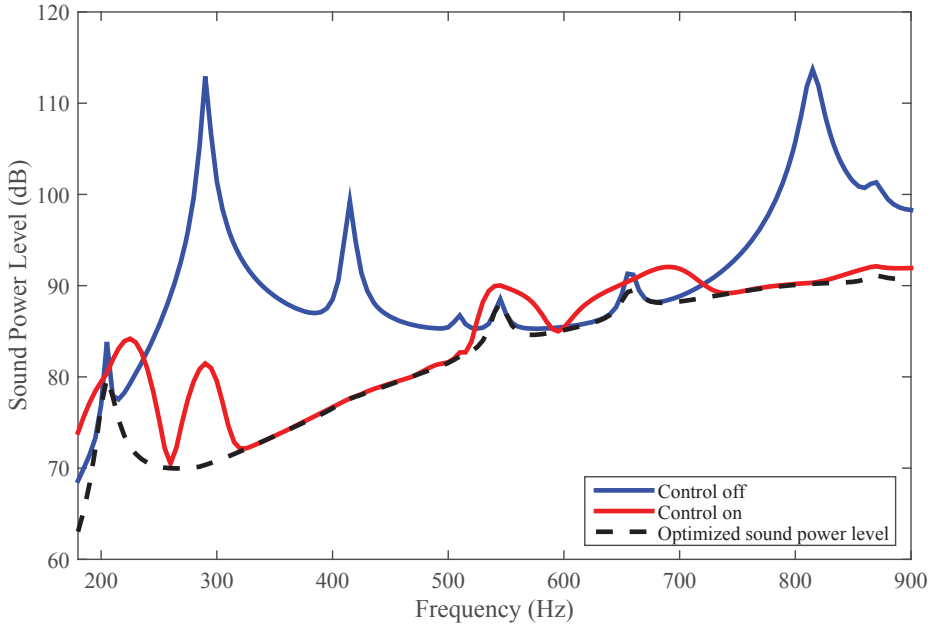

Figure 4.55 WSSG control for configuration I, using the optimized weights in Table 4.12.

4.7 Acoustic radiation before and after control

In order to better understand the mechanism that results in sound power reduction, it is useful to compare the coupling between the vibration before and after control with the most efficient radiation modes at several resonances where WSSG is able to attenuate the radiated sound considerably. Figure 4.57 shows the ten most efficient radiation modes at a frequency of 290.23 Hz associated with the (1,1) structural mode. The corresponding eigenvalues are shown in Fig. 4.58.

The radiation amplitudes, i.e $y_i = \mathbf{Q}(:,i) \cdot \mathbf{u}$ for $i = 1,2,....10$, are calculated for the velocity fields before control (y_{bc}), after WSSG control (y_{ac}), and after minimizing the radiated sound power (y_{ac-opt}) in Table 4.14. As can be seen from the values listed in the table, the uncontrolled amplitude associated with radiation mode 4, (1.21) is the highest, followed by the radiation mode amplitude associated with radiation mode 3 (0.127), which has the next highest value. This can be

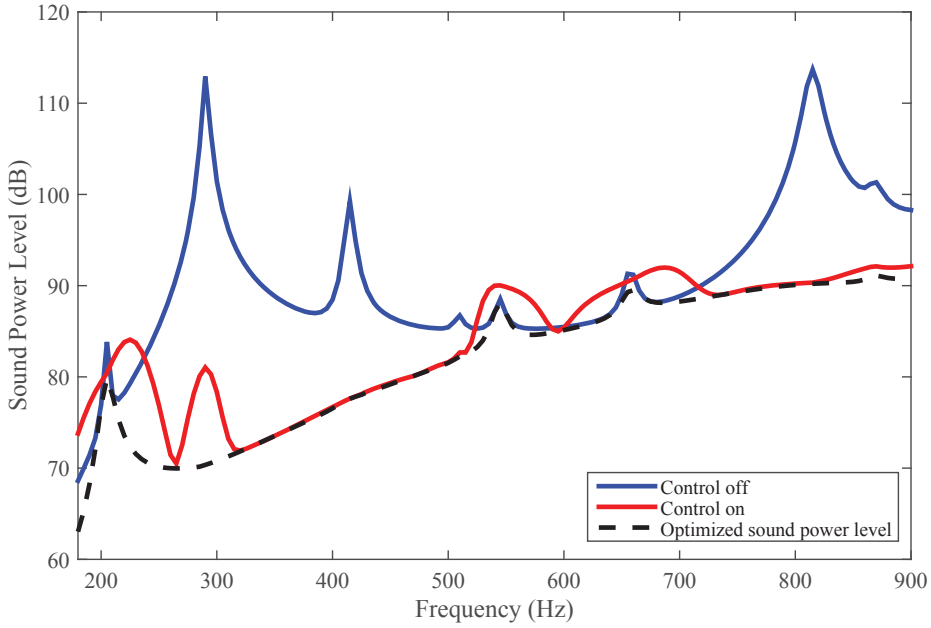

Figure 4.56 WSSG control for configuration I, using the optimized weights in Table 4.13.

understood by considering that the resonance at 290.23 Hz corresponds to the (1,1) mode, which most closely aligns with the velocity distribution of radiation modes 3 and 4, as can be seen in Fig. 4.57. Although the eigenvalues of radiation modes 3 and 4 are not the highest, the radiation mode amplitudes are sufficiently large to result in these modes dominating the resulting radiated sound power. The strong coupling arises from the fact that the high amplitude velocity field of the actual structure at its structural resonance closely matches the velocity distribution of those particular radiation modes. The radiation amplitude of mode 3 is lower due to the 90 degree shift of the velocity distribution in radiation mode 3. On the other hand, even though radiation modes 1 and 2 have the highest eigenvalues, i.e., they are more efficient than other modes at this frequency, since the velocity field of the vibration does not couple with them as strongly, they do not contribute greatly to the radiated sound power. Looking at the radiation amplitudes for higher order modes (for example, modes 7, 8, 9 and 10), we can see that the amplitudes are slightly higher than the

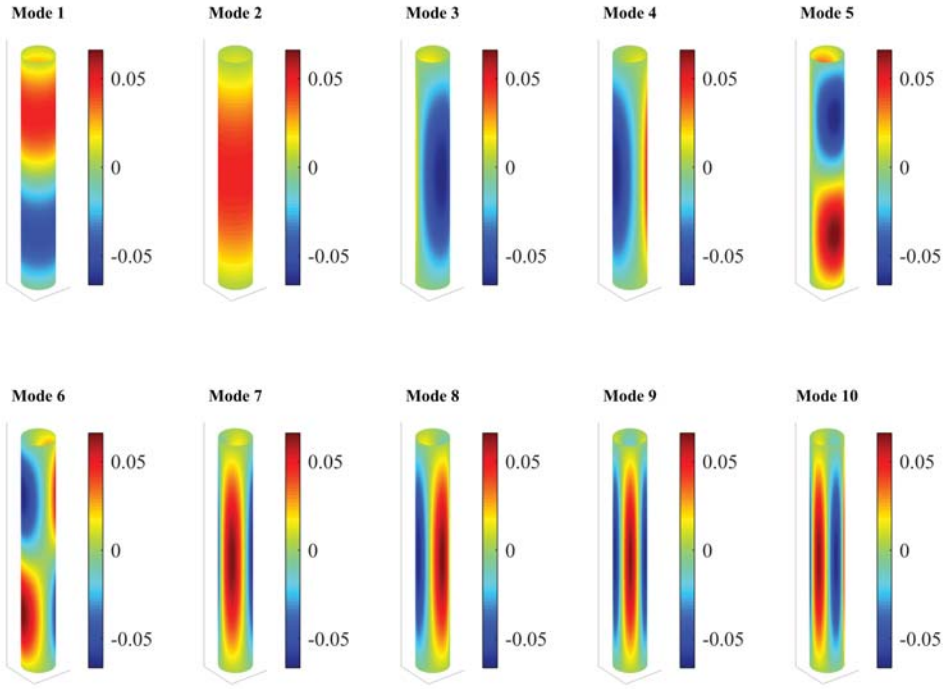

Figure 4.57 Ten most efficient radiation modes at 290.23 Hz.

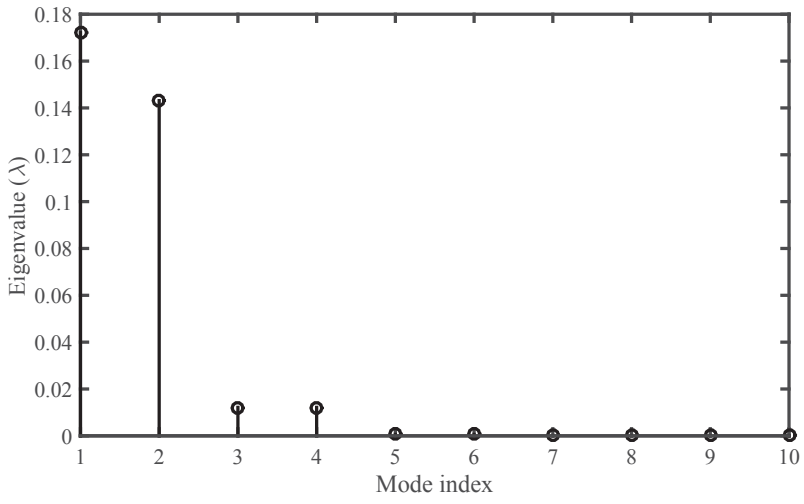

Figure 4.58 Eigenvalues of the ten most efficient radiation modes at 290.23 Hz.

amplitudes for the first two modes. The reason for this is that the velocity field of the structure is projected more effectively onto radiation modes that have the general trend of a $(1,n>0)$ mode shape. Now looking at the values listed for y_{ac} (after WSSG control) for radiation amplitudes associated with radiation modes 3 and 4, the values drop to 3.932×10^{-05} and 3.741×10^{-04}, respectively, which leads to approximately 35 dB of sound power reduction. Comparing these values to the minimized power amplitudes (y_{ac-opt}), for modes 3 and 4, we can see that the values for WSSG control are close to the optimal values listed under (y_{ac-opt}) for radiation modes 3 and 4. This suggests that there is a reasonable correlation between WSSG and the radiated sound power, since optimizing WSSG has led to similar results as for minimizing the radiated power.

Table 4.14 The coupling between the vibration before and after control with the ten most efficient radiation modes at 290.23 Hz.

	y_{bc}	y_{ac}	y_{ac-opt}
Mode 1	-1.1676e-03	-6.0502e-05	-5.9740e-05
Mode 2	2.5131e-03	5.0245e-03	5.0262e-03
Mode 3	1.2722e-01	3.9318e-05	1.9270e-07
Mode 4	1.2104e+00	3.7409e-04	1.8334e-06
Mode 5	-2.2861e-03	-4.4537e-03	-4.4552e-03
Mode 6	-1.1503e-02	-2.2410e-02	-2.2417e-02
Mode 7	1.7763e-02	3.5513e-02	3.5525e-02
Mode 8	-1.3518e-02	-2.7027e-02	-2.7036e-02
Mode 9	3.1516e-02	2.1701e-05	4.7739e-08
Mode 10	-1.0240e-02	-7.0510e-06	-1.5502e-08

We can investigate another case. Consider the same analysis for a frequency of 413.91 Hz. Figures 4.59 and 4.60 represent the radiation modes and the corresponding eigenvalues,

respectively, at 413.91 Hz.

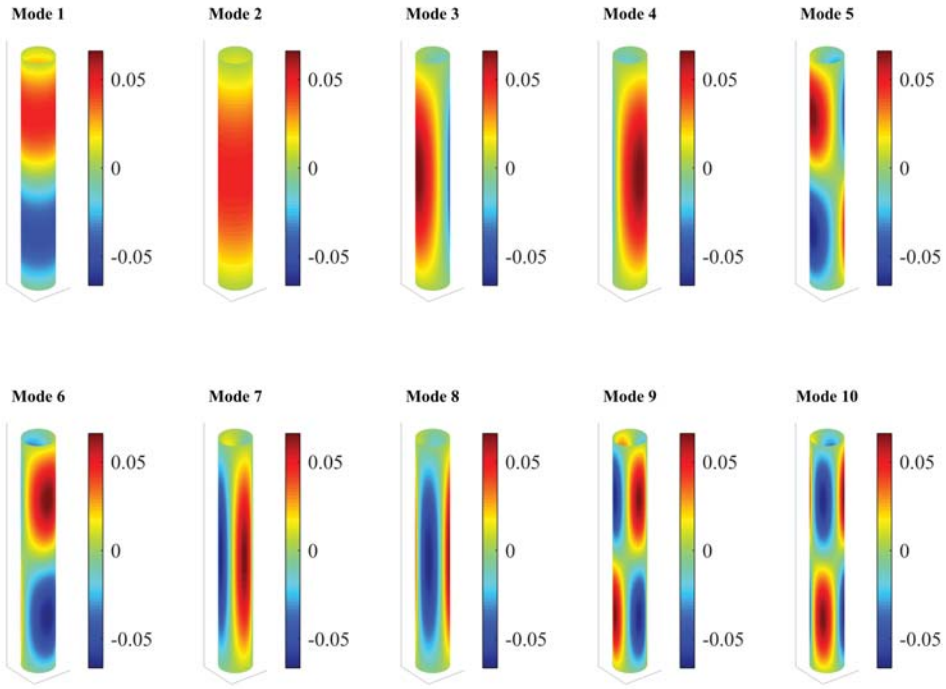

Figure 4.59 Ten most efficient radiation modes at 413.91 Hz.

Table 4.15 lists the values for the radiation modes before control (y_{bc}), after WSSG control (y_{ac}) and for minimizing radiated power (y_{ac-opt}). Taking a look at the values, it is apparent that the values for modes 9 and 10 are the largest in magnitude, which are -11.13 and -2.36 respectively. As shown in Fig. 4.59, radiation modes 9 and 10 correspond closely to a velocity distribution for mode (2,2), and the structural mode at the frequency of 413.91 Hz is the (2,2) mode, which enables the structural velocity field to be mapped very efficiently onto the velocity distribution of the radiation modes. The lower value for radiation mode 10 is again caused by the 90 degree shift of the radiation mode with respect to the velocity distribution. The radiation amplitudes after control for these two modes drop down to -9.995×10^{-02} and -1.912×10^{-02} respectively, which corresponds to an attenuation of approximately 20.9 dB. This corresponds well with what

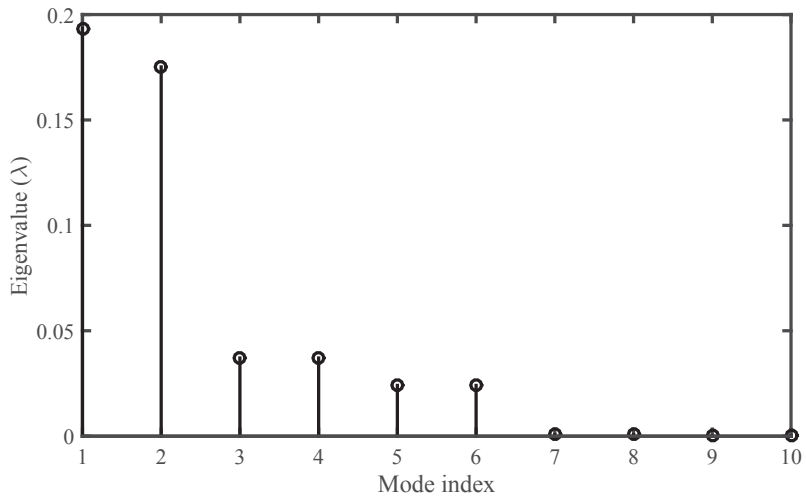

Figure 4.60 Eigenvalues of the ten most efficient radiation modes at 413.91 Hz.

is observed in Fig. 4.44 for the frequencies investigated here.

Table 4.15 The coupling between the vibration before and after control with the ten most efficient radiation modes at 413.91 Hz.

	y_{bc}	y_{ac}	y_{ac-opt}
Mode 1	1.6869e-03	5.4709e-06	9.1858e-07
Mode 2	-3.7863e-03	-7.7637e-03	-7.7745e-03
Mode 3	9.4818e-02	-4.7911e-03	-5.0584e-03
Mode 4	4.7767e-03	-2.4137e-04	-2.5483e-04
Mode 5	-1.8361e-02	-3.6663e-02	-3.6712e-02
Mode 6	-1.2832e-03	-2.5623e-03	-2.5657e-03
Mode 7	6.2387e-02	1.2793e-01	1.2810e-01
Mode 8	1.3261e-02	2.7192e-02	2.7229e-02
Mode 9	-1.1130e+01	-9.9954e-02	-6.0609e-03
Mode 10	-2.3658e+00	-1.9120e-02	-1.2883e-03

This analysis can be continued for all of the resonances shown in Fig. 4.44. It is found that WSSG is able to control all of the resonances in the frequency range of interest, and that the amplitudes of the strongest radiation modes are nearly the same when minimizing either WSSG or the radiated sound power.

4.8 Comparison to other methods

The main objective of developing the WSSG method is to create a control metric that can result in effective and reliable global sound attenuation using one, or a few, point (local) measurements for cylindrical shells. Therefore, it is important to be able to compare WSSG control results with other known methods. One of these methods is minimizing the radiated sound power with respect to the control force. While this can be done numerically, it is not a practical method experimentally. This was explained in the previous section and the results were shown in Fig. 4.44. There are two important points to consider. First, minimizing the radiated sound power with respect to the control force provides the best possible control results, i.e the maximum amount of power attenuation that can be achieved at each frequency. Second, minimizing the radiated sound power requires a global measurement, which means a very large number of vibration sensors would be needed. As mentioned, this limits the practicality of this method.

4.8.1 Volume velocity minimization

Another method that has been proposed for active structural acoustic control is the method of volume velocity attenuation [117]. In this method, the objective is to ideally drive the total volume velocity to zero. To examine this, let us consider the volume velocity, which can be represented as

$$Q = \sum_{i=1}^{N} \mathbf{u}_i \Delta S = \mathbf{q}^{\mathbf{T}} \mathbf{u}, \tag{4.11}$$

where N is the number of elements, ΔS is the area of each element, $\mathbf{u}$ is the velocity vector described by Eq. (4.2) and $\mathbf{q}$ is the vector of element areas. In order to cancel or minimize the volume velocity, Q goes to zero. This results in

$$Q = \mathbf{q^T u_p} + F_c \mathbf{q^T G} = 0 \tag{4.12}$$

Solving this equation leads to an expression for the optimal control force as the following,

$$F_c = -\frac{\mathbf{q^T u_p}}{\mathbf{q^T G}}. \tag{4.13}$$

In order to implement volume velocity cancellation in practice, however, one needs a large number of vibration sensors distributed over the structure in order to sense the global volume velocity. Figure 4.61 shows the control results for the shell being studied when implementing volume velocity control for configuration I.

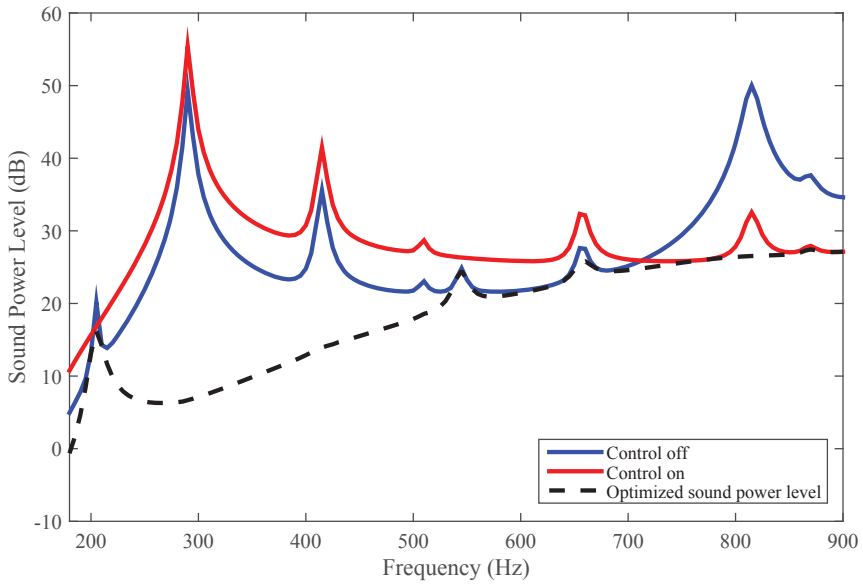

Figure 4.61 Active structural acoustic control using volume velocity cancellation.

As can be seen, this method is not very effective in attenuating the radiated sound power, even

though a global measurement is utilized in order to carry out this control approach. The overall sound power attenuation for this case is -0.44 dB, i.e., the sound power is increased. In simulations carried out in this work, WSSG is able to consistently provide much better results using only one local measurement for the same exact configuration.

4.8.2 Global kinetic energy

Another method that can be used is to minimize the global kinetic energy of the structure [27]. Similar to the previous methods, a large number of vibration sensors is required to sense the structure's global velocity response. In order to minimize the global kinetic energy with respect to the control force one can start from the definition of the kinetic energy, i.e.

$$K = \frac{1}{2} m \mathbf{u}^{\mathbf{H}} \cdot \mathbf{u} \tag{4.14}$$

where m is the mass per area for each element. Using Eq. (4.2), one can expand Eq. (4.14) as

$$K = \frac{1}{2} m [\mathbf{u_p^H u_p} + F_c \mathbf{u_p^H G} + F_c^* \mathbf{G^H u_p} + F_c \cdot F_c^* \mathbf{G G^H}] \tag{4.15}$$

Minimizing Eq. (4.15) with respect to the control force, the optimal control force is given by

$$F = -(\mathbf{G^H G})^{-1} \cdot \mathbf{G^H} \cdot \mathbf{u_p}. \tag{4.16}$$

Using this result, Fig. 4.62 shows the control results for minimizing the global kinetic energy for configuration I. The overall attenuation obtained in this case is 12.1 dB.

This method results in performance that is comparable to using WSSG. However, the WSSG method is still superior, in the sense that it can provide comparable results using only one point measurement, resulting in a global sound power attenuation of 11.4 dB. This is significant since this provides a method that is very practical to implement, whereas the other methods are not easy

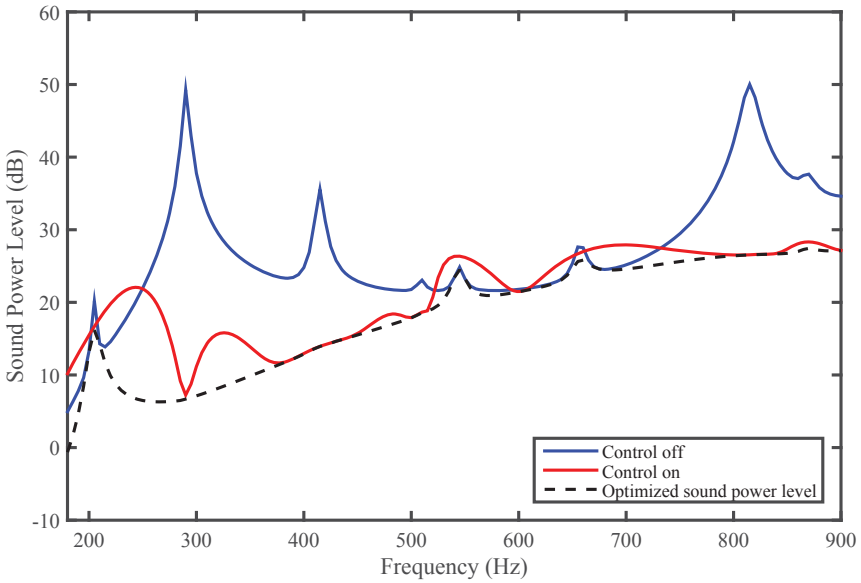

Figure 4.62 Active structural acoustic control using global kinetic energy.

to implement in practice. This is demonstrated by the fact that most of the reported works have investigated the option of using kinetic energy only numerically.

One can notice that in general, the overall performance of WSSG is very close to that of using global kinetic energy. This similarity suggests a correlation between WSSG and the global kinetic energy, which can be linked to the squared spatial derivatives used to form WSSG, which are indeed proportional to structure's squared velocity at the error sensor location. This leads to another concept that can provide insight on the correlation between WSSG and the radiated sound power. Since the radiated sound power is obtained from an integral that has the squared velocity in the integrand, there is a relation between sound power, kinetic energy, and WSSG. Thus, the minimization of WSSG seems to have a strong correlation with the results obtained by minimizing the sound power or the global kinetic energy.

4.8.3 Summary

Table 4.16 summarizes the performance of different control metrics mentioned above when implemented for configuration I.

Table 4.16 Summary of performance of different methods

Method	Sound power level reduction
Sound Power	14.0 (dB)
WSSG	11.4 (dB)
Global Kinetic Energy	12.1 (dB)
Volume Velocity Cancellation	-0.44 (dB)

As a conclusion of this comparison, the theoretical analysis of WSSG shows this method to be an effective method that is able to produce near optimal results by using (in this case) only a single local measurement. This suggests that this method can substitute for any of the methods mentioned above in practice, with a robustness in error sensor positioning and an ease of implementation.

Chapter 5

Experimental results

In order to investigate and verify the results obtained through the model in the previous chapter, a cylindrical shell made out of aluminum is considered, where the length along its axis is 1.21 m (47.5 in), the radius is 0.0780 m (3.06 in) and its thickness is 1.60 mm (0.0625 in). The dynamic parameters of the structure are listed in Table 4.1. The structure is known to be made of aluminum; however, there could be some impurities present, since the structure might be an aluminum alloy. Nonetheless, the simulations have been carried out by slightly modifying some of the known parameters for aluminum to match the resonance frequencies of the actual cylinder as closely as possible.

5.1 Experimental set-up

5.1.1 Setup in the reverberation chamber

In an effort to approximate the simply supported boundary conditions for this cylinder, two circular disks with a diameter slightly larger than the actual cylinder were precisely machined. A groove was machined inside each end of the shell, where the disk goes. Then the disks were cooled to

a very low temperature so that the contraction would facilitate inserting the disks inside each end of the cylinder. As the temperature of the disks rises to be that of the room temperature, through expansion the disks return to their original size, creating a tight connection between the wall of the cylindrical shell. The disks were machined to have a knife-edge in contact with the shell, with the intent that this would come very close to providing simply supported boundary conditions.

As the next step in assembling the experimental set-up, it is important to mount the cylindrical shell in such a way that there would be no distortion of the shell, nor any mass loading. In order to ensure that the cylindrical shell is mounted in such a way to ensure stability, as well as being able to support point excitations, while at the same time avoiding distortion and mass loading, the following frame was designed to hold the cylindrical shell in place, as shown in Fig. 5.1.

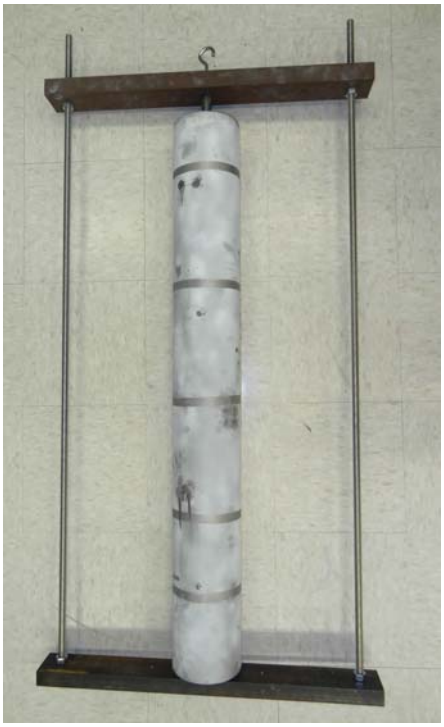

Figure 5.1 Schematic of the frame designed to hold the cylindrical shell in a fixed and stable position.

As can be seen in Fig. 5.1, the frame is constructed of two vertical screw rods that allow for

adjusting the length of the frame. They can get locked into the two horizontal bars in order to keep the cylindrical shell in place, with the help of the bolt that screws into a hook on the top horizontal bar. Once the cylindrical shell is placed securely inside the frame, the frame was moved into the reverberation chamber at BYU, where it was hung from the ceiling and placed on a table stand. Vibration isolation materials were placed between the frame and the table stand in order to reduce vibration transmission to the table stand which could cause error in measurements of radiated sound power.

Additional components for the setup include six microphones, and consequently six microphone stands, in order to support and adjust the locations of the microphones vertically. The microphone stands were located in the chamber according to the ISO 3741 standard. It was ensured that the adjusted position for each microphone was at least 0.5 m from the floor, 1.0 m from the walls and 1.5 m from other microphone positions. The angle between each microphone and the floor was kept to be more than 10 degrees. Half inch Larson Davis LD 2551 pressure microphones were used for this application.

In order to apply a point excitation, as well as a point control force, 2004E ModalShop mini-shakers were used. They were attached to the cylindrical shell at the desired locations by applying Bob Smith Ind Quik-cure 5min Epoxy. It was important to create a secure and reliable connection by applying a thin layer of epoxy. It was observed that with thicker layers of epoxy, variations in the vibration and sound power were observed due to the presence of an additional layer of material which can impose an impedance mismatch. In addition, four PCB 352C68 accelerometers were used in order to sense the WSSG terms. Having a broad frequency range of up to 10 KHz and a light mass of 2.0 g makes these accelerometers a suitable choice for vibration sensors for this application. The accelerometers are connected to the shell surface using "Loctite ultra liquid control super glue", as shown in Fig. 2.6, with a separation distance of 1 inch (0.0254 m) from each other.

5.1.2 Setup in the control room

The next phase of arranging the experimental system consisted of the setup in the control room adjacent to the reverberation chamber, where the control system is run by the operator. A schematic of the complete setup is shown in Fig. 5.2.

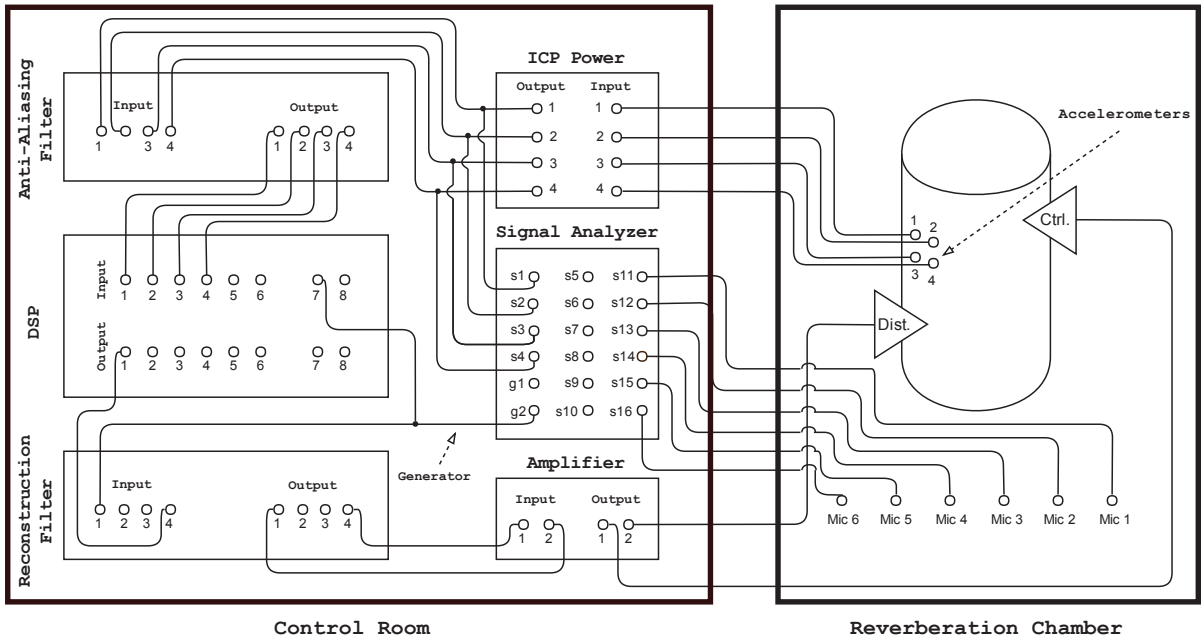

Figure 5.2 Schematic of the complete experimental active control setup for the cylindrical shell.

The setup inside the control room included a PC that is connected to a Digital Signal Processing Board (DSP) utilizing a TI TMS320C6713GDP processor. The DSP used the modified filtered-x algorithm to implement the active control. The setup also includes a Type 3660-C - Brüel & Kjær (B&K) signal analyzer, which includes 16 input channels as well as two generator channels. An excitation output signal is taken from one of the generator channels and directed into the Crown D-45 amplifier and then into the primary, i.e. excitation, shaker. In addition, the signal was directed to the DSP, in order to provide the reference signal for the modified filtered-x LMS algorithm. The six microphones placed in the reverberation chamber are connected to the signal analyzer through

BNC cables that are brought into the control room through a small tube inside the wall. This enables processing the microphone data inside the signal analyzer software (PULSE^{TM}) in order to use them for sound power calculations.

As shown in Fig. 5.2, the accelerometers are connected to an Integrated Circuit Piezoelectric (ICP) power supply through micro-dot cables. The cables in the reverberation chamber are brought into the control room, through a small tube inside the wall. Using the outputs of the ICP power supply, the amplified accelerometer signals are then connected to an analog anti-aliasing filter. In addition, they are connected to the inputs of the B&K signal analyzer in order to be able to keep track of the accelerometer levels before and after control at each frequency. The output signals from the anti-aliasing filter are then transferred to the DSP, which implements the ANC code to obtain the control signal. The accelerometer signals are then processed to form the WSSG terms used to adaptively update the control filter. The output signal is conditioned using a reconstruction filter and amplifier, and then the signal is used to drive the control shaker.

Figure 5.3 shows the actual set up inside the reverberation chamber, showing the cylindrical shell installed in the frame while it is hung from the ceiling, with the shakers and the accelerometers attached. Figure 5.4 also shows the microphone placing.

5.2 Calibration

In order to achieve the best performance in sensing WSSG terms, it is important to choose accelerometers with relatively close sensitivities. The accelerometers are then calibrated using the PCB Handheld Shaker-699A02 which operates at 159.2 Hz. Mounting the accelerometers on top of this calibrator, it measures the relative acceleration with respect to 100 mV/g. This calibration is necessary since the close spacing of the accelerometers requires the accelerometer readings to be accurate and precise.

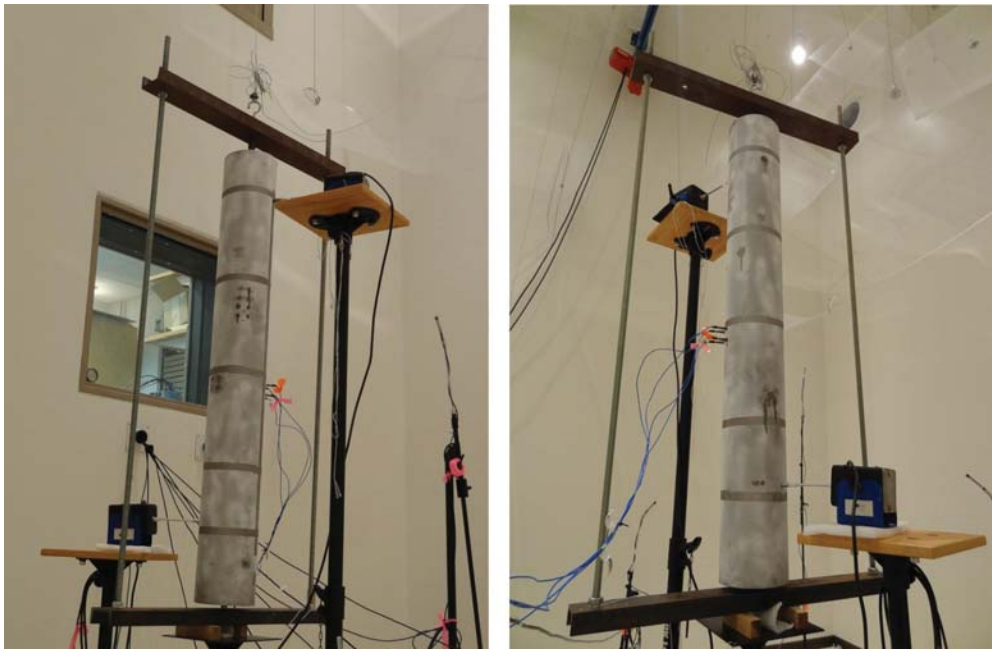

Figure 5.3 The experimental setup showing the mounted cylindrical shell in the frame while the accelerometers and shakers are attached.

Figure 5.4 The experimental setup showing the cylindrical shell, shakers and accelerometers, as well as the microphone placement.

At the beginning of each set of measurements, the microphones are also calibrated using the GRAS type 42AB sound calibrator, using the calibration option available in the PULSE^{TM} signal analyzer software.

5.3 Parameters

Several parameters must be input to the DSP for the ANC code to run properly. The relative sensitivities obtained from the accelerometer calibration are inserted into the ANC code, as well as the distance between the accelerometers. It is also important to insert the proper WSSG weights calculated in Table 4.4 inside the control code.

In addition, it is important to know the temperature, barometric pressure, and humidity for calculation of the radiated sound power. For this purpose, a meteorological instrument was placed inside the reverberation chamber that measures the temperature in °C, pressure in "in-Hg", as well as the humidity in percentage. During post-processing, it is important to convert the pressure to SI units. Furthermore, measured reverberation time (T_{60}) values are needed in order to calculate the radiated sound power at each of the frequencies of interest. The T_{60} is the time that it takes for the sound level of an impulse to drop by 60 dB. The T_{60} values at the measured frequencies can be interpolated for the frequencies of interest.

5.4 Measurements

5.4.1 Dynamic response

The cylindrical shell was scanned using a Polytec 1D SLDV while rotating the shell by 5 degree increments on a turntable. In order to observe the mode shapes and the resonance frequencies, the cylinder was excited at a point location by a shaker. The results were then merged into one file in

order to describe the mode shapes. These data were obtained using a different excitation level than what has been used in the control approach. This work was done by Cameron Jones, a master's student in the Department of Mechanical Engineering at BYU.

In the frequency range of [0-700] Hz, resonance peaks observed in the FFT spectrum were at frequencies of 201.1, 310.6, 406.2, 510.1, 581.4, and 637.9 Hz. The actual frequencies are somewhat different than those of the model, shown in Table 4.2. The shift in the frequencies seems to be inconsistent; for example, the first frequency is lower than predicted in the model but the second frequency is higher than predicted in the model. The discrepancies could be a result of slightly different values of dynamic parameters such as density, Young's modulus, etc. However, the inconsistency in the shifts suggests that this cylinder may not behave as an ideal simply supported cylindrical shell.

5.4.2 Experimental control

With the configuration in place, it is then important to determine the level for the disturbance shaker in order to achieve good control results. As with the modeling, a constant excitation point force is considered for all frequencies. However, the accelerometer levels are different at each frequency depending on if it is on or close to a resonance frequency or not. On the other hand, the maximum input voltage level for the DSP is limited to 2.5 Vrms and therefore it is important to adjust the level of shaker excitation and the output gain of the accelerometers in such a way that it is below 2.5 Vrms for the largest response. Therefore, at the signal generator, typically a single tone sine wave with a fixed source level of 200 Vrms is activated, while further adjustments are made at the amplifier driving the shaker and the output gain of the anti-aliasing filter, in order to excite the shell in such a way that it can produce a reasonable acoustic field while at the same time keeping the amplified accelerometer levels below 2.5 Vrms. In addition to protecting the DSP, this adjustment is important to prevent the accelerometer signals from clipping, which would degrade

the performance of the WSSG control approach, which relies on finite differences of the signals. To adjust these gains, the shell was excited with a broadband signal and the accelerometer levels were recorded. The FFT spectrum of the accelerometer identifies the resonance frequency that has the highest response at that specified sensor location. Hence, the adjustments of the amplifier and the output gain for the accelerometers are done at this frequency. Figure 5.5 shows an example for one of the error sensor locations considered. In this case, for example, one needs to adjust the output gain for the accelerometers with respect to the largest peaks at 480 Hz and 640 Hz.

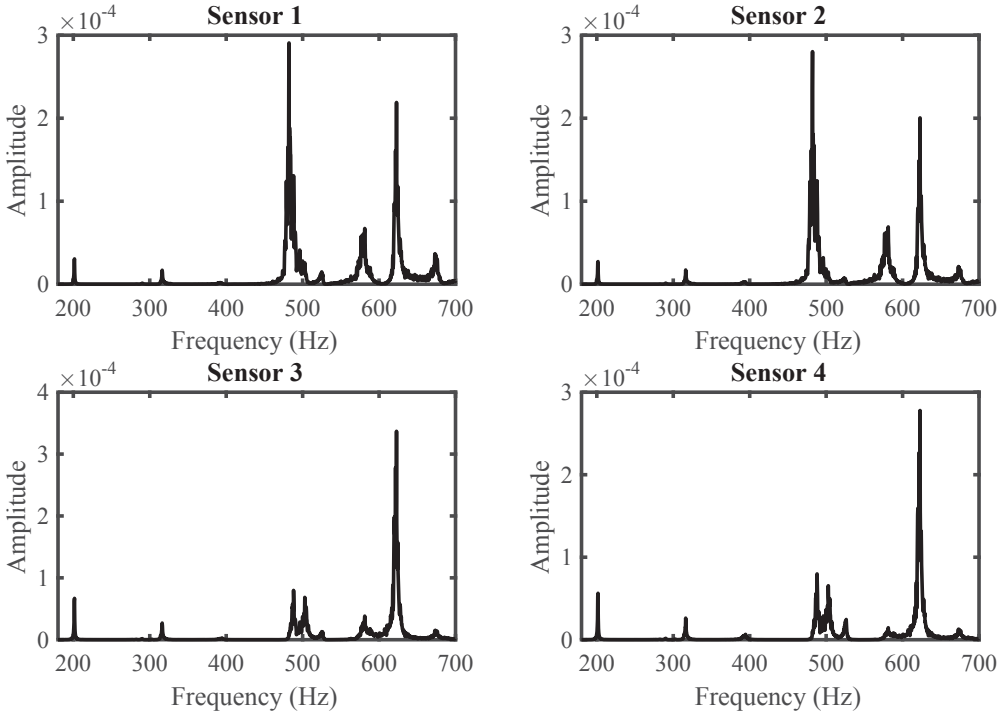

Figure 5.5 Accelerometer signals due to a broadband excitation.

With the parameters loaded into the code, the ANC code is compiled and uploaded. The number of control forces and the number of error sensors can be set using the ANC interactive interface. The leakage factor is set to be 1.0 and 20 coefficients are used for the control filter, as well as for the estimate of the secondary path. Before starting control, the control output is calibrated at the desired frequency and then the SysID routine is run in order for the ANC system

to obtain the estimate of the secondary path, i.e. $\hat{H}$.

Once the SysID has been completed, the disturbance signal is activated and the sound pressure at each of the microphones is recorded due to only the disturbance signal. For this purpose, both the FFT data as well as the constant percentage bandwidth (CPB) data were recorded through the signal analyzer, where the bandwidth is limited to 1/24th octave bands with the center frequency close to the disturbance frequency. After recording the necessary data prior to control, one can measure the same set of data while the ANC system is running.

In order to activate the ANC system, the convergence parameter, i.e. α_c, is set to a value small enough to avoid the divergence of the control force and damaging the control shaker. As mentioned previously, the value of the convergence factor depends on the energy of the reference signal, i.e. the disturbance signal. The higher the energy of the signal, i.e. the level of the signal, the steeper the hyperbolic error surface will be which will require a smaller step size for the optimization process. In this case, the initial value of the convergence factor, α_c, was set to be 10^{-12}. If α_c is too small, one can adjust the convergence factor to a larger value. However, if the value is too large and the control force diverges, one can reset the control system in the ANC interactive interface so that the value of the control signal is set back to zero again. Using this routine, α_c was adjusted so that the control force reached the optimal value and it was stable with time.

There were a few cases in which adjusting α_c alone was not sufficient in order to ensure the stability of the control solution, and the control signal would tend to diverge with time. In these cases, the leakage factor was set to values slightly lower than 1.0 in order to prevent the solution from diverging, while making it possible to achieve a solution very close to the optimal. This problem can occur when the estimate of the secondary path is different or has changed with respect to the actual secondary path response. This will cause the auto-correlation matrix, which is a function of estimated filtered signal, to be ill-posed. Adding the leakage factor prevents instability in the algorithm due to the ill-posed autocorrelation matrix of the estimated filtered reference

signal. Extra caution should be taken into account, since lower values of the leakage factor will degrade the control performance further with respect to the optimal solution.

After reaching optimal and stable control results, the pressure data were recorded again at each of the 6 microphones. The control routine was repeated for each frequency. The frequency range of interest was defined to be [180 Hz - 700 Hz]. Due to the measurement time, the frequency resolution was chosen to be 10 Hz.

5.5 Control results

Figure 5.6 presents the location of the actuators and sensors for configuration A. The exact locations are also listed in Table 5.1

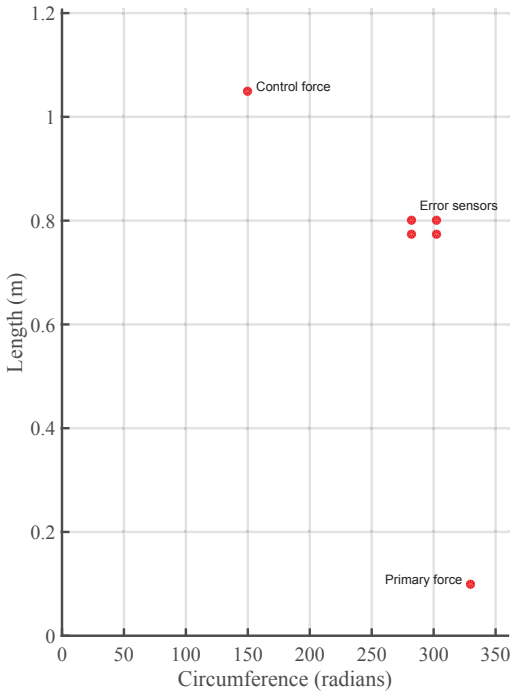

Figure 5.6 Placement of shakers and accelerometers on the shell in configuration A.

Table 5.1 Location of sensors and actuators for configuration A.

	Primary Shaker	Control Shaker	sensor 1	sensor 2	sensor 3	sensor 4
z (m)	0.10	1.05	0.80	0.80	0.77	0.77
θ (degrees)	330	150	282	302	282	302

The WSSG control metric was run for configuration A and the results are shown in Fig. 5.7.

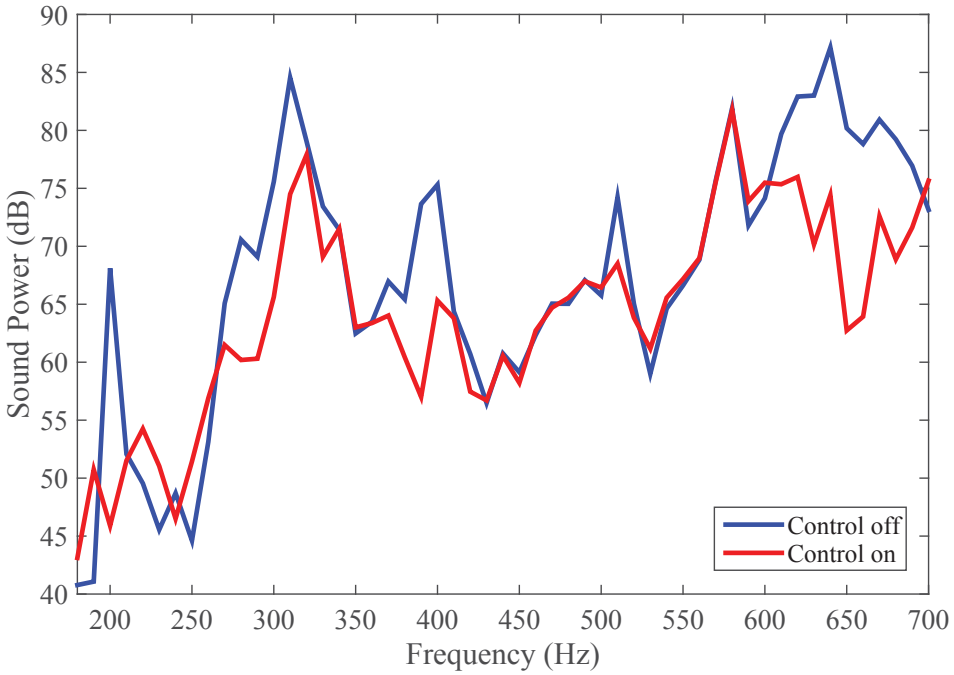

Figure 5.7 WSSG control results for configuration A.

In this configuration, the overall sound power was attenuated by 5.7 dB. The control results predicted by the model are presented in Fig. 5.8. The overall attenuation predicted by the model is 11.4 dB. As can be seen by comparison between Fig. 5.7 and Fig. 5.8, the resonance peaks are not as prominent for the experimental results which can be due to underestimating the amount of damping in the model. This can explain to some extent the difference between the experimental results and the model predictions. However, as can be seen in Fig. 5.7 the WSSG control metric is able to attenuate the radiated sound power effectively for all but one of the resonance peaks. This

can be due to the location of the control force with respect to the primary force. There are some frequencies in which the radiated sound power has been enhanced. Even though the WSSG metric has been minimized at that frequency, one possible reason for the enhancement of power is that the new state of vibration after control may be able to better couple with efficient radiation modes and as a result lead into enhancement of the radiated sound power.

It is worth noting that the Schroeder frequency of the reverberation chamber at BYU is about 410 Hz. The Schroeder frequency is the threshold that determines the boundary between a completely reverberant room and a resonator room, where the modes of the room come into play. Here the room is not completely reverberant below 410 Hz, however, since in this work, measuring the difference in the radiated sound power is the main objective and not the absolute value of the radiated sound power, this does not affect the sound power attenuation at those frequencies. However, the absolute values of the radiated sound power are not reliable below the Schroeder frequency.

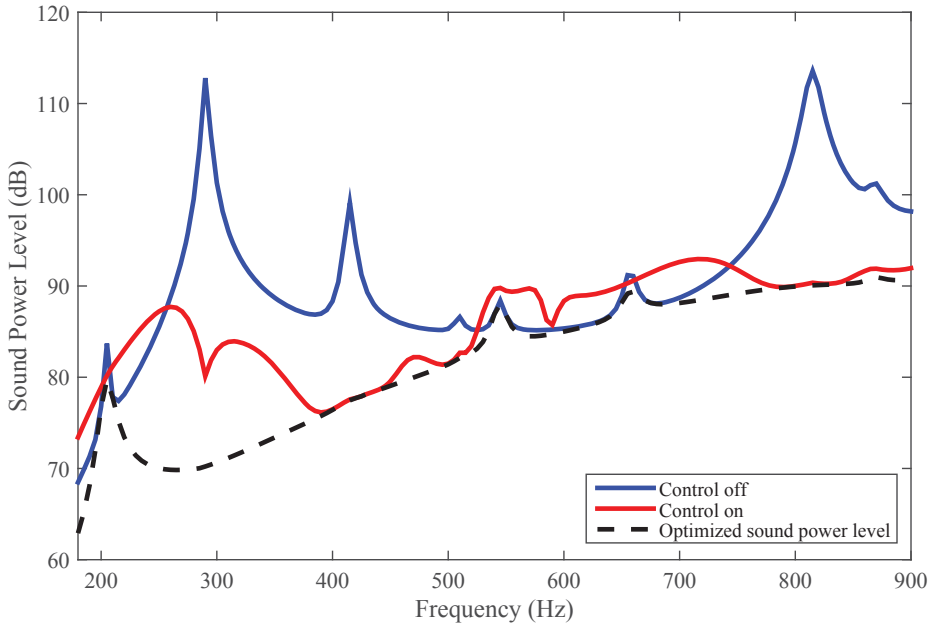

Figure 5.8 WSSG control results predicted by the model for configuration A.

Figure 5.9 shows the sound pressure level at each of the microphones before and after control. These pressure levels are processed through the ISO 3741 standard to yield the radiated sound power at each frequency. As one can see, in general the levels are attenuated at most frequencies and there is not much enhancement of the sound pressure levels in particular.

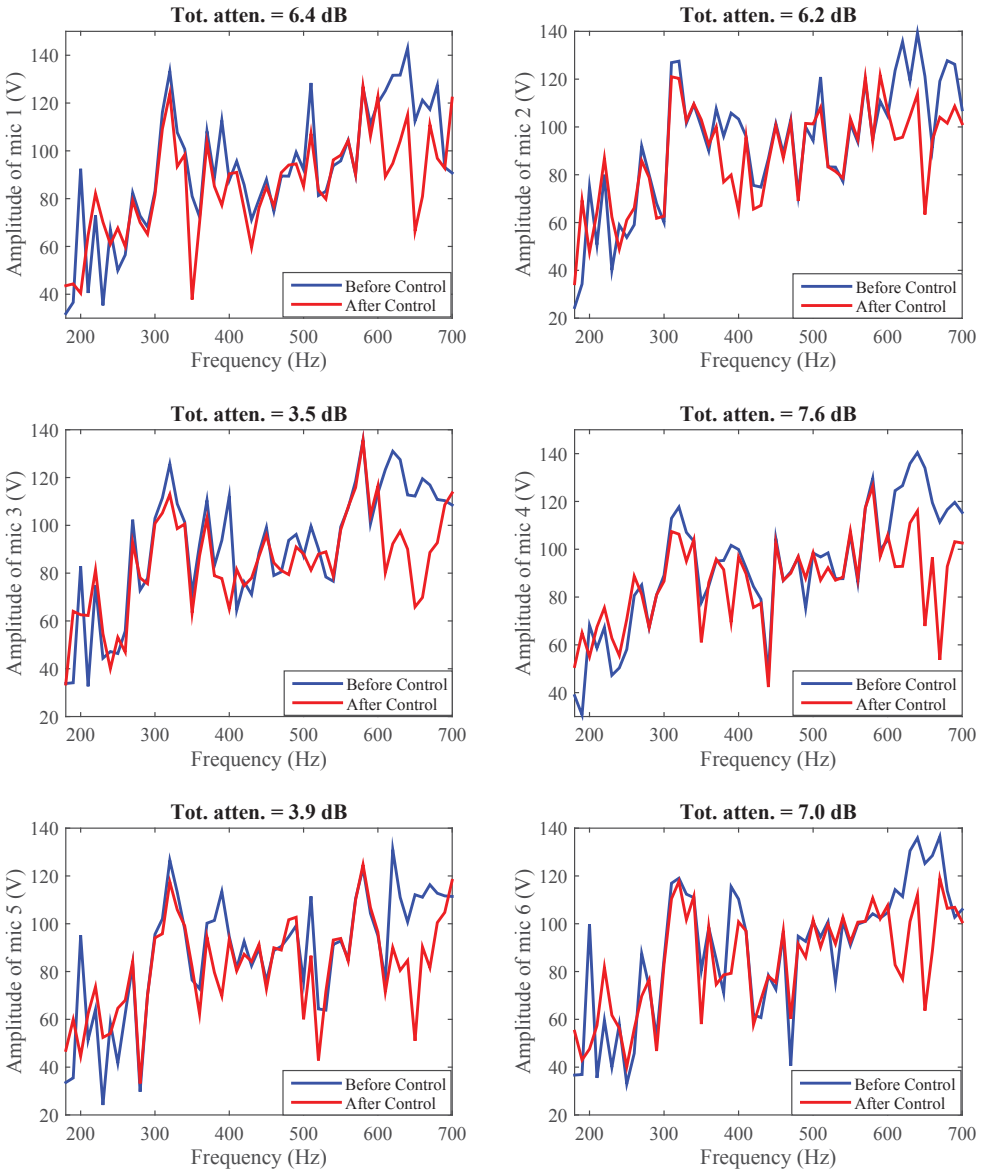

Figure 5.9 Sound pressure levels (dB) at microphones before and after control.

Figure 5.10 presents the accelerometer signals before and after control for configuration A. In this case, the signal level has been attenuated for most of the frequencies. However, there are a few frequencies where the signal level has been enhanced, but this alone is not enough to evaluate the performance of the control, since the accelerometer signals are processed in order to yield the WSSG terms. Therefore, it is important to observe the WSSG signal levels before and after control.

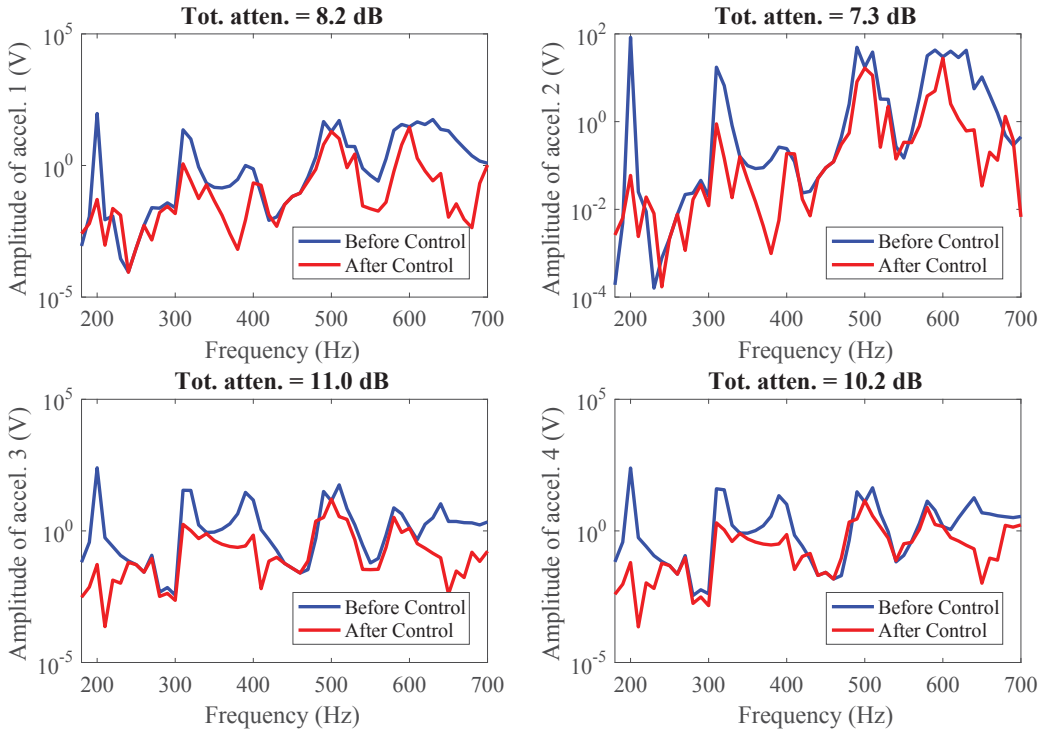

Figure 5.10 Accelerometer levels in (dB) before and after control.

Figure 5.11 shows the WSSG at the error sensor location before and after control. For configuration A, 17.8 dB overall attenuation of WSSG was obtained.

As can be seen, the attenuation of WSSG results in attenuation of the radiated sound power for most frequencies, which suggests that there is a correlation between the radiated sound power and WSSG.

In order to experimentally investigate the effect of sensor location on the control performance, configuration A was modified by placing the sensor locations in a difference place on the shell.

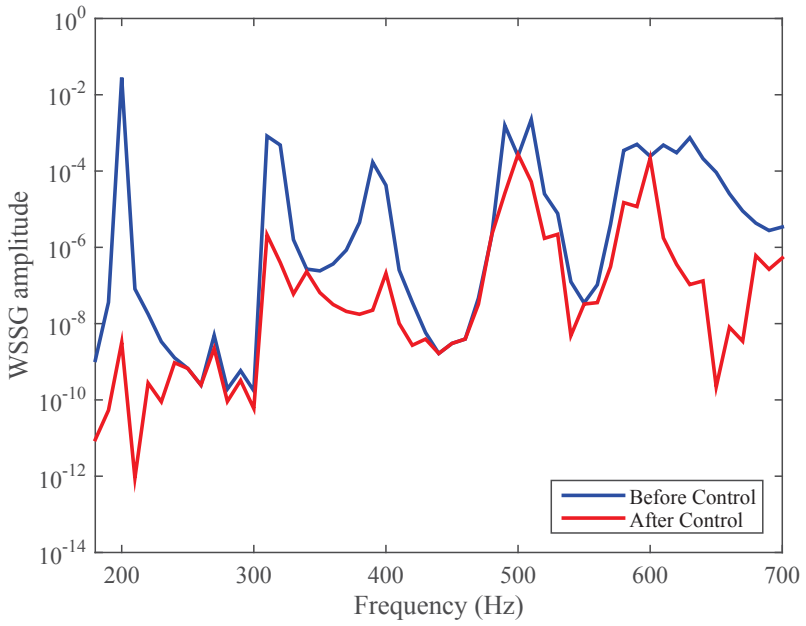

Figure 5.11 WSSG before and after control.

This configuration is illustrated in Fig. 5.12, and the locations of the sensors and actuators are listed in Table 5.2.

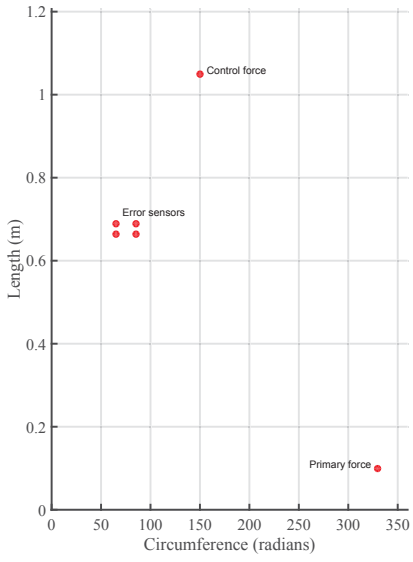

Figure 5.12 Placement of shakers and accelerometers on the shell in configuration B.

Table 5.2 Location of sensors and actuators for configuration B.

	Primary Shaker	Control Shaker	sensor 1	sensor 2	sensor 3	sensor 4
z (m)	0.10	1.05	0.69	0.69	0.66	0.66
θ (degrees)	330	150	65	85	65	85

The control results for configuration B are shown in Fig. 5.13. In this case, the overall sound power attenuation is 4.9 dB. In this configuration, the WSSG control metric is able to perform reasonably well for most resonance peaks.

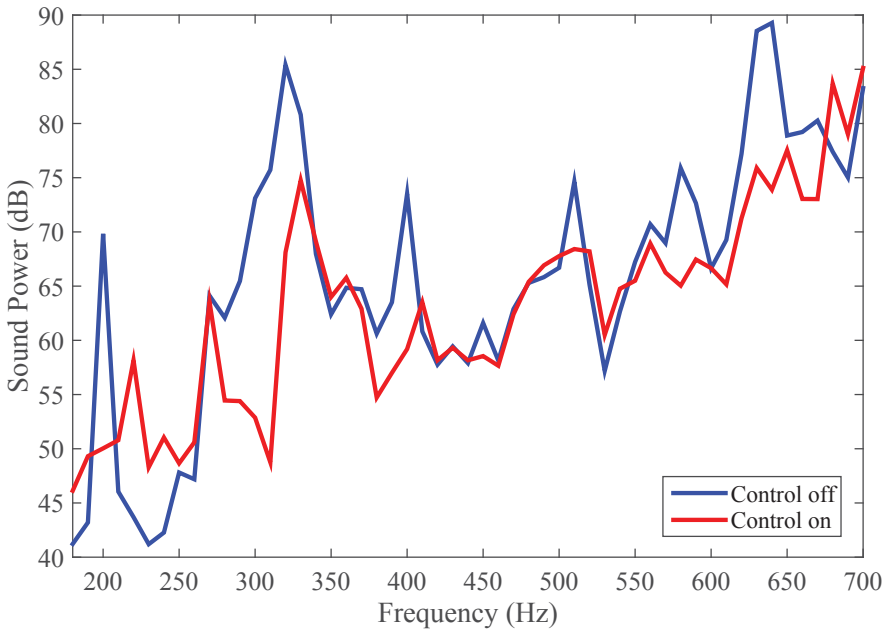

Figure 5.13 WSSG control results for configuration B.

Comparing this result with the control result for configuration A, one can see that there is only a 0.8 dB difference in overall sound power attenuation. As was stated in Chapter 4, there is usually only less than a dB variation when changing the error sensor location. Observing the performance of the WSSG control metric for different sensor locations verifies this result experimentally. Figure 5.14 shows the WSSG control results predicted by the model for configuration B, which predicts 11.0 dB overall attenuation for radiated sound power.

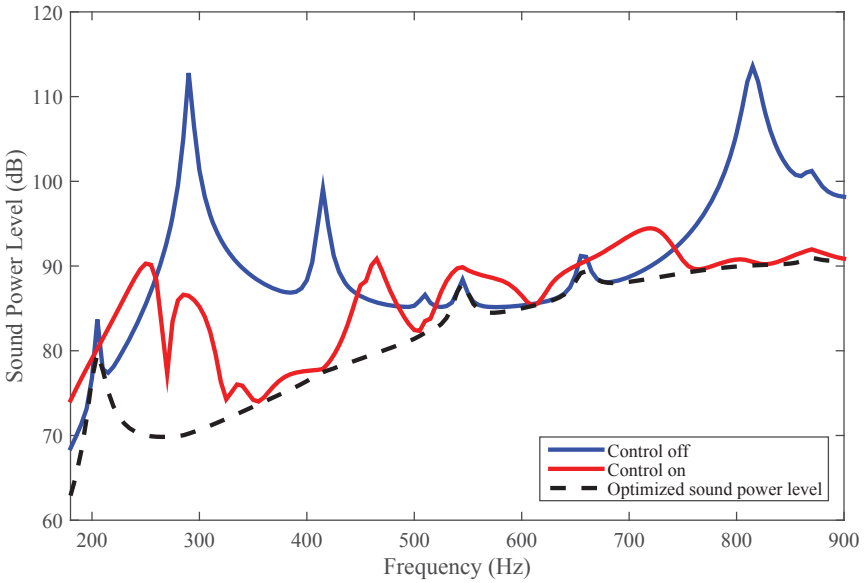

Figure 5.14 WSSG control results predicted by the model for configuration B.

As can be seen from the comparison between Fig. 5.13 and Fig. 5.14, the control results have similar trends. However, an exact comparison may not be reasonable, since the shell does not seem to behave as an ideal simply-supported shell.

Figure 5.15 shows a different configuration, where all the shakers and accelerometers are moved to new locations. The exact locations of the sensors and actuators are also listed in Table 5.3.

Table 5.3 Location of sensors and actuators for configuration C.

	Primary Shaker	Control Shaker	sensor 1	sensor 2	sensor 3	sensor 4
z (m)	0.20	1.08	0.57	0.57	0.54	0.54
θ (degrees)	190	10	320	340	320	340

The control results for configuration C are shown in Fig. 5.16. For this configuration, the overall sound power attenuation obtained using the WSSG control metric is 4.5 dB.

The corresponding control results predicted by the model for this configuration are shown in

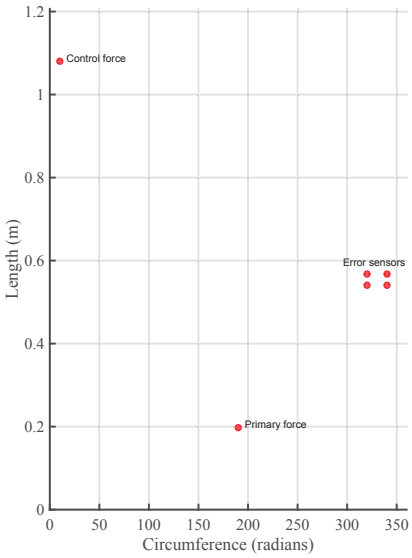

Figure 5.15 Placement of shakers and accelerometers on the shell in configuration C.

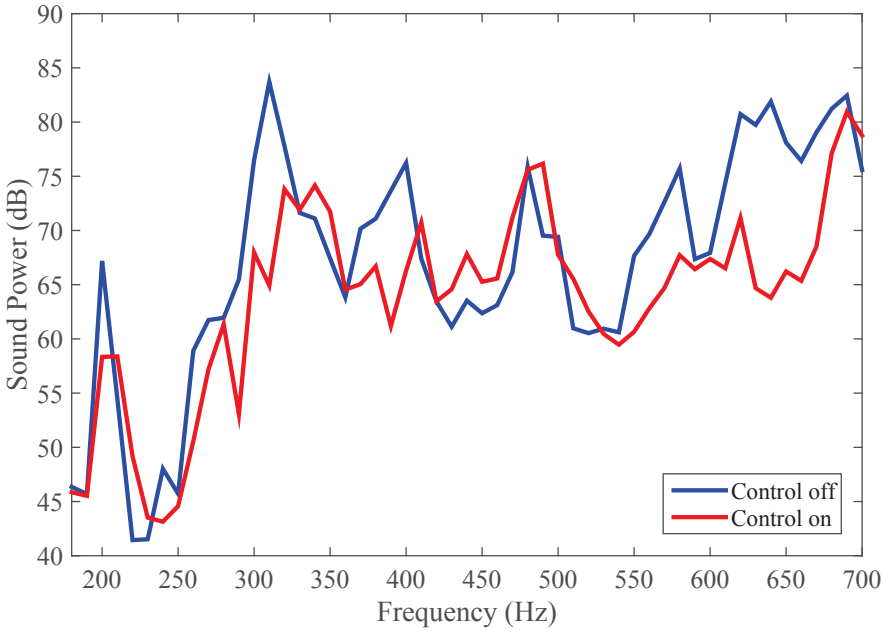

Figure 5.16 WSSG control results for configuration C.

Fig. 5.17. Applying the WSSG control metric through the model yields 10.8 dB overall sound power attenuation for configuration C.

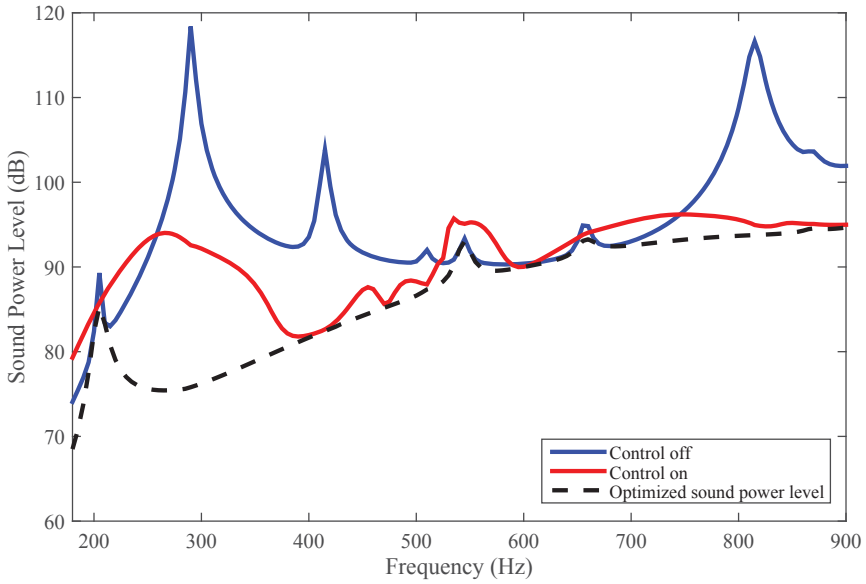

Figure 5.17 WSSG control results predicted by the model for configuration C.

As can be seen, the location for the control force is slightly less favorable in comparison with configurations A and B, with respect to the overall attenuation achieved in each case. The experimental results obtained in Fig. 5.16 also suggest a slight degradation in the control performance for the new location. Although the performance of the WSSG control metric is only mildly dependent on the error sensor location, the location of the control force with respect to the disturbance force can be a much more significant factor in the performance of the control metric.

A different configuration is considered where the location of the primary and the control shakers are exchanged. This is shown in Fig. 5.18 for configuration D. The locations are also listed in Table 5.4.

The control results for configuration D are shown in Fig. 5.19. Applying the WSSG control metric yields an overall sound power attenuation of 3.2 dB. The control results predicted for configuration D are shown in Fig. 5.20.

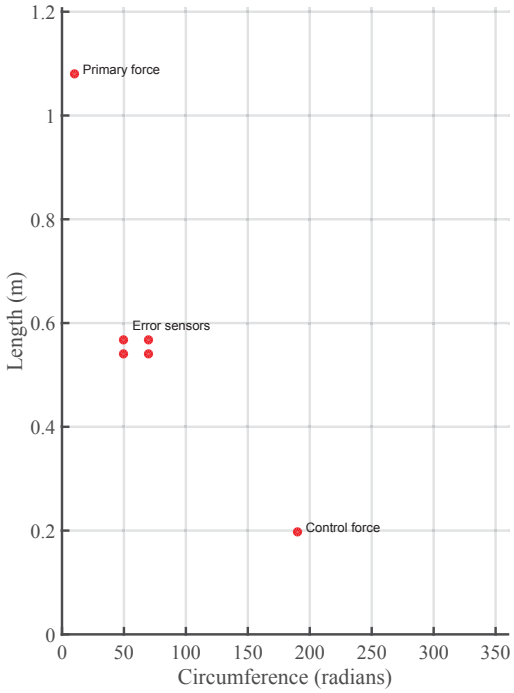

Figure 5.18 Placement of shakers and accelerometers on the shell in configuration D.

Table 5.4 Location of sensors and actuators for configuration D

	Primary Shaker	Control Shaker	sensor 1	sensor 2	sensor 3	sensor 4
z (m)	1.08	0.20	0.57	0.57	0.54	0.54
θ (degrees)	10	190	50	70	50	70

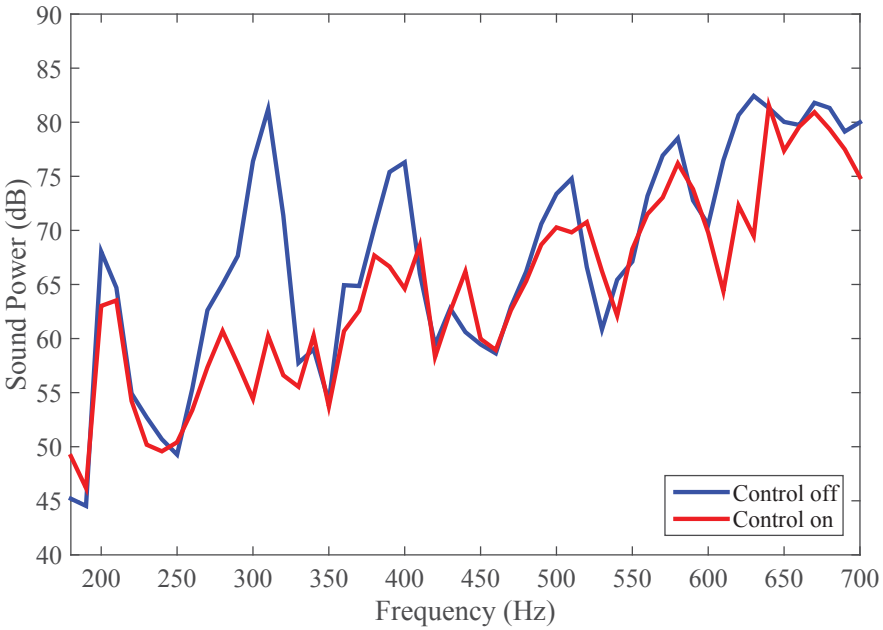

Figure 5.19 WSSG control results for configuration D.

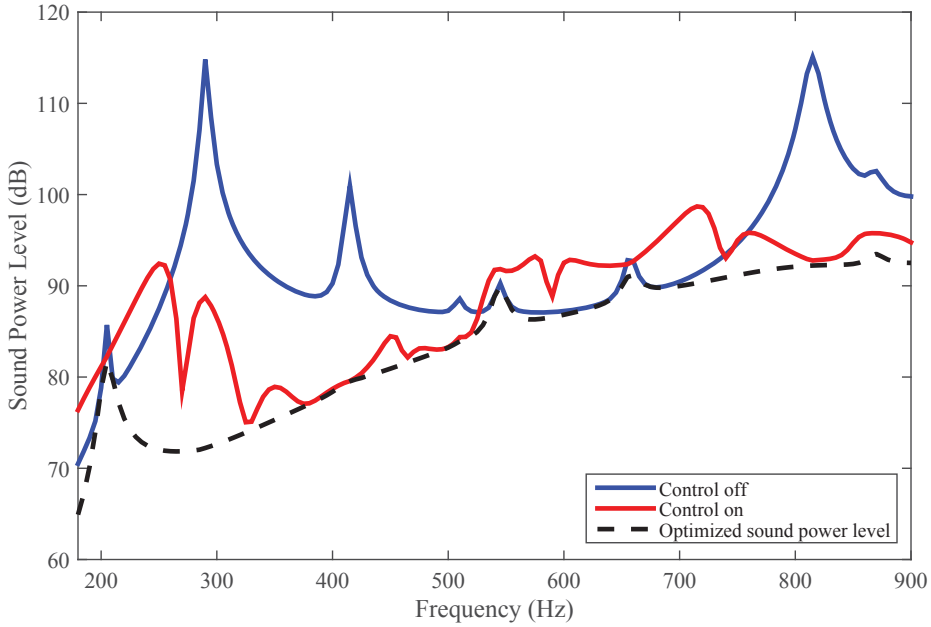

Figure 5.20 WSSG control results predicted by the model for configuration D.

The model predicts an overall attenuation of 9.5 dB. One can see that even though the experimental results do not completely agree with the results predicted by the model, the overall trend seems to agree reasonably well.

As a final configuration, we consider a case where the location of the control force is knowingly chosen to be at a location which will not be able to effectively attenuate the radiated sound power. Figure 5.21 shows such a scenario for configuration E. The exact positions are also listed in Table 5.5.

Table 5.5 Location of sensors and actuators for configuration E

	Primary Shaker	Control Shaker	sensor 1	sensor 2	sensor 3	sensor 4
z (inch)	0.1	0.76	0.57	0.57	0.54	0.54
θ (degrees)	330	102.5	228	248	228	248

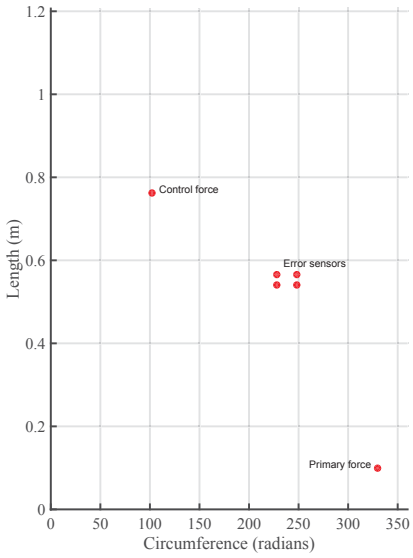

Figure 5.21 Placement of shakers and accelerometers on the shell in configuration E.

Figure 5.22 shows the experimental control results for configuration E. In this case, due to the

unfavorable location of the control force, the WSSG control metric has in fact enhanced the overall radiated sound power by 3.7 dB.

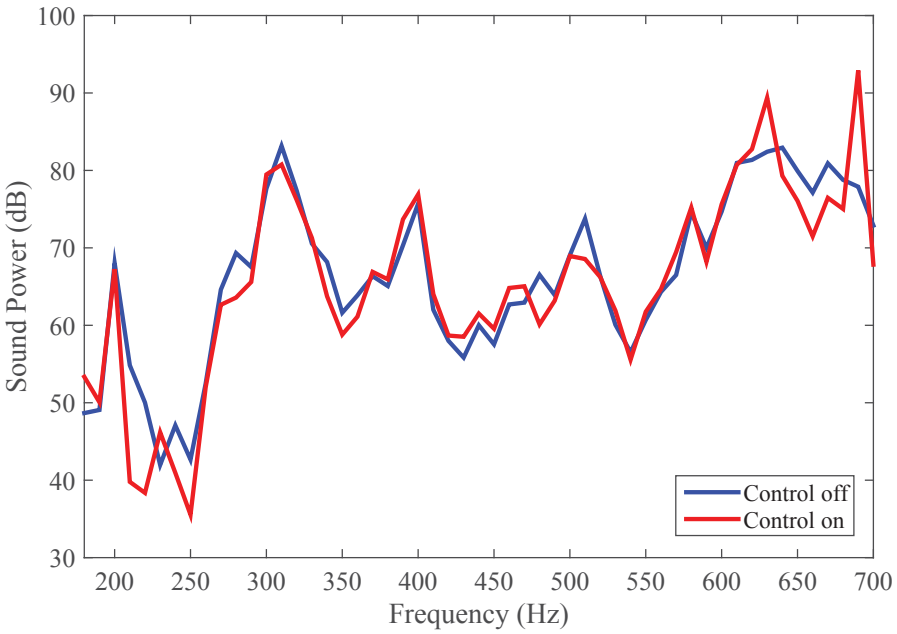

Figure 5.22 WSSG control results for configuration E.

For the same configuration, the control results predicted by the model are shown in Fig. 5.23, which predict an overall enhancement of the radiated sound power by 0.8 dB.

A summary of the tonal attenuation at each of the resonance peaks for each of the configurations is listed in Table. 5.6.

A summary of the overall attenuation of radiated sound power obtained both experimentally and numerically is listed in Table 5.7.

As can be seen from Table 5.7, in general, the experimental results seem to follow the trends presented in the numerical results. As the control configuration is modified into less favorable locations, the control results in both the model and the experiment follow the same trend in yielding reduced sound power attenuation. The experimental results seem to also agree for the case where

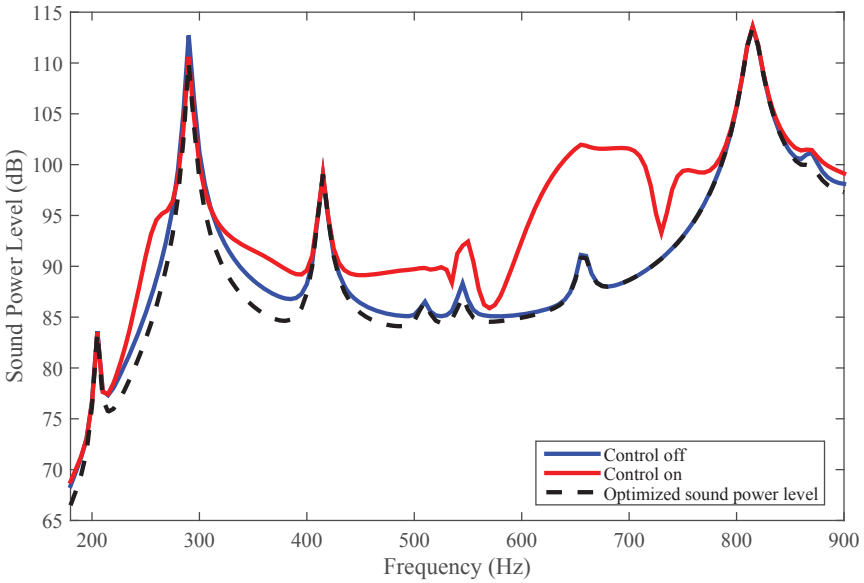

Figure 5.23 WSSG control results predicted by the model for configuration E.

Table 5.6 Summary of the sound power level attenuation of resonance peaks for all configurations.

Res. freq. \ Config.	Config. A	Config. B	Config. C	Config. D	Config. E
201.1 Hz	22.2 dB	19.8 dB	8.85 dB	5.02 dB	0.78 dB
310.6 Hz	10.0 dB	17.3 dB	18.8 dB	20.9 dB	2.40 dB
406.2 Hz	10.2 dB	14.3 dB	9.93 dB	14.7 dB	-1.2 dB
510.1 Hz	5.74 dB	6.21 dB	0.27 dB	4.96 dB	5.20 dB
581.4 Hz	0.18 dB	10.8 dB	8.00 dB	2.30 dB	-0.6 dB
637.9 Hz	12.7 dB	15.4 dB	18.1 dB	-0.2 dB	3.60 dB

Table 5.7 Summary of the experimental and model overall attenuation of radiated sound power for all configurations.

	Experiment	Model
Config. A	5.7 dB	11.3 dB
Config. B	4.9 dB	11.0 dB
Config. C	4.5 dB	10.8 dB
Config. D	3.2 dB	9.50 dB
Config. E	-3.7 dB	-0.83 dB

the simulation results predict enhancement of radiated sound power, rather than attenuation.

Summarizing the results, even though there is not much dependence on the error sensor location for the performance of the control metric, the configuration of the sources can have a significant effect on the attenuation achieved.

As a summary for this chapter, the cylindrical shell chosen for the experimental validation of model results seems to not fully behave as a simply supported cylindrical shell. This has effected the natural frequencies of the shell. However, the WSSG control metric is able to perform well, and the trend of the experimental results is consistent with the numerical predictions.

Chapter 6

Conclusions

Active structural acoustic control (ASAC) methods have been heavily investigated in recent years. Within these methods, the vibration is sensed by error sensors and the control signal tends to control the vibration field rather that the acoustic field. There are certain aspects of these methods that are of great importance in practice. One may categorize them in the following way:

- **Effectiveness:** The method is desired to produce optimal attenuation of the radiated acoustic power.

- **Practicality and convenience:** The method is desired to be practical and convenient to implement, where the degree of practicality is limited by the number of error sensors as well as the number of control sources required.

- **Robustness:** The method is desired to be robust with respect to different error sensor positions for a given control configuration. In general, positioning the error sensor can be considered as good or bad depending on if the sensing capabilities are affected by the nodal lines of the structure's response.

In past work on ASAC methods for cylindrical shells, it was shown that there is a trade-off between these features. Hence, the search for an ASAC metric that is capable of fulfilling these criteria is still ongoing. In this work, development of a metric that is able to satisfy the above criteria for cylindrical shells has been investigated. The resulting method is referred to as the weighted sum of spatial gradients (WSSG) control metric. In addition, in order to quantify and evaluate the performance of this control metric, the radiation modes for the external radiation from cylindrical shells has been developed, so that the radiated sound power can be numerically calculated in an efficient manner.

6.1 Summary of methods

6.1.1 Numerical modeling

In this work, Soedel shell theory has been used to model a simply supported cylindrical shell. Vibration of the shell in the radial direction was modeled using a point force excitation. This was used in order to obtain the spatial gradients for the WSSG control metric at the error sensor location. The spatial gradient terms were then weighted using the averaged weights over the frequency range of interest. The average weights were obtained by averaging the optimal weights at each resonance over all resonances in the frequency range of interest. The WSSG control metric was then minimized with respect to the control force.

A boundary element method was used to calculate the radiation resistance matrix for external radiation from a cylindrical shell. In this method, the cylinder was discretized into elementary radiators, where a single constant-velocity piston excitation was considered for each element individually. Calculation of the self and mutual-radiation impedances between the source element and all other elements then followed. The structural velocity was projected into the space spanned by the eigenvectors of the radiation resistance matrix (radiation modes). The radiated sound

power is the sum of all these (squared) radiation mode amplitudes, weighted by the corresponding eigenvalues, i.e., the efficiency of each radiation mode. The radiated sound power was calculated before and after the WSSG control.

6.1.2 Experimental methods

An aluminum cylindrical shell was considered for the experimental study of WSSG control on cylindrical shells. Simply supported boundary conditions were approximated by precisely machining grooves inside the ends of the cylinder, with a disk being press-fitted inside the groove. The WSSG control metric was implemented using four closely spaced accelerometers. The spatial gradients were obtained using a finite difference method. For optimal accuracy of the finite difference terms, the distance between the accelerometers was set to be 2.54 cm. The WSSG control metric was then adaptively implemented using a modified filtered-x LMS algorithm, incorporating the gradient of the WSSG. The addition of the disturbance signal and the control signal at each of the accelerometers was post processed to yield the actual error signals that are the weighted spatial gradient terms. The filtered-x LMS algorithm iteratively minimized the WSSG control metric in real time with respect to the control signal.

The radiated sound power was measured experimentally in the reverberation chamber at BYU, using the ISO-3741 standard [56]. The radiated sound power was determined before and after the WSSG control, in order to evaluate the amount of attenuation achieved.

6.2 Summary of findings

6.2.1 Radiation modes

Radiation modes to describe the external radiation from a baffled cylindrical shell have been developed analytically, using a Fourier series representation. While symmetric $m = 0$ modes have

been studied previously, radiation modes of higher circumferential index m have been presented here. By considering the wavenumber domain, it was shown that the coincidence effect plays an important role in the cut-on phenomenon observed for radiation modes with different axial mode numbers. The coincidence angle at a specific frequency is a determining factor in describing how efficient each group of radiation modes with a given axial mode number is, and this effect is responsible for the "leapfrog effect," where modes with a higher modal number jump above modes with a lower modal number, in terms of their efficiency. In general, the $(n, m = 0)$ radiation modes are the most efficient modes and therefore contribute most significantly to the radiated sound power. Their efficiencies asymptotically approach a value that is higher than the efficiencies associated with the $(n, m \neq 0)$ modes. With increasing frequency, the $(n, m = 0)$ mode with the highest axial index that has met the coincidence condition is the most efficient mode and leads to enhanced radiated sound power. It has also been observed that there is a degeneracy factor of two for the $(n, m \neq 0)$ modes, due to the circular geometry.

6.2.2 WSSG

It was observed that the WSSG function yields a very spatially uniform field for a simply supported shell, when the proper set of weights is applied. It was shown numerically that minimizing the WSSG function at the error sensor location can lead to significant attenuation of the radiated sound power. This suggests that the WSSG function for cylindrical shells is correlated with the radiated sound power for these structures. Comparison of the numerical results with other known methods that employ global measurements, such as minimizing the radiated sound power, minimizing global kinetic energy and minimizing volume velocity, shows that the WSSG control, using only one sensor location, is able to approximate the optimal performance determined by minimizing the radiated sound power.

By optimizing the performance of the WSSG control with respect to the set of weights used for

weighting the spatial gradient terms, it was shown that there is a large range of choices for weights that can result in near optimal performance of the WSSG control. Averaging the inverses of the squared structural wavenumbers along each axis over the range of frequencies results in a set of weights that falls into this category. Hence, the WSSG control metric is robust with respect to the choice of weights and there is about 1-2 dB variation in the performance of the method by using different choices of weights.

In addition, it was shown numerically that the WSSG control metric is very robust with respect to the error sensor positioning. There is typically less than 1 dB difference in the overall radiated sound power attenuation when the error sensor location is changed. Obviously, the control performance depends on the location of the control source. However, this has not been the focus of this research.

It was shown that the WSSG control is able to effectively attenuate the prominent radiation mode amplitudes. At a given frequency where the WSSG control is able to attenuate the sound effectively, comparing the radiation mode amplitudes after minimizing the WSSG with the radiation mode amplitudes after minimizing the radiated power, shows that the WSSG control metric is able to target the radiating components and attenuate the coupling between the most efficient radiation modes and the structural response.

The experimental results show that the WSSG control metric is able to attenuate the radiated sound power at most resonance frequencies and the general trends seem to agree with what the numerical model predicts. It was shown experimentally that the WSSG control metric is a robust method with respect to the error sensor positioning. It was shown that by changing the control configuration, the experimental results follow the trend observed in the numerical results, such that for a highly unfavorable source configuration, where minimizing the radiated sound power predicts no attenuation possible, the WSSG control metric does nothing both numerically and experimentally in order to avoid enhancing the radiated sound power. Comparing the attenuation

of the WSSG metric at the error sensor location before and after the control, considerable correspondence was observed between the numerical and the experimental results.

6.3 Contributions

This work develops the method of weighted sum of spatial gradients (WSSG) control metric for cylindrical shells. In the field of ASAC, the search for a method that is able to provide optimal control while providing robustness and convenience is still ongoing. This work provides a numerical and experimental development of the WSSG control metric that is able to approximate the optimal control results, while using only a single-point error measurement and providing robustness with respect to the error sensor location. Hence, this method offers a convenient and yet effective method that is practical for many applications.

In addition, an analytical solution was presented for the radiation resistance of cylindrical shells and the radiation modes for the external radiation from cylindrical shells was developed. This provides a method for calculating the radiated sound power efficiently and provides a means of targeting the most efficient radiation modes for developing ANC methods. Furthermore, taking the radiation modes into the wavenumber domain provides further insight in understanding the radiating and non-radiating components of the shell, in terms of the subsonic and supersonic components.

6.4 Recommendations

As mentioned, the WSSG control metric is able to approximate the optimal control results by using only a one-point error measurement. However, there is still room for improvement by finding ways that may drive the control results even closer to the optimal solution. In order to investigate WSSG further, here is a list of recommendations that could result in future improvements:

1. In the WSSG control metric, there are four parameters that are to be determined, i.e., α, β, δ, γ and the control force F_c. One can fix a number of these parameters to solve for the other parameters that result in the optimal control force, while the solution for the optimal control force is provided by minimizing the radiated sound power. This may lead to negative values for some of the weights. It would be interesting to further investigate the concept of negative weights. It may be that the weights can be considered to be complex quantities, where the minus sign corresponds to the phase of each of the terms with respect to each other.

2. In order to verify the mechanism observed for attenuating the radiation modes in the numerical results, it would be useful to scan the cylindrical shell in order to get the global velocity vector of the structure before and after the WSSG control and project them into the radiation modes. This would allow one to observe the mechanism that leads to sound power attenuation experimentally.

3. Since real-life applications are often large in scale, it would be useful to implement WSSG in a decentralized control system for larger structures and investigate the performance of this control metric for such a case.

4. In the past, the WSSG control metric was performed for planar structures, such as simply supported, clamped and ribbed plates. The WSSG control metric showed good performance for all these cases. Hence, the WSSG control metric could be investigated for clamped as well as stiffened cylindrical shells. It is expected that this metric would be able to provide good performance for curved structures with different dynamic conditions.

5. One could experimentally implement the WSSG control metric on a cylindrical shell that is closer to a simply supported shell in order to better compare numerical and experimental results. One could also carry out numerical investigations on shells that have more realistic boundary conditions.

6. For any given configuration, the WSSG control metric is able to provide close to optimal performance for that specific configuration. However, the best possible control performance will correspond to the configuration in which the control force is located in an optimal location with respect to the primary force. There is significant work that could be done to better optimize the control source location(s) for the WSSG control. For this type of geometry, the symmetry plays an important role. Therefore, one may be able to identify a general rule of thumb for optimal control force location(s) with respect to the primary force for this type of symmetry in curved structures.

7. It would be useful to investigate the WSSG control for cases in which more than one primary or more than one control source exists. A desirable outcome is to enhance the control performance. However, there are implications to simply adding more control sources. For example, there are limitations on the available computation time when implementing the control in real time and there may also be causality issues. Furthermore, multiple sources can potentially couple with each other and the control system needs to account for the impact of other control sources to the overall control response. Therefore, a matrix (rather than a vector) of transfer functions between the error sensors and each of the control forces will be needed. This increased complexity for the control system requires additional computation time. Therefore, there will be an optimal number of control forces which will lead to the most effective performance.

In general, the WSSG control metric has proven to be a convenient and practical method while being robust and providing near optimal solutions. However additional research focused on improving WSSG, or any other ASAC method that may come closer to the optimal solution using only a minimal number of local measurements would be valuable.

Bibliography

[1] S. D. Snyder, *Active noise control primer*, 2nd ed. (AIP Press, Springer, US, 2000), p. 43.

[2] S. D. Snyder, *Active noise control primer*, 2nd ed. (AIP Press, Springer, US, 2000), pp. 46-51.

[3] D. Guicking, "On the invention of active noise control by Paul Lueg," J. Acoust. Soc. Am. **87**, 2251-2254 (1990). http://dx.doi.org/10.1121/1.399195

[4] S. J. Elliott and P. A. Nelson, "Active noise control," IEEE Signal Processing Magazine **10**, 12-35 (1993). http://dx.doi.org/10.1109/79.248551

[5] C. R. Fuller, "Active structural acoustic control and smart structures," Final technical report, DTIC, Department of Mechanical Engineering, Virginia Polytech, (1991).

[6] F. Fahy and P. Gardonio, *Sound and structural vibration, radiation, transmission and response*, 2nd ed. (Academic Press, Oxford, UK, 2007), p. 30.

[7] A. Farshidianfar, M. H. Farshidianfar, M. J. Crocker and W. O. Smith, "Vibration analysis of long cylindrical shells using acoustical excitation," J. Sound. Vib. **330**, 3381-3399 (2011). http://dx.doi.org/10.1016/j.jsv.2011.02.002

[8] J. M. Zalas and J. Tichy, "Active attenuation of propeller blade passage noise," NASA CR-172386, (1984).

[9] H. C. Lester and C. R. Fuller, "Active control of propeller induced noise fields inside a flexible cylinder," AIAA Journal, paper no. 86-1957, (1986). http://dx.doi.org/10.2514/6.1986-1957

[10] R. J. Silcox, H. C. Lester and S. B. Abler, "An evaluation of active noise control in a cylindrical shell," NASA TM-89090, (1987).

[11] A. J. Bullmmore, P. A. Nelson and S. J. Elliott, "Theoretical studies of the active control of propeller-induced cabin noise," J. Sound. Vib., **140**, 191-217 (1990). http://dx.doi.org/10.1016/0022-460X(90)90524-4

[12] R. J. Silcox, C. R. Fuller and H. C. Lester, "Mechanisms of active control in cylindrical fuselage structures," AIAA Journal, **28**, 1397-1404 (1990). http://dx.doi.org/10.2514/6.1987-2703

[13] C. M. Dorling, G. P. Eatwell, S. M. Hutchines, C. F. Ross and S. G. C. Sutcliff, "A demonstration of active noise reduction in an aircraft cabin," J. Sound. Vib., **128**, 358-360 (1989). http://dx.doi.org/10.1016/0022-460X(89)90779-7

[14] S. J. Elliott, P. A. Nelson, I. M. Stothers and C. C. Boucher, "Preliminary results of in-flight experiments on the active control of propeller-induced cabin noise," J. Sound. Vib., **128**, 355-357 (1989). http://dx.doi.org/10.1016/0022-460X(89)90778-5

[15] S. J. Elliott, P. A. Nelson, I. M. Stothers and C. C. Boucher, "In-flight experiments on the active control of propeller-induced cabin noise," J. Sound. Vib., **140**, 219-238 (1990). http://dx.doi.org/10.1016/0022-460X(90)90525-5

[16] J. V. Warner and R. J. Bernhard, "Digital control of local sound fields in aircraft passenger compartment," AIAA Journal, **28**, 284-289 (1990). http://dx.doi.org/10.2514/3.10386

[17] C. R. Fuller, S. D. Snyder, C. H. Hansen and R. J. Silcox, "Active control of interior noise in model aircraft fuselages using piezoceramic actuators," AIAA Journal, **30**, 2613-2617 (1992). http://dx.doi.org/10.2514/3.11275

[18] G. H. Koopmann, L. Song and B. Fahnline, "A method for computing acoustic fields based on the principle of wave superposition," J. Acoust. Soc. Am. **86**, 2433-2438 (1989). http://dx.doi.org/10.1121/1.398450

[19] G. V. Borgiotti, "The power radiated by a vibrating body in an acoustic fluid and its determination from boundary measurements," J. Acoust. Soc. Am. **88**, 1884-1893 (1990). http://dx.doi.org/10.1121/1.400211

[20] A. Sarkissian, "Acoustic radiation from finite structures," J. Acoust. Soc. Am. **90**, 574-578 (1991). http://dx.doi.org/10.1121/1.401231

[21] D. M. Photiadis, "The relationship of singular value decomposition to wave-vector filtering in sound radiation problems," J. Acoust. Soc. Am. **88**, 1152-1159 (1990). http://dx.doi.org/10.1121/1.399811

[22] G. V. Borgiotti, "The determination of the acoustic far field of a radiating body in an acoustic fluid from boundary measurements," J. Acoust. Soc. Am. **93**, 2788-2797 (1993). http://dx.doi.org/10.1121/1.405826

[23] K. Naghshineh and G. H. Koopmann, "A design method for achieving weak radiator structures using active vibration control," J. Acoust. Soc. Am. **9**, 856-870 (1992). http://dx.doi.org/10.1121/1.403956

[24] K. Naghshineh and G. H. Koopmann, "Active control of sound power using acoustic basis functions as surface velocity filters," J. Acoust. Soc. Am. **93**, 2740-2752 (1993). http://dx.doi.org/10.1121/1.405850

[25] G. V. Borgiotti and K. E. Jones, "Frequency independence property of radiation spatial filters," J. Acoust. Soc. Am. **96**, 3516-3524 (1994). http://dx.doi.org/10.1121/1.411407

[26] J. M. Fisher, J. D. Blotter, S. D. Sommerfeldt and K. L. Gee, "Development of a pseudo-uniform structural quantity for use in active structural acoustic control of simply supported plates: An analytical comparison," J. Acoust. Soc. Am. **131**, 3833-3840 (2012). http://dx.doi.org/10.1121/1.3699264

[27] D. R. Thomas, P. A. Nelson and S. J. Elliott, "Active control of the transmission of sound through a thin cylindrical shell, part I: The minimization of vibrational energy," J. Sound. Vib. **167**, 91-111 (1993). http://dx.doi.org/10.1006/jsvi.1993.1323

[28] D. R. Thomas, P. A. Nelson and S. J. Elliott, "Active control of the transmission of sound through a thin cylindrical shell, part II: The minimzation of acoustic potential energy," J. Sound. Vib. **167**, 113-128 (1993). http://dx.doi.org/10.1006/jsvi.1993.1324

[29] K. Naghshineh, W. Chen and G. H. Koopmann, "Use of acoustic basis functions for active control of sound power radiated from a cylindrical shell," J. Acoust. Soc. Am. **103**, 1897-1903 (1998). http://dx.doi.org/10.1121/1.421341

[30] X. Pan and C. H. Hansen, "Active conbtrol of vibration transmission in a cylindrical shell," J. Sound. Vib. **203**, 409-434 (1997). http://dx.doi.org/10.1006/jsvi.1996.9987

[31] C.-Y. Wang and R. Vaicaitis, "Active control of vibrations and noise of double wall cylindrical shells," J. Sound. Vib. **216**, 865-888 (1998). http://dx.doi.org/10.1006/jsvi.1998.1740

[32] C. R. Fuller, S. J. Elliott and P. A. Nelson, *Active control of vibration*, (Academic Press, London, 1996).

[33] S. J. Kim and J. D. Jones, "Optimal design of piezoactuators for active noise and vibration control," AIAA Journal, **29** 1991.

[34] J. Qiu and J. Tani, "Vibration control of a cylindrical shell used in MRI equipment," Smart Mater. Struct. **4**, A75-A81 (1995). http://dx.doi.org/10.1088/0964-1726/4/1A/009

[35] J. Tani, J. Qiu and H. Miura, "Vibration control of a cylindrical shell using piezolelectric actuators," Journal of Intelligent Material Systems and Structures, **6**, 380-388 (1995). http://dx.doi.org/abs/10.1177/1045389X9500600309

[36] V. Dogan and R. Vaicaitis, "Active control of nonlinear cylindrical shell vibrations under random excitation," Journal of Intelligent Material Systems and Structures, **10**, 422-429 (1999). http://dx/doi.org/doi/abs/10.1177/1045389X9901000508

[37] J. P. Maillard and C. R. Fuller, "Active control of sound radiation from cylinders with piezoelectric actuators and structural acoustic sensing," J. Sound. Vib. **222**, 363-387 (1999). http://dx.doi.org/10.1006/jsvi.1998.1990

[38] O. R. Lin, Z.-X. Liu and Z.-L. Wang, "Cylindrical panel interior noise control using a pair of piezoelectric actuator and sensor," J. Sound. Vib. **246**, 525-541 (2001). http://dx.doi.org/10.1006/jsvi.2001.3672

[39] T. McGann, *Active vibration control of finite thin-walled cylindrical shells*, Bachelor's thesis, The university of New South Wales, School of mechanical and manufacturing engineering, (2008).

[40] J. W. Sohn and S.-B. Choi, "Active vibration control of a cylindrical structure using flexible piezoactuators: experimental work in air and water environments," Smart Mater. Struct. **23**, (2014). http://dx.doi.org/10.1088/0964-1726/23/11/117002

[41] A. Loghmani, M. Danesh, M. Keshmiri and M. M. Savadi, "Theoretical and experimental study of active vibration control of a cylindrical shell using piezoelectric disks," Journal of

Low Frequency Noise, Vibration and Active Control, **34**, 269-288 (2015). http://dx.doi.org/abs/10.1260/0263-0923.34.3.269

[42] G. Goddu, D. McDowell and B. S. Bingham, "Adaptive control of radiated noise from a cylindrical shell using active fiber composite actuators," Proc. SPIE **3991**, Smart Structures and Materials: Industrial and Commercial Applications of Smart Structures Technologies, 95 (2000). http://dx.doi.org/10.1117/12.388150

[43] K. Song, "Active control of radiated noise from a cylindrical shell using external piezoelectric panels," Ph.D. Thesis, Massachusetts Institute of Technology, Dept. of Aeronautics and Astronautics, (2002). http://hdl.handle.net/1721.1/29244

[44] G. Jin, X. Liu, Zh. Lio and T. Yang, "Active control of structurally radiated sound from an elastic cylindrical shell," Journal of Marine Science and Application, **10**, 88-97 (2011). http://dx.doi.org/10.1007/s11804-011-1046-5

[45] Y. Cao, H. Sun, F. An and X. Li, "Active control of low-frequency sound radiation by cylindrical shell with peizoelectric stack force actuators," J. Sound. Vib. **331**, 2471-2484 (2012). http://dx.doi.org/10.1016/j.jsv.2012.02.001

[46] H. S. Kim, J. W. Sohn, J. Jeon and S.-B. Choi, "Reduction of the radiating sound of a submerged finite cylindrical shell structure by active vibration control," Sensors, **13**, 2131-2147 (2013). http://dx.doi.org/10.3390/s130202131

[47] H. Shen, J. Wen, D. Yu, M. Asgari and X. Wen, "Control of sound and vibration of fluid-filled cylindrical shells via periodic design and active control," J. Sound. Vib. **332**, 4193-4209 (2013). http://dx.doi.org/10.1016/j.jsv.2013.03.007

[48] X. Cao, L. Shi, X. Zhang and G. Jiang, "Active control of acoustic radiation from laminated cylindrical shells integrated with a piezoelectric layer," Smart Mater. Struct. **22**, (2013). http://dx.doi.org/10.1088/0964-1726/22/6/065003

[49] X. Ma, G. Jin and Zh. Liu, "Active structural acoustic control of an elastic cylidnrical shell coupled to a two-stage vibration isolation system," International Journal of Mechanical Sciences, **79**, 182-194 (2014). http://dx.doi.org/10.1016/j.ijmecsci.2013.12.010

[50] S. D. Sommerfeldt and P. J. Nashif, "An adaptive filtered-x algorithm for energy-based active control," J. Acoust. Soc. Am. **96**, 300-306 (1994). http://dx.doi.org/10.1121/1.411308

[51] J. M. Fisher, "Development of Pseudo-uniform structural velocity metric for use in active structural acoustic control," Master's Thesis, Brigham Young University, Department of Mechanical Engineering (2010).

[52] D. R. Hendricks, W. R. Johnson, S. D. Sommerfeldt and J. D. Blotter, "Experimental active structural acoustic control of simply supported plates using a weighted sum of spatial gradients," J. Acoust. Soc. Am. **136**, 2598-2608 (2014). http://dx.doi.org/10.1121/1.4898046

[53] Y. Cao, S. D. Sommerfeldt, W. Johnson, J. D. Blotter and P. Aslani, "An analysis of control using the weighted sum of spatial gradients in active structural acoustic control for flat panels," J. Acoust. Soc. Am. **138**, 2986-2997 (2015). http://http://dx.doi.org/10.1121/1.4934730

[54] Y. Cao, S. D. Sommerfeldt and J. D. Blotter, "Active structural acoustic control of plates with different boundary conditions using a weighted sum of spatial gradients," Proceedings of Inter-Noise 2015, 3260-3270 (2015).

[55] W. R. Johnson, D. R. Hendricks, S. D. Sommerfeldt and J. D. Blotter, "Active structural acoustic control of clamped flat plates using a weighted sum of spatial gradients," Shock and Vibration, **2015**, Article ID 628685, (2015). http://dx.doi.org/10.1155/2015/628685.

[56] Accredited Standards Committe S12, Noise, Acoustical Society of America, "Acosutics - Determination of sound power levels of noise sources using sound pressure - Precision mehtod of reverberation rooms," ANSI Standard, ANSI S12.51-2002. ISO 3741 (1999).

[57] W. Leissa, *Vibration of Shells*, (NASASP-288), US Government Printing Office, Washington, DC, (1973).

[58] M. Amabili and M. P. Paidoussis, "Review of studies on geometrically nonlinear vibrations and dynamics of circular cylindrical shells and panels, with and without fluid structure interaction," Appl. Mech. Rev. *56*, 349–381 (2003). http://dx.doi.org/10.1115/1.1565084

[59] A. E. H. Love, "The small free vibrations and deformations of thin elastic shells," Philos. Trans. Roy. Soc. London. A, **179** 491-546 (1888).

[60] L. H. Donnell, "Stability of thin-walled tubes under tension," NACA Report No. 479, (1993).

[61] S. Timoshenko and S. Woinowsky-Krieger, *Theory of shells*, (McGraw-Hill, New York, 1959).

[62] W. Flügg, *Handbook of engineering mechanics*, (McGraw-Hill, New York, 1962).

[63] A. I. Lur'ye, "General theory of elastic shells," (in Russian), Prikl. Mat. Meh. **4**, 7-34 (1940).

[64] E. Reissner, "A new derivation of the equations for the deformation of elastic shells," Amer. J. Math. **63**, 177-184 (1941).

[65] R. Byrne, "Theory of small deformations of a thin elastic shell," Sem. Rep. Math. Univ. Calif. Publ. Math., **2**, 103-152 (1944).

[66] J. L. Sanders, *An Improved First Approximation Theory for Thin Shells*, NASA TR-R24, U.S. Government Printing Office, Washington, DC (1959).

[67] K. K. Livanov, "Axisymmetric vibrations of a simply-supported cylidnrical shells," PMM, **25**, 742-745 (1961). http://dx.doi.org/10.1016/S0021-8928(61)80014-2

[68] A. L. Goldenveizer, *Theory of thin shells*, (Pergamon Press, Elmsford, New York, 1961).

[69] V. V. Novozhilov, *The theory of thin elastic shells*, (P. Noordhoff, Groningen, The Netherlands, 1964).

[70] V. Z. Vlasov, "General Theory of Shells and Its Applications in Engineering," (Translation from Russian), NASA TTF-99, U.S. Governmental Printing Office, Washington, D.C. (1964).

[71] K. Forsberg, *A Review of Analytical Methods used to Determine the Modal Characteristics of Cylindrical Shells*, (NASACR-613), National Aeronautics and Space Administration, Washington DC, (1966).

[72] H. Kraus, *Thin elastic shells*, (Wiley, New York, 1967).

[73] S. A. Rinehart and J. T. S. Wang, "Vibration of simply supported cylindrical shells with longitudinal stiffeners," J. Sound. Vib., **24**, 151-163 (1972). http://dx.doi.org/10.1016/0022-460X(72)90945-5

[74] X. M. Zhang, G. R. Liu and K. Y. Lam, "Vibration analysis of thin cylindrical shells using wave propagation approach," J. Sound. Vib. **239**, 397-403 (2001).

[75] X. B. Li, "Study on free vibration analysis of circular cylindrical shells using wave propagation," J. Sound. Vib. **311**, 667-682 (2008).

[76] W. Soedel, *Vibrations of shells and plates*, 3rd ed., (Marcel Dekker Inc., New York 2004), pp. 93-102.

[77] A. Farshidianfar and P. Oliazadeh, "Free vibration analysis of cicrular cylindrical shells: Comparsion of different shell theories," International Journal of Mechanics and Applications, **2**, 74-80 (2012). http://dx.doi.org/10.5923/j.mechanics.20120205.04

[78] W. Soedel, *Vibrations of shells and plates*, 3rd ed., (Marcel Dekker Inc., New York 2004). pp. 8-9.

[79] W. Soedel, *Vibrations of shells and plates*, 3rd ed., (Marcel Dekker Inc., New York 2004). pp. 13-22.

[80] W. Soedel, *Vibrations of shells and plates*, 3rd ed., (Marcel Dekker Inc., New York 2004). pp. 22-24.

[81] W. Soedel, *Vibrations of shells and plates*, 3rd ed., (Marcel Dekker Inc., New York 2004). pp. 25-27.

[82] W. Soedel, *Vibrations of shells and plates*, 3rd ed., (Marcel Dekker Inc., New York 2004). pp. 30-35.

[83] W. Soedel, *Vibrations of shells and plates*, 3rd ed., (Marcel Dekker Inc., New York 2004). pp. 207-225.

[84] C. R. Fuller and J. D. Jones, "Experiments on reduction of propeller induced interior noise by active control of cylinder vibration," J. Sound. Vib. **112**, 389-395 (1987). http://dx.doi.org/10.1016/S0022-460X(87)80208-0

[85] C. R. Fuller, "Analysis of active control of sound radiation from elastic plates by force inputs," Proceedings of Inter-Noise '88, Avignon, **2**, 1061-1064 (1988).

[86] C. R. Fuller, "Active control of sound tranmission/radiation from elastic plates by vibration inputs. I: Analysis," J. Sound. Vib. **136**, 1-15 (1990). http://dx.doi.org/10.1016/0022-460X(90)90933-Q

[87] B. T. Wang, C. R. Fuller, and E. K. Dimitriadis, "Active control of structurally radiated noise using multiple piezoelectric actuators," AIAA Journal, **29**, 1802-1809 (1991). http://dx.doi.org/10.2514/3.10805

[88] C. R. Fuller, C. H. Hansen, and S. D. Snyder, "Active control of sound radiation from a vibrating panel by sound sources and vibration inputs: An experimental comparison," J. Sound Vib. **145**, 195-216 (1991). http://dx.doi.org/10.1016/0022-460X(91)90587-A

[89] S. D. Snyder and C. H. Hansen, "Mechanisms of active noise control using vibration sources," J. Sound Vib. **147**, 519-525 (1991). http://dx.doi.org/10.1016/0022-460X(91)90499-A

[90] R. L. Clark and C. R. Fuller, "A model reference approach for implementing active structuiral acoustic control," J. Acoust. Soc. Am. **92**, 1534-1544 (1992). http://dx.doi.org/10.1121/1.403945

[91] R. L. Clark and C. R. Fuller, "Experiments on active control of structurally radiated sound using multiple piezoceramic actuators," J. Acoust. Soc. Am. **91**, 3313-3320 (1992). http://dx.doi.org/10.1121/1.402821

[92] J. Pan, S. D. Snyder, C. H. Hansen, and C. R. Fuller, "Active control of far field sound radiated by a rectangular panel: A general analysis," J. Acoust. Soc. Am. **91**, 2056-2066 (1992). http://dx.doi.org/10.1121/1.403691

[93] C. Guigou and C. R. Fuller, "Active control of sound radiation from a simply supported beam: Influence of bending near-field waves," J. Acoust. Soc. Am. **93**, 2716-2725 (1993). http://dx.doi.org/10.1121/1.405847

[94] B. J. Brevart and C. R. Fuller, "Active control of coupled wave propogation in fluid-filled elastic cylindrical shells," J. Acoust. Soc. Am. **94**, 1467-1475 (1993). http://dx.doi.org/10.1121/1.408149

[95] J. P. Carneal and C. R. Fuller, "Active structural acoustic control of noise transmission through double panel system," AIAA Journal, **33**, 618-623 (1995). http://dx.doi.org/10.2514/3.12623

[96] Z. Li, C. Guigou, C. R. Fuller and R. A. Burdisso, "Desing of active structural acoustic control systems using a nonvolumetric eigenproperty assignment approach," J. Acoust. Soc. Am. **101**, 2088-2096 (1997). http://dx.doi.org/10.1121/1.418139

[97] C. R. Fuller, S. J. Elliott, and P. A. Nelson, *Active Control of Vibration* (Academic, London, 1997), pp. 223-251.

[98] M. E. Johnson and S. J. Elliott, "Active control of sound radiation from vibrating surfaces using arrays of discrete actuators," J. Sound. Vib. **207**, 743-759 (1997). http://dx.doi.org/10.1006/jsvi.1997.1166

[99] R. H. Cabell and C. R. Fuller, "A principal component algorithm for feedforward active noise and vibration control," J. Sound. Vib. **227**, 159-181 (1999). http://dx.doi.org/10.1006/jsvi.1999.2338

[100] P. Masson and A. Berry, "Comparison of several strategies in the active structual acoustic control using structural strain measurements," J. Sound. Vib. **233**, 703-722 (2000). http://dx.doi.org/10.1006/jsvi.1999.2839

[101] B. Bingham, M. J. Atalla and N. W. Hagood, "Comparison of structural-acosutic control designs on an active composite panel," J. Sound. Vib. **244**, 761-778 (2001). http://dx.doi.org/10.1006/jsvi.2000.3536

[102] A. P. Berkhoff, "Piezoelectric sensor configuration for active structural acosutic control," J. Sound. Vib. **246**, 175-183 (2001). http://dx.doi.org/10.1006/jsvi.2000.3580

[103] J. P. Carneal and C. R. Fuller, "An analytical and experimental investigation of active structural acoustic control of noise transmission through double panel systems," J. Sound. Vib. **272**, 749-771 (2004). http://dx.doi.org/10.1016/S0022-460X(03)00418-8

[104] J. T. Lee, "Active structural acoustic control of beams using active constrained layer damping through loss factor maximization," J. Sound. Vib. **287**, 481-503 (2005). http://dx.doi.org/10.1016/j.jsv.2004.11.006

[105] S.-B. Choi, "Active structural acoustic control of a smart plate featuring piezoelectric actuators," J. Sound. Vib. **294**, 421-429 (2006). http://dx.doi.org/10.1016/j.jsv.2006.01.040

[106] G. Pinte, R. Boonen, W. Desmet and P. Sas, "Active structural acoustic control of repetitive impact noise," J. Sound. Vib. **319**, 768-794 (2009). http://dx.doi.org/10.1016/j.jsv.2008.07.016

[107] S. G. Hill, N. Tanaka, S. D. Snyder, "A generalized approach for active control of structural-interior global noise," J. Sound. Vib. **326**, 456-475 (2009). http://dx.doi.org/10.1016/j.jsv.2009.06.014

[108] G. Pinte, S. Devos, B. Stallaert, W. Symens, J. Swevers and P. Sas, "A piezo-based bearing for the active structural acoustic control of rotating machinery," J. Sound. Vib. **329**, 1235-1253 (2010). http://dx.doi.org/10.1016/j.jsv.2009.10.036

[109] S. G. Hill, N. Tanaka and H. Iwamoto, "A generalised approach for active control of structural-interior global noise: Practical implementation," J. Sound. Vib. **331**, 3227-3239 (2012). http://dx.doi.org/10.1016/j.jsv.2012.02.027

[110] K. Chevva, F. Sun, A. Blanc and J. Mendoza, "Active vibration control using minimum actuation power," J. Sound Vib. **340**, 1-21 (2015). http://dx.doi.org/10.1016/j.jsv.2014.06.019

[111] Y. Li, X. Wang, R. Huang and Zh. Qiu, "Active vibration and noise control of vibro-acosutic system by using PID controller," J. Sound. Vib. **348**, 57-70 (2015). http://dx.doi.org/10.1016/j.jsv.2015.03.017

[112] G. Zhao, N. Alujevic, B. Depraetere, G. Pinte, J. Swevers and P. Sas, "Experimental study on active structural acoustic control of rotating machinery using rotating piezo-based inertial actuators," J. Sound. Vib. **348**, 15-30 (2015). http://dx.doi.org/10.1016/j.jsv.2015.03.013

[113] A. Manela and L. Pogorelyuk, "Active noise control of a vibrating surface: Continuum and non-continuum investigations on vibroacoustic sound reduction by a secondary heat-flux source," J. Sound Vib. **358**, 20-43 (2015). http://dx.doi.org/10.1016/j.jsv.2015.08.016

[114] R. Boulandet, M. Michau, P. Micheau and A. Berry, "Aircraft panel with sensorless active sound power reduction capabilities through virtual mechanical impedances," J. Sound. Vib. **361**, 2-19 (2016). http://dx.doi.org/10.1016/j.jsv.2015.09.042

[115] T. Kiazuka, N. Tanaka and K. Nakano, "Active control of sound transmission using structural modal filters," J. Sound. Vib. **381**, 14-29 (2016). http://dx.doi.org/10.1016/j.jsv.2016.06.018

[116] S. D. Snyder and N. Tanaka, "On feedforward active control of sound and vibration using vibration error signals," J. Acoust. Soc. Am. **94**, 2181-2193 (1993). http://dx.doi.org/10.1121/1.407489

[117] M. E. Johnson and S. J. Elliott, "Active control of sound radiation using volume velocity cancellation," J. Acoust. Soc. Am. **98**, 2174-2186 (1995). http://dx.doi.org/10.1121/1.413332

[118] X. Pan and C. H. Hansen, "Active vibration control of waves in simple structures with multiple error sensors," J. Acoust. Soc. Am. **103**, 1673-1676 (1998). http://dx.doi.org/10.1121/1.421259

[119] T. C. Sors and S. J. Elliott, "Volume velocity estimation with accelerometer arrays for active structural acoustic control," J. Sound. Vib. **258**, 867-883 (2002). http://dx.doi.org/10.1006/jsvi.2002.5186

[120] G. Jin, X. Liu, Zh. Liu and T. Yang, "Active control of structurally radiated sound from an elastic cylindrical shell," J. Marine Sci. Appl. **10**, 88-97 (2011). http://dx.doi.org/1671-9433(2011)01-0088-10

[121] S. D. Sommerfeldt and P. J. Nashif, "A comparison of control strategies for minimizing the sound field in enclosures," Proceedings of Noise-Con, **91**, 299-306 (1991).

[122] P. J. Nashif and S. D. Sommerfeldt, "An active noise control strategy for minimizing the energy density in enclosures," Proceedings of Inter-Noise, **92**, 357-362 (1992).

[123] H. Schneider and G. P. Barker, *Matrices and linear algebra*, 2nd ed. (Dover Publications, Inc. New York, 1989).

[124] Lord Rayleigh, *The theory of sound*, 2nd ed. (Dover Publications, Inc. New York, 1978), pp. 116-118.

[125] D. Guicking, "Active noise control - A review based on patent applications," Proceedings Noise, **93**, 153-158 (1993).

[126] C. H. Hansen, "Basics of Active Noise Control," Australian Acoustical Society Institution for Engineers, Notes for a half day workshop, (1996).

[127] C. H. Hansen, *Understanding active noise cancellation*, (Spon Press, London, 2001), Ch. 1.

[128] S. D. Snyder, *Active noise control primer*, (AIP Press, Springer, New York, 2000), pp. 112-126.

[129] C. H. Hansen, *Understanding active noise cancellation*, (Spon Press, London, 2001).

[130] S. D. Snyder, *Active noise control primer*, (AIP Press, Springer, New York, 2000).

[131] O. Tokhi and S. Veres, *Active sound and vibration control, theory and applicaiton*, (The Institution of Electrical Engineering, London, 2002).

[132] S. J. Elliott, *Signal processing for active control*, (Academic Press, New York, 2001), pp. 154-160.

[133] S. J. Elliott, *Signal processing for active control*, (Academic Press, New York, 2001), pp. 136-137.

[134] S. J. Elliott, *Signal processing for active control*, (Academic Press, New York, 2001), p. 133.

[135] S. J. Elliott, *Signal processing for active control*, (Academic Press, New York, 2001), pp. 134-136.

[136] F. Fahy, P. Gardonio, *Sound and structural vibration, radiation, transmission and response*, 2nd ed., (Academic Press, Oxford, UK, 2007), pp. 159-175.

[137] S. J. Elliott and M. E. Johnson, "Radiation modes and the active control of sound power," J. Acosut. Soc. Am. **94**, 2194-2204 (1993). http://dx.doi.org/10.1121/1.407490

[138] P.- T. Chen and J. H. Ginsberg, "Complex power, reciprocity and radiation modes for submerged bodies," J. Acoust. Soc. Am. **98**, 3341-3343 (1995). http://dx.doi.org/10.1121/1.413821

[139] B. S. Cazzolato and C. H. Hansen, "Active control of sound transmission using structural error sensing," J. Acoust. Soc. Am. **104**, 2878-2889 (1998). http://dx.doi.org/10.1121/1.423872

[140] F. Fahy and P. Gardonio, *Sound and structural vibration, radiation, transmission and response*, 2nd ed., (Academic Press, Oxford, UK, 2007), p. 160.

[141] K. A. Cunefare and G. H. Koopmann, "A boundary element approach to optimization of active noise control sources on three-dimensional structures," ASME J. Vib. Acoust. **113**, 387-394 (1991). http://dx.doi.org/10.1115/1.2930196

[142] K. A. Cunefare, G. H. Koopmann, "Global optimum active noise control: Surface and far field effects," J. Acoust. Soc. Am. **90**, 365-373 (1991). http://dx.doi.org/10.1121/1.401259

[143] C. G. Molo and R. J. Bernhard, "Generalized method of predicting optimal performance of active noise controllers," AIAA Journal. **27**, 1473-1478 (1989). http://dx.doi.org/10.2514/3.10290

[144] C. G. Molo and R. J. Bernhard, "Numerical evaluation of the performance of active noise controllers," ASME J.Vib. Acoust. **112**, 230-236 (1990). http://dx/doi.org/10.1115/1.2930117

[145] F. Fahy and P. Gardonio, *Sound and structural vibration, radiation, transmission and response*, 2nd ed. (Academic Press, Oxford, UK, 2007), pp. 170-172.

[146] K. A. Cunefare and M. N. Currey, "On the exterior acoustic radiation modes of structures," J. Acoust. Soc. Am. **96**, 2302-2312 (1994). http://dx.doi.org/10.1121/1.410102

[147] M. N. Currey and K. A. Cunefare, "The radiation modes of baffled finite plates," J. Acoust. Soc. Am. **98**, 1570-1580 (1995). http://dx.doi.org/10.1121/1.413423

[148] M. C. Junger, "Radiation loading of cylindrical and spherical surfaces," J. Acoust. Soc. Am. **24**, 288-289 (1952). http://dx.doi.org/10.1121/1.1906892

[149] M. C. Junger, "The physical interpretation of the expression for an outgoing wave in cylindrical coordinates," J. Acoust. Soc. Am. **25**, 40-47 (1953). http://dx.doi.org/10.1121/1.1907005

[150] M. C. Junger and D. Feit, *Sound, structures, and their interactions*, 2nd ed. (Acoustical Society of America, 1993), pp. 166-181.

[151] D. H. Robey, "On the radiation impedance of an array of finite cylinders," J. Acoust. Soc. Am. **27**, 706-710 (1955). http://dx.doi.org/10.1121/1.1908001

[152] C. H. Sherman, *Mutual radiation impedance between pistons on spheres and cylinders*, (US Navy USL Research No. 405, 1958).

[153] M. C. Junger, "Surface pressures generated by pistons on large spherical and cylindrical baffles," J. Acoust. Soc. Am. **41**, 1336-1346 (1967). http://dx.doi.org/10.1121/1.1910479

[154] P. M. Morse and K. U. Ingard, *Radiation from Cylinders, in: Theoretical Acoustics*, 1st ed., (Princeton University Press, New Jersey, 1986), pp. 356-366.

[155] W. Soedel, *Vibrations of shells and plates*, 3rd ed. (Marcel Dekker Inc., New York 2004), pp. 502-505.

[156] B. G. Korenev, *Bessel functions and their applications, analytical methods and special functions*, (Taylor and Francis, NY, 2002), pp. 11-12.

[157] F. Fahy and P. Gardonio, *Sound and structural vibration, radiation, transmission and response*, 2nd ed. (Academic Press, Oxford, UK, 2007), pp. 27-29.

[158] F. Fahy and P. Gardonio, *Sound and structural vibration, radiation, transmission and response*, 2nd ed. (Academic Press, Oxford, UK, 2007), pp. 217-219.